POLYMORPHISM WITHIN THE FENAMATE FAMILY:

THE CONSEQUENCES OF CHLORO-METHYL

REPLACEMENT

Rona Elizabeth Watson

July 2016

University College London
Department of Chemistry
20 Gordon Street
London
WC1H 0AJ
United Kingdom

Declaration

I, Rona Elizabeth Watson, confirm that the work presented in this thesis is my own. Where information has been derived from other sources, I confirm that this has been indicated in the thesis.

Rona Elizabeth Watson

Abstract

Both mefenamic acid (MA) and tolfenamic acid (TA) are polymorphic with three and five forms respectively. MA and TA are structurally similar molecules that differ in the replacement of a methyl on MA with a chloro group on TA. This thesis uses a joint computational and experimental approach to investigate the polymorphism of MA and TA and explores differences in the packings upon chloro-methyl replacement.

To compliment an earlier crystal structure prediction (CSP) study on TA, the crystal energy landscape of MA was computed. Analysis showed there were a number of predicted structures that were competitive in energy with the known forms of MA.

Isostructural relationships between MA and TA that were identified from the observed polymorphs and the predicted forms from the CSP studies were investigated in a range of templating experiments. The isostructural, not isomorphous, relationship between MA I and TA IV was explored and a solid solution series, isomorphous with MA form I, was obtained from ethanol and characterised by low temperature single crystal X-ray diffraction (SCXRD). Seeding an ethanol solution of TA with MA form I seeds nucleated a new polymorph of TA (VI) that was characterised by SCXRD and was isomorphous with MA form I.

A second new form of TA (VII) was discovered, and identified by powder X-ray diffraction, when exploring the sublimation of TA onto a copper surface. Thermal analysis showed that TA VII transformed to TA I upon heating. Using a similar sublimation procedure, it was observed that if MA was sublimed onto copper, form I was obtained, yet if MA was sublimed onto glass, form II was obtained.

The CSP methodology was tested by participation in the CCDC blind test and was successful in predicting the observed crystal structure of the cocrystal XXV as the global minimum.

Acknowledgements

Table of Contents

List of Figures

List of Tables

List of Abbreviations

Abbreviation	Definition
3,5-DNBA	3,5-dinitrobenzoic acid
API	active pharmaceutical ingredient
CBZ	carbamazepine
CCDC	Cambridge Crystallographic Data Centre
CSD	Crystal Structure Database
CSP	crystal structure prediction
CYH	cyheptamide
DFT	density functional theory
DHC	dihydrocarbamazepine
DMA	distributed multipole analysis
DSC	differential scanning calorimetry
DSC-XRD	simultaneous DSC-synchrotron X-ray diffraction
FA	fenamic acid
FDA	U.S. Food and Drug Administration
FFA	flufenamic acid
GDMA	Gaussian distributed multipole analysis
GRAS	generally recognised as safe
HBPC	hydrogen bond propensity calculation
HT	high-throughput
LAM	local approximate model
MA	mefenamic acid
NSAID	non-steroidal anti-inflammatory
PCM	polarisable continuum model
PIHn	polymer-induced heteronucleation
PXRD	powder X-ray diffraction
QCM	quartz crystal microbalance
SAM	self-assembled monolayer
SCXRD	single crystal X-ray diffraction
TA	tolfenamic acid
TS	Tkatchenko-Scheffler dispersion correction

1 Introduction

1.1 Polymorphism

Polymorphism is the ability of a compound to crystallise in multiple crystal forms, each with a unique unit cell. There are two main types of polymorphism (packing and conformational) that are exhibited depending on the compound in question. Packing polymorphism is the only type of polymorphism that rigid molecules can display and is observed when a fixed molecular conformation is found in different packing arrangements within the crystal lattices of different polymorphs. Additionally, flexible molecules can display conformational polymorphism where the molecule is found in different conformations in different polymorphs.[1]

Although polymorphs of a particular compound are identical in chemical composition, they can have differing physical properties. Research surrounding the phenomenon of polymorphism is mainly concerned with predicting, controlling and characterising polymorphic systems in order to determine the relevant crystalline form for a specific application within different industries including the fields of explosives, agrochemicals, dyestuffs, foods, pigments and pharmaceuticals.

One of the difficulties within the field of polymorphism is the ability to predict whether a compound will exhibit polymorphism or not. A recent statistical study by Cruz-Cabeza et al.[2] analysed crystallographic data from the Crystal Structure Database (CSD, a community built database of crystallographic data hosted by the Cambridge Crystallographic Data Centre, CCDC) and concluded that one in three compounds display polymorphism. Similar analysis by Cruz-Cabeza on two industrial solid form screens (conducted at Hoffmann-La Roche and Eli Lilly). showed that at least one in two compounds display polymorphism.[2] Furthermore, they found no correlation between either molecular flexibility or the size of the molecule and the ability of the compound to be polymorphic. Cruz-Cabeza et al. also noted that each compound is unique and without appropriate experimentation, there is no way of knowing how many crystal forms will exist for a given system. There is also no way of knowing which crystallisation methods should be attempted in order to obtain potential polymorphs or know what the physical properties of the polymorphs might be, should they exist.

Within the pharmaceutical industry, the dissolution rate and solubility of different polymorphs can affect the bioavailability of a drug that is administered in the solid form.[3] Therefore, it is important to understand and fully characterise polymorphic systems of active pharmaceutical ingredients (APIs) to ensure that the most appropriate polymorph of an API is developed in terms of application, storage and production and that the chosen form is safe for use and effective when administered to a patient.[4]

It is important to screen compounds for polymorphism in order to avoid cases where the late discovery of a new polymorph can compromise the use of medication and cause a company to incur great costs. In 1998, two years after Ritonavir, a treatment for Acquired Immunodeficiency Syndrome (AIDS), had originally been marketed, a new, more stable, crystal form was discovered when a batch failed the dissolution requirements.[5, 6] The late nucleation of this more stable form highlighted a lack of control in the production process. Accidental seeding of the marketed form (form I) with even just a trace of the more stable form (form II) resulted in form I transforming to the less bioavailable form II.[6]

The Ritonavir case highlights the risk that a thermodynamically stable polymorph can remain elusive for a length of time. It also provides an example of the phenomenon of "disappearing polymorphs";[7, 8] that once a more stable form has been obtained, it may not be possible to reliably reproduce the original form even when following an exact experimental recipe. This was also the case with the disappearing enantiomorphic form II of progesterone which was eventually re-discovered by the novel route of fusion with the structurally similar pregnenolone. This highlighted the possible role of impurities in the original synthesis of progesterone form II when it was routinely being reproduced.[9]

1.2 Polymorph and Solid Form Screening

Pharmaceutical companies subject potential drug formulations to rigorous polymorph screening to ensure repeats of the Ritonavir case are avoided. Solid form screening is also a licensing requirement for the formulation of new APIs.[10] Solid form screening methods are continually developed to incorporate a broad variety of experimental methods and crystallisation techniques so that as many polymorphs, hydrates and solvates as possible can be characterised in order to enable the optimal form of an API be identified and developed.[11] Pharmaceutical companies also carry out extensive polymorph screening to protect their intellectual property.

To date, there is not one universal screening method that can guarantee to ascertain the extent of polymorphism. This makes it hard to know how thorough a solid form screen should be and when to decide to stop screening for polymorphs experimentally.[12, 13] Braun et al.[14] suggest that before you can consider how exhaustive your polymorph screen should be, you need to consider the purpose of your polymorph screen. For example, do you want to confirm that the most thermodynamically stable form at 25 °C has been found or do you want identify all accessible solid forms in order to select a metastable form with superior properties? It is also important to consider time limitations, costs, the availability of material and any stability issues alongside the knowledge that it is impractical to sample all the possible nucleation conditions for a given compound. Braun et al. suggest that a solid form screen should

be sufficiently diverse so that the thermodynamically most stable polymorph is obtained as well as hydrate form(s) and any metastable forms that are kinetically stable at ambient conditions. Furthermore, other crystallisation products including intermediates, amorphous product and solvates should also be identified and any transformation pathways need to be characterised.[14]

1.2.1 Pure Compound Screening

This section goes into detail about some of the different experimental techniques that can be used during a solid form screen.

Table 1. Methods used to generate various solid forms.[11]

Method	Degrees of freedom
Crystallisation by cooling a solution	Solvent, cooling profile, concentration, mixing
Solvent Evaporation	Solvent, initial concentration, evaporation rate, temperature, pressure, ambient relative humidity
Precipitation	Solvent, anti-solvent, rate of anti-solvent addition, mixing, temperature
Vapour diffusion	Solvent, anti-solvent, temperature, concentration
Suspension equilibration	Solvent, temperature, solubility, temperature programs, mixing, equilibration time
Crystallisation from the melt	Temperature changes (min, max, gradients)
Quench cooling the melt	Cooling rate
Heat induced transformations	Temperature changes
Sublimation	Temperature gradient, pressure, surface type
Desolvation of solvates	Temperature, pressure
pH change	Temperature, rate of change, acid/conjugate base ratio
Mechanical treatment (e.g. milling, cryo-grinding)	Milling time, mill type, solvent
Freeze-drying	Solvent, concentration, temperature programs
Spray drying	Solvent, concentration, drying temperature

Different polymorphs are often found upon changing the conditions of crystallisation. Therefore, in order to conduct a reliable polymorph screen, solvent type (polar, non-polar, protic and aprotic), crystallisation conditions and crystallisation environments need to be varied as much as possible since they have a major influence over what solid form is produced.[15] Table 1

highlights some of the numerous experimental techniques, methods and variables that can affect the solid form of an API.

However, it is not only different crystallisation methods that can produce different polymorphs. Ostwald's Rule of Stages states that during a crystallisation process, a series of polymorphs should be obtained, starting with the least and ending with the most, thermodynamically stable polymorph.[16] Therefore, if a compound displays phase transformations during the crystallisation process, then the polymorph obtained will depend on the point in the crystallisation process that the particular solid form was harvested. Rapid transformation from one metastable form to the next may result in only the most stable form being isolated, though further measurement may be required to confirm this.[17]

1.2.2 Heterogeneous Nucleation

Although Table 1 provides a good overview of potential crystallisation methods, it should not be considered a comprehensive list as it only indicates crystallisation approaches that start from the pure compound. A thorough solid form screen would include the crystallisation methods listed in Table 1, but would also need to consider the role of heterogeneous nucleation, such as seeding, impurities, additives and surfaces, as a route to obtain desired polymorphs.

1.2.2.1 Seeding, Impurities and Additives

Seeding is generally thought of as the addition of previously nucleated solid partides of the compound in the desired solid form (homo-seeding) to the crystallisation process to induce crystal growth in the preferred form.[11] Depending on the size of the seed, either micro-seeding or macro-seeding (seed transfer) can be used, often alongside other optimisation techniques,[18] to produce more crystals of the desired form. Seeding can reduce the kinetic barrier to nucleation by providing a surface for the compound to nucleate upon.

The presence of impurities or additives (hetero-seeding) can induce the crystallisation of new and different solid forms of a compound.[11, 19-22] Heterogeneous particles provide surfaces for crystals to grow upon, removing the energy barrier to nucleation. A wide variety of additives and impurities have been shown to influence the polymorphism exhibited by a molecule. These range from the addition of structurally related compounds to the addition of polymers.[23] Modifying the crystallisation process to include the use of a hetero-seed can be a useful route to obtaining metastable forms of compounds as the additive surface can facilitate heteronucleation by kinetic control.[11, 22]

If the chemical purity of the compound is in dispute then the role of impurities in the crystallisation process should not be overlooked. Therefore, it is reasonable to suggest that

successful experimental screening should take place once the chemical purity of the compound has been optimised to ensure all forms starting from the pure compound are found.

Additives are different to impurities as they are specifically chosen to perform a role in the crystallisation process. In comparison, impurities can be present in crystallisations, but are often unwanted or unknown as mentioned previously in relation to progesterone and disappearing polymorphs.

(a)   (b)
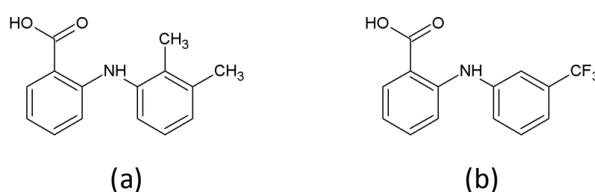
Figure 1 Diagrams showing structural similarity of (a) mefenamic acid and (b) flufenamic acid.

Structurally related additives have been used to obtain metastable forms of mefenamic acid (MA) and sulfamerazine. In the case of MA, a metastable phase, form II, was obtained by cooling a supersaturated solution of MA that contained a small amount of flufenamic acid form I (FFA) additive[22] (see Figure 1 for structural similarities between MA and FFA). In the case of sulfamerazine, structurally related N4-acetylsulfamerazine, sulfamethazine and sulfadiazine (Figure 2) were all used as additives to isolate metastable sulfamerazine.[19] These examples show how structurally related additives can affect the kinetics of crystallisation so that nucleation of a metastable polymorph is preferred.

(a)   (b)   (c)   (d)
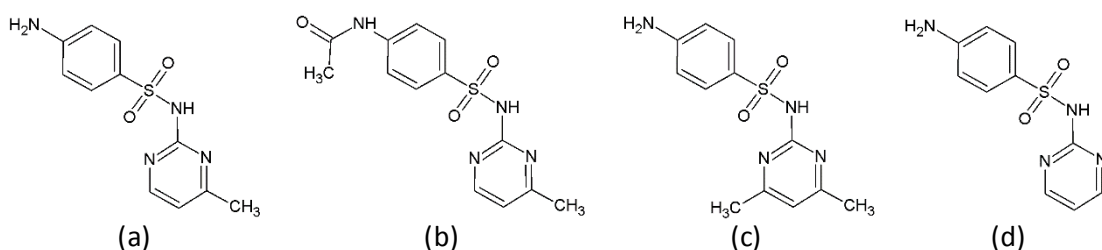
Figure 2. Diagrams showing the structural similarity of (a) sulfamerazine, (b) N4-acetylsulfamerazine, (c) sulfamethazine and (d) sulfadiazine.

Other examples of the use of structurally related additives can be observed in cases that consider a chloro-methyl interchange. Chlorine and methyl substituents have similar van der Waals volumes and can therefore be thought to be interchangeable[24, 25] within crystal lattices. This chloro-methyl exchange was exploited to obtain a new polymorph of para-methyl benzyl alcohol (p-MeBA I) via heteronucleation with microseeds of para-chloro benzyl alcohol (p-ClBA).[21] The new polymorph of p-MeBA was isomorphous to the form of the microseeds of p-ClBA that were used as an additive. Interestingly, seeding p-ClBA with p-MeBA did not yield a

new polymorph but investigations into mixed crystals of p-MeBA and p-ClBA showed that a solid solution was formed.

Similarly, cocrystallisation of o-toluic acid (o-methylbenzoic acid) and o-chlorobenzoic acid also formed a solid solution of the two compounds.[20] Complimentary computational studies on o-toluic acid and o-chlorobenzoic acid have indicated that there are no large structural differences upon the substitution of the chloro and methyl groups yet heteroseeding failed to produce crystals that were isomorphous.[20] This could be because the inductive effects of Cl and CH_3 are different[21] or because the formation of Cl···Cl interactions could prevent the development of isomorphous crystal structures of isostructural molecules.[25] Even though research into heteroseeding using isostructural molecules with either CH_3 or Cl substituents has not always yielded new results, successes have shown that the incorporation of heteroseeding with structurally related molecules should be considered a useful technique in polymorph screening.

1.2.2.2   Polymer-Induced Heteronucleation

The use of polymers, specifically polymer-induced heteronucleation (PIHn),[23] has led to the discovery of new polymorphs of a large range of small organic molecules and proteins and is a useful technique to incorporate into polymorph screening. The polymers utilised in PIHn are highly cross linked and tend to be insoluble so they interact with molecules at the solid-liquid interface providing a range of surfaces upon which to nucleate. As nucleation is a decisive step in determining the crystal form of a compound,[23] a range of different polymer surfaces can lead to the production of a range of different polymorphs. The range of polymer surfaces can be explored using either singular polymers in each crystallisation experiment or combinations of polymers.

Highly cross linked polymers lack crystallinity and so nucleation of crystals using PIHn by the epitaxial mechanism is unlikely.[26] It is thought that the PIHn mechanism depends on the accessibility of the functional groups present in the polymers which affect interfacial interactions between the polymer surface and the compound in solution, directing the nucleation of different crystal forms with preferred orientations.[26] The strength of polymer-solute interactions[27] and the addition of tailor made polymers[28] have been shown to affect nucleation kinetics, yet little is known about how polymer surfaces direct the formation of different polymorphs and polymers have not been designed or used to target specific forms. Therefore, large libraries of polymers with a broad variety of surfaces have to be investigated to increase the likelihood that all possible forms have been found.

Carbamazepine (CBZ) forms I-III are prepared readily. CBZ form I is obtained by heating forms II or III to 160 °C and 182 °C respectively.[29] CBZ form II is obtained from supersaturated ethanol solution held at 5 °C and CBZ form III is obtained from supersaturated ethanol solution held at 25 °C.[29] The previously unobserved fourth form of CBZ was obtained by crystallisation in the presence of four different polymers from a whole library of polymers with differing functional groups.[30] CBZ was used as an example compound to test the effectiveness of PIHn without consideration of the lattice or surface chemistry of potential polymorphs. The results indicated that the use of polymers is an effective way of obtaining new polymorphs.

The use of PIHn as an effective technique of screening for polymorphs is also evident in the case with FFA where the use of a polymer library enabled eight polymorphs, six of them new, to be isolated.[31] Three new forms of tolfenamic acid (TA) were also obtained using PIHn making TA a pentamorph.[32]

1.2.2.3 Self-assembled Monolayers

Self-assembled monolayers (SAMs) have also been used to isolate different polymorphic forms of compounds. SAMs are molecular assemblies of organic molecules that form on a surface by adsorption in regular arrays (Figure 3). Organic synthesis can be used to tailor the surface functionality by changing the terminal functional group of the organic interphase. Additionally, the metallic substrate surfaces can be etched (forming islands) giving the surface nanoscale geometrical variations.[33] A screen using SAMs can be performed by varying the size of the islands, the rate of evaporation, the concentration of the API solution and the type of SAM used.[34]
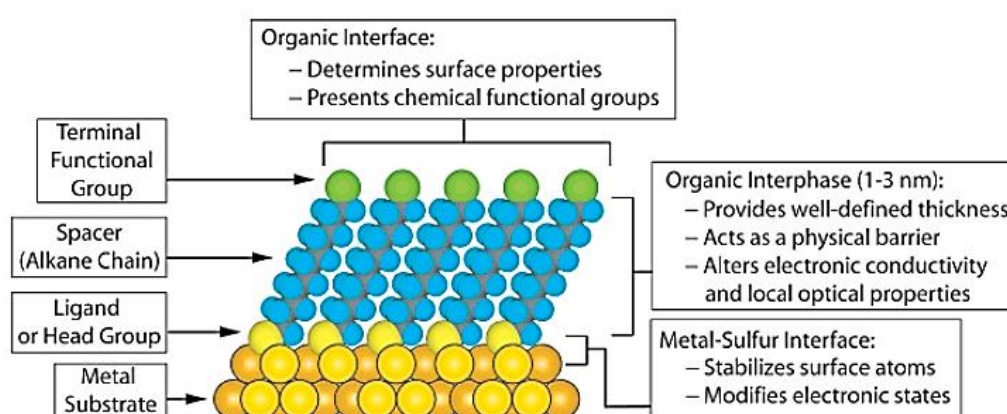
Figure 3. Schematic diagram of an ideal, single-crystalline SAM with a metal-sulfur interface. The anatomy and characteristics of the SAM are highlighted.[33]

Functionalised metallic islands have been used to template the crystal growth of many compounds including MA.[35, 36] Upon altering the size of the metallic islands, the wetting properties and the droplet dimensions of the MA solution on the islands were altered and two different polymorphic forms of MA (forms I and II) were obtained.[35] In some cases, the two forms of MA nucleated simultaneously (concomitant polymorphism) on the SAMs. The presence of the two polymorphs of MA on the SAMs highlights the interplay between kinetic and thermodynamic factors that can affect polymorphism. The use of SAMs also shows the use of another surface that can be used to template the growth of different polymorphic forms.

1.2.2.4   Epitaxy

Epitaxy is the two dimensional growth of a crystalline material on a crystal substrate (seed) from either the vapour or liquid phase and can either be onto a substrate of the same compound (homoepitaxy) or onto a related, or different, compound (heteroepitaxy).

Epitaxial growth has been observed during sublimation experiments when a crystalline substrate is present. Investigations into the epitaxial growth of sublimed MA on both FFA form I and FFA form III substrates indicate that although the same form of MA (form I) was obtained from both, the growth rates and orientation of the MA crystals on the FFA substrate differed depending on the polymorphic form.[37] Concurrent computational investigations into the epitaxial growth of MA on FFA showed that lattice matching as well as molecular conformation influenced the orientation and nucleation rate of MA form I crystals.

Similarly, sublimation of 5-methyl-2-[(2-nitrophenyl)amino]-3-thiophenecarbonitrile (named ROY due to its red, orange and yellow polymorphs) onto a pimelic acid substrate displayed selective epitaxial growth in one orientation of only one polymorph of ROY whereas, sublimation of ROY onto a succinic acid surface produced two different polymorphs in multiple orientations.[38]

The examples mentioned above show that it is possible for different polymorphic forms to be obtained upon changing the substrate or surfaces present during crystallisation. Therefore, in a solid form screen, it is important to consider and investigate both structurally related substrates and surfaces that bear little relation to the studied compound as well as potential additives to ensure that the extent of polymorphism is investigated as fully as possible.[19]

1.2.3   Automated Screening

As the number of potential methods for finding solid forms and polymorphs of a particular compound increases, there is an increasing need to find a more comprehensive

approach to screening. Therefore, automated robotic systems are frequently used in experimental screening to carry out multiple simultaneous crystallisations. These high-throughput (HT) crystallisation systems use a combinatorial approach to solid form screening where a large range of conditions, combinations and compositions are processed in parallel using minimal solute.[12] For example, a HT system, CrystalMax, developed by TransFrom Pharmaceuticals can screen up to 18,000 crystallisation conditions in parallel.[39]

HT technologies consist of both hardware and software components that drive the experiments as well as track, analyse and store the results.[12] Analysis of automated HT systems is regularly carried out *in situ* with Raman spectroscopy often being the preferred method of characterisation due to the short acquisition time in comparison to other techniques (such as powder X-ray diffraction).[39-41]

The results of HT experiments can indicate that a compound is polymorphic or show that there is evidence of hydrates and solvates that should also be considered when developing the relevant pharmaceutical. Using fully automated systems can save time and labour in the pharmaceutical industry, but they cannot cover a fully comprehensive list of controllable variables that can affect the solid form of an API such as thermal variables, length of time for crystallisations, high pressure and the de-solvation of solvates.[11, 41] Therefore, if the solid form landscape of an API needed to be fully characterised, HT methods should be considered alongside other experimental techniques.

1.2.4   Solid Forms

Different polymorphs of a pure compound have different physicochemical properties and so choosing to develop one polymorph over another will allow some control over the properties of an API. Another way of altering or manipulating the properties of an API is by creating multi-component crystals that can be in the form of solvates, hydrates, salts or cocrystals.

1.2.4.1   Solvates and Hydrates

During crystallisation, it is possible for solvent molecules to be incorporated into crystal structures of the parent compound to form solvates, and where the solvent is water, form hydrates. The incorporation of such molecules into the crystal lattice is thought to occur readily as two components can often pack together more easily than a single component.[3] It has been estimated that up to one third of pharmaceutically relevant molecules are capable of forming hydrates.[3, 42] It is important to note that solvates themselves can also exhibit

polymorphism if the arrangement of the molecules in each crystal lattice is different yet the stoichiometric ratio of the components is the same.[43]

Hydrates and solvates are of interest when developing APIs due to the different properties that they possess in comparison to the parent API. Knowledge of the solid state chemistry of the API is important during the development of the drug molecule as hydration, dehydration, solvation or desolvation of a pharmaceutical solid can have effects on the physical, chemical and/or biological properties of the API as well as its long term stability.[43]

1.2.4.2   Cocrystals

Crystalline cocrystals are materials formed with two (or more) neutral molecular components, in a stoichiometric ratio, in the unit cell. It has been shown that cocrystals of drug compounds can have enhanced physical properties compared to the API alone[44, 53]. For example, the dissolution and stability of adefovir dipivoxil is improved by cocrystallisation with saccharin,[54] and the physical stability of both caffeine[55] and theophylline,[56] with respect to humidity, is improved by cocrystallisation of each molecule with oxalic acid.

In theory, all molecules should be able to form cocrystals if the correct coformer is chosen, in comparison to salt formation which is only relevant to ionisable molecules. Additionally, a salt screen will typically only consider a small number of counter ions for toxicological reasons whereas there are many more potential molecules that can be used in the formation of cocrystals that have been *"generally recognised as safe"* (GRAS) by the U.S. Food and Drug Administration (FDA).[44] Furthermore, cocrystals are not limited to binary mixtures as tertiary and quarternary mixtures are also possibilities[45] and cocrystals also provide the opportunity for more than one API to be administered simultaneously to the patient if two or more APIs can crystallise together.

As there are thousands of possible GRAS coformers that could be considered in cocrystallisation experiments, recent attention has been focused on developing methods and knowledge that will help determine whether a cocrystal (or salt) is likely to form, potentially reducing the amount of experimental work required. Such approaches consider the intermolecular interactions between coformers[46] using informatics tools such as hydrogen bond propensity calculations (HBPC) that statistically analyse the likelihood of hydrogen bonds forming based on relevant structures in the CSD.[44] This approach allows coformers to be pre-screened and has been used to analyse synthon competition in theophylline (a bronchodilator) cocrystals[47] as well in determining the salts or cocrystals formed between pyrimethamine (an anti-malarial) and a number of acids and benzene derivatives[48] as well as between pyrimethamine and various other APIs and GRAS molecules.[49]

As the interest in cocrystals and salts as alternative solid forms of APIs has increased, so too has interest in experimental methods and screening processes that can identify and characterise potential cocrystals, salts and other solid forms of APIs. There is a broad range of experimental techniques used to target salt and cocrystal formation, including more traditional solution based crystallisation methods as well as mechanosynthesis such as solid-state and solvent-drop grinding. Many of the methods used for traditional polymorph screening, mentioned in Table 1, can also be used to screen for cocrystals and salts if the starting materials include potential coformers. High-throughput methods[50-52] can also target cocrystal and salt formation saving time in obtaining the optimal solid state form of an API.

1.2.4.3   Salts

In cases where the API is ionisable, the formation of a crystalline salt is often the easiest way to improve the solubility and bioavailability as well as alter other desirable properties. When a salt is formed, a counter ion is chosen from the GRAS list and the choice is often based on the difference between the pK_a values of the API and the coformer.

The pK_a rule of thumb has been developed over a number of years within the pharmaceutical industry and has more recently been verified by a statistical study on 6465 crystalline compounds found on the CSD.[57] It states that if $\Delta pK_a > 4$ then a salt will exclusively be formed, however, if $\Delta pK_a < -1$ then a cocrystal will be formed. A linear relationship exists between the probability of salt formation and ΔpK_a when the values of ΔpK_a fall in the region of -1 and 4 (zone 2, Figure 4).[57] Figure 4 shows the relationship between ΔpK_a and the occurrence of structures on the CSD; zone 1 ($\Delta pK_a < -1$), zone 2 ($-1 < \Delta pK_a < 4$) and zone 3 ($\Delta pK_a > 4$).
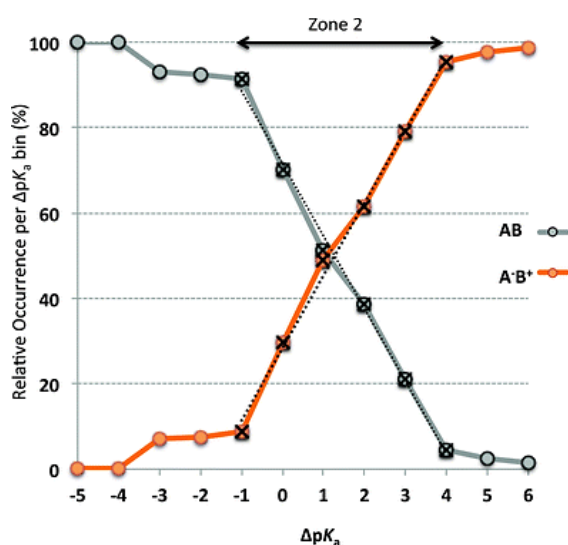
Figure 4. Relative occurrences of AB cocrystal (grey) and A⁻B⁺ salt (orange) as a function of the calculated ΔpK_a from the study of 6465 crystalline structures by Cruz-Cabeza.[57] ΔpK_a is the difference in pK_a between coformers A and B. Zone 2 is defined, $−1 \leq \Delta pK_a \leq 4$, zone 1 ($\Delta pK_a < -1$), zone 3 ($\Delta pK_a > 4$).

Salts and cocrystals can form similar crystal structures and as such, the protons have to be located by crystallography to definitively say whether a structure is a salt or a cocrystal. Therefore, when analysing crystal structures from the CSD or literature, it is important to note the difficulty in finding the position of protons by crystallography. Did the crystallographer care about the position of the proton? Was the diffraction data good enough to experimentally locate the proton? These are questions that should be considered before too much information is derived from CSD data on salts and cocrystals.

An experimental investigation into the crystal structures formed from the cocrystallisation of a series of five carboxylic acids with pyridine and 4-dimethylaminopyridine highlighted the problems of predicting multicomponent systems as salts, cocrystals or disordered solid forms.[58] Furthermore, periodic electronic structure calculations showed there was a significant energy penalty in moving the proton from salt formation to cocrystal and vice versa, yet this energy penalty was reduced for disordered structures.[58] The importance of the positon of the proton was also highlighted in a further investigation into carboxylic acid – pyridine crystals that showed the relative stability of the complexes changed significantly when the proton was moved away from its observed position in the experimental crystal structure.[59]

Cocrystals and salts can also exist in different polymorphic forms and, similar to pure compound screening, the most comprehensive method of identifying as many solid forms as possible is by considering a large range of different crystallisation techniques. An example of how multiple experimental methods can simultaneously be used to screen the solid state landscape of a multicomponent system is observed in the study of the phenazine-mesaconic acid, 1:1 cocrystal system. Table 2 shows that multiple experimental approaches produced three polymorphs of the 1:1 cocrystal, a monohydrate and a DMSO solvate.[60] Table 2 also shows that more than one method of crystallisation can be used to obtain forms I and II of the 1:1 cocrystal.

Table 2. Summary of the results from polymorph screening with the 1:1 phenazine-mesaconic acid cocrystal by Eddleston.[60]

Cocrystal form	Cocrystallisation methods which have yielded this form
Form I	Solution crystallisation, dry grinding, liquid assisted grinding, sublimation, thermal methods, desolvation of the monohydrate
Form II	Cocrystallisation at the interface between two saturated solutions, liquid assisted grinding, desolvation of the DMSO solvate
Form III	Thermal methods (crystallisation from the melt of a physical mixture of both components and from heating form I in the DSC)
Monohydrate	Cocrystallisation at the interface between two saturated solutions (phenazine in xylene and mesaconic acid in water)
DMSO solvate	Liquid assisted grinding

The multiple experimental screening approach requires a lot of time and resources yet will hopefully produce all the potential solid forms of a given multi component system including polymorphs, solvates, hydrates and even cocrystals of salts. However, it can never be proven that all the solid forms have been found.

1.2.4.4   Solid Solutions

An alternative outcome of a cocrystallisation experiment could be the formation of a solid solution which can occur between two or more compounds if their molecular structure is similar and they have almost the same type, size and position of atoms (molecular isostructurality). This means that the different molecular components can occupy equivalent crystallographic sites and thus the crystal structure of the parent (major) component can be retained with the minor component incorporated within the crystal lattice substitutionally. Other solid solutions exist where the minor component is found interstitially in crystallographic sites that would normally be vacant.[61]

Much of the original work on organic molecular solid solutions, or mixed crystals, was carried out by Kitaigorodsky[62, 63] who suggested that in order for a solid solution to exist, the components had to be molecularly isostructural and the individual components had to have similar crystal structures that were either isomorphous (same space group and unit cell dimensions) or isostructural (same packing arrangement, but not the same unit cell dimensions). Crystal isostructurality is limited to substituent pairs whose members can replace each other without altering the existing packing of the crystal. Chloro and methyl substituents have very similar van der Waals volumes and thus permit isostrucurality.[64]

There are a number of descriptors of crystal isostructurality including terms used by Kálmán *et al.* such as the *unit-cell similarity index* (Equation 1)[64] the *isostructurality index* (Equation 2)[64] and the *volumetric isostructurality index* (Equation 3).[65]

Equation 1
$$\Pi = \frac{(a+b+c)}{(a'+b'+c')} - 1$$

Equation 2
$$I_i(n) = \left| \sqrt{\frac{\sum(\Delta R_i)^2}{n}} - 1 \right| \times 100$$

Equation 3
$$I_v = \frac{2V_\cap}{V_1 + V_2} \times 100 \ \%$$

The *unit cell similarity index, Π,* compares the orthogonalised cell parameters (a, b, c and a', b', c') of the related structures and has a value of zero for identical cells. The

isostructurality index, $I_i(n)$, can also be calculated where n is the number of differences in distance (ΔR_i) between crystal coordinates of identical non-hydrogen atoms.[64] The *volumetric isostructurality index*, I_v, takes into account the volumes occupied in the unit cells of related structures where V_1 and V_2 are the volumes of the compared molecules and $V_\cap$ is the intersection of these volumes, the volume that is the same in both molecules.[65]

Isostructural crystal structures or structures with a high degree of structural similarity can also be identified using a number of computational programs such as XPac[66] and COMPACK.[67] XPac is useful for identifying pairs of structures that have one-dimensional (chains of molecules in common), two-dimensional (sheets of molecules in common) or three-dimensional structural similarity. COMPACK analyses the packing environments of two crystal structures using interatomic distances and the default coordination sphere considers the closest 15 molecules. Similarities are quantified by $rmsd_n$ values which are the root-mean-square deviations of the distances between the non-hydrogen matched atoms of the two molecular structures that are being compared for n molecules overlain within the specified tolerances (20 % and 20 ° for distances and angles respectively).

The similarity comparisons of fenamate molecules can be carried out for molecules with different functional groups by allowing for molecular differences and matching only the similar atoms. To generalise the results, if n = 2 it suggests that the hydrogen bonding dimer is readily retained, if n = 6 it suggests that there are similarities in the planes of the two structures and if n = 15, it suggests that the compared structures are isostructural, differing only at the second nearest neighbour level.

If the crystal structures of two compounds are isostructural, Kitaigorodsky suggested that it would be possible to form a solid solution of these compounds. Such crystals consist of a single lattice where the lattice sites are occupied at random by two or more species with the overall populations equal to the bulk composition of the material.[68] As the stoichiometry of the different molecular constituents in the solid solution crystals is not limited to integer values, the structural and physical properties of the material can be tailored, often in a continuous linear fashion, by varying the relative compositions of the two compounds within experimental constraints.[69] Furthermore, if a solid solution of two or more APIs can be formed then solid solutions can have advantages over cocrystals as the ratio of the APIs can be varied for use in combination therapy. Solid solutions of cocrystals also exist.[68]

1.2.5   Computational Screening

Recent advances in computational methods of crystal structure prediction (CSP) have provided researchers with a complimentary approach[70] with which to investigate the

phenomenon of polymorphism. Advances in computational power and programs have allowed thermodynamically feasible crystal structures to be generated for molecules of increasing complexity. Originally, the computational CSP methods were only applicable to rigid molecules, but the recent successes of CSP methods for highly flexible, pharmaceutically relevant, molecules under blind test conditions highlight the advancements made in the field of CSP. [71, 72] (See chapter 6 for more information on the blind tests.)

CSP methods produce thermodynamically feasible crystal structures of a given compound. CSP can be used to compliment experimental screening to give a more thorough understanding of the polymorphic behaviour of a particular compound. In principle, a comparison of the structures generated by CSP methods with experimental forms can give reassurance that the low energy thermodynamically feasible forms have been found experimentally.[73] Furthermore, powder X-ray diffraction (PXRD) patterns of predicted structures to can be simulated for comparison with PXRD patterns from experimental screening which can help identify unknown polymorphs if a single crystal cannot be grown.[74]

At present, there is no routine CSP method for polymorph screening and CSP approaches are continually adapted in line with the studied compound or API and the purpose of the polymorph screen. However, the use of CSP methods in polymorph screening is becoming increasingly apparent with CSP programs like Neumann's GRACE (the Generation, Ranking and Characterisation Engine) being commercially available.[75] CSP methods have also recently been used in collaboration with industrial-style solid form screening processes[76-78] and have been shown to help direct experimental methods (through solvent choice etc.) so that new polymorphs[79, 80] and additional metastable forms are obtained.[78]

CSP methods often predict more low energy, thermodynamically feasible, structures than are observed experimentally. This is because kinetic parameters that are involved in the crystallisation process such as cluster nucleation, formation, phase transformation and crystal growth are beyond the scope of the calculations.[15] Low energy structures generated using CSP methods are the result of the compromises between favourable intermolecular interactions such as close packing, hydrogen bonds and π-π interactions as well as conformational preferences/flexibility[81] of the molecules within crystal lattices.

The set of structures generated by CSP methods that have the lowest lattice energies are usually summarised on a crystal energy landscape[82] (see Figure 5 for examples) that plots the densities (or packing coefficients) against the lattice energies. Crystal energy landscapes are a visual summary of the thermodynamically feasible structures that are produced from CSP methods with each point representing a structure. These crystal energy landscapes can help indicate whether a certain compound is expected to be monomorphic, polymorphic or will tend

towards disorder (Figure 5). The structures with the lowest lattice energies on the crystal energy landscape are expected to be the most thermodynamically stable.
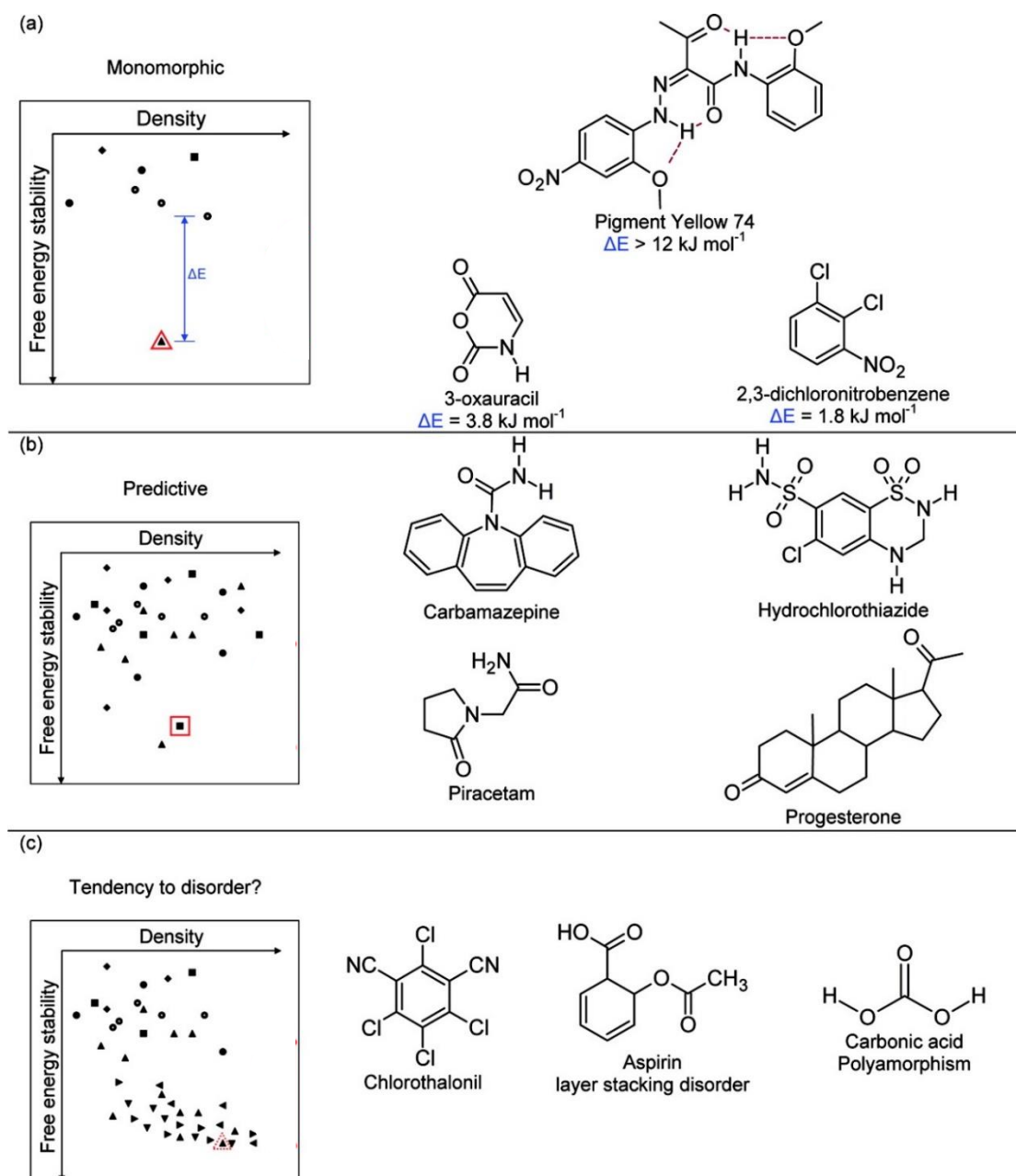
Figure 5. Price's idealized types of crystal energy landscape and examples of molecules that exhibit this behaviour.[81]

Figure 5 shows the idealised types of crystal energy landscapes, as summarised by Price,[81] alongside some examples of molecules that fall within each type. Figure 5a shows a typical monomorphic system where the large energy gap (ΔE) between the energy of the lowest predicted structure and the energy of other structures indicates that one structure is significantly the most stable and likely to be the only form obtained. Figure 5b shows an idealised predictive system that indicates the presence of two polymorphs as there are two structures

that are both low in energy, but that differ in their crystal packing as shown by different shaped points on the crystal energy landscape, a square and a triangle. Figure 5c shows a crystal energy landscape that indicates disorder could be expected as there are numerous structures that are similar in both energy and packing. If these structures are related, but differ in the stacking of the same sheet of molecules, then it is feasible that stacking errors could occur and disorder is likely.

The information that different crystal energy landscapes provide is obvious in the example of the related molecules caffeine and isocaffeine. Isocaffeine appears to be monomorphic with an energy gap of 6.05 kJ mol^{-1} between the global minimum and the next most stable crystal structure, in line with experimental observations where only one form of isocaffeine has been obtained. In comparison, the crystal energy landscape of caffeine is significantly different and helps explain the observed disorder in caffeine form II. [83]

Alongside the successes of CSP methods under blind test conditions,[71] CSP methods have also managed to predict a new polymorph of carbamazepine (form V)[84] that was subsequently found after extensive further experimental investigation. The isolation of CBZ form V was the first time computational calculations directly influenced the development of the experimental procedure that was used to specifically target the predicted form.[84] CSP studies of CBZ indicated that there was a thermodynamically feasible form with a catermeric structure that was competitive in lattice energy with the previously known forms that all contained the amide hydrogen bond dimer.[73, 85, 86] Even though CBZ had previously undergone extensive experimental screening, CBZ form V remained elusive until CSP techniques showed the structural similarity between CBZ form V and dihydrocarbamazepine (DHC) form II. Experimental procedures were subsequently developed which first obtained a solid solution of CBZ and DHC[87] and then targeted the crystallisation of CBZ form V by sublimation of CBZ onto a template crystal of DHC form II (Figure 6).[84] Both the solid solution and CBZ form V are isostructural with the predicted catermeric CBZ structure and DHC form II. Interestingly, the CBZ form V crystals are formed on the smallest edge faces of the crystal and not directly on a large crystal face (Figure 6). This suggests that it is not just the isomorphous nature of the seed crystal that is a factor in the growth of CBZ form V as this would lead to growth over much of the seed crystal.

CSP methods had previously been used to tailor experimental procedures to target specific packing motifs by choosing specific solvents with relevant hydrogen bond donor or acceptor groups to try and produce crystal structures with the desired hydrogen bonding motifs.[79, 80] In comparison, the results of the investigations into CBZ highlight the potential applications of CSP methods in developing templating experiments where a specific surface is chosen to target a specific form. If experimentally known forms of related molecules are isomorphous or isostructural to predicted, thermodynamically feasible polymorphs, then there

exists the possibility that templating experiments could be used to enable the isolation of predicted forms.
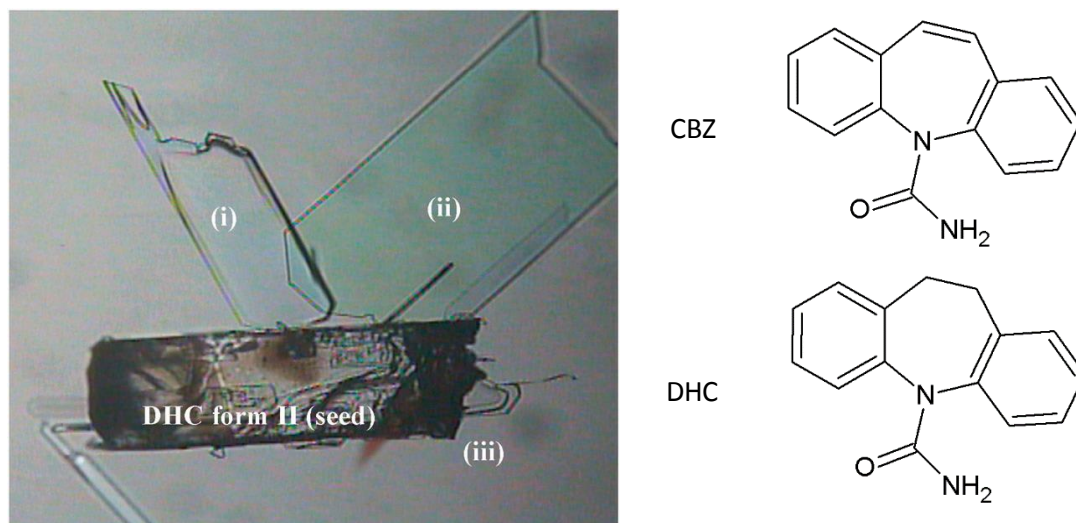
Figure 6. DHC II seed crystal with thin plates of CBZ V (i–iii) emerging from the edge faces.[84]

During the course of this thesis, further experimental investigations have been carried out templating CBZ form V using DHC form II seed crystals by sublimation. The latest set of experiments used polycrystalline DHC form II as a template surface rather than a single crystal which increases the surface area and orientations of different crystal faces that are available for vapour deposition of CBZ.[88] A separate surface of ordered single crystals of DHC was also prepared and both the ordered surface and the polycrystalline surface templated the nucleation of CBZ form V. In comparison to the previous templating experiments (Figure 6),[84] the latest results showed no evidence of face selectivity.

To further examine the usefulness of the templating experiments, the same polycrystalline and single crystal surfaces of DHC form II were used in experiments with another related molecule, cyheptamide (CYH). CSP methods had predicted a thermodynamically feasible crystal structure of CYH was competitive in energy with known polymorphs and was isostructural to DHC II and CBZ V.[88] The DHC form II surface successfully templated the growth of the predicted isostructural polymorph of CYH, CYH form III, for the first time.

The results of the experiments concerning the isostructural polymorphs of CBZ form V, DHC form II and CYH form III show that targeted crystallisation with isomorphous template surfaces can be used to nucleate novel polymorphs that are not found in conventional screening methods.

1.3 Thesis Aims and Outline

Sections 1.1 and 1.2 give an overview of the reasons why full characterisation of the solid form landscape of an API is important and introduce many experimental techniques that are used to investigate the solid form diversity of a compound. This thesis investigates the polymorphism displayed by mefenamic acid (MA) and tolfenamic acid (TA) and explores the consequences of chloro-methyl replacement in the crystal structures of MA and TA using a joint computational and experimental approach.

1.3.1 Research Approach

Chapter 2 introduces the compounds MA and TA and their known polymorphs. The crystal structure similarities and differences between known forms of MA and TA are described and chloro-methyl replacement within the crystal structures is discussed.

Chapter 3 conducts a CSP study on MA by adapting the methodology already used in the CSP study on TA.[89] The calculated crystal energy landscape of MA was then analysed to identify any potential polymorphs that are competitive in energy with the known forms of MA. Isostructural relationships between MA and other fenamates, in particular TA, were also analysed.

Alongside the computational work, the use of isostructural heteroseed surface templates was explored experimentally, targeting the nucleation of existing forms by new routes as well as the nucleation of new forms of MA and TA. The isostructural relationships of MA and TA were investigated using solution based crystallisation techniques (chapter 4) as well as sublimation techniques (chapter 5). The sublimation techniques were guided by the successes of the methods used to nucleate CBZ form V and CYH form III on DHC form II seed templates.[84]

Chapter 6 tests the validity of the CSP methodology used in this thesis by participation in the 6th blind test held by the CCDC.

2 Crystal Structures of Fenamate Molecules

Chapter 1 introduced the concept of polymorphism, highlighted the importance of fully characterising the solid form landscape of a given API and presented some of the various experimental methods that are utilised to find novel forms.

This thesis investigates the polymorphism of mefenamic acid (MA) and tolfenamic acid (TA). MA and TA are molecularly isostructural and have the same skeleton of bonds, but differ in the replacement of a methyl group on MA with a chloro group on TA (Figure 7). Investigations into the polymorphism of MA and TA will provide insights into the possibility of chloro-methyl replacement in the crystal structures of MA and TA.

(a)   (b)
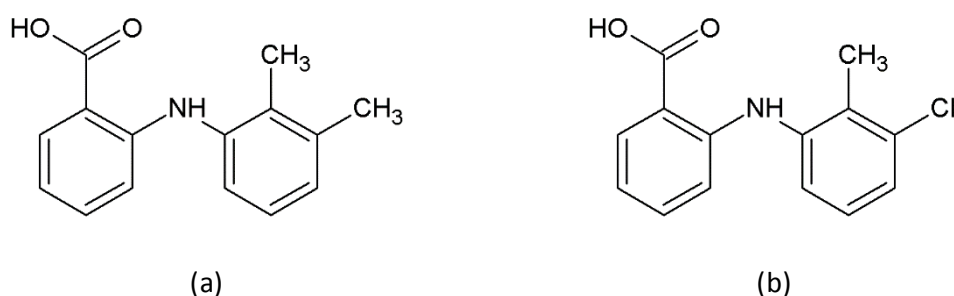
Figure 7. Diagrams of (a) mefenamic acid and (b) tolfenamic acid. The diagrams shows the molecular similarity of the two molecules that differ in the replacement of a CH$_3$ group on MA with Cl on TA.

MA and TA belong to the fenamate group of molecules which are non-steroidal anti-inflammatory drugs (NSAIDs) that have been used in the pharmaceutical industry since the 1960s.[90] NSAIDs have been used to treat pain from a variety of causes including migraines, musculoskeletal/joint disorders and menstrual cramps.[91-94] The fenamate group of molecules are highly polymorphic with each fenamate exhibiting conformational polymorphism and MA having three known polymorphs, TA having five known polymorphs and flufenamic acid (FFA), having nine polymorphs, of which eight are fully characterised by X-ray diffraction.[31] FFA previously held the record for the molecule with the highest number of known crystal structures, but this was recently beaten by aripiprazole which has twelve reported anhydrous forms, nine of which are characterised crytallographically.[95]

The decision to investigate the fenamate group of molecules was influenced by the results of a previous CSP study on two fenamates, fenamic acid (FA) and TA. Comparisons of the structures of FA and TA, including experimental forms and their most stable hypothetical structures, with known crystal structures of other fenamates found in the CSD, suggests that there is a high degree of structural similarity between the fenamates (Table 3). The hypothetical crystal structure entries in Table 3 are indicated with a #.

The structural similarity comparisons were carried out using the Crystal Packing Similarity[67] module in the program Mercury[96, 97] (produced by the CCDC) which considers the similarity of the coordination environments of the molecules.

Table 3. The crystal packing similarity of the experimental structures of FA, TA (with three ordered models for disordered form V of TA) and their most stable hypothetical crystal structures with the known crystal structures of other fenamates in the CSD (denoted by their refcodes). The similarity is given in the form n(rmsd$_n$), with the overlays of six or more molecules highlighted as bold. The column for MA (the focus of this research alongside TA) is highlighted in grey. The table was copied and reformatted from previous work by Uzoh.[89]
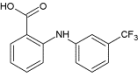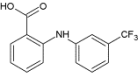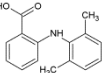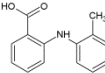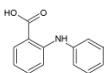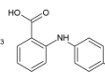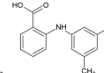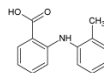
	FPAMCA	FPAMCA11	LAHLOW	PEFMET	PEFNAQ	SURMEY	SURMOI	MA XYANAC
FA								
QQQBTY02	2(0.71)	4(1.33)	**7(0.84)**	3(1.28)	**6(0.62)**	3(0.50)	3(1.20)	4(0.49)
#1FA_22	2(0.41)	5(1.91)	**6(1.31)**	2(0.13)	**11(0.96)**	4(0.98)	4(1.08)	3(1.80)
#2FA_2	2(0.43)	3(0.56)	**7(1.01)**	2(0.10)	**11(0.51)**	3(1.07)	**7(0.98)**	3(0.86)
TA								
II	1(0.89)	2(0.15)	2(0.59)	2(0.11)	1(0.61)	2(0.12)	**12(1.87)**	2(0.29)
I	2(0.59)	2(0.48)	3(0.61)	1(0.70)	**13(0.38)**	**6(1.78)**	4(1.20)	2(0.62)
III	1(0.81)	**7(0.75)**	2(0.48)	**13(0.33)**	2(0.55)	**13(0.61)**	3(0.41)	**13(0.45)**
IV	2(0.87)	**6(0.71)**	3(1.09)	**11(0.49)**	2(0.46)	**13(0.84)**	3(0.56)	**15(0.30)**
V_a	2(0.57)	2(0.46)	5(0.42)	1(0.68)	3(0.39)	2(0.22)	2(0.18)	2(0.57)
V_b	2(0.75)	3(0.32)	**7(0.64)**	2(0.47)	4(1.10)	5(0.41)	4(1.19)	5(0.72)
V_c	2(0.95)	2(0.84)	5(0.41)	1(0.42)	4(1.10)	4(0.51)	2(0.29)	3(0.46)
#2TA_15	2(0.52)	2(0.53)	3(0.91)	1(0.77)	14(0.4)	4(0.82)	4(1.22)	2(0.70)
#3TA_876	1(0.93)	4(1.56)	**7(1.42)**	3(0.43)	1(0.66)	3(0.71)	4(0.47)	2(0.37)
#4TA_6243	2(0.54)	3(1.15)	3(1.76)	1(0.69)	4(0.16)	4(1.49)	2(0.17)	3(0.91)
#6TA_82	1(0.92)	2(0.17)	2(0.61)	2(0.12)	2(0.64)	2(0.08)	**15(0.28)**	2(0.28)

Table 3 shows that there is a high level of crystal structure similarity between MA form I (CSD refcode: XYANAC) and TA forms III (CSD refcode: KAXXAI02) and IV (CSD refcode: KAXXAI03). This thesis addresses the structural similarities of the MA and TA crystal lattices further and investigates the effect of chloro-methyl substitution in the fenamates.

Previous investigations on the fenamate group of molecules have been mentioned in the previous chapter (chapter 1) including the role of heteronucleation in obtaining different polymorphs. For example, FFA as an additive can lead to the isolation of metastable MA form II,[22] use of polymers have led to new forms of FFA[31] and TA[32] and SAMs have led to the observation of concomitant polymorphism of MA.[35, 36]

2.1 Mefenamic Acid

There are currently three known polymorphs of MA, form I,[98] a disordered form II[22] and a recently discovered, metastable form III.[99] All three polymorphs belong to the *P-1* space group, have just one molecule in the asymmetric unit (*Z′* = 1) and consist of hydrogen bonded dimers (Figure 8). The MA molecules in all three polymorphs have an internal hydrogen bond (Figure 8). The two most widely reported polymorphs of MA; forms I and II, are enantiotropically related,[35, 99] with form I being the most stable at room temperature and form II the most stable at elevated temperatures or 170 °C.[36] DSC has been reported to show that MA form I transforms to form II at 170 °C[100] and in the temperature range of 178 – 180 °C.[99] Additionally, MA form II has been obtained by holding MA form I at 160 °C for a week.[35]
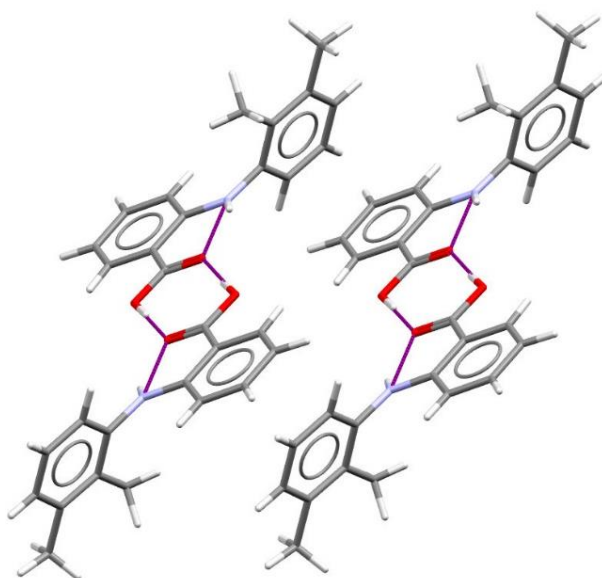
Figure 8. Hydrogen bonded dimers of MA. Inter and intra molecular hydrogen bonds are shown in purple.
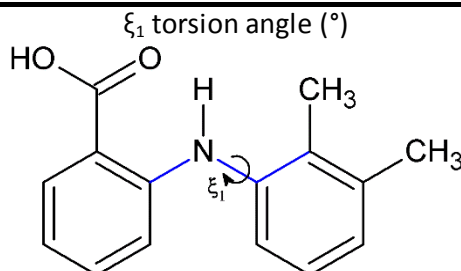
MA form I has been reported to crystallise from a variety of solvents.[101-103] MA form II can be obtained by crystallisation from chloroform,[99] from a solution of *N,N*-dimethylformamide,[101] by heating form I to around 150 °C – 160 °C[35, 101, 102, 104, 105] or by heteronucleation using SAMs.[35, 36] Form III was obtained serendipitously from a cocrystallisation experiment of MA with adenine in a 1:1 DMF/methanol mixture followed by slow evaporation of the solvent at room temperature.[99]

Studies on MA show that the infrared spectra of MA forms I and II are different, therefore infrared spectroscopy can be a useful technique in determining the polymorphic form. It has been reported that upon transformation from form I to form II, the N-H stretching band in the infrared shifts from 3313 cm^{-1} to 3347 cm^{-1}.[104] The change in the position of the N-H stretching peak was originally attributed to a conformational difference in the polymorphs

involving 180 ° rotation of the carboxyl group.[101, 104] This meant that the N-H bond would be stronger in form II as the internal hydrogen bond is weaker (C-O···H versus C=O···H hydrogen bonding), thus resulting in the increase in wavenumber of the peak for the N-H stretch in the infrared spectrum. However, a more recent computational study has shown that differences in the IR spectra can be explained by rotation about the N-C bond[106] and the difference in the torsion angle ξ_1 (Table 4). This latter explanation was confirmed by the crystallographic data when a single crystal of MA form II was isolated for the first time.[22] The ξ_1 torsion angle is different in the three polymorphs of MA (Table 4).

As well as infrared spectroscopy, Raman spectroscopy has been used to differentiate between polymorphs of MA with three distinct vibrational band differences between MA form I and MA form II.[35] Low wavenumber Raman spectroscopy can also be used.[105]

Table 4 The ξ_1 torsion angle (C$_2$-N$_1$-C$_8$-C$_9$) in the different polymorphs of MA. The ξ_1 torsion angle is shown by the blue bonds in the diagram. ξ_1 for forms I and II are taken from single crystal data in this research. MA form II is disordered in the ratio (a) 0.654 and (b) 0.346.

Polymorph	I	II		III[99]
		(a)	(b)	
ξ_1 torsion angle (°)	119.38	69.72	-78.97	80.82

2.1.1 Redeterminations of MA form I and MA form II

2.1.1.1 Methods

Materials. MA was purchased from Sigma Aldrich and was used without further purification. A large range of reagent grade solvents were used.

Preparation of Single Crystals. Single crystals of MA form I were obtained by room temperature solvent evaporation to dryness of MA from a number of solvents including ethanol, 1-butanol, acetonitrile and 1,2-dichloroethane.

Single crystals of MA form II were obtained by sublimation onto a glass surface under a static vacuum (1.0 x 10^{-5} Pa) for 48 hours. See chapter 5 for further experimental details on the sublimation setup.

Single Crystal X-ray Diffraction. Single crystals of MA forms I and II were chosen using a microscope equipped with a rotatable polarising stage. Crystallographic data were collected

at 150 K using an Agilent SuperNova diffractometer, equipped with an Oxford Instruments cryostat and Cu-Kα radiation (λ = 1.54184 Å). Using Olex2[107], structures were solved with the SHELXS[108] structure solution program using direct methods and were refined using SHELXL[109] using least squares minimisation. In form I the data quality was such that the hydrogen atoms were located and subsequently refined in the final difference map. In form II the hydrogen atoms were included with a riding model.

Infrared Spectroscopy. Crystals were analysed using solid state infrared spectroscopy. Infrared spectra were obtained using a Perkin-Elmer Spectrum One FTIR fitted with a diamond ATR accessory. Spectra were collected over the range 4000–650 cm^{-1} at a resolution of 4 cm^{-1} and analysed using the ACD/Spectrus Processor software.[110]

Thermal Analysis. Differential Scanning Calorimetry (DSC) measurements were performed on a TA Q2000 (TA Instruments, LLC, USA) that was calibrated at heating rate of 10 °C min^{-1} for a temperature range of 0 − 250 °C using an Indium melting point standard. Nitrogen (50 mL min^{-1}) was used as a purge gas. Sample sizes were between 0.88 mg and 1.75 mg. Tzero non-hermetic aluminium pans and lids were used. The data analysis was carried out using the Universal Analysis 2000 software.[111]

2.1.1.2 Results

The crystallographic data for MA forms I and II are reported in Table 5 alongside the crystallographic data for MA form III as reported by SeethLekshmi et al.[99] The thermal ellipsoid plot, set at 50 % probability, for MA form I is shown in Figure 9 and for MA form II is shown in Figure 12.
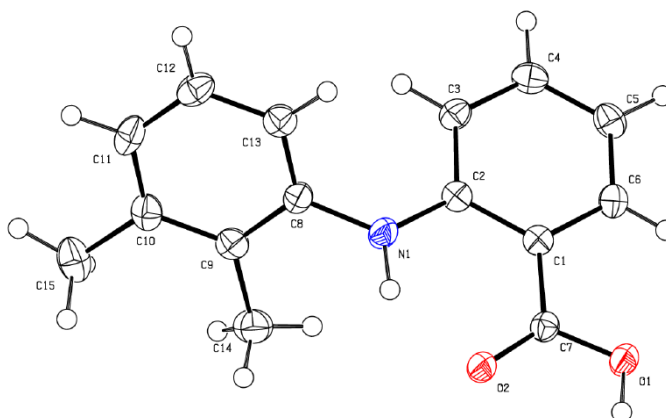
Figure 9. Thermal ellipsoid plot, set at 50 % probability, of MA form I.

The infrared spectra collected for MA forms I and II are shown in Figure 10. The spectra are in agreement with previous literature and show that forms I and II of MA can be distinguished by the position of the N-H stretching peak.[104] The N-H stretching peak appears at

3308 cm^{-1} for MA form I and at 3342 cm^{-1} for form II. The infrared spectrum for MA form III has not been found in current literature.
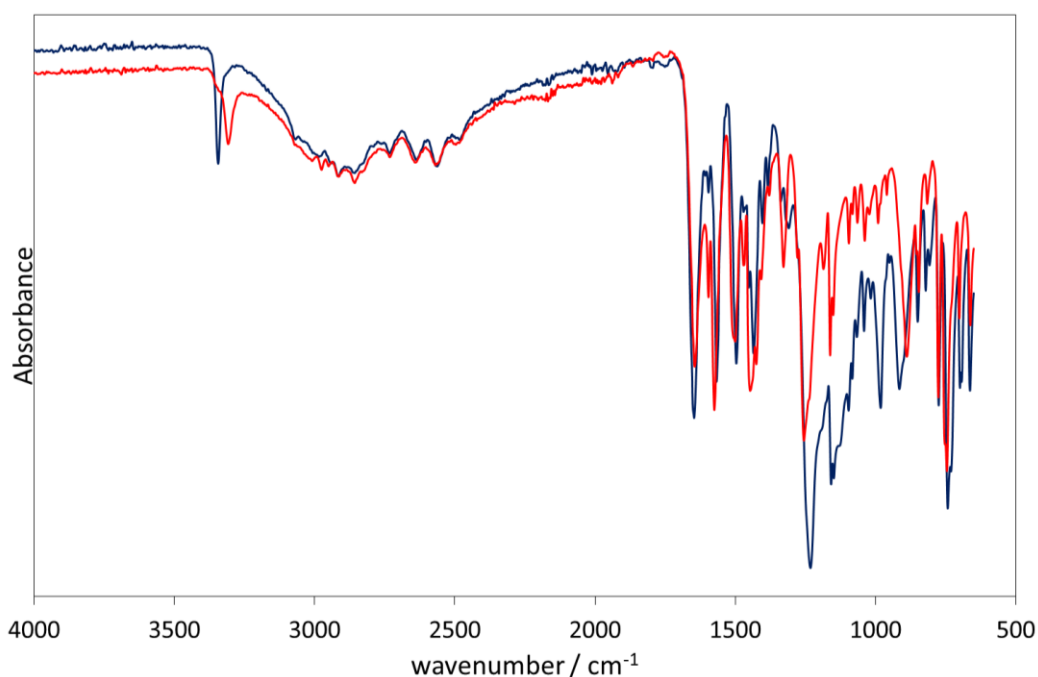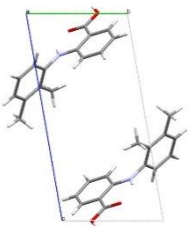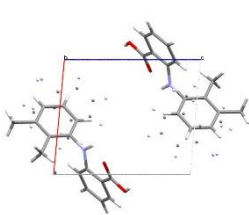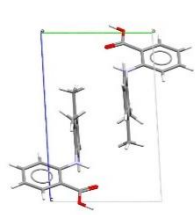
Figure 10. The infrared spectra of MA form I (red) and MA form II (blue).

MA forms I and II were analysed by DSC in the temperature range 0 − 250 °C at a heating rate of 10 °C min^{-1} and the scans are shown in Figure 11. Figure 11 shows that there is a single melting endotherm for MA form II at 231.4 °C. The DSC scan for MA form I shows an endothermic phase transition at 168.5 °C followed by a melting endotherm at 230.7 °C. The results from the DSC scans are in agreement with previous literature which show that MA form I transforms to MA form II upon heating to 170 °C.[100]
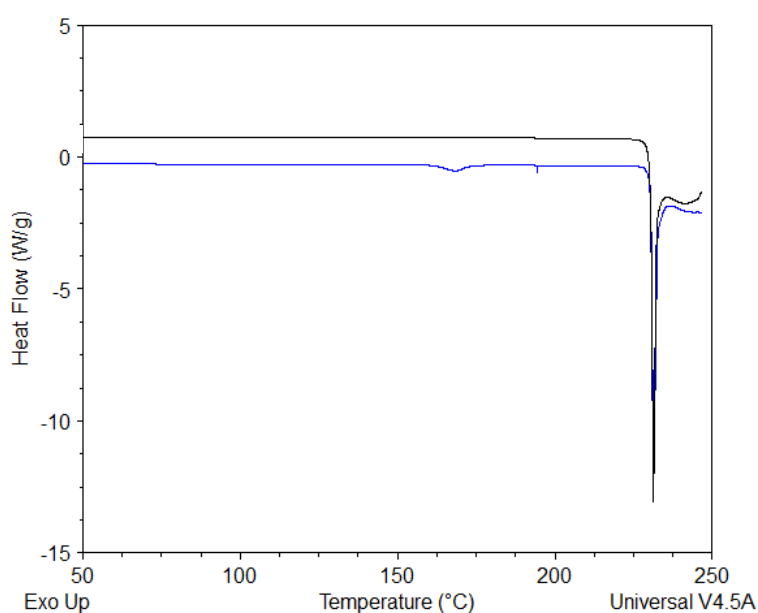
Figure 11. DSC scan of MA form I (blue) and MA form II (black). The scans were carried out at a heating rate of 10 °C min^{-1}.

Table 5. The crystallographic data of MA polymorphs.

	I[this work]	II[this work]	III[99]
Unit Cell Diagram			
Crystal System	triclinic	triclinic	triclinic
Space Group	P-1	P-1	P-1
Temperature (K)	150	150	298(2)
a (Å)	6.7887(3)	7.7300(3)	7.723(2)
b (Å)	7.3613(2)	9.1275(4)	7.9340(10)
c (Å)	14.0330(4)	9.4027(3)	11.2320(10)
α (°)	76.868(3)	107.112(4)	83.590(10)
β (°)	79.857(3)	91.604(3)	80.940(10)
γ (°)	64.863(3)	101.683(3)	67.510(10)
Cell Volume (Å^3)	615.74(4)	618.19(4)	626.96(19)
Z	2	2	2
Z′	1	1	1
Unique reflections	2170	2436	2287
Refined parameters	223	205	169
GOF	1.037	1.053	1.037
R1 (I > 2σ(I))	0.0317	0.0454	0.042
wR2 (all)	0.0841	0.1248	0.109
R1 (all)	0.0326	0.0525	

MA form II is disordered with two different conformations of MA in the unit cell with a population distribution of 65:35. The two conformations differ most in the rotation of the alkylated phenyl ring (the ξ_1 torsion angle as shown in Table 4) and the position of the amino bridging group relative to the phenyl ring with the carboxyl group. The disorder exists at low temperature (150 K) which suggests it could be of static nature or is kinetically trapped.

The disorder of MA form II is summarised in Figure 12 with the major component shown by solid black bonds and the minor component shown by dashed bonds (Figure 12a). The disorder in the single crystal of MA form II collected in this study was 0.654:0.346, but the disorder reported for other determinations on the CSD are 0.705:0.295 (at 150 K)[22] and 0.555:0.445 (at 298 K).[99] Data on the disorder for the crystal structure on the CSD with the refcode XYANAC05[36] cannot be located. The different occupancies that are reported for the disorder observed in MA form II suggest that the disorder is affected by the method of nucleation or could also vary from crystal to crystal.

(a)

(b)   (c)
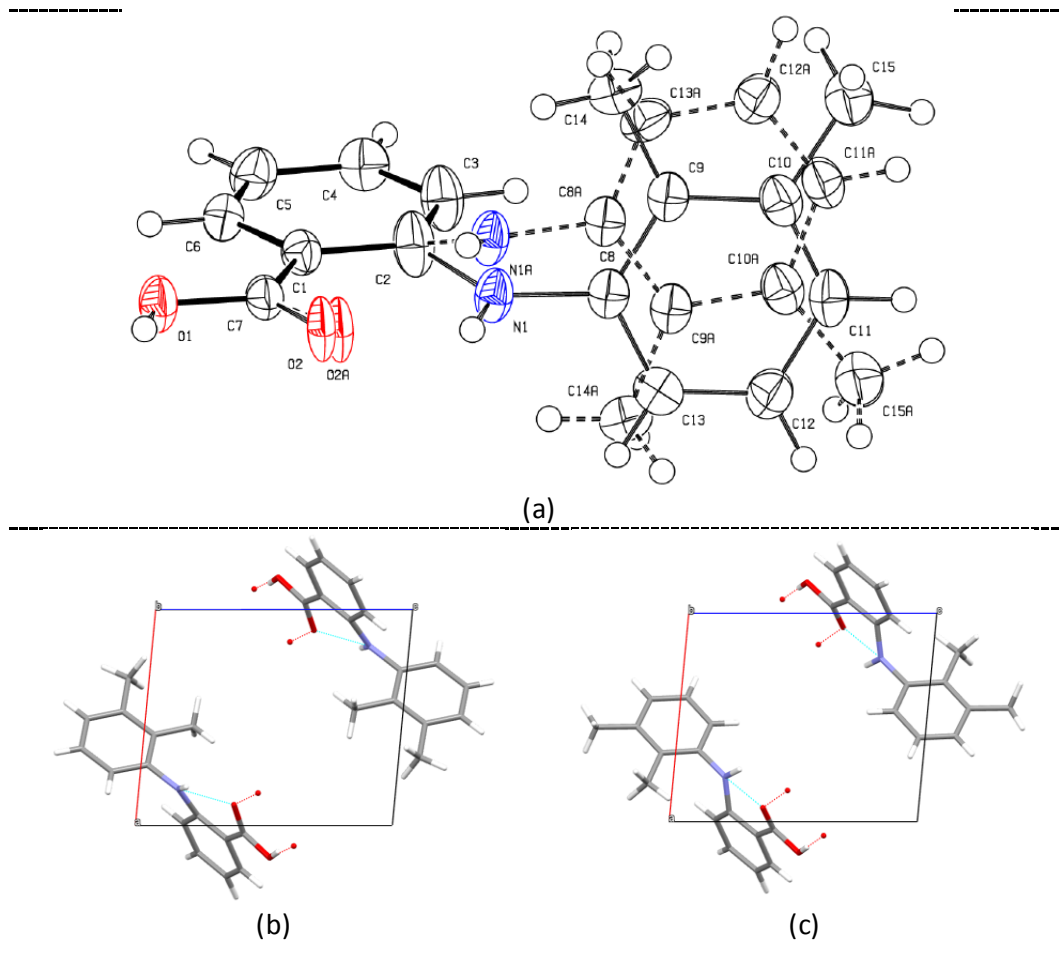
Figure 12. The disorder in MA form II. (a) thermal ellipsoid plot of 50 % probability showing both components of the disorder, (b) the unit cell of the major component with 0.654 occupancy and (c) the unit cell of the minor component with 0.346 occupancy.
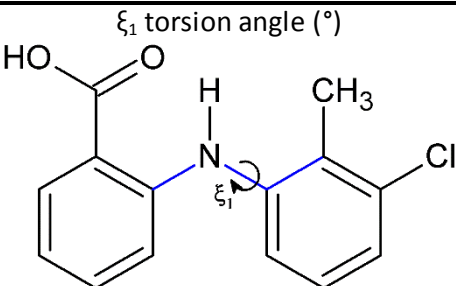
Two ordered models of MA form II have been created by separating the two components of disorder present in the redetermination of MA form II in this thesis (Figure 12b and Figure 12c). The MA molecule in each ordered model is found in just one conformation. These ordered models will enable crystal packing similarity calculations to be carried out with ease later in this thesis.

2.2 Tolfenamic Acid

TA has five known polymorphs that are found on the CSD. TA form I can be obtained by recrystallisation from absolute ethanol and form II can be obtained from rapid cooling of boiling ethanol (96%) in an ice bath.[112-114] Experimental and computational investigations have also suggested that the form of TA obtained from ethanol can be affected by the starting concentration of TA with form II being favoured at low supersaturation and form I being obtained at high supersaturation.[114, 115] TA forms I and II are often referred to as the white and yellow form respectively due to the colour of the crystals.[113] TA forms III, IV and V were isolated from an ethanol solution in the presence of nonpolar aromatic polymers, by PIHn.[32]

As in MA, the five polymorphs of TA all contain the $R_2^2(8)$ carboxylic acid dimers, but differ in conformation as shown by the values of the ξ_1 torsion angles for each polymorph reported in Table 6. Where all the polymorphs of MA were $Z' = 1$, only TA forms I, II and V are $Z' = 1$. TA form III is $Z' = 2$ and TA form IV is $Z' = 3$. TA form V is disordered with two conformations of TA in the unit cell and was identified to be isostructural with MA form II from PXRD data.[116]
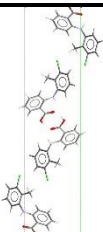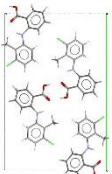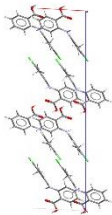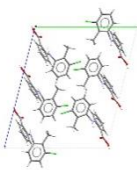
Table 6. The ξ_1 torsion angle (C_2-N_1-C_8-C_9) in the different polymorphs of TA. The ξ_1 torsion angle is shown by the blue bonds in the diagram.

Polymorph	I[113]	II[113]	III[32]	IV[32]	V[32]
ξ_1 torsion angle (°)	74.95	142.63	126.78 138.37	115.85 125.92 134.14	71.36 -91.63

The different polymorphs of TA can be distinguished using Raman spectroscopy.[32, 105] Infrared spectroscopy can also be used to differentiate between polymorphs I and II of TA. Polymorphs I and II of TA are reported to have different N-H stretching peak positions. Gilpin et al. report peaks at $3340 - 3341$ cm^{-1} and $3324 - 3325$ cm^{-1} for forms I and II respectively[117] whilst Jabeen et al. report peak positions of 3342 cm^{-1} and 3315 cm^{-1} respectively.[106]

Table 7 shows the crystallographic data of the five known polymorphs of TA taken from the CSD. Comparison of the unit cell data of TA form V with MA form II shows that the unit cells are isomorphous.

Table 7. Crystallographic data for the five known polymorphs of TA taken from the CSD.

Polymorph	I[113]	II[113]	III[32]	IV[32]	V[32]
Crystal System	monoclinic	monoclinic	monoclinic	triclinic	triclinic
Space Group	$P2_1/c$	$P2_1/n$	$P2_1/c$	$P-1$	$P-1$
Temperature (K)	110	110	85(2)	85(2)	85(2)
a (Å)	4.826(2)	3.836(2)	7.6356(15)	7.5237(8)	7.6488(13)
b (Å)	32.128(1)	21.997(5)	11.305(2)	14.3308(16)	9.0160(15)
c (Å)	8.041(4)	14.205(7)	28.065(6)	17.592(2)	9.4184(15)
α (°)	90	90	90	103.680(2)	107.385(3)
β (°)	104.88(3)	94.11(4)	93.03(3)	98.253(2)	92.062(3)
γ (°)	90	90	90	93.038(2)	101.662(3)
Z	4	4	8	6	2
Z′	1	1	2	3	1
Cell Volume (Å³)	1204.95	1195.54	2419.2	1816.41	603.806
R-Factor	0.052	0.029	0.0448	0.0723	0.0658

2.2.1   Obtaining TA form I and TA form II

2.2.1.1   Methods

Materials. TA was purchased from LKT Laboratories Inc. and was used without further purification.

Preparation of Single Crystals of TA form I. Single crystals of TA form I were obtained from recrystallisation from ethanol by room temperature solvent evaporation to dryness. Single crystals of TA form I were also obtained by sublimation onto a glass surface under a static vacuum (3.0 x 10^{-2} Pa) for 48 hours. See chapter 5 for further experimental details on the sublimation experiment.

Preparation of TA form II. TA form II was obtained by cooling a solution of TA in boiling ethanol using an ice bath, following directions in the literature.[112-114]

Single Crystal X-ray Diffraction. See section 2.1.1.1. Unit cell data was collected for crystals of TA obtained from ethanol solution and by sublimation. The crystals were confirmed to be TA form I by the unit cell data.

Infrared Spectroscopy. See section 2.1.1.1.

2.2.1.2   Results

The unit cell data collected by SCXRD showed that both recrystallisation from room temperature ethanol solution and sublimation onto a glass surface produce TA form I.

In comparison, rapid cooling of TA in boiling ethanol produced TA form II which was confirmed by infrared spectroscopy. The infrared spectra of TA form I (obtained by recrystallisation from room temperature ethanol solution) is shown in Figure 13 alongside the spectra of TA form II (obtained by rapid cooling of TA in boiling ethanol). The different positions of the N-H stretching peaks in Figure 13 indicate the polymorphic form with a peak at 3339 cm^{-1} for TA form I and a peak at 3323 cm^{-1} for TA form II.
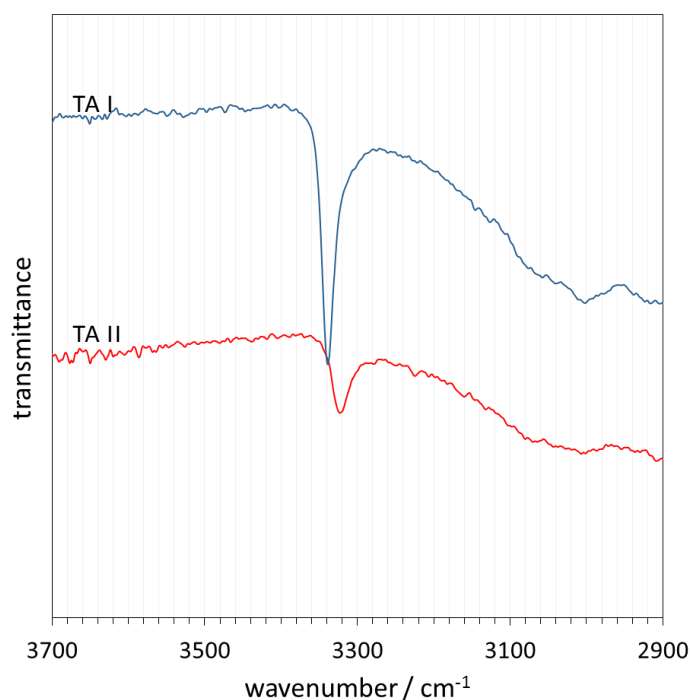
Figure 13. The infrared spectra of TA form I and TA form II.

2.3   Chloro-Methyl Replacement within MA and TA Crystal Structures

Although the molecules MA and TA are molecularly isostructural, with the same skeleton of bonds, current literature on their respective polymorphs shows that there are both similarities as well as numerous differences in the way that the two compounds crystallise.

Table 3 shows the crystal structure similarities between the polymorphs of TA and MA form I as calculated by Uzoh.[89] The work by Uzoh shows that TA form IV and MA form I are isostructural with a 15 molecule overlay, $rmsd_{15} = 0.30$ Å, and that TA form III and MA form I are structurally similar with a 13 molecule overlay, $rmsd_{13} = 0.45$ Å. López-Mejías et al. identified MA form II and TA form V as isostructural from PXRD data.[116]

Crystal structure similarities have been carried out between all the known polymorphs of TA and MA using the crystallographic data from this work. The isostructural pairs of crystal structures presented in Figure 14 show that MA form I is isostructural to TA form IV and MA form II is isostructural to TA form V. No isostructural relationships exist between known polymorphs of MA and TA for MA form III or TA forms I, II and III.

The existence of isostructural polymorphs of MA and TA is likely to be due to the fact that MA and TA differ only in the replacement of a methyl group on MA with a chloro group on TA (see Figure 7). As mentioned previously in section 1.2.2.1, methyl and chloro groups have similar van der Waals volumes and as such can be interchangeable within crystal lattices [24, 25] following the Kitaigorodsky principle of close packing. [62]

Although it is widely agreed that methyl and chloro groups have similar van der Waals volumes, there is much disagreement in the literature as to which substituent is larger. In 1986, Desiraju and Sarma stated that the chloro group was smaller than the methyl group with a van der Waals volume of 19 $Å^3$ compared to 24 $Å^3$ for the methyl. [24] The van der Waals volumes of Cl and CH_3 groups have also been reported to be 20 $Å^3$ and 24 $Å^3$, respectively. [118-120] However, most recent literature states that the methyl group is the smaller substituent with a van der Waals volume of 19 $Å^3$ compared to 21 $Å^3$ for the chloro group. [21, 25, 121] Whichever substituent (methyl or chloro) is larger, the van der Waals volumes are similar enough in size to facilitate isostructurality between two pairs of known polymorphs of MA and TA (Figure 14).

The occurrence of isostructural crystal pairs that result from a chloro-methyl interchange has previously been investigated by analysing the extensive number of structures on the CSD. [119, 122] Results suggest that only approximately 25 % of molecularly isostructural compounds, that differ by chloro-methyl interchange, are crystallographically isostructural. [119, 122] Furthermore, only 2 out of 22 isostructural crystal structure pairs that have just a singular chloro-methyl group interchange, have Cl···Cl distances less than 4.0 Å. [25] This information would tend to suggest that isostructural crystal structures would be less likely to be observed if there are short Me···Me or Cl···Cl interactions and the facile interchange of methyl and chloro substituents may not take place. [24] The Me···Me distance in MA form I is 3.63 Å and is as short as 3.09 Å in MA form II depending on the components of disorder. Similarly, the Cl···Cl distances in TA form IV are 3.44 Å on average and are 3.51 Å on average in TA form V depending on the disordered components. These Me···Me and Cl···Cl distances do not support suggestions from the literature. It is possible that in the case of MA and TA, isostructurality is retained because the chloro group occupies a space filling role [123] and does not have a structure directing role.

There are differences in the way that the isostructural pairs (MA form I - TA form IV and MA form II – TA form V) crystallise as well as differences in the number of known polymorphs of MA and TA. PIHn was used to obtained all forms of TA, including forms III, IV and V for the

first time, alongside the previously known forms I and II.[32] In comparison, the use of PIHn with MA only produced forms I and II and was not successful in obtaining form III or any additional polymorphs.[116] This information suggests that molecular differences between MA and TA influence the nucleation of different forms.

Additionally, sublimation experiments carried out in this thesis (see chapter 5 for more details) show that under the same conditions, MA and TA behave differently. For example, as has already been reported in sections 2.1.1.2 and 2.2.1.2, subliming MA onto glass obtains MA form II, but subliming TA onto glass under the same conditions obtains TA form I which is not isostructural to MA form II.

$rmsd_{15}$ = 0.332 Å

(a)

$rmsd_{15}$ = 0.164 Å $rmsd_{15}$ = 0.172 Å

(b)
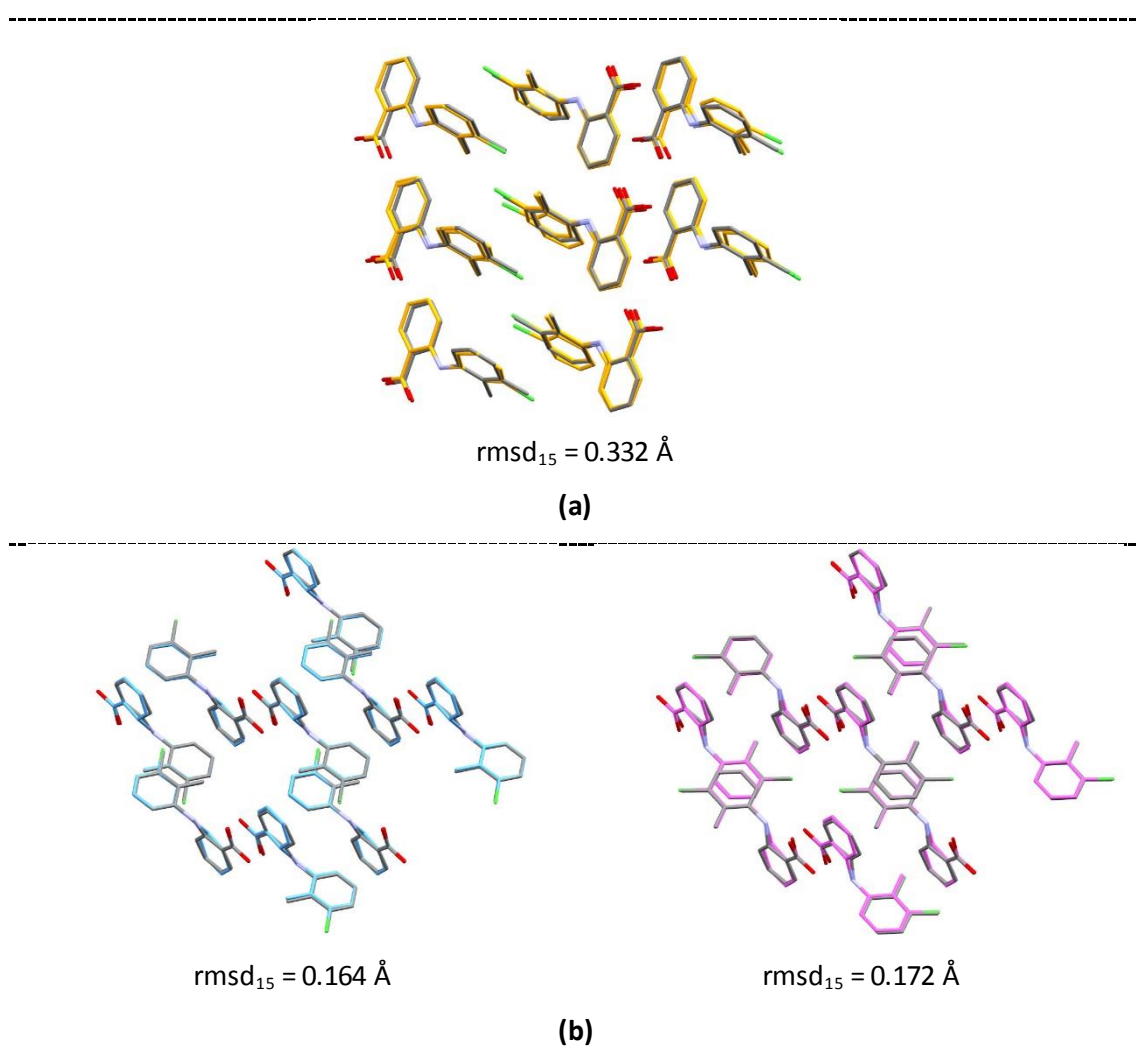
Figure 14. Crystal packing similarities of isostructural crystal structures of TA and MA. (a) MA form I (coloured by element) and TA form IV (coloured by orange carbons), $rmsd_{15}$ = 0.332 Å (b) MA form II (coloured by element) and TA form V (coloured by blue and pink carbons) – showing the overlays of ordered componenets of the disordered structure, $rmsd_{15}$ = 0.164 Å, 0.172 Å. The crystal structures for MA used in the similarity calculations are the redeterminations in this work.

3 Crystal Structure Prediction of Mefenamic Acid

The polymorphic landscape of a compound is most frequently investigated experimentally, but the ability to predict the polymorphs can reduce product development time scales and add confidence to the fact that all potential polymorphs have been identified experimentally. Therefore, CSP methods are continually being developed and tested for increasingly difficult systems including large, pharmaceutically relevant, flexible molecules,[72, 77, 78, 124] cocrystals,[125-127] salts[59] and hydrates.[128, 129]

3.1 Introduction

CSP methods find the range of different packings of molecules in a system that are thermodynamically feasible crystal structures. A common assumption is that the most stable packings correspond to observed crystal structures and that the most stable polymorphs will be found as minima on the crystal energy landscape if entropic effects are ignored.

In this chapter, the crystal energy landscape of MA is computed. The predicted structures were analysed and were compared to known polymorphs of MA. Additionally, the generated structures of MA were compared to known polymorphs of other known fenamates.

3.2 Computational Methodology

The computational methodology employed in this study on MA was adapted from that used to calculate the crystal energy landscapes for two other fenamates, FA and TA,[89] which was in turn adapted from that used for the successful crystal structure prediction of a flexible, pharmaceutically relevant, molecule in the fifth blind test.[71, 72] The methodology follows a multistep process involving conformational analysis, a global search of the possible crystal packings and then energy minimisation using quantum-mechanical calculations to evaluate the lattice energies, E_{latt}, of the generated structures.

As the lattice energies at each step in the methodology are evaluated with greater accuracy, the cost of the computational calculation increases. Therefore, as the model for E_{latt} improves, the number of unique structures that are considered is reduced. However, care must be taken to ensure that enough structures are considered at each stage to allow for the possible re-ranking of the relative stabilities of the crystal structures

3.2.1 Overview

The success of CSP methods does not solely depend on the generation of all the possible crystal structures for a particular crystal system, but also on the accurate ranking of lattice energies. The lattice energy, E_{latt}, is the energy of the static crystal relative to infinitely separated molecules in their lowest energy conformation, the gas phase minimum.[70] The crystal energy is approximated as the lattice energy, E_{latt}, which is the energy at 0 K and 0 Pa ignoring the zero-point energy and thus is related to the thermodynamic stability of the system. The CSP calculations ignore kinetic factors that affect nucleation.

3.2.1.1 Conformational Analysis and Selection of Degrees of Freedom

The lattice energy, E_{latt}, can be broken into two components, the intermolecular interactions between two molecules, U_{inter}, and the molecular energy penalty associated with distorting the molecule from its gas phase conformation, ΔE_{intra},

Equation 4 $$E_{\text{latt}} = U_{\text{inter}} + \Delta E_{\text{intra}}$$

Early CSP calculations on rigid molecules could ignore the ΔE_{intra} term. However, as CSP studies have developed and flexible molecules are now considered, there exists the possibility that the conformation of the molecule may change. Conformational changes incur a ΔE_{intra} energy penalty, but may allow for improvements in the hydrogen bonding or close packing of molecules in the crystal structures. As such, the division of E_{latt} into the two components, U_{inter} and ΔE_{intra}, is used in many current CSP methodologies.

In general, a molecule will generally adopt a low energy conformation in crystal structures, however, small changes in the conformation of a molecule can greatly improve the stability of a crystal structure by permitting more favourable intermolecular interactions.[70] In such cases, the conformational energy penalty paid, ΔE_{intra}, is generally quite small. In other more exceptional cases, a molecule might change conformation and break an internal hydrogen bond, resulting in a large ΔE_{intra} energy penalty, but this conformation change allows the molecule to form more favourable intermolecular hydrogen bonds, thus adopting a stable crystal structure.[78]

Small conformational changes (such as methyl group rotation or minor changes in torsion angles) that significantly affect the crystal stability can be considered later on in the CSP methodology when optimising the crystal structures. Initial conformational analysis helps identify the flexible degrees of freedom that require consideration in the global search so that a

balance is reached between reliable modelling of the effect of conformational changes and the computational costs.

3.2.1.2   Choice of Computational Model.

The next step in the CSP process involves identifying an appropriate model that accurately represents both the intra- and intermolecular interactions in the crystal structures. This involves deciding upon the level of theory and basis set for quantum-mechanical calculations on the isolated molecule which are used to calculate the intramolecular energy and electrostatic intermolecular interactions.[130] Additionally, an appropriate potential function needs to be decided upon to be used for the description of repulsion/dispersion intermolecular interactions. The choice of computational model is most often aided by testing the ability of the model to reproduce crystal structures of existing polymorphs or related molecules.

3.2.1.3   Global Search.

The extent of the crystallographic space involved in the search is influenced by the number of independent molecules in the asymmetric unit. Most searches consider just one molecule in the asymmetric unit (Z' = 1) to minimise computational costs. The search space increases with more molecules in the asymmetric unit (for example cocrystals and salts) as the number of variables required to describe the positions of the molecules relative to each other increases.

The global search must also take into consideration the range of possible space groups of the crystal system. Most organic molecules crystallise in a small range of the 230 space groups. It is common for the global search to only consider the 59 most populated space groups[131] on the CSD as a compromise between computational costs and the completeness of the search.

The global searches in this thesis are performed using the CrystalPredictor algorithm for flexible molecules,[132, 133] but there are a number of other computational search methods such as GRACE[75] and MOLPAK[134] that can also be used to generate crystal structures. CrystalPredictor generates a large number of crystal structures that vary in the selected conformational degrees of freedom of the molecule and in all the lattice variables for the chosen space groups such as unit-cell dimensions and angles and the relative positions and orientations of the molecules.

CrystalPredictor optimises the lattice energy of the generated crystal structures using pre-calculated atomic charges and intramolecular energies (ΔE_{intra}) for the isolated molecule in the range of conformations covered by the search. The atomic charges are used to model the

electrostatic interactions and an appropriate potential function is used to describe the repulsion/dispersion interactions that contribute to U_{inter}.

The search space is considered complete when the lowest energy structures have been found numerous times by the search algorithm. The generated structures are clustered together if they are deemed to be similar from comparisons of simulated PXRD patterns and molecular coordination spheres. Therefore, the number of unique structures found in a search will be less than the number of structures generated.

3.2.1.4   Accurate Lattice Energy Minimisation.

The lowest energy structures produced by the search are then used as starting points for local lattice energy minimisation with improved models for E_{latt}. Local lattice energy minimisation is often a multistep process.

3.2.1.4.1   CrystalOptimizer

Generated structures are re-minimised using the CrystalOptimizer[135, 136] algorithm which significantly improves the modelling of the lattice energy. Lattice energy minimisation can be considered a two-level problem which CrystalOptimizer solves by firstly optimising the conformation of the molecule and then using this fixed conformation as the input for rigid body calculations that optimise the lattice geometry of the crystal structure and minimise the lattice energy, E_{latt}.

CrystalOptimizer more accurately calculates E_{latt} than in previous steps because it allows minor conformation changes and molecular flexibility (such as small torsion angle changes and methyl group rotations) to be considered in energy minimisations. CrystalOptimizer uses GAUSSIAN[137, 138] to calculate the intramolecular energy and the wavefunction of the molecule. DMACRYS[139, 140] then minimises the lattice energy using extracted multipoles to evaluate the electrostatic interactions alongside an appropriate potential function for the repulsion/dispersion interactions.

CrystalOptimizer finds the optimum balance between intra- and intermolecular energies as the conformation of the molecule varies. This could be computationally demanding as new quantum mechanical calculations would have to be performed for each new conformation for each of the crystal structures being optimised. To overcome this, CrystalOptimizer uses local approximate models (LAMs) to reduce the computational costs of calculations. LAMs model the intramolecular energy and multipole representation of the charge density with reference to a particular conformation stored in a database. If the conformation of the molecule differs by more than the tolerance of accuracy of the LAMs approximation, from

any conformation in the database, then a new quantum mechanical calculation will be performed and added to the database. Hence, the CrystalOptimizer calculations become progressively faster as more crystal structures are optimised.

3.2.1.4.1.1 Distributed Multipole Moments

Previous steps in the computational methodology use point charges to represent the electrostatic interactions between molecules. However, due to the anisotropic nature of charge density at short range, a more accurate representation is achieved when the electrostatic potential of a molecule is represented by a multipole expansion (charge, dipole, quadrupole, octupole and hexadecapole) around a number of centres. Distributed multipole analysis (DMA)[141, 142] assigns multipole moments to each atom (or other sites defined in the molecule). Distributed multipoles need to be recalculated for changes in conformation of the molecules. The computational DMA approach derives the charge distribution from the *ab initio* wavefunction of a molecule calculated using GAUSSIAN and describes it using distributed multipoles extracted using the Gaussian Distributed Multipole Analysis (GDMA)[143] program.

3.2.1.4.1.2 Repulsion-Dispersion Potential

The dispersion and repulsion terms are modelled with an empirical *exp*-6 atom–atom potential. The exponential term represents the repulsive contributions that are present at short distances while the negative R^{-6} term models the long range dispersion contributions.

Equation 5. $$U_{repul-disp} = \sum_{i,k} A_{\iota\kappa}\exp(-B_{\iota\kappa}R_{ik}) - C_{\iota\kappa}R_{ik}^{-6}$$

where the interactions are between atom i of type ι in molecule 1 and atom k of type κ in molecule 2. Equation 5 assumes that the interactions between molecules or ions can be approximated by the interactions of their constituent atoms. It is also assumed that the atom-atom parameters $A_{\iota\kappa}$, $B_{\iota\kappa}$ and $C_{\iota\kappa}$ are transferrable between different molecules. The parameters $A_{\iota\kappa}$, $B_{\iota\kappa}$ and $C_{\iota\kappa}$ are specific to the pair of interacting non-bonded atoms and determine the strength of the repulsion-dispersion forces as a function of the intermolecular separation, R_{ik}. The repulsion-dispersion potential has been derived by empirically fitting the parameters to known crystal structures.[144, 145]

3.2.1.4.2 Polarisable Continuum Model

It has been noted that the CrystalOptimizer calculated lattice energies that combine density functional theory (DFT) intramolecular energies with atom-atom potentials for

intermolecular interactions do not always accurately distinguish the observed crystal structures from other low energy generated alternatives when the electrostatic contribution to the lattice energy is derived from isolated molecule calculations.[146] This is because the effect that the bulk crystalline environment has on distorting the molecular charge distribution is not considered.

Therefore, another refinement to the lattice energy can be made by considering a model for the bulk crystalline environment and the polarisation of the molecular charge distribution of molecules. The polarisable continuum model (PCM)[147] can be applied to the most stable crystal structures following CrystalOptimizer by calculating the intramolecular energy and wavefunction of the molecule using GAUSSIAN with a dielectric of $\varepsilon = 3.0$, shown to be typical of organic crystals.[146]

The PCM has been used in many CSP studies[78, 89, 124, 128, 148] and is routinely used as a method of refining the lattice energies of organic crystals.[70]

3.2.1.4.3   Sensitivity of Lattice Energy to Computational Model

The sensitivity of the calculated lattice energies to the choice of computational model is often evaluated to estimate any uncertainties in the relative energy estimates of the thermodynamically plausible crystal structures. A number of different computational models are applied to the putative structures and any stability re-ranking due to a change in method of calculation is analysed to confirm that the relative stabilities of the generated structures are not just an artefact of the choice of computational model.

Often the use of the PCM is an initial test to see how sensitive the lattice energies are to a change in computational model. The Helmholtz free energy at 298 K[149] can also be estimated and different potentials, such as the Williams W99[150] or custom potentials are often tested. Periodic electronic structure calculations have also been used to estimate lattice energies.[88, 148] In principle, the effect of temperature could be estimated to give a free energy.

3.2.2 Application of Methodology to Mefenamic Acid

This section describes the how the computational methodology outlined in section 3.2.1 is implemented in the CSP study on MA.

3.2.2.1 Conformational Analysis

The conformational flexibility of MA was initially analysed by comparing the molecular conformations of the known polymorphs of MA (Figure 15a) noting that a comparison of the different conformations of MA in MA form II was mentioned previously in section 2.1.1.2. Figure 15a shows that the conformations of MA differ most in the rotation of the alkylated phenyl ring and the position of the amino bridging group relative to the phenyl ring with the carboxyl group. These conformational differences are mirrored in the molecular overlays of TA which are shown in Figure 15b.

(a)   **(b)**
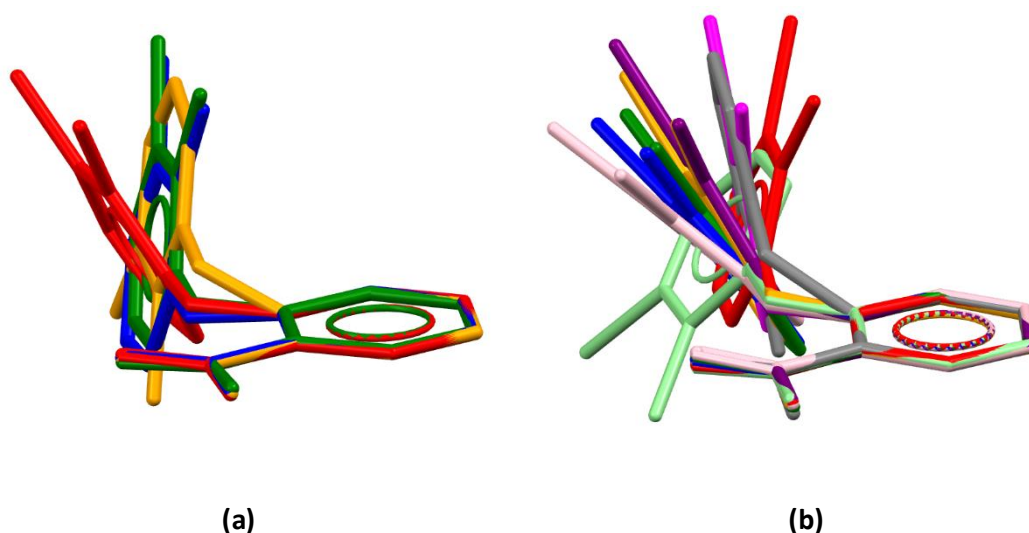
Figure 15. Molecular overlays of (a) MA and (b) TA showing the conformations of the molecules as found in the known polymorphs of each compound on the CSD.

The conformational overlays of MA and TA in Figure 15 indicate that the major degree of freedom that needs to be considered is the ξ_1 torsion angle (defined previously in Table 4). This was the only degree of freedom investigated in the initial conformation scans which is justified by the presence of the internal hydrogen bond which keeps the carboxyl group, the adjacent ring and the bridging amino group planar (see Figure 8).

Quantum mechanical, *ab initio* calculations were carried out on the isolated molecule using GAUSSIAN03[137] at the PBE0/6-31+G(d) level of theory to provide a relaxed conformational scan of the ξ_1 torsion angle. The conformational energy of MA was scanned in the range -180 ° to 0 ° in 10 ° steps. The aim of the torsion angle scan was to observe how the relative conformational energy of MA changes as a function of ξ_1. This indicates the range of

conformations (that are the lowest in energy) that should to be considered when performing a search using CrystalPredictor which uses an approximate conformational energy surface in the initial stage in the search for feasible crystal structures.

The decision to only analyse the effect of changing the ξ_1 torsion angle on the conformational energy of MA echoes the choice made by Uzoh in the calculation of the crystal energy landscape of TA.[89] The potential energy surface of isolated MA was calculated at the PBE0/6-31+G(d) level of theory as this was the level of theory used by Uzoh. This CSP study on MA mirrors many of the decisions made by Uzoh in order to compute a crystal energy landscape of MA that will be comparable to that of TA.

3.2.2.2   Choice of Computational Model

The choice of computational model for the final lattice energy minimisation was verified for MA by testing the accuracy of reproduction of the known forms of MA at the PBE0/6-31+G(d) level of theory using the FIT potential, an exp-6 atom-atom repulsion-dispersion potential with empirically fitted parameters.[145]

3.2.2.3   Global Search

Before the crystal structures were generated in the global search, GAMESS[151] was used to produce an approximate conformational energy surface to be used in the input for CrystalPredictor. The most recent versions of CrystalPredictor allow the use of GAUSSIAN at this stage, but this CSP study was conducted using CrystalPredictor 1.6 which was only compatible with GAMESS. Therefore, as GAMESS cannot carry out calculations at the PBE0/6-31+G(d) level of theory, the molecule was first optimised at the B3LYP/6-31G(d,p) level of theory and then the atomic charges and single point energies were also calculated at the B3LYP/6-31G(d,p) level of theory. The conformational energy surface produced by GAMESS as a function of the ξ_1 torsion angle closely follows the conformational energy surface produced in section 3.2.2.1 and is an adequate representation of the conformational energy surface of MA. A comparison of the conformational energy scans carried out by GAMESS at the B3LYP/6-31G(d,p) level of theory and GAUSSIAN at the PBE0/6-31+G(d) level of theory can be found in Appendix 1 on page 196.

Crystal structures were generated with one molecule in the asymmetric unit (Z' = 1) over the low conformational energy region of MA, determined following the conformational analysis, varying the torsion angle, ξ_1, from 40° to 180°. The structures were generated using CrystalPredictor in the following 59 space groups: *P1, P-1, P2$_1$, P2$_1$/c, P2$_1$2$_1$2, P2$_1$2$_1$2$_1$, Pna2$_1$, Pca2$_1$, Pbca, Pbcn, C2/c, Cc, C2, Pc, Cm, P2$_1$/m, C2/m, P2/c, C222$_1$, Pmn2$_1$, Cmc2$_1$, Aba2, Fdd2, Iba2, Pnna, Pccn, Pbcm, Pnnm, Pmmn, Pnma, Cmcm, Cmca, Fddd, Ibam, P4$_1$, P4$_3$, I-4, P4/n, P4$_2$/n,*

I4/m, I4$_1$/a, P4$_1$2$_1$2, P4$_3$2$_1$2, P-42$_1$c, I-42d, P3$_1$, P3$_2$, R3, P-3, R-3, P3$_1$2$_1$, P322$_1$, R3c, R-3c, P6$_1$, P6$_3$, P6$_3$/m, P2$_1$3, Pa-3. The intermolecular contributions to the energy of the lattice of the generated structures were calculated from the atomic charges and the FIT potential.

3.2.2.4 Accurate Lattice Energy Minimisation

Following the CrystalPredictor search, DMAflex-Quick[152] was used to improve the description of electrostatic interactions by including multipoles in calculating the lattice energy for the unique crystal structures following CrystalPredictor. The DMAflex-Quick code uses multipoles from the lowest energy conformation and analytically rotates them to minimise the lattice energy using DMACRYS. DMACRYS calculated the lattice energy, U_{inter}, using the PBE0/6-31+G(d) distributed multipoles and the FIT potential.

Following DMAflex-Quick, the unique crystal structures lying within 30 kJ mol^{-1} of the global minimum were reminimised using CrystalOptimizer. CrystalOptimizer optimised the structures to minimise the lattice energy E_{latt}, by allowing the conformational degrees of freedom shown in Figure 16 to change as well as the geometry of the crystal structure. The intramolecular energy, ΔE_{intra}, was calculated using distributed multipoles at the PBE0/6-31+G(d) level of theory which were extracted from GAUSSIAN calculations using GDMA.
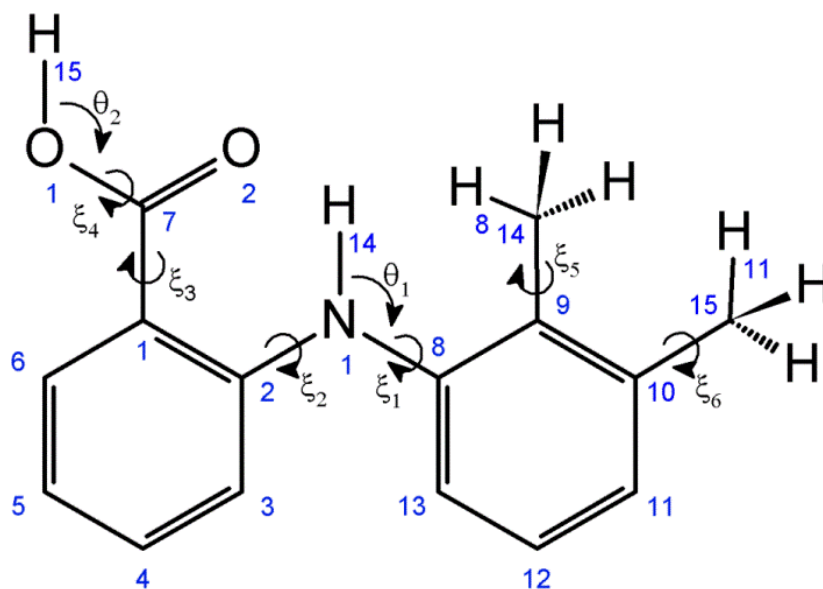
Figure 16. The degrees of freedom optimized by CrystalOptimizer for crystal structures of MA ($\xi_1 \equiv$ C$_2$-N$_1$-C$_8$-C$_9$, $\xi_2 \equiv$ C$_1$-C$_2$-N$_1$-C$_8$, $\xi_3 \equiv$ O$_1$-C$_7$-C$_1$-C$_2$, $\xi_4 \equiv$ H$_{15}$-O$_1$-C$_7$-C$_1$, $\xi_5 \equiv$ H$_8$-C$_{14}$-C$_9$-C$_8$, $\xi_6 \equiv$ H$_{11}$-C$_{15}$-C$_{10}$-C$_9$, $\theta_1 \equiv$ H$_{14}$-N$_1$-C$_8$, $\theta_2 \equiv$ H$_{15}$-O$_1$-C$_7$). The diagram shows the dihedral angle, ξ_1, which was the only flexible angle in the CrystalPredictor search. The molecule is symmetric about the dihedral angle, ξ_1, thus + ξ_1 = - ξ_1. The diagram also shows the numbering of the atoms used in all calculations.

The flexible degrees of freedom that were considered in the CrystalOptimizer calculations for MA mirror the degrees of freedom that were considered in CrystalOptimizer calculations on TA. However, MA requires consideration of an additional degree of freedom to TA, the ξ_6 torsion angle (Figure 16), due to the replacement of the chloro group on TA with the methyl group on MA which will rotate.

In order to estimate the effect of the crystal environment, the PCM was applied to the unique crystal structures following CrystalOptimizer calculations. The bulk crystalline environment was modelled using GAUSSIAN03 to calculate the wave function of the molecular structure in a dielectric of $\varepsilon = 3.0$, shown to be typical of organic crystals. GDMA was then used to extract the distributed multipoles and the crystal structures were re-minimised, keeping the molecule rigid, using DMACRYS. The resulting U_{inter} was combined with ΔE_{intra} (the intramolecular energy penalty with respect to the lowest intramolecular energy of the set of predicted crystal structures) to evaluate the final lattice energies. The resulting structures from CSP methods were labelled #yMA_x where x is the energy ordering after CrystalPredictor and y is the energy ordering following the PCM calculations. Labelling in this way will allow for immediate identification of the extent of the re-ranking of structures due to improved models for the lattice energy.

For comparison with the generated structures, analogous CrystalOptimizer calculations were also carried out using the experimental structures of the MA polymorphs as the input structures. This enabled the CSP methods to be analysed to see how rigorous the CSP methods were to verify that the known experimental forms were found in the search and that the search was extensive enough.

3.2.2.4.1   Sensitivity of Lattice Energy to Computational Model

To test the sensitivity of the calculated lattice energies of a selected number of structures of interest, the lattice energies were re-evaluated using different computational models. Initially, the Williams W99 potential was tested with CrystalOptimizer and the PCM. Alternative estimates of the lattice energy were also obtained by Rui Guo who carried out periodic electronic structure calculations, a plane wave DFT+D approach using the CASTEP[153] code with the PBE functional and the Tkatchenko-Scheffler (TS)[154] dispersion correction. Rui Guo carried out the periodic DFT+D calculations on the UK National High Performance Computing Facility, ARCHER.

3.3 Results and Discussion

3.3.1 Conformational Energy Surface

The conformational potential energy surface of the isolated MA molecule is shown in Figure 17a. Outside of the low energy conformational region (-180° to -40°), the energy penalty for conformational change, ΔE_{intra}, is greater than what is expected to be observed in crystal structures. For these reasons, the approximate conformational energy surface that was used in the CrystalPredictor search only considered conformations where the ξ_1 torsion angle was between -40° and -180°. The high energy conformational region corresponds to the presence of steric hindrance due the bulky methyl groups approaching the benzene ring.

The conformational scan of MA shows that the global energy minimum is around -140° and there is another shallow, local, energy minimum around -70°. The experimental ξ_1 torsion angle value for MA form I is -119.42° which is located in the same well as the global minimum. The ξ_1 torsion angle values for MA form II and MA III correspond closely to the local energy minimum. The range of conformations that MA adopts in the known polymorphs shows the importance of considering the whole low energy region in the global search.

These results are in agreement with the results of the previous study on fenamic acid (FA) and TA carried out by Uzoh (Figure 17b).[89] In the case of FA, the energy penalty for conformational change is less than 6 kJ mol^{-1} over all possible conformations.[44] This is due to the fact that there is less steric hindrance than is observed in MA and TA as there are no substituent groups on the benzene ring that rotates as the ξ_1 torsion angle changes. In comparison, as TA is molecularly similar to MA with bulky substituents, the conformational energy scan also displays a high energy conformational region.

The conformational energy scans of MA, FA and TA are also in agreement with an earlier study on TA that was carried out by Mattei and Li[155] who computed the conformational energy of TA as a function of the same ξ_1 torsion angle in the gas phase as well as in ethanol and tetrachloromethane solvent media. The calculations by Mattei and Li were carried out using GAUSSIAN03 and the B3LYP functional with the basis sets 6-311G(d,p) and 6-311++G(d,p). They report a global minimum at -142° and a local minimum at -75° for the isolated molecule of TA.
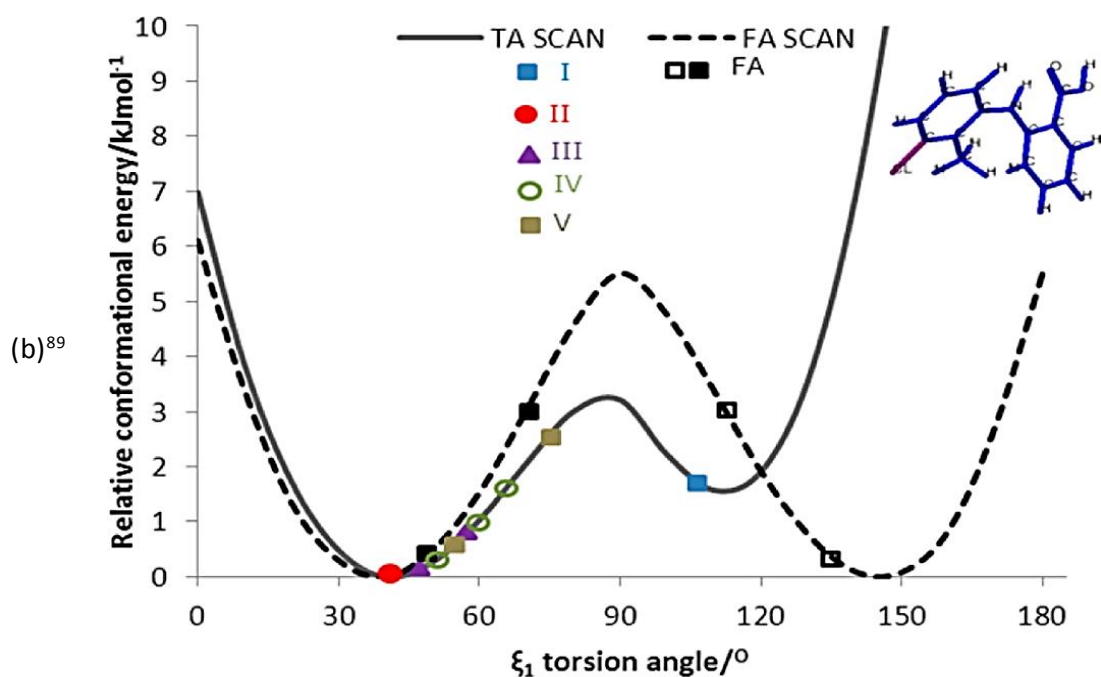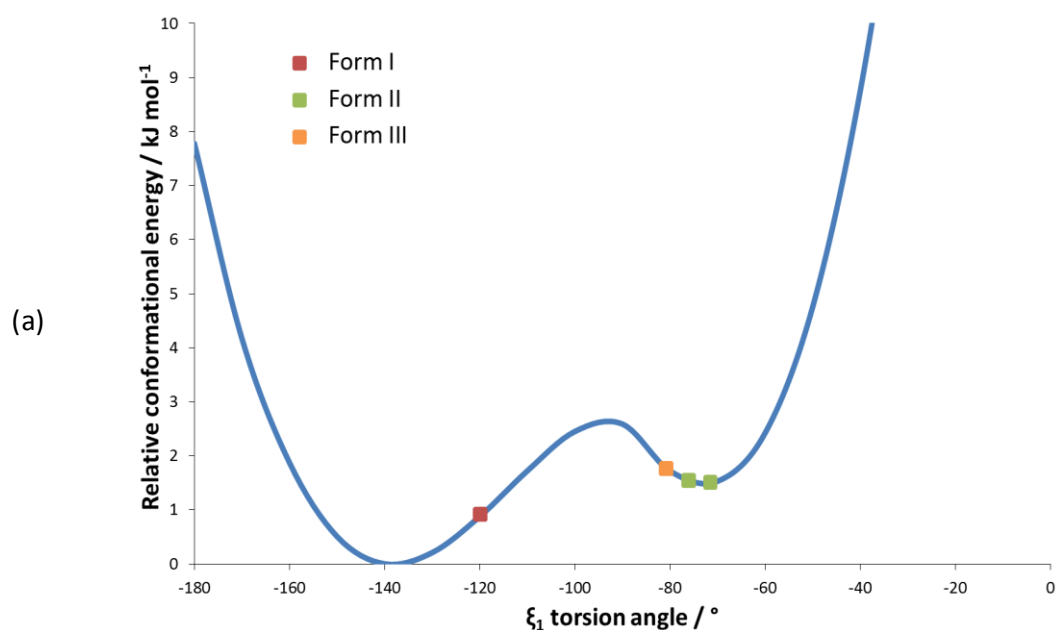
Figure 17. Relaxed scan of the relative conformational energy as a function of the ξ_1 torsion angle calculated at the PBE0/6-31+G(d) level of theory, including the experimental values of ξ_1 for (a) MA. (b) shows the conformational energy scans of fenamic acid and TA as calculated by Uzoh.[89] The symmetry equivalent FA conformations are denoted by open black squares and an inset diagram shows the steric hindrance for TA in the high-energy region. The conformational scans in Figure 17 can be compared because the difference in the ξ_1 –axis corresponds to the difference in how ξ_1 was defined for MA and TA. For MA the torsion angle was defined as C_2-N_1-C_8-C_9, but in TA it was defined as C_2-N_1-C_8-C_{13} using the numbering system for MA in Figure 16.

3.3.2   Validation of the Computational Model

The chosen computational method was able to satisfactorily reproduce the ordered structures of MA form I, MA form III and the major component of disordered form II as minimums in the lattice energy following CrystalOptimizer and PCM calculations (Table 8). The minor component of MA form II overlays nine molecules with the Z = 2 model for the experimental minor component, $rmsd_9 = 0.851$ Å.

Table 8. Comparison of the experimental structures of the polymorphs of MA taken from the CSD (forms I, II and III) and this work (redetermination of MA form I) with the computationally modelled structures (Comp) following CrystalOptimizer and PCM calculations.

		E_{latt} (kJ mol^{-1})	a (Å)	b (Å)	c (Å)	α (°)	β (°)	γ (°)	$rmsd_{15}$ (Å)
MA I	XYANAC		14.556	6.811	7.657	119.57	103.93	91.30	**0.240**
	This work		6.7887	7.3613	14.0330	76.868	79.857	64.863	**0.166**
	Comp	**-149.1612**	14.2140	6.9602	7.6574	118.8731	103.0429	93.8582	
MA II (major)	XYANAC02		7.6969	9.1234	9.4535	107.113	91.791	101.481	**0.464**
	Comp	**-148.7365**	7.9760	8.7303	9.8305	109.5327	95.6673	97.7283	
MA III	XYANAC03		7.723	7.9340	11.2320	83.590	80.940	67.510	**0.569**
	Comp	**-146.4427**	7.8068	8.2872	11.1171	77.1428	81.0798	62.3338	

$rmsd_{15} = 0.240$ Å $rmsd_{15} = 0.166$ Å

(a)   **(b)**
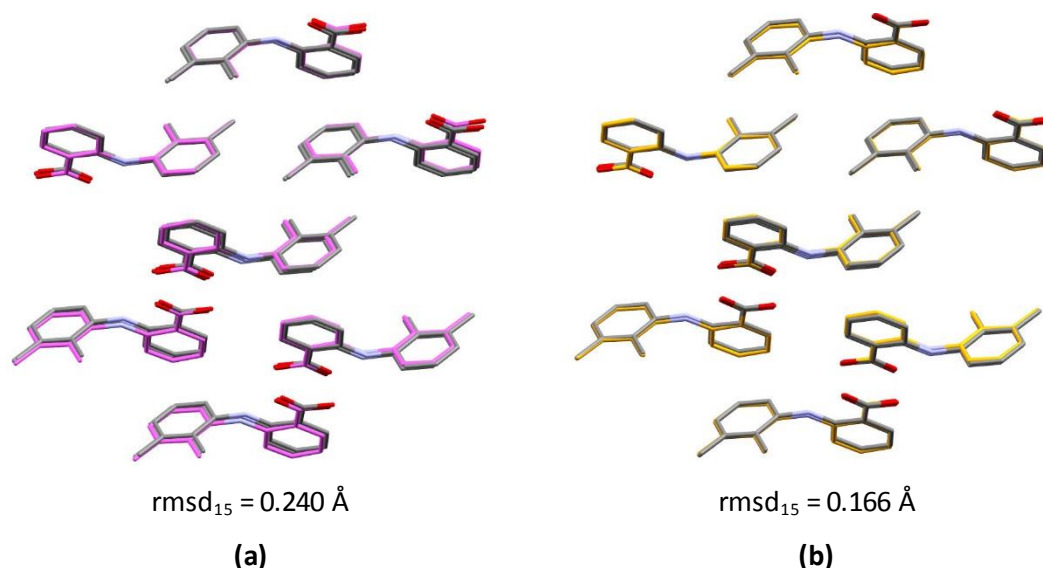
Figure 18. Crystal packing similarity of the computational model of MA form I (coloured by element) with (a) MA form I from the CSD, XYANAC, (pink) and (b) MA form I from the redetermination in this work (orange).

The computational model has a better 15 molecule overlay with MA form I from this work than with XYANAC from the CSD with an $rmsd_{15}$ value of 0.166 Å compared to 0.240 Å. This would be expected from the lower temperature redetermination; as SCXRD data was collected at 150 K in this work and at room temperature for XYANAC.

The range of lattice energies of the MA polymorphs is less than 3 kJ mol^{-1} which is consistent with the small energy range expected for such polymorphs. The order of stability of the polymorphs from the lattice energy minimisations is I > II > III (if we only consider the ordered model of the major component for MA form II) which is in agreement with experimental observations of the stability at ambient temperatures.[99]

3.3.3   Crystal Energy Landscape

The CrystalPredictor search produced 440,086 structures of which 17,591 were unique and 9102 were within 30 kJ mol^{-1} of the global minimum. DMAflex-Quick calculations were carried out on the 9102 structures. The number of unique structures was reduced to a total of 7312 after the minima determined by the DMAflex-Quick calculations were clustered.

Clustering carried out crystal packing similarity calculations by comparing the simulated PXRD patterns of the generated structures and then using 20 molecule clusters to determine equivalent structures. Structures were deemed to be equivalent if they had a PXRD similarity greater than 0.97 and a $rmsd_{20}$ value below 0.1 Å.

CrystalOptimizer calculations were then carried out on the 1859 unique structures within 20 kJ mol^{-1} of the global minimum after DMAflex-Quick. Finally, PCM calculations were carried out on the 1260 structures that were determined to be unique lattice minima. Clustering occurred between each stage to eliminate duplicate structures.

Figure 19 shows the calculated crystal energy landscape of the structures that are within 10 kJ mol^{-1} of the most stable structure. A cut-off of 10 kJ mol^{-1} was used following a statistical study[2] that showed 23 % of conformational polymorphs differ in lattice energy by 6 to 10 kJ mol^{-1}. All the crystal structures in Figure 19 contain the same, approximately planar, $R_2^2(8)$ carboxylic acid dimers. However, the structures differ in packing because the orientations of the phenyl ring with the methyl substituents changes due to differing values of the ξ_1 torsion angle. Appendix 2 on page 197 details the ξ_1 torsion angles for the most stable 23 structures which take values from 60.66 ° to 157.07 ° and the distribution of ξ_1 torsion angles is shown in Appendix 3 on page 198. The majority of the generated structures have ξ_1 torsion angle values between 135 ° and 140 ° that correspond to the global minimum conformational energy for MA as described in section 3.3.1. However, as will be discussed and as is shown in Figure 20, the two lowest energy structures are both isostructural to MA form I, but differ in the ξ_1 torsion angle by 17 °.
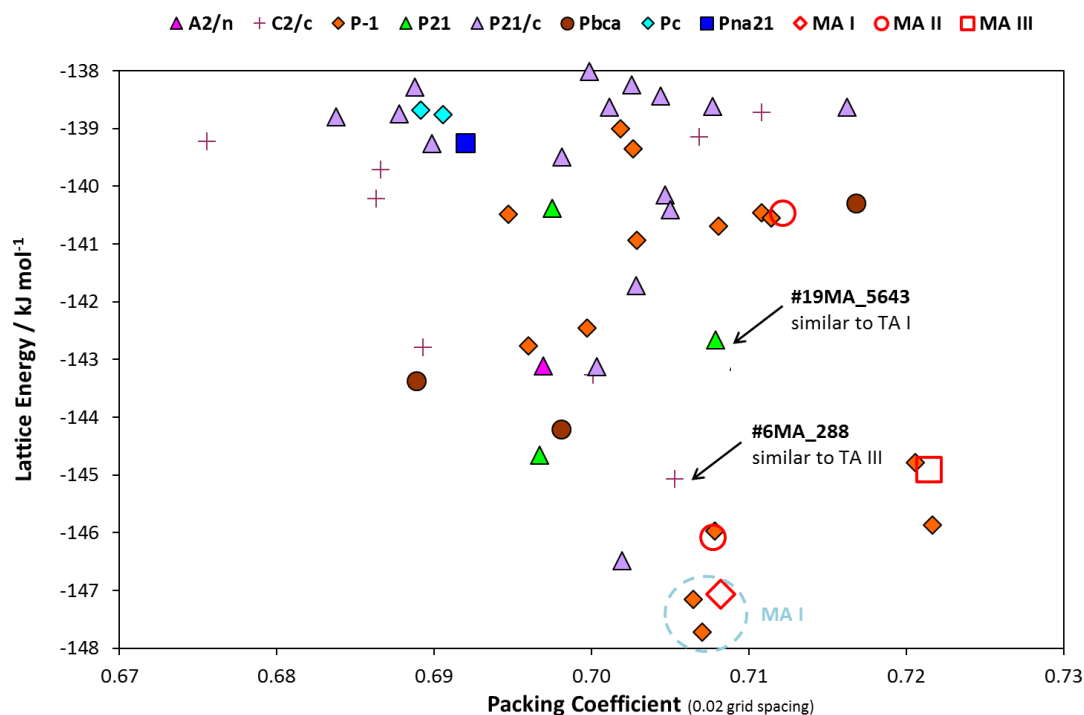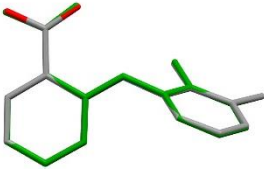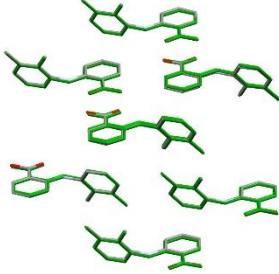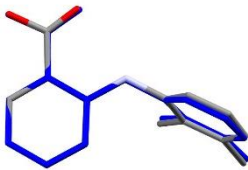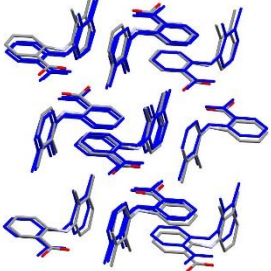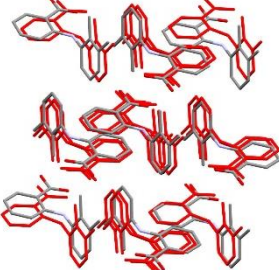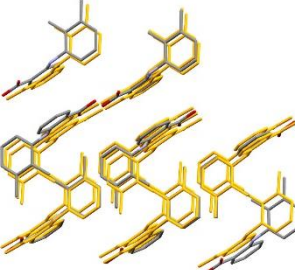
Figure 19. The lowest 10 kJ mol⁻¹ of the crystal energy landscape of MA where each symbol represents a crystal structure of the specified space group which is a minimum in the lattice energy (calculated within the polarizable continuum). In total, 1260 lattice energy minimisations were carried out. Appendix 2 on page 197 details the lattice energy minima and unit cell dimensions of the 23 structures of MA that lie lowest in energy following the PCM calculations. The structure similarity of generated structures with known polymorphs of TA is discussed in section 3.3.4. The two structures around the global minimum are both isostructural with MA form I. The lattice energy minima starting from the three observed polymorphs of MA using the same computational model (Table 8) are also shown. The packing coefficient is the proportion of the cell volume[156] occupied by the molecule calculated using a grid spacing of 0.02 Å.

The energy ranking of the structures following CrystalPredictor was markedly different to the final energy ranking following PCM calculations. This is because the lattice energies of the generated structures are sensitive to the quality of method used which was increased at each stage of the calculations. The labels of the structures (list of 23 most stable in Appendix 2, page 197) on the crystal energy landscape show how the energy ranking of each structure changed as the method improved from using fixed point charges at the B3LPY/6-31G(d,p) level of theory in CrystalPredictor to using the PCM and distributed multipoles at the PBE0/6-31+G(d) level of theory. For example, structure #19MA_5643 was 5643rd lowest in energy after CrystalPredictor but 19th lowest in energy following the PCM calculations.

The energy rankings changed less after the introduction of the distributed multipole electrostatic model, but was still significant (see Appendix 4 on page 199 for a comparison of the crystal energy landscapes after (a) DMAflex-Quick, (b) CrystalOptimizer and (c) PCM calculations). In particular, the application of the PCM model made #1MA_128 0.569 kJ mol⁻¹ more stable than #2MA_978, whereas these two approximations to MA form I were almost

isoenergetic after CrystalOptimizer (at which stage the global minimum structure was #2MA_978 which was only 0.055 kJ mol^{-1} lower in energy than the next structure, #1MA_128).

Table 9. Comparison of the experimental structures of the three polymorphs of MA with the closest matching structures generated in the search. The PXRD similarity was calculated using Mercury.

Polymorph	Similar structure from search	PXRD similarity	rmsd$_1$ (Å)	rmsd$_{15}$ (Å)
I	#1MA_128	0.988	0.0412	0.158
II - major	#4MA_889	0.934	0.1167	0.438
II - minor	#23MA_497	0.894	0.1200	0.609
III	#7MA_1666	0.941	0.1534	0.584

The global minimum structure on the crystal energy landscape, #1MA_128 (Z'=1, space group P-1), matches the single crystal X-ray result for MA form I, reproducing both the 15 molecule coordination sphere, rmsd$_{15}$ = 0.229 Å, and the molecular conformation, rmsd$_1$ = 0.0516 Å (Table 9).

The other two experimental forms of MA were also found in the search (Table 9). MA form III is structurally similar to #7MA_1666, the ordered model of the major component of disordered form II was found to be structurally similar to #4MA_889 and an ordered model of the minor component of the disordered form II was found to be structurally similar to #23MA_497. Although the ordered models of MA form II have the same unit cells (by definition), the two structures that were found in the search, #4MA_889 and #23MA_497, did not have identical unit cells and had a large difference (5.275 kJ mol^{-1}) in lattice energy. This energy gap is too large for a configurational entropy term to account for the disorder.[70] This is consistent with the structural difference between the two components, meaning that the disorder in MA form II is kinetically trapped as rearrangement to an ordered form would involve rotating the phenyl rings of one component of disorder by ~ 180° in the solid.

The energy ordering for the generated structures in the search suggests that the order of stability for the three polymorphs of MA would be I > II > III (#1MA_128 > #4MA_889 > #7MA_1666). This is in agreement with the previous calculations using the experimental crystal structures as starting points for lattice minimisation as well observations of the stabilities at ambient temperatures,[99] giving us reasonable belief in the relative energies of the generated structures as a whole.

(a)   (b)
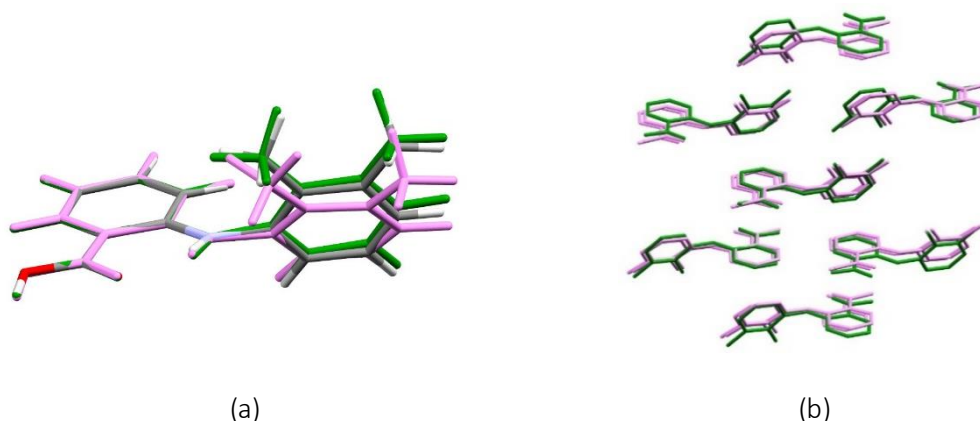
Figure 20. (a) Conformational overlay of one molecule of experimental MA form I (coloured by element) with generated structures #1MA_128 (green) and #2MA_978 (pink). The main difference in conformation is the ξ_1 torsion angle which is 119.40° (experimental), 117.15° (#1MA_128) and 134.19° (#2MA_978). There is also a noticeable difference in the orientation of a methyl group on #2MA_978 compared to the other two structures. (b) 15 molecule overlay of #1MA_128 and #2MA_978 with rmsd$_{15}$ = 0.448 Å.
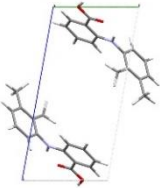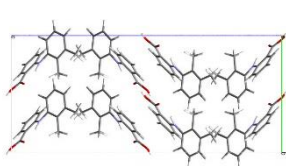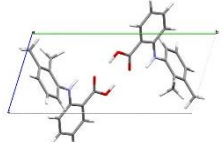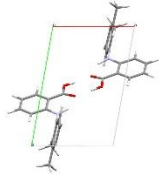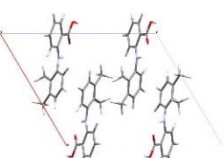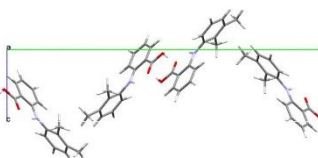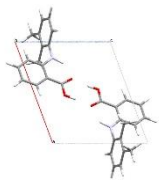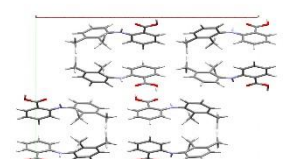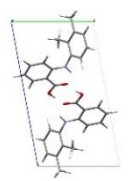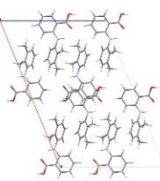
Structure #2MA_978 is the second lowest structure on the crystal energy landscape and like the global minimum structure, has a 15 molecule overlay with the experimental MA form I, but a significantly worse rmsd$_{15}$ = 0.419 Å. The generated structures #1MA_128 and #2MA_978 are not significantly different considering the likely amplitude of thermal motion, differing by a 'tilt' in the orientation of the phenyl ring with methyl substituents (Figure 20). Hence, it is not expected that #2MA_978 would be observed experimentally as a distinct

polymorph. Therefore, MA form I (optimised from XYANAC), #1MA_128 and #2MA_978 are grouped together on the crystal energy landscape in Figure 19 by the dashed light blue circle.

MA form III is the 7th most stable structure on the crystal energy landscape. There are three generated crystal structures that are competitive in lattice energy with the observed forms of MA; #3MA_237, #5MA_510 and #6MA_288. As indicated by the space group symbols in Figure 19, structures #3MA_237 and #6MA_288 belong to the $P2_1/c$ and C2/c space groups respectively. These space groups are different to the space groups of the known polymorphs of MA, which are all P-1. Therefore, unsurprisingly, there is no significant similarity between #3MA_237 and #6MA_288 and any of the known MA structures. Structure #5MA_510 belongs to the P-1 space group, but is not crystallographically similar to any of the known forms of MA.

Table 10 shows the unit cell diagrams of the ten most stable, unique crystal structures on the crystal energy landscape after duplicates that were not clustered together were removed manually.

Table 10. Unit cell diagrams of 10 unique most stable crystal structures on the crystal energy landscape following manual clustering to eliminate similar structures.

#1MA_128		#6MA_288	
#2MA_978		#7MA_1666	
#3MA_237		#8MA_2853	
#4MA_889		#11MA_1069	
#5MA_510		#14MA_318	

3.3.4 Structure Similarity of Generated Structures with Known Fenamates

The next stage of analysis involved comparing the computationally generated structures of MA with the structures of known forms of other fenamate molecules. The crystal structure similarity of the known fenamates with the low energy putative structures gave an indication as to whether fenamate crystals could possibly be used as templates surfaces in the search for predicted forms of MA following a similar approach to that used to nucleate CBZ form V for the first time using DHC form II.[84]

The crystal structure comparisons were carried out pairwise comparing the 57 generated structures that were within 10 kJ mol^{-1} of the global minimum with the known fenamates structures taken from the CSD. Full results of the comparisons are detailed in Appendix 5 on page 201, but pairings that had the highest level of similarity (15 molecules in the coordination sphere) are highlighted in Table 11. The fenamate structure that had the highest level of similarity with any of the generated structures of MA was SURMOI (Figure 21a) which was similar to #48MA_480 (rmsd$_{15}$ = 0.1907 Å). The other fenamates with high levels of similarity to the generated structures are KAXXAI# (tolfenamic acid) and PEFNAQ (Figure 21b).

Table 11. Summary of the generated structures of MA with the highest level of similarity to other fenamate structures from the CSD.
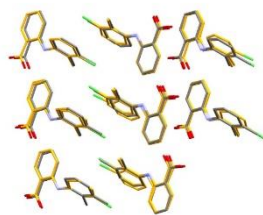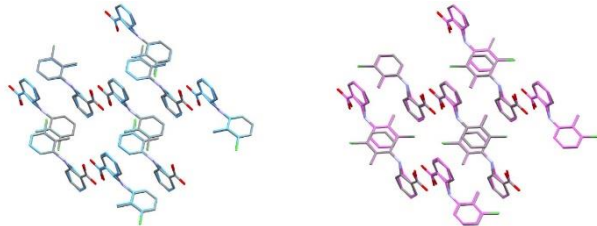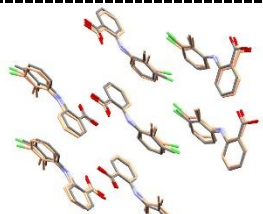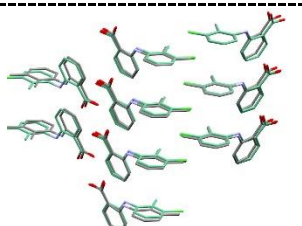
Reference structure	Comparison structure (CSD refcode)	rmsd$_{15}$ (Å)	PXRD similarity
#48MA_480	SURMOI	0.1907	0.9812
#6MA_288	KAXXAI02	0.3431	0.9629
#1MA_128	KAXXAI03	0.3950	0.9528
#19MA_5643	KAXXAI01	0.4203	0.9434
#4MA_889	KAXXAI04-major	0.4218	0.9510
#23MA_497	KAXXAI04-minor	0.5851	0.9515
#5MA_510	PEFNAQ	0.6346	0.9285

(a)   (b)
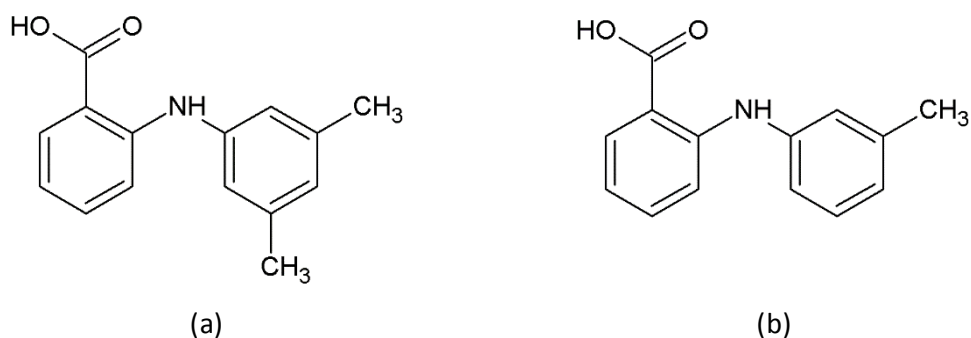
Figure 21. Structural diagrams of the fenamate molecules with CSD refcodes (a) SURMOI and (b) PEFNAQ.

It is not surprising that the generated structures of MA are similar to those of TA due to the similar packings of the structures that are possible because of chloro-methyl replacement. Table 11 highlights again the similarity of TA form IV and TA form V with MA form I (#1MA_128) and MA form II (#4MA_889 and #23MA_497) respectively. Table 11 also indicates that generated structures #6MA_288 and #19MA_5643 are similar to TA form III and TA form I respectively. The isostructural relationships between MA and TA are summarised in Table 12.

Table 12. Summary of the isostructural relationships that exist between MA and TA. MA form II and TA form V are disordered.

Pairing	Crystallisation details	Crystal Packing Similarity overlay
MA I	Recrystallisation from variety of solvents	
TA IV	PIHn	$rmsd_{15} = 0.332$ Å
MA II	Sublimation under static vacuum onto glass	
TA V	PIHn	$rmsd_{15} = 0.164$ Å $rmsd_{15} = 0.172$ Å
#6MA_288	Predicted structure	
TA III	PIHn	$rmsd_{15} = 0.361$ Å
#19MA_5643	Predicted structure	
TA I	Recrystallisation from absolute ethanol	$rmsd_{15} = 0.418$ Å

The key output of this analysis, is that computer generated MA structures which are similar to with form III and form I of TA are predicted to be competitive in energy with observed metastable forms. Hence structures #6MA_288 and #19MA_5643 have been highlighted on the crystal energy landscape of MA in Figure 19 due to their crystal structure similarity with form III and form I of TA respectively which is shown in Table 12. The unit cell similarities are shown in

Appendix 6 on page 203. The calculated lattice energy of #19MA_5643 indicates that it is around 5 kJ mol^{-1} less stable than the global minimum structure (MA form I) and could therefore be too high in energy to be considered a potential polymorph. In comparison, structure #6MA_288, is shown to be competitive in energy as it is more stable than MA form III and therefore could be a possible target polymorph for experimental investigations.

3.3.5 Relative Stability of Structures Using Different Computational Models

Following the identification of isostructural relationships between MA and TA, the relative stabilities of the structures of interest were investigated further by calculating the lattice energies using different computational models so that the sensitivity of the structures to the method of calculation could be evaluated.

The lattice energies of MA forms I, II (ordered models) and III were compared alongside the lattice energies of generated structures #1MA_128, #6MA_288 and #19MA_5643. The lattice energies were calculated using CASTEP (for the periodic electronic structure calculations) as well as CrystalOptimizer and the PCM with both the FIT and Williams potential.

The sensitivity analysis results are depicted in Figure 22 which shows that there is some degree of re-ranking of stabilities of the structures depending on the computational model. #1MA_128 and MA form I minimise to have the same lattice energy when the Williams potential is used in place of the FIT potential as well as in the DFT+D (TS) calculations.

The DFT+D (TS) calculations estimate MA form III to be more stable than MA form I by about 1 kJ mol^{-1} which is not in line with any experimental observations.[99] For all other computational models, the relative stability of the known polymorphs of MA calculated at 0 K is in agreement with experimental observations at ambient temperature.

The relative stability of the two generated structures of MA that are isostructural to TA polymorphs (#6MA_288 and #19MA_5643) changes depending upon the computational model. The CrystOpt+PCM (Williams potential) and DFT+D (TS) calculations estimate that #6MA_288 is less stable than MA form III which casts doubt upon the possibility that it could be found experimentally using TA form III as a template surface.

The results of the sensitivity analysis show that the crystal structures of MA are sensitive to the computational model used to evaluate the lattice energy, in particular to the choice of dispersion/repulsion potential. The differences arise because the hydrogen bonding motifs are the same throughout the structures, but the ξ_1 torsion angles differ significantly which affects the packing of the molecules in the unit cell and the close contacts.
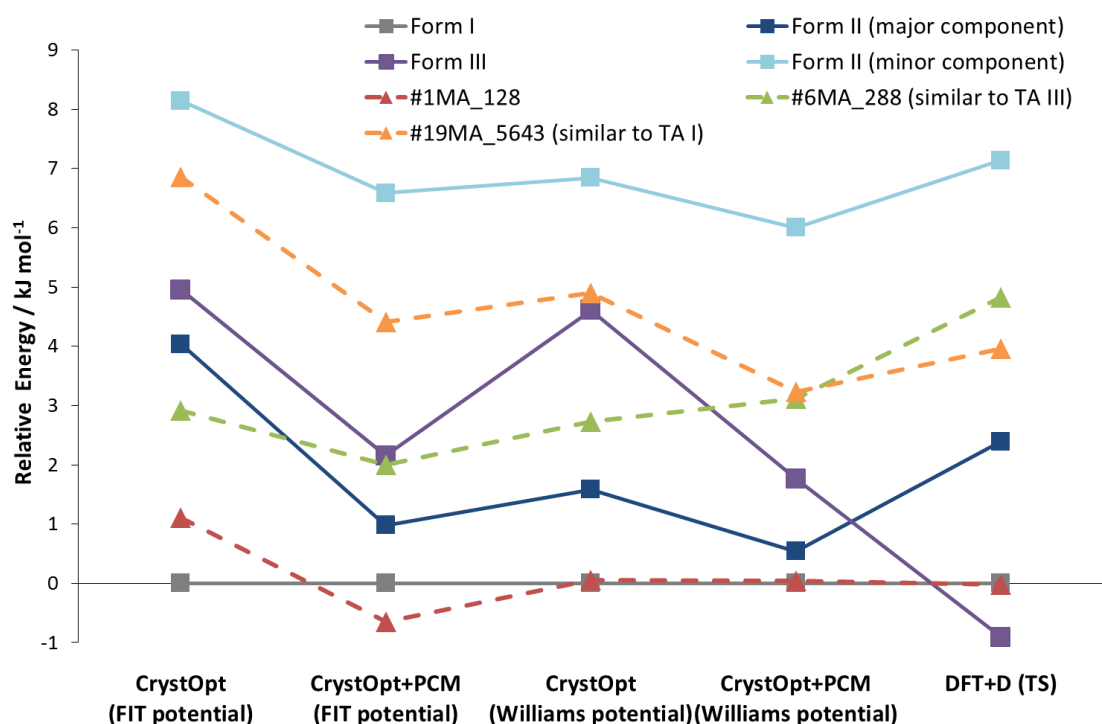
Figure 22. Energies of MA crystal structures relative to the most stable polymorph at ambient temperature (MA form I), calculated by different methods: CrystalOptimizer (CrystOpt) with the FIT potential; CrystOpt+PCM with the FIT potential; CrystOpt and the Williams potential; CrystOpt+PCM with the Williams potential; DFT, periodic PBE density functional calculations with the TS (Tkatchenko-Scheffler) dispersion correction. Squares represent known forms of MA, triangles represent generated structures of MA.

3.4   Conclusion

Computation of the crystal energy landscape of MA has shown that there are a number of thermodynamically feasible crystal structures that are competitive in energy with the three known polymorphs. In particular, using CrystalOptimizer, the PCM and the FIT potential, there are three distinct structures that are more stable than MA form III and another 12 that are lower in energy than the ordered model for the minor component of disordered form II. Such results suggest that should the right experiment be performed, the predicted low energy polymorphs could be nucleated for the first time.

The search for predicted forms by identification of an isostructural heteroseed or template surface has previously been exploited in the nucleation of CBZ form V and CYH form III using DHC form II seeds.[84, 88] Comparisons of the predicted structures of MA with known fenamate structures from the CSD, in particular TA, have been carried out in this work to identify any isostructural relationships that could be exploited in the search for new polymorphs of MA.

The difference between MA and TA is the replacement of a methyl group with a chloro group. As methyl and chloro groups have similar van der Waals volumes, they can be expected to occupy the same space in a crystal lattice and are therefore interchangeable, following the

Kitaigorodsky principle of close packing.[62] Therefore, it is not surprising that four isostructural pairings have been observed (Table 12) between known forms of TA and two known forms of MA as well as two low energy predicted structures of MA.

Experimental work in this thesis that follows these calculations focuses on the identified isostructural pairs of structures of MA and TA to investigate the consequences of chloro-methyl replacement on the crystal structures. It was hoped at this point that TA form III and/or TA form I could be used as heteroseeds in the nucleation of new, predicted, forms of MA. However, the calculations using different computational models (Figure 22) have cast doubt over the relative stability of these two predicted forms, in particular #6MA_288 which was initially thought to be more stable that MA form III following CrystalOptimizer and PCM calculations with the FIT potential. Additionally, there is the added issue of obtaining TA form III which has only been reported to have nucleated using PIHn methods.

4 Solid Solution Series and Solution Seeding of Mefenamic Acid and Tolfenamic Acid

4.1 Introduction

The previous chapters have introduced the molecular similarity of MA and TA that differ with the replacement of one methyl group on MA with a chloro group on TA. Computational comparisons carried out in the previous chapter have shown that there is a high degree of crystal structure similarity between known polymorphs of MA and TA and also between the known polymorphs and computationally generated structures from CSP methods.

This chapter experimentally investigates the possibility of chloro-methyl replacement in the crystal structures of MA and TA polymorphs using solution based crystallisation methods.
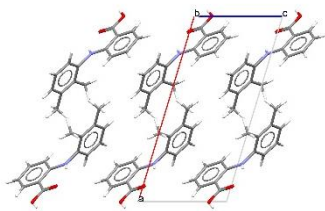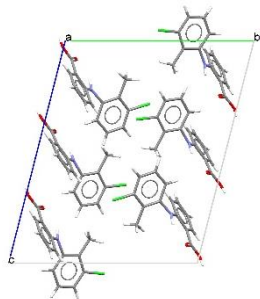
4.1.1 Crystal Similarity of Mefenamic Acid form I and Tolfenamic Acid form IV

This chapter examines the crystallographic similarities between MA form I and TA form IV as highlighted in the previous chapter. This relationship was picked due to the ease of producing MA form I crystals from a number of solvents (see chapter 2). There is a high degree of similarity between MA form I and TA form IV crystal structures which are isostructural (they have a good 15 molecule overlay with $rmsd_{15} = 0.332$ Å, Figure 23), but not isomorphous (Table 13). MA form I and TA form IV crystallise under very different conditions with MA form I crystallising from a variety of solvents[101-103] whereas TA form IV is only obtained using polymer-induced heteronucleation (PIHn).[32]
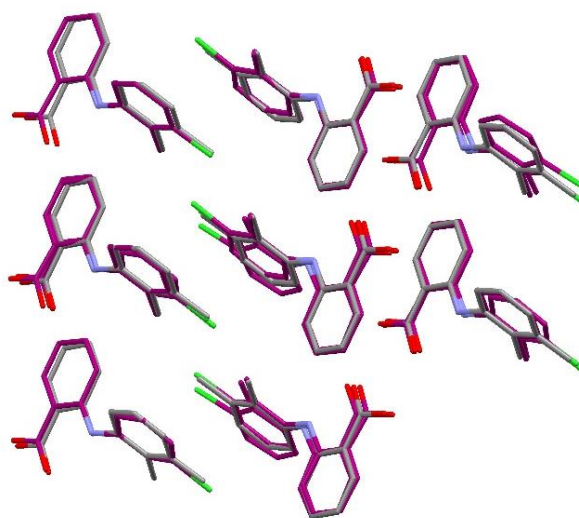
Figure 23. Crystal packing similarity of MA form I (coloured by element) with TA form IV (purple) showing a 15 molecule overlay, $rmsd_{15}$ = 0.332 Å.

Table 13. Crystallographic data of MA form I and TA form IV.

	MA form I[this work]	TA form IV[32]
Crystal System	triclinic	triclinic
Space Group	P-1	P-1
a (Å)	6.7887(3)	7.5237(8)
b (Å)	7.3613(2)	14.3308(16)
c (Å)	14.0330(4)	17.592(2)
α (°)	76.868(3)	103.680(2)
β (°)	79.857(3)	98.253(2)
γ (°)	64.863(3)	93.038(2)
Cell Volume (Å³)	615.74(4)	1816.41
Z	2	6
Z'	1	3
Crystallisation Method	Crystallises from room temperature solvent evaporation of a variety of solvents	Polymer-induced heteronucleation (PIHn)

The first section of this chapter investigates the possibility of producing a solid solution of MA and TA by cocrystallisation from different solvents. Solid solutions can occur between compounds, with almost the same type and position of atoms, that have crystal structures that are either isomorphous (same space group and unit cell dimensions) or isostructural (same packing motifs, but not the same unit cell dimensions). Thus we might hope a solid solution to form between MA and TA where the lattice sites are randomly occupied by either MA or TA molecules with the relative populations of MA and TA equal to the bulk composition and the input molar ratio. Results show that a solid solution can be formed between MA and TA with the same unit cell as MA form I.

The second section of this chapter further investigates the relationship between MA and TA using MA form I as hetero-seeds to try and nucleate TA form IV via an alternative route to PIHn. Results show that hetero-seeds of MA form I produced crystals of TA that although similar to TA form IV, are in fact a new form of TA that is isostructural to MA form I.

4.2   Solid Solution Series in the Same Unit Cell as Mefenamic Acid Form I

4.2.1   Methods

Materials. MA was purchased from Sigma Aldrich as form I while TA form I was purchased from LKT Laboratories Inc. Both compounds were used without further purification.

Preparation of the Solid Solution. Preliminary cocrystallisation experiments of MA with TA from ethanol produced single crystals that had the same unit cell as MA form I, but detailed crystallographic analysis showed both MA and TA were present. The thermal ellipsoid plot for this preliminary cocrystal structure is shown in Figure 24 and crystallographic data can be found in the first column of Table 14.
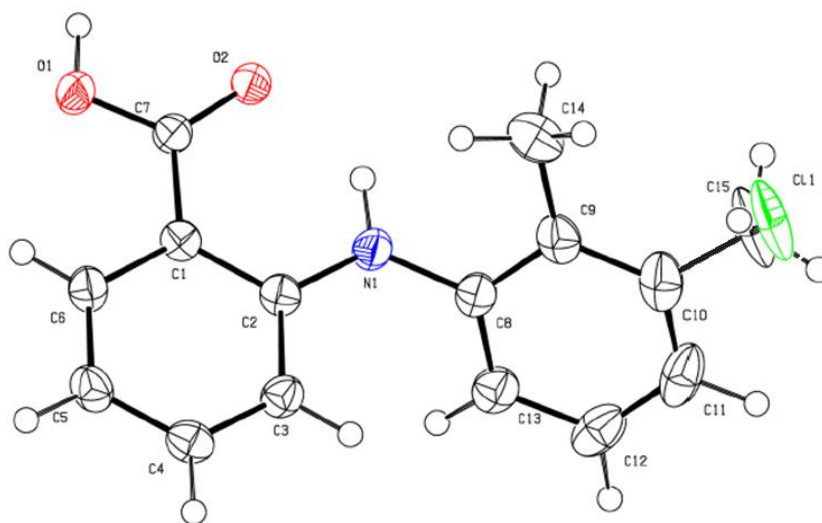
Figure 24. Thermal ellipsoid plot, set at 50 % probability, of the crystal structure resulting from the preliminary cocrystallisation experiment of MA and TA. SCXRD analysis shows that both MA and TA are present

Subsequently, further cocrystallisation experiments were carried out by room temperature solvent evaporation to dryness from ethanol, di-ethyl ether and acetonitrile. The molar ratios of TA:MA were 50:50, 60:40, 70:30, 80:20 and 90:10 (mole fraction of TA = 0.5, 0.6, 0.7, 0.8, 0.9) in each solvent.

Colourless block crystals were obtained after a few days and had crystal morphologies that were similar to that of MA form I. A series of solid solution crystals from ethanol were analysed using single crystal X-ray diffraction (SCXRD) and ^{1}H NMR spectroscopy in order to determine the crystal structure and the relative composition of TA and MA in the single crystals. The crystals were then further analysed by DSC and Raman spectroscopy to determine that they were a single phase.

Single Crystal X-ray Diffraction. Single crystals from the ethanol series were chosen using a microscope equipped with a rotatable polarising stage. Crystallographic data were collected at 150 K using an Agilent SuperNova diffractometer, equipped with an Oxford

Instruments cryostat and Cu-Kα radiation ($\lambda = 1.54184$ Å). Using Olex2[107], structures were solved with the SHELXS[108] structure solution program using Direct Methods and were refined using SHELXL[109] using Least Squares minimisation. The relative TA:MA ratio in the experimental solid solution crystals was determined by refining the site occupancy of the CH_3 and Cl groups in the least squares minimisation cycles using appropriate entries on the FVAR card (and sometimes EADP) commands in SHELXL. All non-hydrogen atoms were refined anisotropically and where possible, hydrogen atoms were located in the final difference maps and refined with a riding model.

^{1}H NMR Spectroscopy. A number of crystals from the solid solution vials were transferred to NMR tubes and dissolved in duetero-chloroform. Commercial MA and TA were also dissolved in $CDCl_3$ in NMR tubes. The ^{1}H NMR spectra were collected on a Bruker Avance 300 MHz NMR spectrometer operating at room temperature. Data was analysed using the ACD/NMR Processor Academic Edition software.[157]

Thermal Analysis. Differential Scanning Calorimetry (DSC) measurements were performed on a TA Q2000 (TA Instruments, LLC, USA) that was calibrated at a heating rate of 10 °C min^{-1} in a temperature range of 0 – 250 °C using an Indium melting point standard. Nitrogen (50 mL min^{-1}) was used as a purge gas. Sample sizes were between 0.88 mg and 1.75 mg. Tzero non-hermetic aluminium pans and lids were used. The data analysis was carried out using the Universal Analysis 2000 software.[111]

Infrared Spectroscopy. Crystals were analysed using solid state infrared spectroscopy. Infrared spectra were obtained using a Perkin-Elmer Spectrum One FTIR fitted with a diamond ATR accessory. Spectra were collected over the range 4000–650 cm^{-1} at a resolution of 4 cm^{-1} and analysed using the ACD/Spectrus Processor software.[110]

Raman Spectroscopy. Multiple crystals from the 0.5 mole fraction vial were analysed using Raman spectroscopy. The crystals were mounted on a glass microscope slide and focused upon using a x50 objective mounted on a Renishaw InVia Raman microscope. Spectra were collected using a laser wavelength of 514 nm in the range of 3200-100 cm^{-1} and analysed using the WiRE software package.[158]

4.2.2   Results

The cocrystallisations of TA:MA, of varying compositions, in ethanol produced a solid solution series that was analysed and identified using SCXRD, ^{1}H NMR spectroscopy, DSC, infrared spectroscopy and Raman spectroscopy.

4.2.2.1   *SCXRD Refinement*
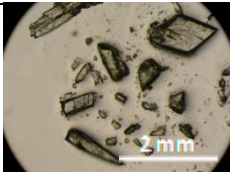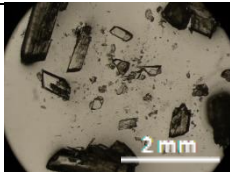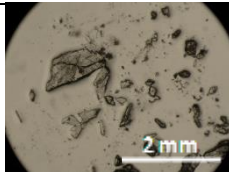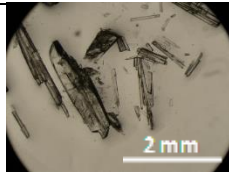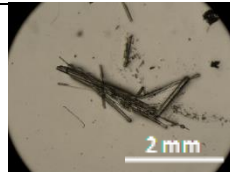
Single crystals from the vials containing mole fractions of TA = 0.5, 0.6, 0.7 and 0.8 in ethanol solution were analysed using SCXRD. No suitable crystals were obtained from the 0.9 mole fraction of TA vials. Inspection by eye suggests that the 0.9 TA crystals had a needle like morphology (Table 14), more similar to the morphology of TA form I, than MA form I which forms blocks.

Unit cell determination from SCXRD showed that all the chosen solid solution crystals from the ethanol series had a unit cell indistinguishable from MA form I. Further analysis showed that the unit cells contained molecules of both MA and TA identified by refining the occupancies of the chloro and methyl groups that are interchangeable within the crystal lattice.[123] The stoichiometry of the two compounds in the solid solutions was not limited to integer values[69] and the mole fraction of TA calculated from the SCXRD refinement approximately reflected the target mole fraction of TA indicating the existence of a solid solution series.

The single crystals of the 0.7 mole fraction sample were very small and gave poorer quality data than the other samples studied. A weakly diffracting crystal gave the cell and mole fraction reported in Table 14, but full data on this sample is not reported.

Table 14 reports crystallographic data for the crystals in the MA-TA solid solution series from ethanol (CIF files for the series can be found on CD). All the crystals have the same unit cell, which does not show any systematic change in volume with the inclusion of more TA in the crystal structure.

Table 14. The morphologies and crystallographic data of the crystals in the MA-TA solid solution series. Data in the first column relates to the crystal structure from the preliminary cocrystallisation experiment.

Target mole fraction of TA	Preliminary cocrystallisation experiment	0.5	0.6	0.7	0.8	0.9
	-					
a (Å)	6.7452(4)	6.7312(9)	6.7336(4)	6.7295(16)	6.7241(8)	-
b (Å)	7.3151(4)	7.2896(10)	7.2720(4)	7.2619(15)	7.2432(8)	-
c (Å)	14.1796(8)	14.2268(15)	14.2713(10)	14.269(4)	14.3139(15)	-
α (°)	77.092(5)	77.197(10)	77.150(5)	77.25(2)	77.181(9)	-
β (°)	79.765(5)	79.624(10)	79.547(6)	79.59(2)	79.411(10)	-
γ (°)	65.318(5)	65.533(13)	65.678(6)	65.74(2)	65.937(11)	-
Cell Volume (Å³)	616.85(7)	616.52(15)	617.66(7)	616.9(3)	617.27(13)	-
R1 (I > 2σ(I))	0.0507	0.0737	0.0609	0.0937	0.0710	-
R factor (all)	0.0547	0.0981	0.0690	0.2355	0.0832	-
Mole fraction of TA by SCXRD refinement	0.37(1)	0.43(1)	0.58(1)	0.64(1)	0.78(1)	-

Table 15. The thermal ellipsoid plots, set at 50 % probability, of the MA-TA solid solution crystal structures. The mole fraction of TA reported in this table is calculated from the relative occupancy of Cl in the structures from refinement of the SCXRD data. Ellipsoids are shown for both the CH₃ and Cl components of the solid solution.

Mole fraction of TA by SCXRD refinment	Thermal Ellipsoid Plot
0.43	
0.58	
0.78	

Table 15 shows the thermal ellipsoid plots, set at 50 % probability, of the MA-TA solid solution crystal structures. The thermal ellipsoid plots show the positions of both the chloro and methyl groups that interchange within the solid solution series. As the mole fraction of TA increases and more TA is included in the solid solution crystal, the thermal ellipsoids of the chloro and methyl interchangeable groups generally increase in size as do the thermal ellipsoids on some neighbouring carbons atoms, consistent with slight, but unresolved, differences in phenyl carbon atom placement.

(a)   (b)
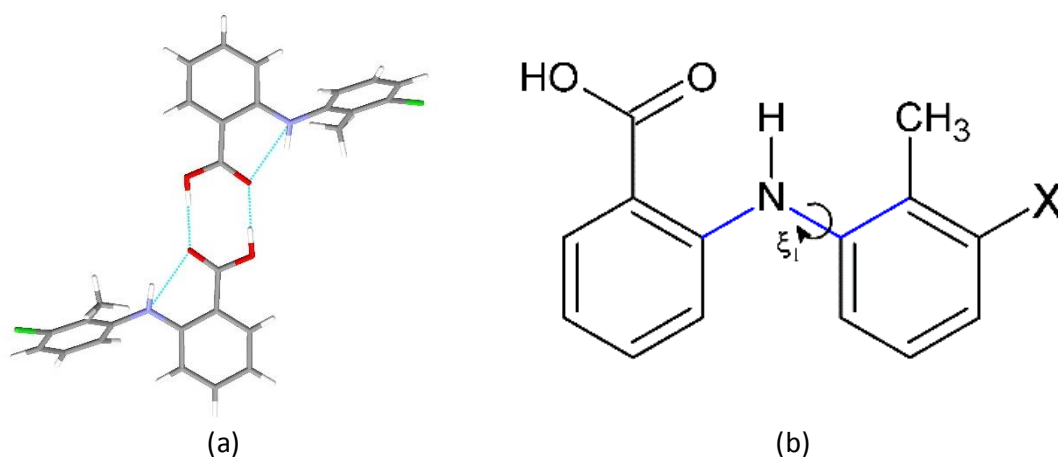
Figure 25. (a) The $R_2^2(8)$ carboxylic acid dimer observed in all the MA-TA solid solution crystals as well as MA form I, shown here between two TA molecules. (b) The structure diagram of MA/TA (X = Cl on TA, X = CH₃ on MA) showing the ξ_1 torsion angle with the relevant bonds coloured blue. The ξ_1 torsion angle is the torsion angle that varies the most amongst polymorphs of MA and TA (see section 3.2.2.1).

As observed in MA form I, the crystal structures of the MA-TA solid solution series all form $R_2^2(8)$ carboxylic acid dimers (Figure 25a). The ξ_1 torsion angle (shown in Figure 25b) is the torsion angle that varies the most amongst polymorphs of MA and TA as shown in section 3.2.2.1. Table 16 shows that as more TA is incorporated into the solid solution crystal, the ξ_1 torsion angle deviates away from its value in pure MA form I (119.99 ° in XYANAC[98] and 119.39 ° from the redetermination of MA form I earlier in this thesis). Table 16 also reports the Cl⋯Cl interaction distances which tend to increase as the torsion angle increases with the exception of the 0.78 mole fraction. However, the thermal ellipsoids for the Cl group in this crystal structure (Table 15) are larger than in the other mole fractions and this could affect the Cl⋯Cl distance reported by Mercury.

Table 16. The ξ_1 torsion angle and Cl⋯Cl distances in the MA-TA solid solutions.

Mole Fraction of TA from SCXRD	0.37	0.43	0.58	0.78
Torsion Angle ξ_1 (°)	121.79	122.66	123.86	124.89
Cl⋯Cl distance (Å)	3.369	3.374	3.381	3.366

^{1}H NMR spectra were collected for the MA-TA solid solution series, as well as for commercial MA and commercial TA. Integration of the ^{1}H NMR spectra was used to determine the mole fraction of TA present in the bulk solid solution crystals to support the SCXRD data.
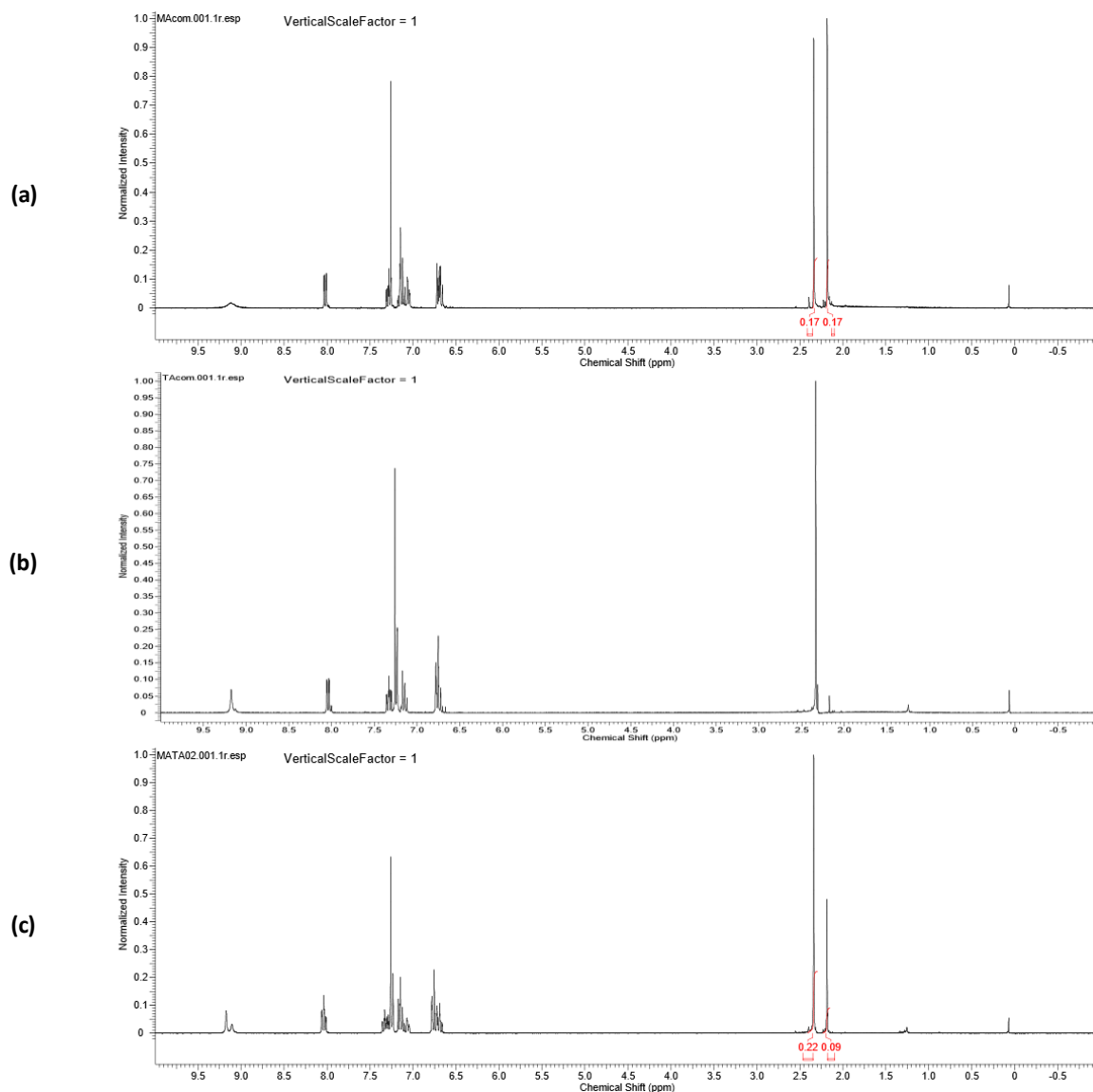
Figure 26. NMR spectra of (a) commerical MA, (b) commercial TA and (c) a MA-TA solid solution (target mole fraction of TA is 0.6).

Figure 26a shows the ^{1}H NMR spectra for commercial MA which has two peaks, of equal integral, at 2.34 ppm and 2.18 ppm arising from the presence of two methyl groups on the MA molecule. In comparison, Figure 26b shows the ^{1}H NMR spectra of commercial TA which has only one peak at 2.34 ppm as the TA molecule has only one methyl group. Figure 26c shows the ^{1}H NMR spectra for the target 0.6 mole fraction of TA which has two peaks that differ in integral, at 2.34 ppm and 2.18 ppm. The content of TA in each solid solution crystal can be

determined by integration of the peaks at 2.34 ppm and 2.18ppm, noting that the 2.18 ppm peak is only present due to MA in the solid solution crystals. The ^{1}H NMR spectra for the other solid solutions can be found in Appendix 7 on page 204.

The mole fractions of TA from integration of the ^{1}H NMR data are reported in Table 17 alongside the results from the SCXRD data. The mole fraction of TA from the two different methods of analysis are in good agreement considering the experimental error. The experimental mole fractions of TA in the solid solutions from SCXRD and ^{1}H NMR data are also in relatively good agreement with the target mole fractions.

Table 17. The mole fractions of TA present in the MA-TA solid solution series as determined from SCXRD and ^{1}H NMR spectroscopy.

Target mole fraction of TA	**0.5**	**0.6**	**0.7**	**0.8**
Mole fraction of TA from SCXRD refinement	0.43(1)	0.58(1)	0.64(1)	0.78(1)
Mole fraction of TA from integration of ^{1}H NMR spectra	0.43	0.60	0.69	0.76

Each of the solid solutions were investigated by DSC in the temperature range $0 - 250$ °C at a heating rate of 10 °C min^{-1}. The DSC scans in Figure 27 show melting endotherms for each of the MA-TA solid solution crystals and show that the melt is from a single phase as the slope of the onset is smooth. The melting points show that there is an approximately linear relationship between the amount of TA incorporated into the solid solution crystal and the melting point.[68, 69] As the content of TA in the MA-TA solid solution increases, the melting point decreases which is to be expected as MA form I has a higher melting point (onset temperature of 229 °C and melting point of 230 °C)[99, 159, 160] than TA (forms I – V have melting points between 206.78 °C and 215.17 °C).[32]
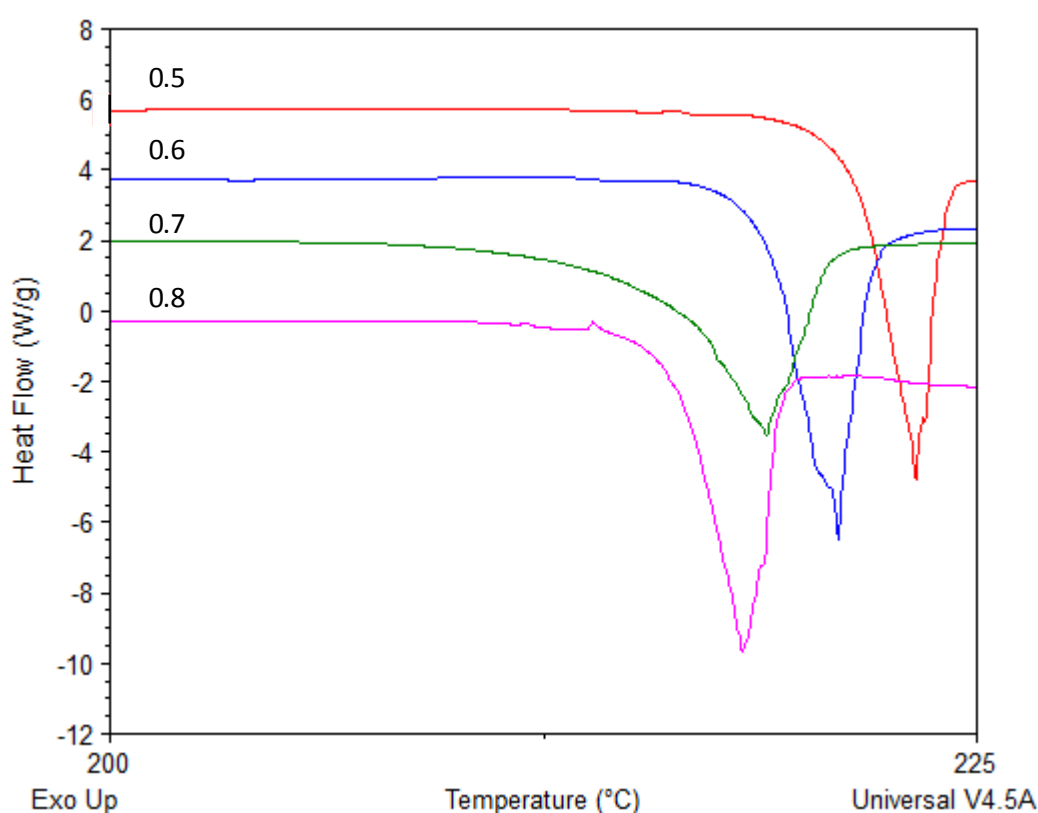
Figure 27. DSC scans for the MA-TA solid solutions labeled with the target mole fraction of TA. The scans were carried out at a heating rate of 10 °C min^{-1}.

The infrared spectra in Figure 28 show the N-H stretching peak of the spectra of commercial MA with a peak at 3307 cm^{-1} and commercial TA with a peak at 3339 cm^{-1}. Figure 28 also shows the infrared spectra of the MA-TA solid solution crystals. The infrared spectra for the target mole fractions of TA = 0.5, 0.6, 0.7 and 0.8 could indicate that both MA and TA are present in the solid solution crystals. This conclusion is reached because of the presence of a broad peak that encompasses a main peak due to MA (around 3307 cm^{-1}) and a shoulder peak due to TA (around 3339 cm^{-1}). As the target mole fraction of TA increases, the infrared spectra show evidence that more TA is present in the MA-TA solid solution crystals as the relative heights of the two peaks change with composition.
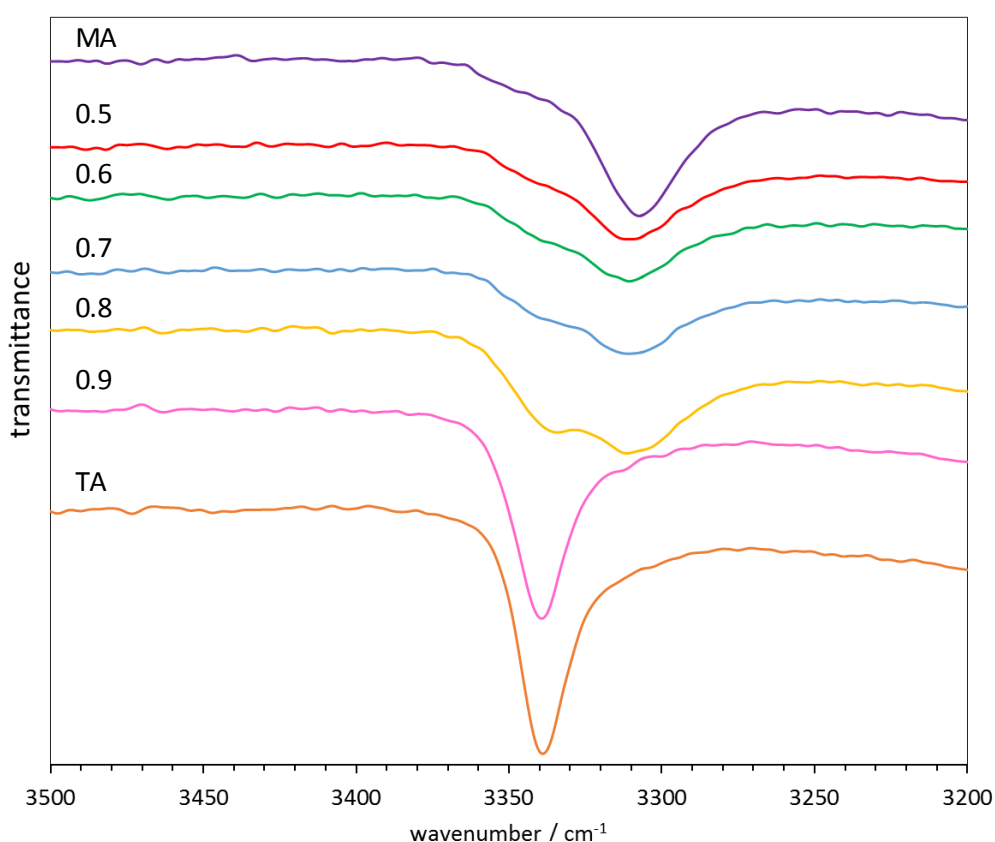
Figure 28. Infrared spectra of the N-H stretching peak of commercial MA, the solid solutions of MA-TA (labelled with the target mole fraction of TA) and commercial TA.

However, it should be noted that the different polymorphs of TA also have different peak positions. Gilpin et al. report that TA forms I and II have peaks at $3340 - 3341$ cm^{-1} and $3324 - 3325$ cm^{-1} respectively[117] and Thybo et al. additionally report that TA form I has an additional component in the spectrum at $3310 - 3312$ cm^{-1}.[161] Similarly, Jabeen et al. report that TA polymorphs I and II have peaks at 3342 cm^{-1} and 3315 cm^{-1} respectively.[106] Jabeen et al. also calculated the vibrational spectra for TA and MA for different conformations of the molecules using DFT methods. The conformations of TA and MA used in their calculations varied by

changing the ξ_1 torsion angle (Figure 25b). The results of the DFT calculations indicated that for both MA and TA, the conformation of the molecule can affect the position of the N-H stretching peak. For example, in TA, if the ξ_1 torsion angle is 142.08 ° the N-H stretching peak would appear at 3301 cm^{-1}, however, if the ξ_1 torsion angle is 70.43 ° the N-H stretching peak would appear at 3315 cm^{-1}. The infrared spectra for TA forms III – V have not been reported.

The infrared spectrum of the 0.9 target mole fraction of TA does not show any clear evidence that MA is present as there is just one strong peak observed in the same position as commercial TA. This infrared spectrum for TA = 0.9 suggests that the crystals chosen for analysis by infrared spectroscopy are pure TA. This result is in line with the observation that the crystal habit of the TA = 0.9 crystals are more similar to TA form I than MA form I (Table 14), although the presence of a small amount of MA cannot be completely ruled out.
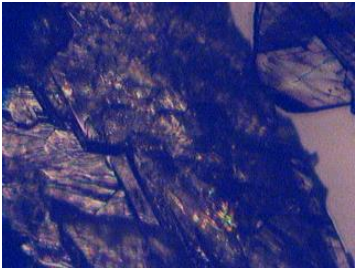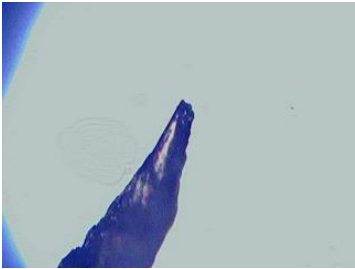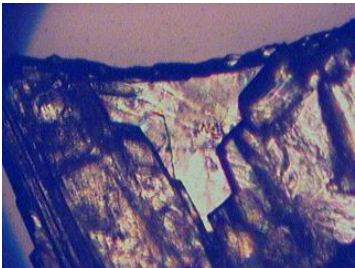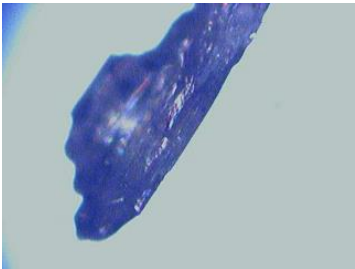
4.2.2.5   Raman Spectroscopy

Raman spectra were collected for five different crystals from the vial containing the 0.5 target mole fraction of TA. The Raman spectra taken at points on the five chosen crystals are shown in Figure 29 and images of the different morphologies of the five different crystals are shown in Table 18. There are no significant differences in the Raman spectra of the five different crystals which suggests that the crystallographic structure is the same throughout the sample even if the crystal habit is not consistent across all five samples.
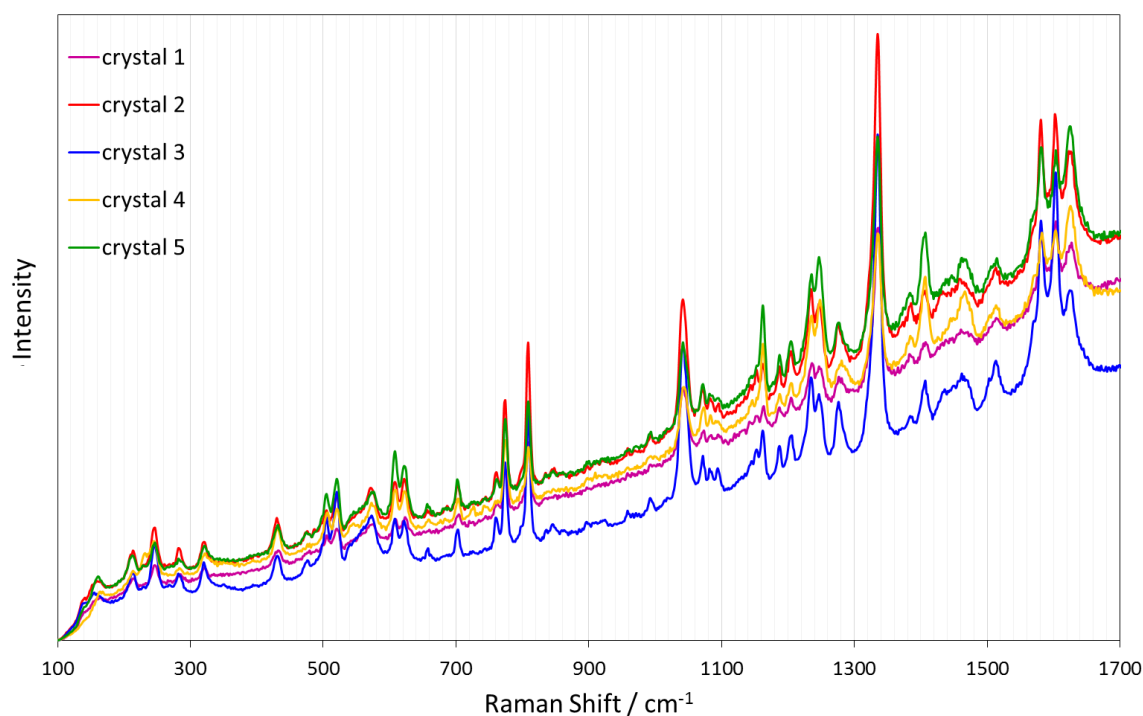
Figure 29. Raman spectra for five different crystals of the 50:50, MA-TA solid solution.

Table 18. Optical images of the different morphologies of the 0.5 target mole fraction of TA solid solution crystals from which Raman spectra were collected.

Magnification x5
crystal 1
crystal 2
crystal 3
crystal 4
crystal 5

4.2.3   Discussion

The results presented in section 4.2.2 confirm that MA and TA can cocrystallise from ethanol solution to form solid solution crystals that are isomorphous with MA form I. The MA and TA molecules occupy the same sites in the crystal lattice at random with the overall populations equal to the bulk composition. The experimentally determined composition of the MA-TA solid solution series reflects the target mole fraction and the input ratios of the MA and TA compounds before crystallisation by solvent evaporation to dryness. The results show that TA is soluble in MA up to around 80 %.

As MA form I and TA form IV are isostructural, the fact that the MA-TA solid solution is isomorphous with MA form I was not unexpected. However, it is important to note that other outcomes were also possible. For example, TA form I crystallises from ethanol and has an isostructural crystal structure of MA, #19MA_5643, that was predicted in the CSP study in chapter 3. However, as discussed in chapter 3, the relative stability of #19MA_5643 is dependent on the computational model and may be too high in energy to be observed experimentally. Additionally, MA is reported to be less soluble than TA[162-164] therefore nucleation rates of MA and TA would be different and it's possible that MA would nucleate more readily.

The DSC scans of the MA-TA solid solutions reported in section 4.2.2 show the existence of single phase crystals as shown by the single melting endotherms. These DSC results are complemented by the Raman spectra which is the same at different sampled positions on different crystals. This indicates that the solid solution crystals are homogeneous.

The similarities between the target and the experimental mole fractions of TA are important discussion points concerning the MA-TA solid solution series. In general, as reported in Table 17, there is good agreement between the target mole fraction of TA and the experimental mole fraction of TA. The mole fractions of the solid solutions determined from the two experimental methods (SCXRD and ^{1}H NMR) are in good agreement with each other, giving the same mole fraction for TA = 0.5 and differing by just 2 % for TA = 0.6 and 0.8. However, the two methods of calculation of the mole fraction for TA = 0.7 differ by 5 % which is most likely to be due to the comparison of a single crystal with bulk analysis by ^{1}H NMR. It is likely that the bulk ratio would more representative of the target mole fraction than a single crystal as the mole fraction of individual single crystals might vary slightly depending on which crystal was picked for analysis. Furthermore, it is important to note the size and quality of the crystal used for SCXRD for TA = 0.7. The X-ray data for the TA = 0.7 crystal is less reliable, than for the other solid solution crystals, due to the poor crystal quality.

In general, there is also a good agreement between the target mole fraction of TA and the mole fraction calculated from the ^{1}H NMR spectra with all reported values differing by no

more than 4 %. However, the mole fraction by SCXRD and ^{1}H NMR of the solid solution for TA = 0.5, does not match the target molar fraction of TA. This suggests that excess TA would be present and that this might be observed in bulk analysis measurements. If there had been excess (pure) TA crystals present then the ^{1}H NMR data should demonstrate this. Additionally, the DSC data would show two melting endotherms, one relating to pure TA, and another for the MA-TA solid solution at a higher temperature. The DSC data shown in Figure 27 shows no evidence of pure TA.

Another useful method of bulk analysis, that could have indicated the presence of pure TA crystals amongst the solid solution crystals, is powder X-ray diffraction (PXRD). If excess TA had been present in the sample, the PXRD pattern could have shown peaks, that correspond to TA form I (obtained from ethanol in the absence of MA) in addition to peaks that correspond to the solid solution crystal that is isomorphous to MA form I. PXRD was not collected for the MA-TA solid solution series as there was insufficient sample.

The MA-TA solid solution exists because the chloro and methyl groups are similar in size which allows them to be interchangeable within crystal lattices, following the Kitaigorodsky principle of close packing.[62] Replacing a methyl group with a chlorine, or vice versa, does not significantly alter the size or shape of the molecule as methyl and chloro groups have similar van der Waals volumes with the smaller substituent being about $79 - 91$ % of the size of the larger depending on the literature source (see section 2.3, page 50, for additional information).

Kitaigorodsky suggested that replacing larger molecules with smaller ones in a solid solution happens more readily than the reverse. In comparison to other isostructural systems such as caffeine and theophylline[165] which involved replacing a methyl group with a hydrogen, the difference in the van der Waals volumes of the chloro and methyl groups is not significant and as such it would be difficult to predict which substituent would most easily be replaced.

Examples of chloro-methyl interchange in solid solutions and isostructural systems from literature[20, 21, 25, 119, 120, 166] suggests that as more methyl substituents are introduced into the unit cell, the unit cell volume increases. For example, the isomorphous unit cells of fuchsone derivatives (Figure 30)[123] show an increase in volume when two chloro and two methyl substituents in dichlorodimethylfuchsone are changed for four methyl groups in tetramethylfuchsone.[123] The unit cell of pure tetramethylfuchsone is 1741 $Å^3$ and the unit cells of pure dichlorodimethylfuchsone crystal structures are $1719 - 1727$ $Å^3$. The solid solutions of the fuchsone derivatives with varying ratios of chloro and methyl substituents have unit cell volumes of $1731 - 1737$ $Å^3$, between the values of the pure compounds.
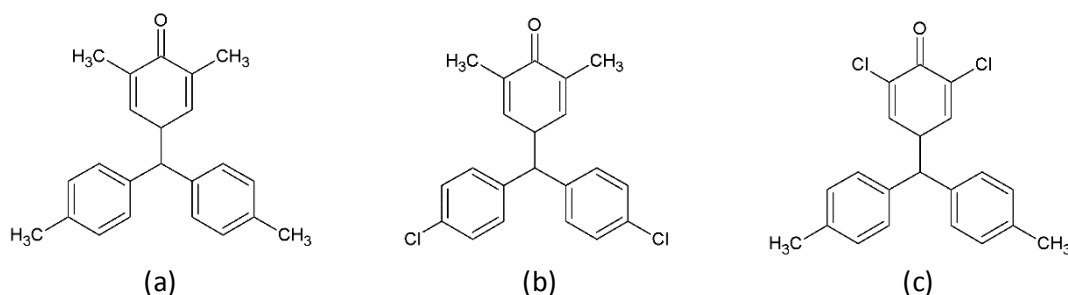
Figure 30. Structure diagrams of the fuchsones studied by Nath et al. (a) tetramethylfuchsone, (b) and (c) dichlorodimethylfuchsones.

The inclusion of 2,6-dimethyl *N*-phenylformamide (Figure 31)[167] molecules into the crystal structure of 2,6-dichloro *N*-phenylformamide to form a solid solution also shows an increase in unit cell volume.[167] Likewise a unit cell volume increase is also observed in binary cocrystals of 1,4-diazabicyclo[2.2.2]octane with 4-X-phenols (X = Cl, CH$_3$) as more of the methyl substituted molecule is included in the crystal structures.[120]
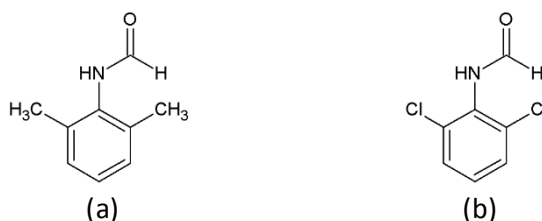
Figure 31. Structure diagrams of (a) 2,6-dimethyl *N*-phenylformamide and (b) 2,6-dichloro *N*-phenylformamide.

Although there is some disagreement in the literature about which substituent is larger, the isomorphous crystal structures just mentioned suggest that the unit cell volume increases as chloro groups are replaced with methyl groups. This would suggest that the unit cell volume of the MA-TA solid solution series found in this work would decrease with increasing replacement of methyl groups with chloro groups, as more TA is included. However, the unit cell volumes reported in Table 14 do not show this trend.

Table 14 shows that as more Cl substituted molecules are included in the solid solution crystal, there is a small increase in unit cell volume. The cell volume is 615.74(4) Å^3 for MA form I, 616.52(15) Å^3 for the 0.5 mole fraction and 617.27(13) Å^3 for the 0.8 mole fraction. The unit cell volume of MA form I and the MA-TA solid solution series could be influenced by the conformation of the molecules in the unit cell. As Table 16 shows, the ξ_1 torsion angle increases as more TA molecules are incorporated in the solid solution crystals which could affect the unit cell volume. It is interesting to note the differences in unit cell volumes for MA form I and the MA-TA solid solution series, but it is important not to place too much emphasis on this variation. Small unit cell volume variations can arise due to differing crystal quality as well as how well centred the sample is in the X-ray beam.

4.3   Seeding of Tolfenamic Acid in Ethanol with Mefenamic Acid Form I

Following on from the results of the solid solution series, hetero-seeding experiments were attempted that used MA form I crystals to seed a solution of TA in ethanol. It was hoped that hetero-seeding a solution of TA with MA form I would provide a new route to nucleating TA form IV which is only reported to be obtainable by PIHn.[32]

4.3.1   Methods

Materials. As in section 4.2.1.

Hetero-seeding. MA form I seeds were obtained by recrystallization of MA from acetonitrile by room temperature solvent evaporation to dryness. Several small MA form I seeds were transferred to a saturated solution of TA in ethanol. After room temperature evaporation of the TA ethanol solution to dryness, clusters of single crystals were observed and were separated and analysed by SCXRD.

Single Crystal X-ray Diffraction. As in section 4.2.1. All non-hydrogen atoms were refined anisotropically and hydrogen atoms were refined with a riding model. Disorder in the phenyl ring was modelled by using PARTS and the AFIX 66 constraint.

Raman Spectroscopy. As in section 4.2.1.

Thermal Analysis. As in section 4.2.1, but the TA Q2000 (TA Instruments, LLC, USA) was calibrated at heating rate of 100 °C min^{-1} for a temperature range of $0-250$ °C.

Infrared Spectroscopy. As in section 4.2.1.

4.3.2   Results – New Polymorph of Tolfenamic Acid (form VI)

Seeding of TA in ethanol solution with MA form I crystals produces crystals with a different habit from that of TA form I which is routinely obtained by recrystallisation from ethanol. TA form I forms needle crystals from ethanol whereas the crystals obtained when the solution is seeded with MA show clusters of block crystals (Figure 32).

(a)   (b)
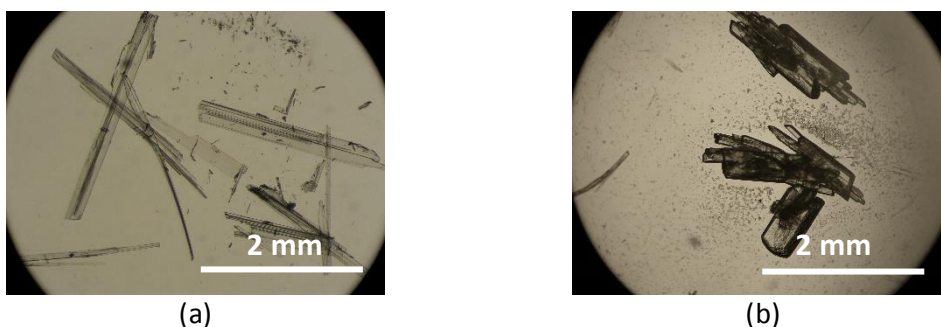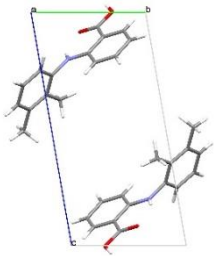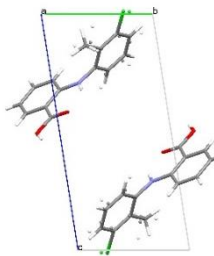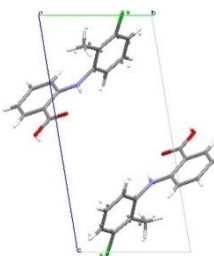
Figure 32. The crystal morphologies of (a) TA form I and (b) TA form VI.

SCXRD data collected from TA seeded with MA show that a new form of TA is produced with a unit cell isomorphous to the MA form I heteroseed and the MA-TA solid solution series reported in section 4.2 (Table 19).

The crystallographic refinement of the new form of TA (herein referred to as TA form VI) showed that TA is disordered and adopts two different conformations within the crystal lattice. Two data sets were obtained for two different crystals of TA VI which are labelled TA VI[a] and TA VI[b], both of which had essentially the same unit cell dimensions as MA form I (Table 19).

Table 19. Crystallographic data for isomorphous crystals of MA form I and TA form VI. The table shows crystallographic data for two different crystals of TA fom VI (TA VI[a] and TA VI[b]).

	MA form I	TA form VI[a]	TA form VI[b]
Unit Cell Diagram			
Crystal System	triclinic	triclinic	triclinic
Space Group	P-1	P-1	P-1
Temperature (K)	150	150	150
a (Å)	6.7887(3)	6.7482(4)	6.7233(3)
b (Å)	7.3613(2)	7.2034(5)	7.2430(4)
c (Å)	14.0330(4)	14.3406(9)	14.3109(9)
α (°)	76.868(3)	77.497(6)	77.245(5)
β (°)	79.857(3)	78.947(5)	79.405(5)
γ (°)	64.863(3)	65.963(7)	65.867(6)
Cell Volume (Å^3)	615.74(4)	617.34(8)	616.85(7)
Z	2	2	2
Z'	1	1	1
Unique reflections	2170	2427	2390
Refined parameters	223	227	227
GOF	1.037	1.063	1.064
R1 (I > 2σ(I))	0.0317	0.0503	0.0614
wR2 (all)	0.0841	0.1538	0.1839
R1 (all)	0.0326	0.0624	0.0667
Ratio of disorder	-	48:52	55:45

The differences in unit cell volume upon the replacement of a methyl group with a chloro group has already been discussed in section 4.2.3. Investigations into the extent of chloro-methyl interchange in structures found on the CSD have provided additional isostructural pairs

of crystal structures to compare.[119, 122] Brief analysis of these structures from the CSD, concentrating on the unit cell volumes, suggests that the unit cell volume decreases when methyl groups are replaced by chloro groups. This trend is also retained in the unit cell volumes of known polymorphs of MA and TA (Table 20). Table 20 shows that on average, the unit cell volume per molecule of MA in its different polymorphs is greater than the unit cell volume per molecule of the TA polymorphs.

Table 20. The unit cell volumes, Z and Z' values of the known polymorphs of MA and TA.

	Polymorph	Unit Cell Volume ($Å^3$)	Z	Z'	Unit cell volume per molecule to nearest whole number ($Å^3$)
MA	I[this work]	615.74(4)	2	1	308
	II[this work]	618.19(4)	2	1	309
	III[99]	626.96(19)	2	1	313
TA[32]	I	1205(2)	4	1	301
	II	1196(2)	4	1	299
	III	2419.1(8)	8	2	302
	IV	1816.41	6	3	303
	V	603.81(17)	2	1	302

However, the SCXRD data shows that the unit cell volume of TA VI is similar in size to that of MA form I (Table 21). This is contrary to the literature and could be due to the fact that the packing is poorer in the presence of disorder.

The two different conformations of TA (labelled conformations A and B) can be seen in the thermal ellipsoid plot in Figure 33 and in the molecular overlay diagram in Figure 34c and Figure 34d. The two conformations that TA adopts in TA VI arise due to variations in the ξ_1 torsion angle, shown previously in Figure 25b. The values of the ξ_1 torsion angle in TA VI[a] are 124.35 ° for conformation A and 128.10 ° for conformation B. The two disorder components are present in the ratio 48:52. The ξ_1 torsion angle values for TA VI[b] are 121.68 ° for conformation A and 127.43 ° for conformation B. The two disorder components are present in the ratio 55:45. As the ξ_1 torsion angle for MA form I is 119.38 °, conformation A has a much better conformational overlay with MA form I, with a $rmsd_1$ value of 0.0398 Å compared to 0.1360 Å for conformation B in TA VI[a] (Figure 34c).
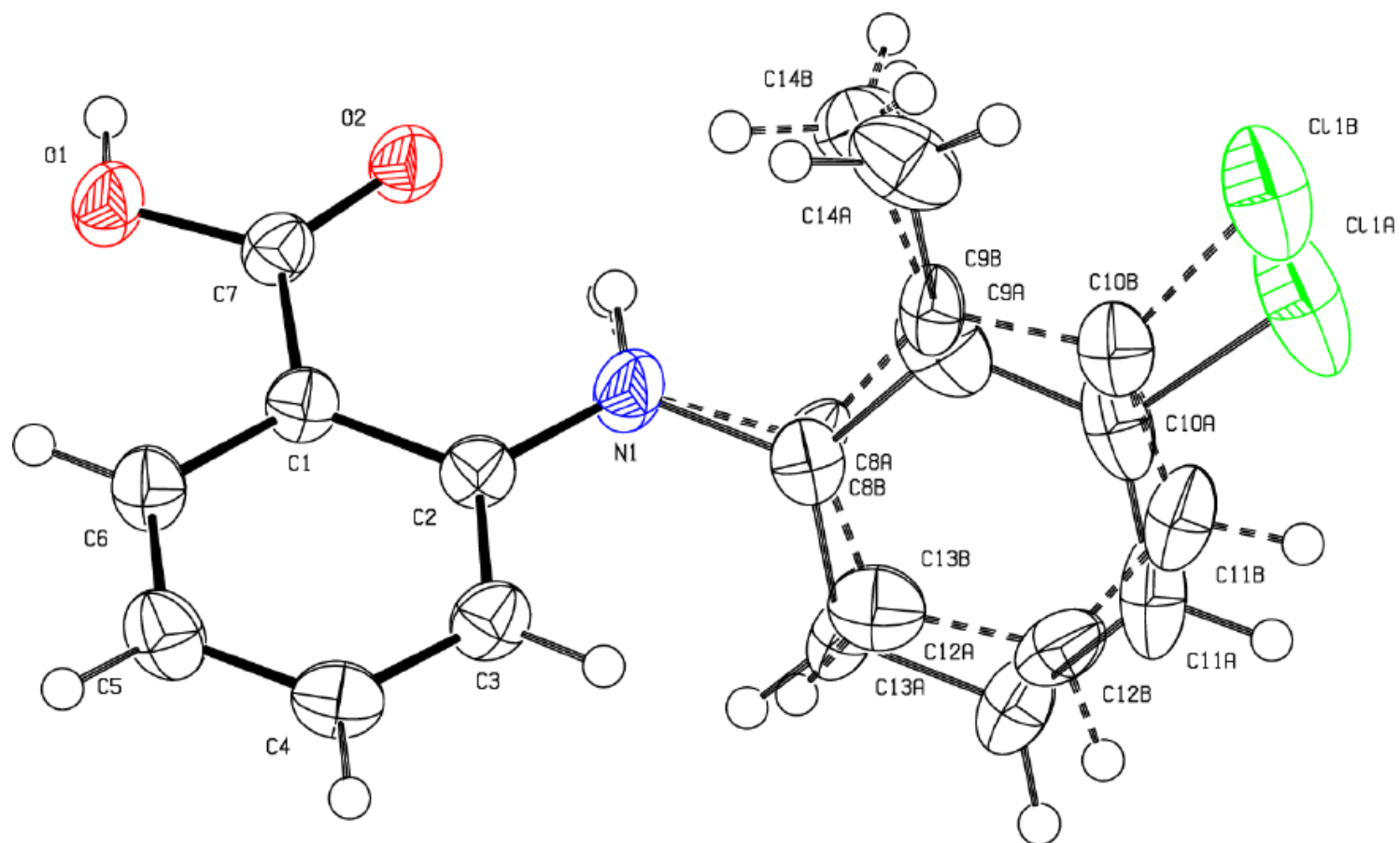
Figure 33. Thermal ellipsoid plot, at 50 % probability, of TA VIᵃ. Conformation A is shown by the solid black bonds and conformation B is shown by the dashed bonds.

The two conformations of TA in TA form VI can be considered individually as two ordered $Z' = 1$ structures. The crystal structure of MA form I can be separately overlaid with each component of TA form VI as shown in Figure 34. The 15 molecule overlays with MA form I are better for conformation A than conformation B, shown by the $rmsd_{15}$ values in Table 21.

The crystal structure of TA form IV has also been separately overlaid with each component of TA form VI. There is only a 14 molecule overlay, between TA form IV and TA form VI (Table 21). TA form VI is similar to TA form IV, but has a different unit cell. TA form IV is $Z' = 3$ whereas TA form VI is $Z' = 1$, but is disordered with two different conformations of TA in the unit cell. The coordination sphere and unit cell data of TA IV and TA VI are different and as such TA form VI can be considered a quite different polymorph.

(a)   (b)

(c)   (d)
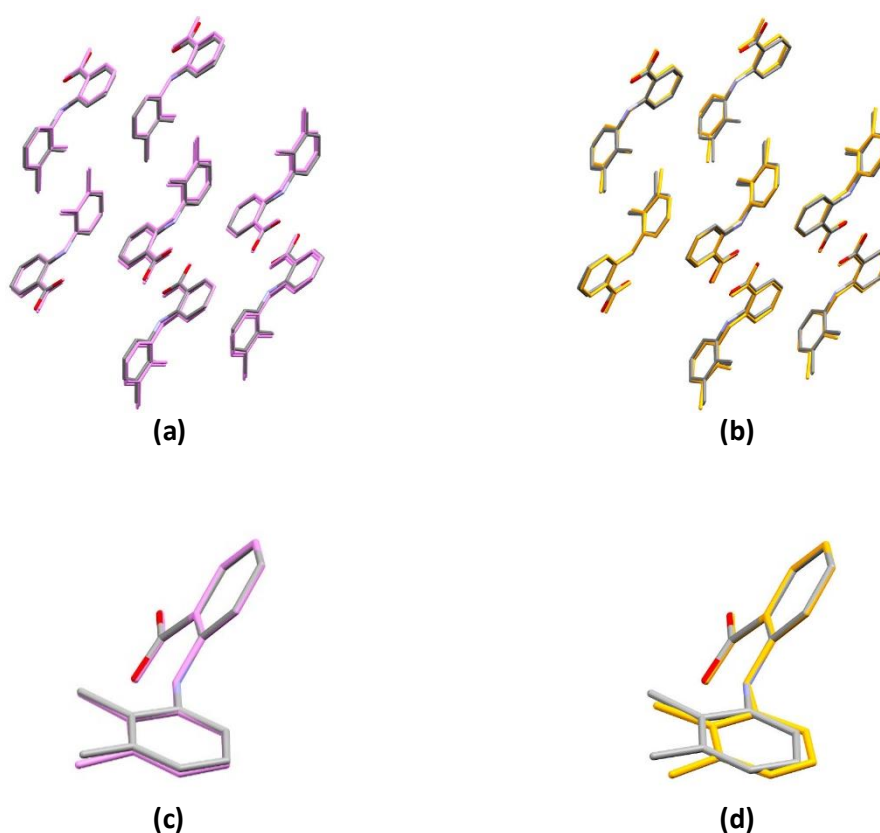
Figure 34. Overlays of MA form I with two ordered components of disordered TA VI[a]. The disorder of TA form VI exists because the TA molecule adopts two different conformations, A (pink) and B (orange). (a) 15 molecule overlay of MA form I with an ordered componenet of TA form VI[a] using conformation A, $rmsd_{15}$ = 0.218 Å, (b) 15 molecule overlay of MA form I with an ordered componenet of TA form VI[a] using conformation B, $rmsd_{15}$ = 0.234 Å (c) molecular overlay of MA form I with conformation A, $rmsd_1$ = 0.0398 Å and (d) molecular overlay of MA form I with conformation B, $rmsd_1$ = 0.136 Å.

Table 21. Crystal structure similarities of TA VI[a] and TA VI[b] with MA form I and TA form IV. The results are given as $n(\text{rmsd}_n)$ values where n is the number of molecules matched in the coordination sphere.

| | | ξ_1 torsion angle (°) | $n(\text{rmsd}_n$ / Å) | |
			MA I	TA IV
TA VI[a]	Conf. A	124.35	15(0.218)	14(0.311)
	Conf. B	128.10	15(0.234)	14(0.372)
TA VI[b]	Conf. A	121.68	15(0.175)	14(0.304)
	Conf. B	127.43	15(0.203)	14(0.373)

The simulated PXRD patterns of TA form IV and TA form VI have been generated from single crystal data and are shown in Figure 35. The simulated PXRD patterns show that the crystal structures of TA form IV and TA form VI are generally similar. However, there are also differences visible in the pattern as some peaks visible in TA form IV are not visible in the TA form VI pattern and vice versa. For example one of the most prominent differences in the PXRD patterns include a peak for TA VI at 15.9 ° compared to a peak at 16.16 ° for TA IV, more peaks for TA IV than TA VI in the region 17.5 – 20 °, a difference in the peaks around 20.4 ° and an extra peak for TA VI at 30.5 °. The differences in the simulated PXRD patterns confirm that the two forms are distinct.
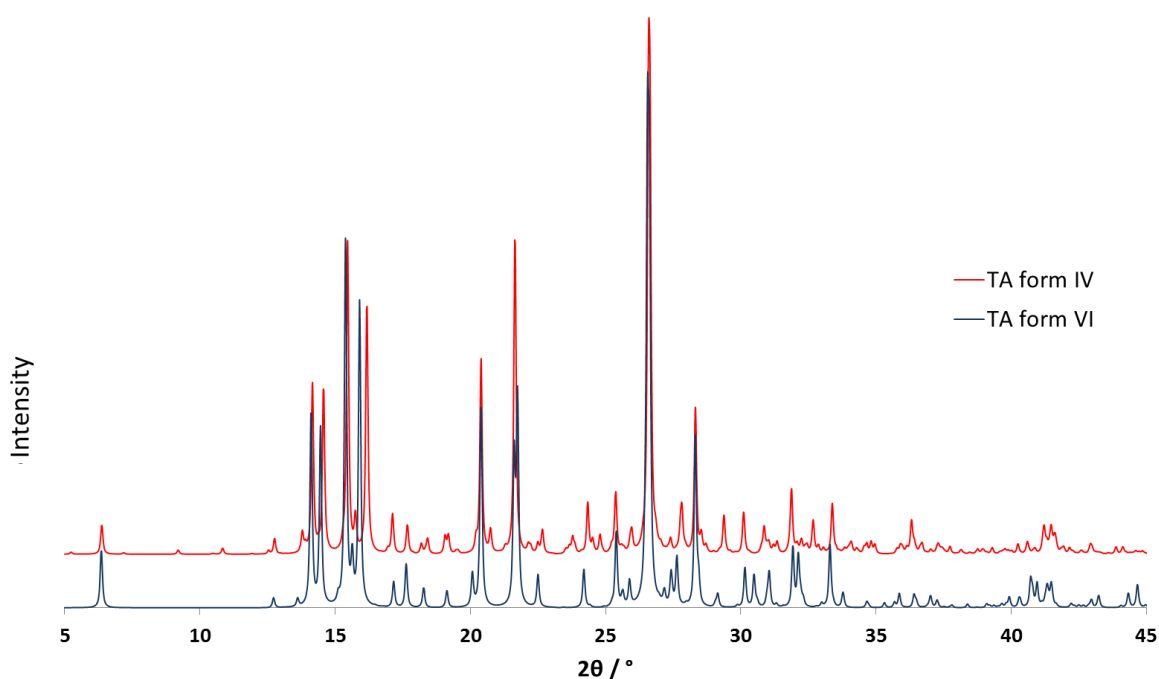
Figure 35. The simulated PXRD patterns of TA form IV (red) and TA VI (blue) generated from single crystal data.

The Raman spectrum collected for TA form VI is shown alongside the Raman spectra for MA form I and the MA-TA solid solution 0.5 mole fraction in Figure 36. The Raman spectra of three different TA form VI crystals are shown in Appendix 8, page 208, alongside a peak list. The Raman spectrum for TA form VI is different to both the spectra of MA form I and also the MA-TA solid solution. The Raman spectrum for TA form VI has also been compared to the Raman spectra collected by López-Mejías et al. for the other five polymorphs of TA (found in the supporting information)[32]. The spectrum for TA VI is similar to that of TA IV which is to be expected due to the crystal structure similarity, however, there are some notable differences. TA form VI has a peak at 658 cm^{-1} which is not reported for TA form IV. Similarly, TA form IV has peaks at 683 cm^{-1}, 959 cm^{-1}, 1235 cm^{-1}, 1965 cm^{-1}, and 2566 cm^{-1} which are not visible in the spectra for TA form VI.
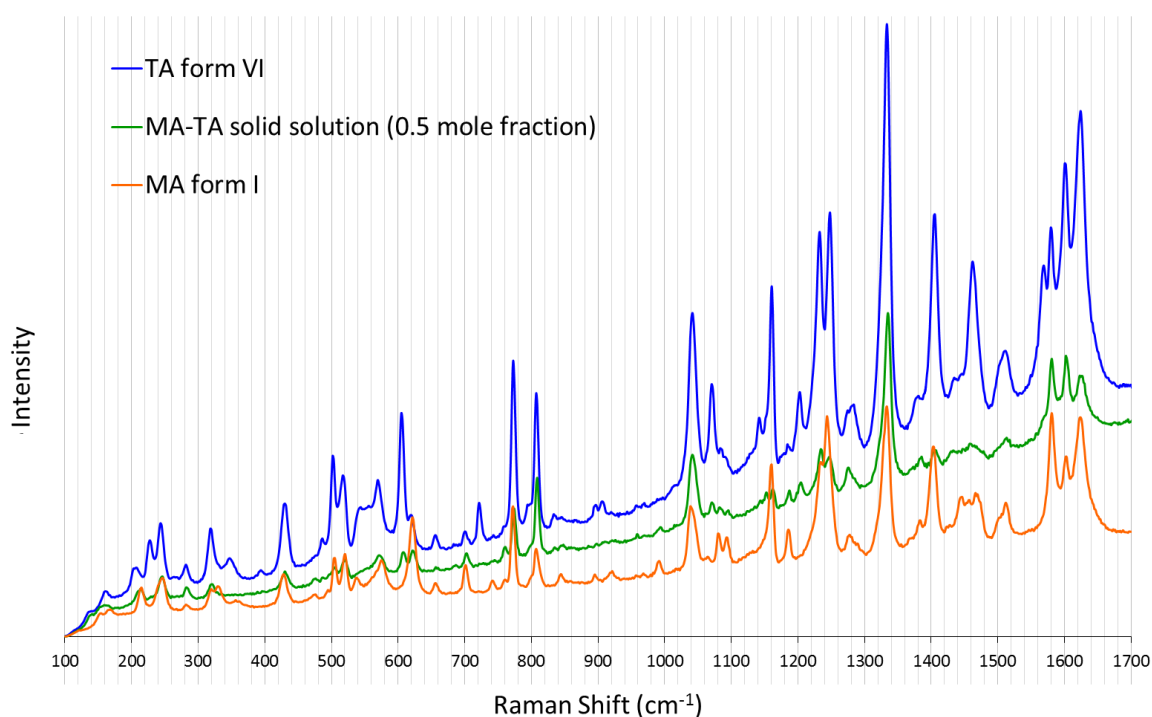
Figure 36. Raman spectra for TA form VI, MA form I and the 0.5 mole fraction MA-TA solid solution.

The DSC scan for TA form VI (sample size of 1.055 mg) was carried out at a heating rate of 100 °C min^{-1} in the range of 0 − 250 °C (Figure 37). TA form VI has the highest melting endotherm (T_m) of all the TA polymorphs showing a melting endotherm at 218.11 °C (Table 22). Even though the DSC scans for TA forms I − V were carried out at a heating rate of 20 °C min^{-1}, the melting points can still be compared because melting is a thermodynamic process and therefore is not affected by the heating rate.[168]

In addition to the data in Table 22, Tybo et al. note a melting endotherm for TA at around 216 °C for the starting material, but do not explicitly state which polymorph of TA this is.[161]

It is interesting to note that the melting points of TA form IV and TA form VI are significantly different even though the crystal structures are very similar.

Table 22. The DSC data for TA forms I-V, taken from the supplementary information provided by López-Mejías et al.[32] and for TA form VI in this thesis.

TA polymorph	T_m (°C)
I	213.10
II	213.52
III	214.09
IV	206.78
V	215.17
VI	218.11
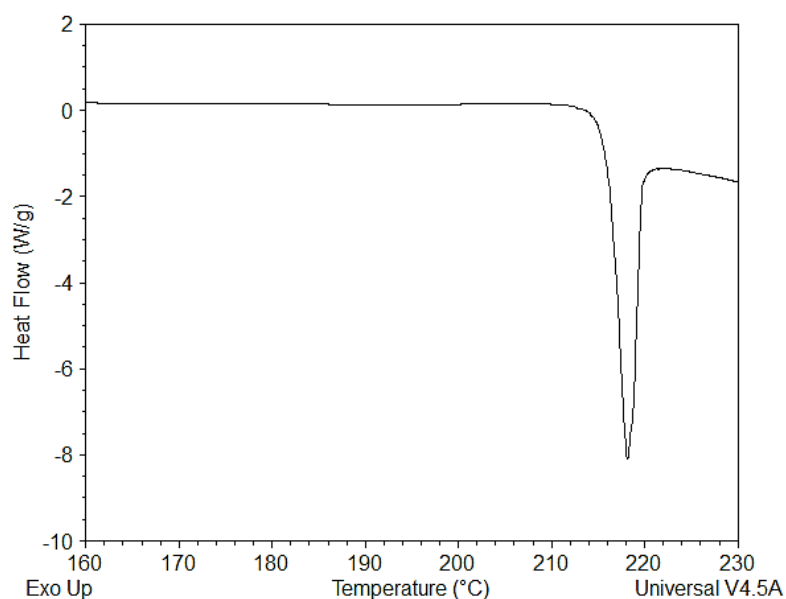
Figure 37. The DSC scan for TA form VI carried out at a heating rate of 100 °C min^{-1}.

4.3.3   Discussion

A new form of TA (form VI) can be obtained by seeding a supersaturated solution of TA in ethanol with MA form I seeds. The MA form I heteroseeds facilitate the first nucleation of TA form VI which is isomorphous to MA form I. SCXRD refinements have been carried out on two separate single crystals of TA form VI and show that the structure is disordered with the TA molecules adopting two different conformations within the unit cell. The conformations of TA in TA form VI are similar to the conformation of MA in MA form I.

The unit cell data, simulated PXRD patterns and DSC data show that TA form VI is distinct from all other forms of TA yet in its three dimensional packing of molecules it is crystallographically similar to TA form IV, with a $rmsd_{14}$ value around 0.3 Å.

Given that the Cl···Cl distances in TA form VI are as short as 3.352 Å, it is somewhat surprising in light of the literature and statistical studies,[25] that the relationship between MA form I and TA form VI has shown that the chloro and methyl groups are interchangeable in the crystal lattice with the same unit cell as MA form I. It is possible that in the case of MA form I and TA form VI, isostructurality is retained because the chloro group occupies a space filling role[123] and does not have a structure directing role.

4.4   Review of Previous Crystal Structure Prediction Study of Tolfenamic Acid – What have we learnt from finding this new polymorph and the solid solution series?

Kitaigorodsky suggested that for a solid solution to exist between two (or more) compounds, the compounds needed to be molecularly isostructural as well as able to crystallise as isostructural solid forms.[63] This chapter began by highlighting the crystal structure similarity of MA form I and TA form IV which appeared to be isostructural as there was a good 15 molecule overlay of the coordination spheres of both structures with an $rmsd_{15}$ value of 0.332 Å. Thus, MA form I and TA form IV appeared to satisfy the conditions stated by Kitaigorodsky.

The results of the investigation into the possible chloro-methyl interchange between MA and TA has shown that (a) TA can cocrystallise with MA forming a solid solution and (b) TA can crystallise as a new polymorph when seeded with MA form I heteroseeds. Both the MA-TA solid solution series and the new polymorph of TA have essentially the same unit cell as MA form I.

TA had previously been studied using CSP methods by Uzoh[89] who produced the crystal energy landscape in Figure 38. The crystal energy landscape shows a number of predicted structures that are competitive in energy with the previously known polymorphs of TA, yet the

polymorph of TA found in this study (form VI) was not found on the original crystal energy landscape. The identification of two isomorphous crystal structures on the two separate crystal energy landscapes of MA and TA was suggested as a criteria for the prediction of a solid solution form by Habgood et al.[169] Therefore, had the new polymorph of TA been predicted by Uzoh, it would have allowed a more confident prediction of the existence of the solid solution in the same unit cell as MA form I. It would also have pointed towards the use of MA form I heteroseeds as possible route to nucleate a new polymorph of TA.
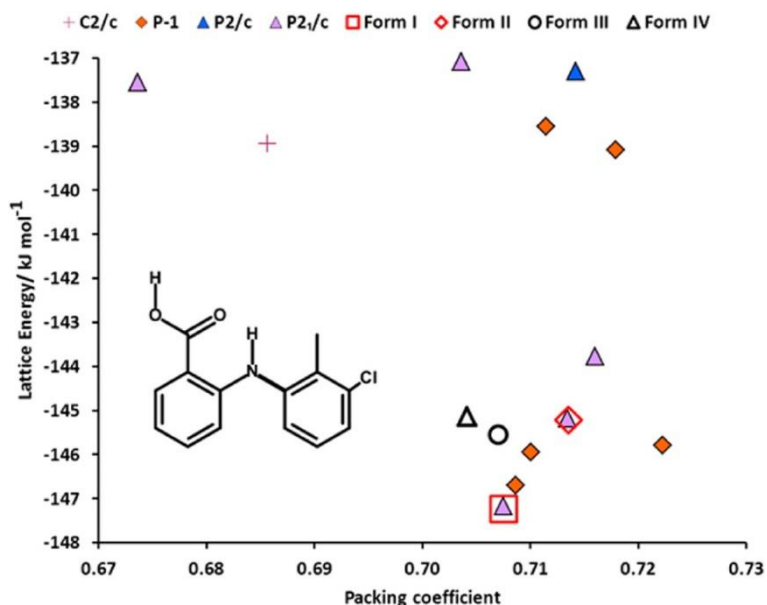
Figure 38. Taken from the previous CSP study on TA by Uzoh.[89] The crystal energy landscape of TA where each symbol represents a crystal structure of the specified space group, which is a minimum in the lattice energy (calculated within the polarizable continuum). The open symbols correspond to the minima starting from the experimental polymorphs. The packing coefficient is the proportion of the cell volume[156] occupied by the molecule calculated using a grid spacing of 0.1 Å.

The discovery of the new form of TA (form VI) with the same unit cell as MA form I led Uzoh to revisit his CSP work on TA to investigate why the observed structure was not on the final crystal energy landscape even though it was a Z' = 1 structure. However, upon re-examination of Uzoh's CSP study, it was found that one component of TA form VI (conformation A) with the same unit cell as MA form I, had been generated albeit high in energy. In order to minimise computational costs, the number of structures evaluated at each level of theory was reduced and in the final stage of lattice energy minimisation of TA, Uzoh only minimised 100 structures. The structure that matched conformation A of TA form VI was too high in energy and above the cut off (ranked 137) to be minimised in the last step before the crystal energy landscape was produced.

After the discovery of TA VI, Uzoh subsequently re-minimised the hypothetical TA form VI structure found in his search which was then calculated to have a lattice energy of -144.97 kJ

mol^{-1} and a packing coefficient of 0.7043 making it competitive in energy with the known polymorphs of TA.[170] This showed that in the last step of the computational methodology, there is a significant amount of energy re-ranking of hypothetical crystal structures of TA and Uzoh concluded that more minimisations and lattice energy refinements were required on a greater number of structures.

Had CrystalPredictor failed to find TA form VI in the search space this would have brought the computational methodology followed in this work into doubt. However, the experimental discovery of TA form VI has highlighted the need to minimise as many hypothetical crystal structures as possible, within computational and time restrictions, at each stage of calculating the crystal lattice energy. The extent of re-ranking of the lattice energies of the hypothetical crystal structures in a CSP study should be considered in more detail to ensure that all the structures that minimise to be competitive in energy with known polymorphs or the global minimum have been refined at the optimum level of theory.

CSP studies in this thesis have accounted for the possible re-ranking of the lattice energies of structures at improved levels of theory by minimising thousands of structures rather than hundreds (see chapters 3 and 6) and by looking at the lattice energy difference between different computational models.

4.5 Conclusions

Work in this chapter has shown that MA and TA can cocrystallise from ethanol solution to form solid solution crystals that are isomorphous with MA form I. The ratio of MA:TA is representative of the target mole fraction and TA is soluble in MA form I up to around 80%. In a separate series of experiments, MA form I seed crystals were used to obtain a new polymorph of TA, form VI, with the same unit cell as MA form I.

The unit cell volumes of MA form I, the MA-TA solid solution series and TA form VI do not appear to be significantly affected by chloro-methyl replacement. The results in this chapter show no clear evidence as to which substituent is larger

The discovery of TA form VI also raised questions about the computational methodology that was followed by Uzoh for TA (and subsequently in this thesis for MA) as TA VI was not found on Uzoh's crystal energy landscape. However, re-examination of Uzoh's TA crystal energy landscape showed that the computational methodology did accurately generate the TA VI crystal structure, but that not enough crystal structure minimisations were carried out to account for the re-ranking of structures.

5   Sublimation of Mefenamic Acid and Tolfenamic Acid

Chapter 4 has shown that MA and TA can cocrystallise from ethanol solution to form solid solution crystals and a new form of TA, form VI, can be obtained by seeding a supersaturated solution of TA in ethanol with MA form I. Both the solid solution crystals and TA form VI are isomorphous with MA form I. These results provide rationale for investigating the sublimation behaviour and vapour deposition of MA and TA which aimed to nucleate targeted forms of MA and TA as identified by the isostructural pairings shown in Table 12, page 72, by introducing template surfaces into the vapour deposition experiments. The sublimation techniques were guided by the successes of the methods used to nucleate CBZ form V on isostructural DHC form II seed templates.[84] The DHC/CBZ sublimation experiments followed the identification of a possible new polymorph of CBZ from CSP studies and the cocrystallisation of CBZ and DHC which formed a solid solution that was isostructural to DHC form II.[87]

5.1   Introduction

Two different approaches were taken to investigate the sublimation behaviour of both MA and TA. Initially, MA and TA were sublimed in a glass tube under a static vacuum of around 3.0×10^{-2} mbar, subsequently more sophisticated sublimation experiments were carried out using bespoke apparatus and a dynamic vacuum of around 5.0×10^{-6} mbar. The results from both approaches showed that MA and TA display different behaviour from one another upon sublimation onto different surfaces. The sublimation experiment under dynamic vacuum employed a copper surface which nucleated a new form of TA that was identified by PXRD. No new forms of MA were identified, but MA was deposited as form I on the copper surface, but form II on glass surfaces. The use of crystal surfaces as templates in the experiments failed to nucleate targeted forms of MA and TA that were previously identified as isostructural or isomorphous.

5.2   Sublimation Under Static Vacuum

The first approach was to investigate the sublimation of pure MA and pure TA under a static vacuum. The initial experiments identified the temperatures at which MA and TA sublimed using the apparatus shown in Figure 39 as well as the position at which the sublimed material recrystallised. This information helped optimise the experimental set up when template crystals were introduced to target the nucleation of specific forms of MA and TA by exploiting the isostructural relationships.

5.2.1   Methods

Materials. MA was purchased from Sigma Aldrich as form I and TA was purchased from LKT Laboratories Inc. as form I. Both compounds were used without further purification.

Preparation of Sublimed Crystals. MA and TA were sublimed using the apparatus shown in the schematic diagram in Figure 39. A sample of MA or TA was loaded into a glass tube (length, 300 mm and diameter, 10 mm) followed by a small amount of glass wool which was used to stop mass transport of the loaded material. A Schlenk line[171, 172] with a two stage vacuum pump was used to evacuate the glass tube to a pressure around 3.0×10^{-2} mbar. The glass tube was sealed and placed horizontally inside copper piping which was in turn inserted into a tube furnace (the heat source) which could be set to the required temperature. The copper piping provided a temperature gradient ensuring that the temperature of the glass tube was elevated above room temperature. Measurements of the temperature gradient were not taken so specific temperatures along the sublimation tube are unknown.
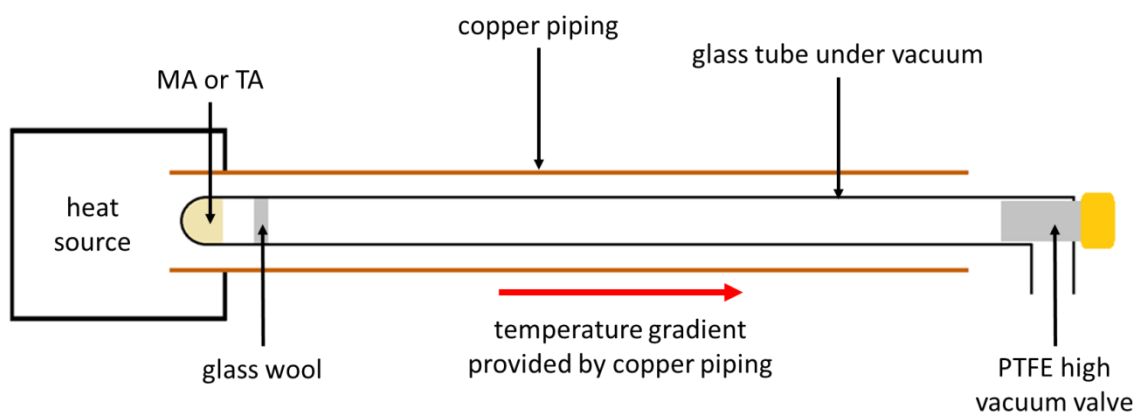
Figure 39. Schematic diagram of the apparatus used in the sublimation of MA and TA under a static vacuum.

Once the apparatus was set up, the tube furnace was switched on and the temperature was gradually increased to observe at what temperature the material under investigation sublimed and how far along the glass tube the sublimed product was deposited. Temperatures of between 230 – 250 °C were required to sublime MA and temperatures of between 180 – 205 °C were needed to sublime TA. For both MA and TA, the sublimed material grew as single crystals after 48 hours on the glass walls of the tube around 50 - 70 mm along from where the starting material was loaded (Figure 40a). The sublimed crystals were scraped off the walls of the glass tube for analysis.

The apparatus was subsequently modified so that a template crystal surface could be present during the sublimation experiments. The template crystal was first attached to a wire using superglue and then positioned in the middle of the glass tube around 60 mm away from

the end of the tube (Figure 40b). After sublimation, the template crystal on the wire was carefully removed so that any crystals that had nucleated on the surface of the crystal and the wire could be analysed.
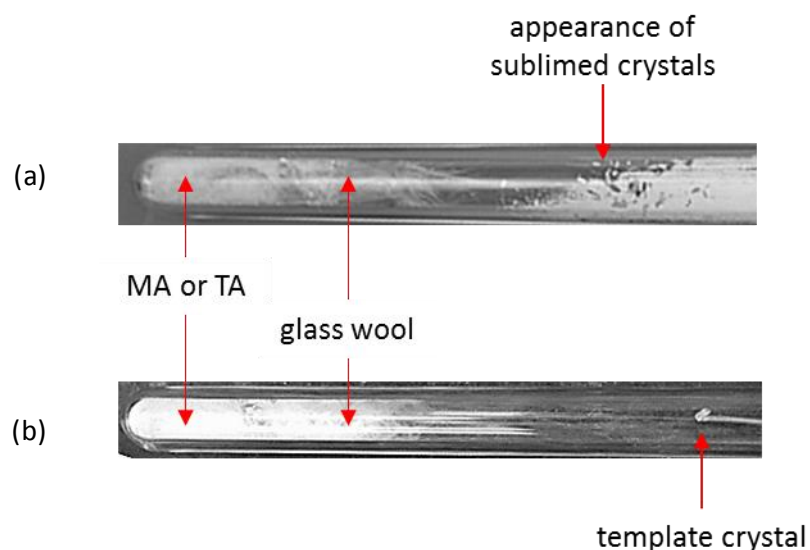
Figure 40. Images of the glass tube used in the sublimation experiments under static vacuum. (a) sublimation of pure MA and the appearance of sublimed crystals on the glass walls and (b) the introduction of a template crystal surface before sublimation. Pictures are not to scale and are for illustrative purposes only.

Single Crystal X-ray Diffraction. See section 2.1.1.1. Sublimation under static vacuum gave high quality single crystals for sublimed MA, in the absence of template crystal surfaces, from which a complete data set could be obtained. All non-hydrogen atoms were refined anisotropically and due to the disorder, hydrogen atoms were refined using a riding model. For sublimed TA and crystals of MA and TA that grew in the presence of a template crystal surface, only unit cell data was collected to identify the polymorph.

Powder X-ray Diffraction. Microcrystalline samples were ground and loaded into a 0.5 mm capillary tube. The PXRD patterns were recorded at room temperature on a Stoe STADI-P powder X-ray capillary diffractometer equipped with Cu-Kα_1 radiation (using 40 kV and 30 mA, λ = 1.5406 Å). The instrument was operated between initial and final 2θ angles of 2.000 ° and 45.065 °, in an increment of 0.495 °. Counts were accumulated for 20 seconds at each step.

5.2.2 Results

5.2.2.1 *Tolfenamic Acid – Sublimation without Templating*

TA was heated to around 200 °C for 48 hours and colourless needle crystals were observed on the glass walls of tube. Multiple crystals were analysed by collecting SCXRD unit cell data which identified the sublimed crystals to be TA form I, the most stable form.

5.2.2.2 *Mefenamic Acid – Sublimation without Templating*

MA was heated to around 230 °C for 48 hours before colourless crystals were observed to nucleate on the walls of the glass tube. The crystals were identified as MA form II from SCXRD unit cell data. A complete data set was then collected and refined. The crystallographic data for MA form II has already been reported in Table 5 on page 46. At the time of writing, it appears that this is the first time a single crystal of MA form II has been obtained using a sublimation technique.

It is not surprising that the sublimed crystals of MA were form II considering that MA form II is reported to be the most stable form at elevated temperatures and literature reports that MA form II can be obtained by heating form I to above the transition temperature of 150 – 175 °C depending on the literature.[35, 99, 101, 102, 104, 105] During the sublimation experiment, the bulk sample of MA was heated above the transition temperature to 230 °C for 48 hours.
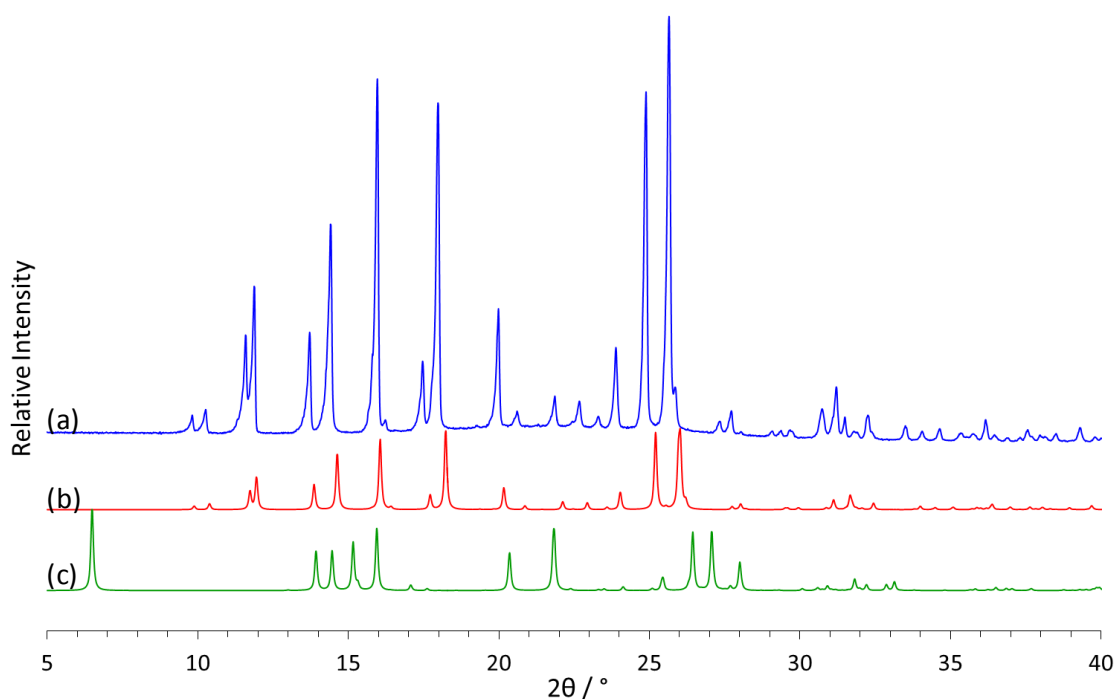
Figure 41. PXRD patterns of polymorphs of MA: (a) experimental PXRD pattern of the bulk MA, used in the sublimation experiments under static vacuum, after being heated to around 230 °C for 48 hours; (b) calculated PXRD pattern of MA form II using single crystal data from this work and (c) calculated PXRD pattern of MA form I using single crystal data from this work.

After the sublimation experiment, small crystallites were observed in the glass wool as well as in the bulk sample of MA that was originally loaded into the glass tube. The bulk sample of MA was analysed using PXRD and the PXRD pattern was compared to simulated PXRD patterns of MA forms I and II from single crystal data (Figure 41). The experimental data of the bulk MA has the same peaks as the calculated PXRD pattern of MA form II. Peaks relating to MA form I are absent. These results confirm that the loaded MA sample had transformed from MA form I to MA form II during the experiment and that there was no remaining trace of MA form I. The experimental PXRD data for the bulk MA was collected at room temperature in whereas the single crystal data for MA form II was collected at 150 K. The differences in the temperature of data collection gives rise to small differences in the peak positions observed in Figure 41.

5.2.2.3   Experiments Involving the use of Template Surfaces

In more sophisticated experiments, template crystal surfaces were provided within the sublimation apparatus to investigate the nucleation of a targeted form of MA or TA by exploiting isostructural relationships that have been discussed in previous chapters.

5.2.2.3.1   Tolfenamic Acid Form I Template Surface

A single crystal of TA form I was introduced into the sublimation apparatus as a template surface. TA form I is isostructural with a predicted form of MA, #19MA_5643. TA form I and #19MA_5643 have a good 15 molecule overlay with a rmsd$_{15}$ value of 0.418 Å (Table 12, page 72). However, as was discussed in section 3.2.2.4.1, calculations indicated that the relative stability of #19MA_5643 was sensitive to the method of calculation which cast doubt as to whether #19MA_5643 would nucleate or grow.

The sublimation experiment using TA form I as a template surface was explored despite concerns that it might not nucleate the predicted form of MA. Commercial MA was loaded into the glass tube followed by the glass wool and a TA form I crystal was placed inside the tube around 50 mm away from the commercial MA. The commercial MA was heated to around 210 °C and the MA was left to sublime over the period of a week. The temperature of sublimation in these templating experiments was less than that in the sublimation of pure MA onto the glass walls to try and encourage slower nucleation and growth.

Figure 42 shows the TA form I on the wire (a) before the sublimation and (b) after the sublimation where the TA form I template crystal has decreased in size, indicating it may have partially sublimed.

Figure 42b shows that following the sublimation, small crystals of MA have grown on both the wire and the remains of the TA form I template crystal. Crystals were gently removed

from both the wire and the template crystal and SCXRD unit cell data was collected. The unit cell data indicated that all crystals were MA form I. Under the current experimental conditions, TA form I template failed to nucleate or grow an isostructural form of MA. It is possible that the nucleation of MA form I on the wire was occurring before any other form was able to nucleate. Therefore, it is possible that MA form I growing over the TA form I template crystal inhibited the formation of other potential forms. Lowering the sublimation temperature and moving the template crystal further away from the heat source did not alter the observations.

(a)   (b)
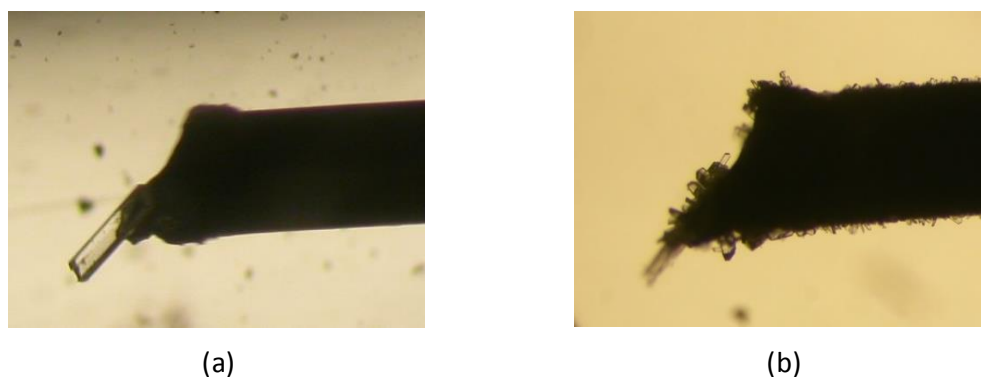
Figure 42. Optical image of the TA form I template surface as attached to metal wire (a) before and (b) after sublimation of MA.

5.2.2.3.2   *Mefenamic Acid Form I Template Surface*

The isomorphous relationship between MA form I and TA form VI, that has already been investigated using solution based crystallisation techniques in chapter 4, was examined. The MA form I template crystal used in these experiments was large enough that it could be cut and one surface crushed in order to increase the number of different crystallographic faces that would be exposed to the sublimed TA. Different crystallographic faces are of interest when designing crystalline surfaces that control the nucleation of specific forms by heteroepitaxy. It has been shown that as well as the chemical functionality of the exposed surface, the geometrical lattice similarity can also affect nucleation and polymorph selectivity.[38, 173]

The template crystal was aligned so that the crushed surface of MA faced the bulk commercial TA that was loaded into the glass tube. Figure 43 shows the MA form I crystal after TA had been sublimed at 200 °C for a week. The sublimed TA crystals grew as needles all over the template crystal in multiple, random orientations. Often there was just one nucleation point for several needle crystals that grew at different angles from the surface. The exposed crushed surface did not appear to favour or promote the nucleation of TA crystals.

Multiple crystals of sublimed TA were analysed by collecting SCXRD unit cell data. All crystals that nucleated on the surface of the MA form I template were TA form I, the most stable polymorph, not the isomorphous TA form VI.
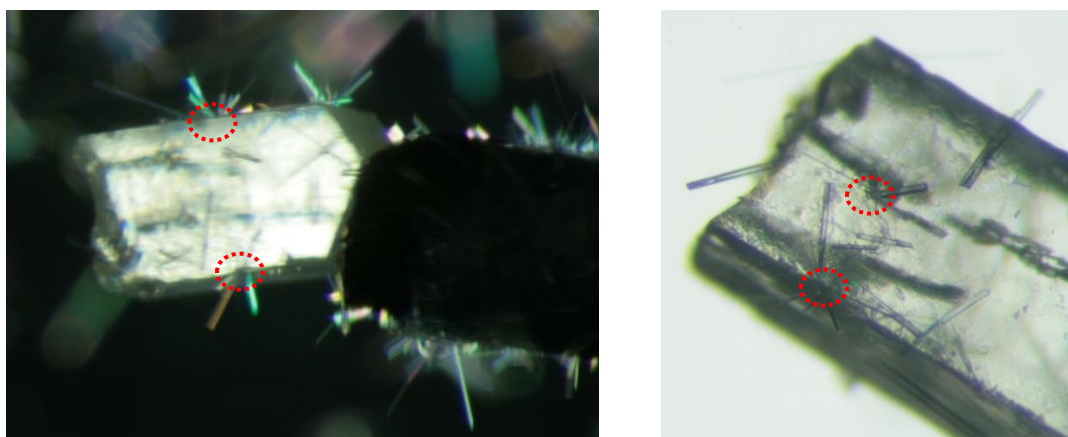
Figure 43. Optical images of the MA form I seed template covered in crystals after sublimation of TA. Some of the nucleation points of multiple crystals that grow at different angles are indicated by the dashed red rings. The MA form I seed was roughly 2 mm x 1 mm x 1 mm in size.

5.2.3   Discussion

The results of the sublimation experiments that have been carried out under a static vacuum of around 3.0×10^{-2} mbar using the apparatus in Figure 39 have indicated differences in the behaviour of MA and TA.

Sublimed MA grows as form II on a heated glass surface. This observation was initially thought to be due to the fact that the glass walls of the sublimation tube were held at a temperature above the transition temperature of MA form I to MA form II (due to the temperature gradient provided by the copper piping). However, when the metallic wire and the TA form I crystal surfaces were introduced into the sublimation tube, and held at temperatures above the transition temperature, MA crystallises as form I. These additional results suggest that the surface and not just the temperature is affecting the nucleation and polymorphic selectivity of MA, however, the specific role of the surface cannot be quantified.

In comparison, TA crystallises as form I both on the heated glass walls of the sublimation tube as well as on the surface of MA form I template crystals and the metal wire. Thus, the surface does not appear to be affecting the nucleation and growth, or polymorphic form, of sublimed TA.

The introduction of TA form I and MA form I templates into the sublimation apparatus did not nucleate the targeted forms of MA or TA. However, as the template and target crystals are isomorphous, epitaxial growth might be expected to give rise to a uniform layer of the target crystal structure covering the template seed.[88] Such an observation would be hard to confirm as the layers of epitaxial growth would be too thin to observe on the time scale of the experiment. The results of the sublimation of TA onto the MA form I template (Figure 43) show crystals of TA form I growing on, and out from, the template crystal. These observations do not disprove the

theory that a uniform layer epitaxially grows on the surface of the template as it is possible that the nucleation of TA form I occurs at small defects on the surface of the template crystal. The defects on the surface could promote nucleation of TA form I in multiple directions with a growth rate significantly higher than that of any uniform epitaxial layers.

5.3   Sublimation Under Dynamic Vacuum

This section describes the experimental apparatus, the methodology used and the results obtained from more sophisticated sublimation experiments. These experiments made use of bespoke sublimation apparatus that was previously used to study amorphous solid water[174, 175] and can reach pressures of around 5.0 x 10^{-6} mbar using a dynamic vacuum. The experimental procedure in this section is notably different to those described in section 5.2 and the main differences are summarised in Table 23. Details of the two types of sublimation apparatus are described in the respective *Methods* sections 5.2.1 and 5.3.1.

Table 23. Summary of the main differences between the two different sublimation experiments detailed in sections 5.2 and 5.3.

	Section 5.2	Section 5.3
Type of vacuum	static	dynamic
Pressure	3.0 x 10^{-2} mbar	5.0 x 10^{-6} mbar
Temperature of target surface	elevated	room temperature
Direction of sublimation	horizontal (along temperature gradient)	vertical
Distance travelled by sublimed product	50 mm	250 mm
Duration	2 – 7 days	3 – 4 hours
Temperature required to heat sample	180 – 250 °C	100 – 150 °C
Method of analysis	SCXRD	PXRD

5.3.1 Methods

Materials. See section 5.2.1.

Preparation of sublimed product. See section 5.3.1.1.

Powder X-ray Diffraction. See section 5.2.1. The sublimed product was scraped off the respective surface using a nickel spatula and loaded straight into a 0.5 mm capillary tube.

^{1}H NMR Spectroscopy. See section 4.2.1. The product of sublimed TA and commercial TA were analysed using ^{1}H NMR spectroscopy.

Infrared Spectroscopy. See section 4.2.1. Data was analysed using the ACD/Spectrus Processor software.[110]

Thermal Analysis. See section 4.2.1. The TA Q2000 (TA Instruments, LLC, USA) DSC was calibrated at heating rates of both 10 °C min^{-1} and 100 °C min^{-1} in a temperature range of 0 – 250 °C using an indium melting point standard.

Raman Spectroscopy. See section 4.2.1.

Simultaneous DSC-synchrotron X-ray diffraction (DSC-XRD). Simultaneous PXRD and DSC data were collected for samples of the sublimed/deposited TA and commercial TA. Experiments were performed on Beamline I12 of Diamond Light Source synchrotron.[176] This beamline generates a continuous spectrum of X-rays over the energy range from 50 to 150 keV. All experiments reported here were conducted with the beam monochromated to an energy of ca. 53 keV ($\lambda = 0.2337$ Å). DSC measurements were performed with TA Q20 DSC (TA Instruments LLC) using Tzero aluminium pans. The DSC furnace was modified to allow the X-ray beam to pass through the sample by having two holes drilled in both sides of the DSC cell. The DSC was calibrated with indium following the manufacturer's instructions. A Thales Pixium RF4343 detector was sited 2.5 m away from the DSC pans. The PXRD patterns were collected every 6 seconds (4 seconds data collection plus 2 seconds pause). Data was collected at heating rates of 10 °C min^{-1} and 2 °C min^{-1} in the range 40 – 250 °C. Data were analysed using the Fit2D program[177] to convert the 2D data collected on the Pixium to 1D patterns.[178] These patterns were background-subtracted using in-house routines. The method has previously been described.[179, 180]

5.3.1.1 Sublimation Apparatus

The apparatus used was initially developed to study amorphous solid water,[174, 175] but was adapted to include an organic evaporation source used to sublime organic compounds such as MA and TA. A schematic diagram of the apparatus is shown in Figure 44. More detailed diagrams can be found in Jacob Shephard's thesis titled, 'Structure-Property Relationships In Two-Component Liquids: Hydrophobic Effects and Azeotropy', see reference.[175]

The main variables that were investigated by the apparatus were (a) the rate of deposition and (b) deposition onto different surfaces (copper and glass). Analysis focused on the effect of these variables on the product including the polymorphic form and phase purity.
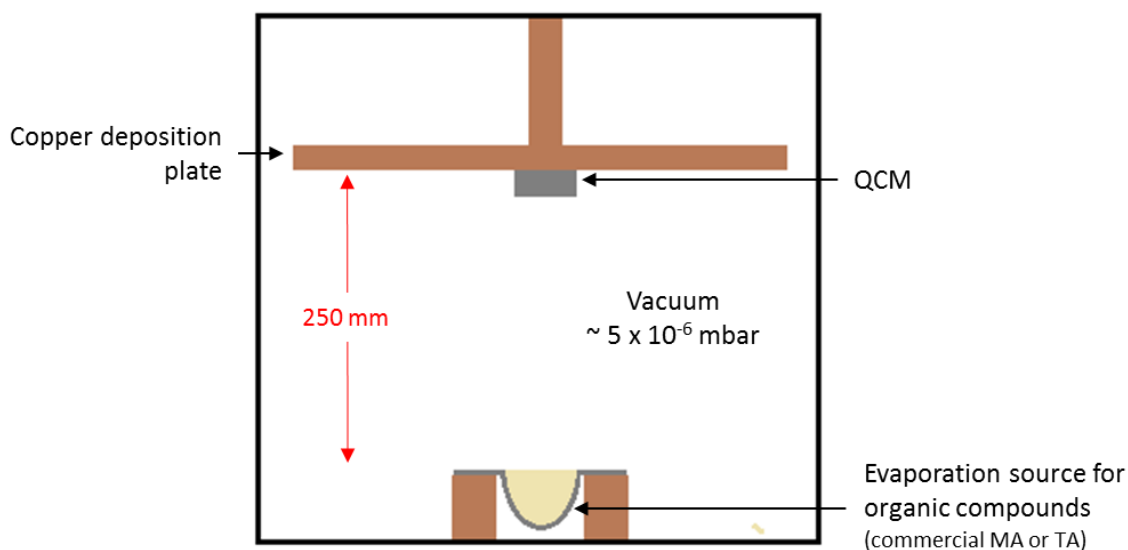
Figure 44. Schematic diagram of the apparatus used in the sublimation of MA and TA using a dynamic vacuum at pressures of ca. 5.0 x 10^{-6} mbar.

5.3.1.1.1   Vacuum Chamber

The following description is adapted from that given by Shephard.[175] The vacuum chamber was purpose built (Kurt J. Lesker, Kastings, UK) with internal dimensions of 24 x 12 x 12 inches. There are several large KF40 and LF100 flanges and a full sized door for easy access with a glass viewing window. A base pressure of around 5.0 x 10^{-6} mbar can reliably achieved using a diffusion pump (Diffstack 63, BOC Edwards, Crawley, UK) containing polyphenol ether oil (Santovac5, BOC Edwards) backed with a two-stage rotary vane pump (model 12, BOC Edwards). A liquid nitrogen baffle, which requires topping up throughout the deposition experiments, is positioned above the diffusion pump to trap any oil residues. The pressure within the vacuum chamber was measured using a dual Pirani/cold cathode ionisation pressure gauge (Penning Vac PTR 90, Oelikon Leybold Vacuum, Cologne, Germany) and recorded using RS232 connections to a computer using Labview software.

The vacuum chamber is equipped with the ability to adjust the height of the copper deposition plate (203 mm in diameter, 6 mm thick), but all sublimations in this thesis were carried out with the deposition plate set 250 mm above the evaporation source. Although the deposition plate can be cooled to liquid nitrogen temperatures, all the depositions in this work were carried out with the deposition plate at room temperature. Lower pressures can be achieved if the deposition stage is cooled as it acts as a cryopump.

The sublimation of MA and TA was carried out using two different evaporation sources. The first evaporation source was the one described by Shephard for the deposition of C_{60}.[175] It consisted of an aluminium oxide crucible, (EVC1A0, Kurt J. Lesker), tungsten filament, (EVB8B3025W+, Kurt J. Lesker), and a high current (20 A, 1.3 mm diameter copper conductors) electrical base plate feed-through (264-13Cu1K-2-BP, Allectra, Sussex, UK). A purpose built power supply containing transformers (MPI-400-12, SignalTransformer, New York, USA) was able to regulate the electric potential across the filament to between 0 and 6 V. The current flowing through the filament was monitored with a current sense resistor by measuring the voltage across two 20 mΩ/50 W resistors in parallel (1 A = 10 mV) with a multimeter, (IDM72, ISO-TECH, Gyeonggi-do, Korea). Due to restrictions on the way the current was set and monitored when using this evaporation source, it was hard to repeat the experiments with exactly the same current. Therefore, measurements of the deposition rate from a quartz crystal microbalance (QCM) were integral to the interpretation of the results.

During the course of this study, modifications were made to the bespoke vacuum chamber that enabled the temperature of the crucible to be set and controlled to within ± 0.1 °C. An OLED Low Temperature Evaporator (LTE10, Kurt J. Lesker) was used which was equipped with a thermocouple in contact with the base of the crucible for accurate temperature readings. An aluminium oxide crucible (EVCEF−10AO, Kurt J. Lesker) was heated using the low temperature evaporator which was connected to a single channel controller (BM833-01S, Kurt J. Lesker) which set the temperature.

It should be noted that as well as there being significant differences between the heating of the two evaporation sources, there were also differences in the size and shape of the crucibles that were compatible with each evaporation source (Figure 45). Although the distance from the loaded material to the deposition plate was kept constant across all experiments, due to significant differences in the geometries of the two crucibles, there were differences in the extent to which they were filled, Figure 45.
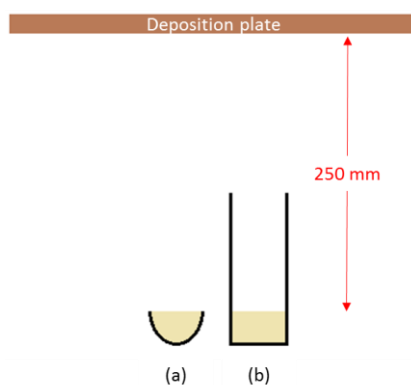
Figure 45. Schematic diagram of the differences in the two crucibles used with (a) the original evaporation source and (b) the more sophisticated evaporation source.

The deposition of MA and TA was monitored using a quartz crystal microbalance (QCM) which was attached to the centre of the copper plate (Figure 46). A QCM is a very precise balance that uses the piezoelectric effect to monitor mass change. A potential is applied across a quartz crystal that has two electrodes attached to the top and the bottom of the crystal which is held in a quartz crystal holder and sensor. When the correct frequency of alternating current is applied, the crystal will start vibrating at its fundamental frequency. One surface of the quartz crystal is exposed and the crystal reacts quickly and precisely to any changes at the surface, in this case, the deposition of MA or TA. The resonant frequency of the crystal decreases with increasing mass on the surface.

Equation 6
$$\Delta f = \frac{2f_0^2 \Delta m}{A\sqrt{\rho_q \mu_q}}$$

Using the Sauerbrey equation (Equation 6), the mass change can be monitored over time and the deposition rate can be calculated. Where Δf is the change in frequency (Hz), f_0 is the resonant frequency (Hz), m is the mass (g), A is the active electrode area (cm^2), ρ_q is the density of quartz (2.648 g cm^{-3}) and μ_q is the shear modulus of quartz (2.947x10^{11} g cm^{-1} s^{-2}).

6 MHz, gold plated, AT-cut quartz crystals (Sycon Instruments, USA) were placed inside the QCM crystal holder which was connected via a coaxial cable (CCSMA-MM-RG316DS-24, Crystek, USA) to a 0.5 – 60 MHz, N2PK vector network analyser. AT cut crystals are cut at an angle of 35 ° 15 ' to the z axis of the crystal. The T in the cut name marks a temperature compensated cut. AT cut crystals were used because they are forgiving of room temperature deposition. The deposition rate was monitored by recording the change in Sauerbrey mass over time using myVNA and QTZ software. The gradients of graphs of Sauerbrey mass against time were compared to identify which deposition experiments were the fastest.
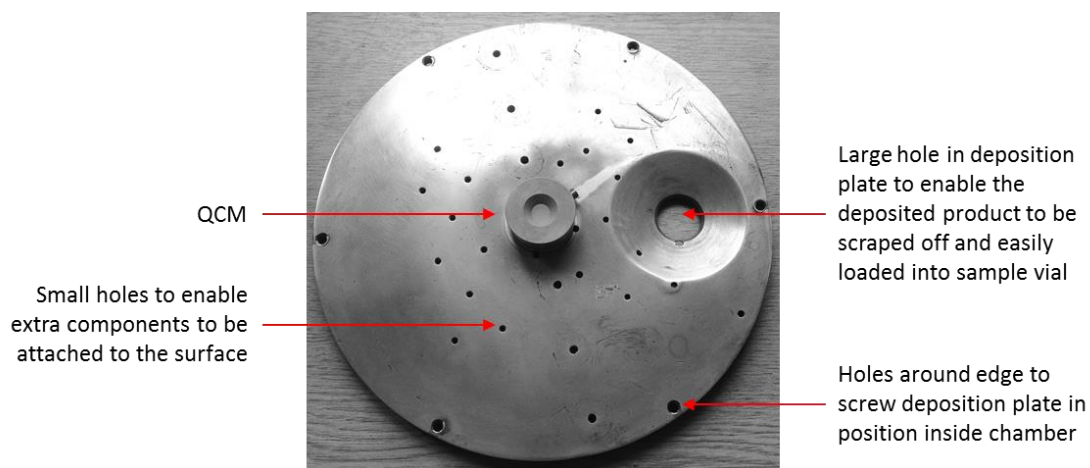
Figure 46. The copper deposition plate used in the sublimation of MA and TA showing the position of the QCM crystal holder in the middle alongside other features of the plate.

115

A glass surface was introduced into the sublimation apparatus by attaching microscope slides onto the surface of the copper deposition plate (Figure 47). This enabled deposition onto both glass and copper surfaces simultaneously. It also meant that one compound could be sublimed onto the glass surface and then the other compound could be sublimed on top of it in a subsequent deposition experiment.
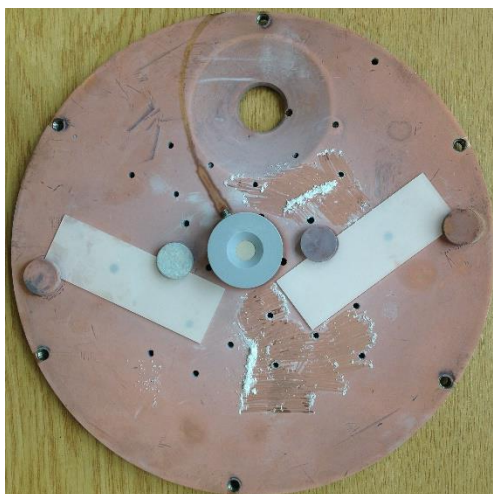
Figure 47. Photograph of the deposition plate following simultaneous deposition onto both the copper and glass microscope slide surfaces. The picture shows some product being scraped off and the positions of the microscope slides and QCM.

5.3.1.2   Sublimation Procedure

Preparing the apparatus. The material to be sublimed (around 2 g of MA or TA) was loaded into the crucible, secured in place at the base of the vacuum chamber and connected to the relevant heat source. The surface of the copper deposition plate was prepared using sandpaper (aluminium oxide, 80 μm grit) and ethanol to remove the copper oxide layer. The QCM and microscope slides (if required) were then attached to the plate before it was fixed in the chamber and the height was adjusted so that it was 250 mm above the evaporation source (Figure 45). High vacuum grease was applied to the chamber door before closure and all chamber vents were closed.

Procedure for evacuating the chamber. To evacuate the chamber, the pressure was first reduced to between $2 \times 10^{-2} - 4 \times 10^{-2}$ mbar using the rotary vane pump. A two way tap was then used to change from actively evacuating the chamber to begin evacuating the diffusion pump. The liquid nitrogen baffle was then filled which reduced the pressure in the chamber to around 2×10^{-4} mbar. The pressure in the chamber increased very slightly when the chamber was not being actively evacuated. After at least a further 20 minutes, a butterfly valve above the diffusion pump was opened and the chamber pressure reduced further to around 5×10^{-6} mbar.

Figure 48 shows how the pressure in the vacuum chamber changes during the evacuation of the chamber.
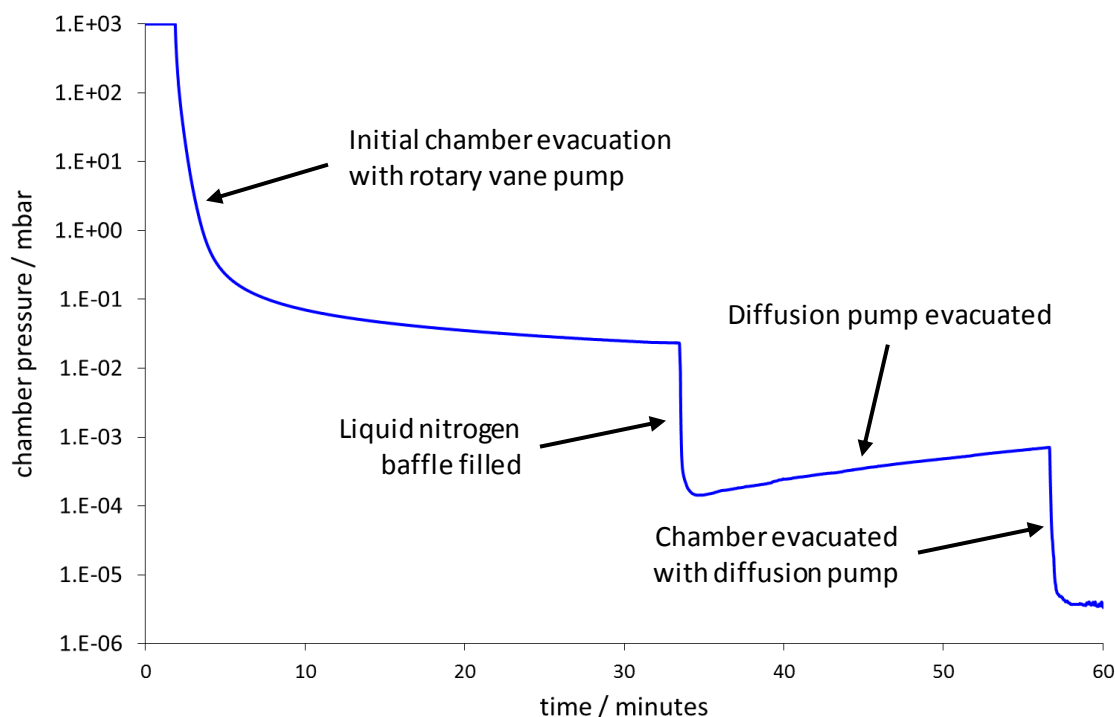
Figure 48. Evacuation of the chamber showing how the pressure changes with the different stages of the evacuation process over time.

Procedure for starting sublimation. When the chamber reached constant pressure, the evaporation source was heated so that the product sublimed and deposition began. The procedure was different depending on the evaporation source. Deposition of MA and TA from the original evaporation source was started by adjusting the transformer to give a desired filament current which would heat the crucible. Deposition from the more sophisticated evaporation source was started by setting the required temperature and ramp rate on the single channel controller.

Monitoring the deposition. As the material in the crucible was deposited onto the copper plate, the deposition was monitored using the QCM. For the original evaporation source, the QCM data was used to determine (a) that the filament current was high enough that the material was subliming and (b) to compare the relative deposition rates of a series of repeated experiments. For the second evaporation source, the QCM was used to confirm that the material was subliming at the selected crucible temperature. A screen grab of the QTZ software is shown in Appendix 9, page 209, which shows that the resonant frequency of the crystal decreases as the Sauerbrey mass increases.

Figure 49 shows the rate of deposition of MA as a change in Sauerbrey mass over time. The data was collected by the QCM that was attached to the copper deposition plate monitoring

117

the deposition of MA from the first evaporation source. The different deposition rates were achieved by manually altering the filament current. The steeper the gradient, the faster the deposition.
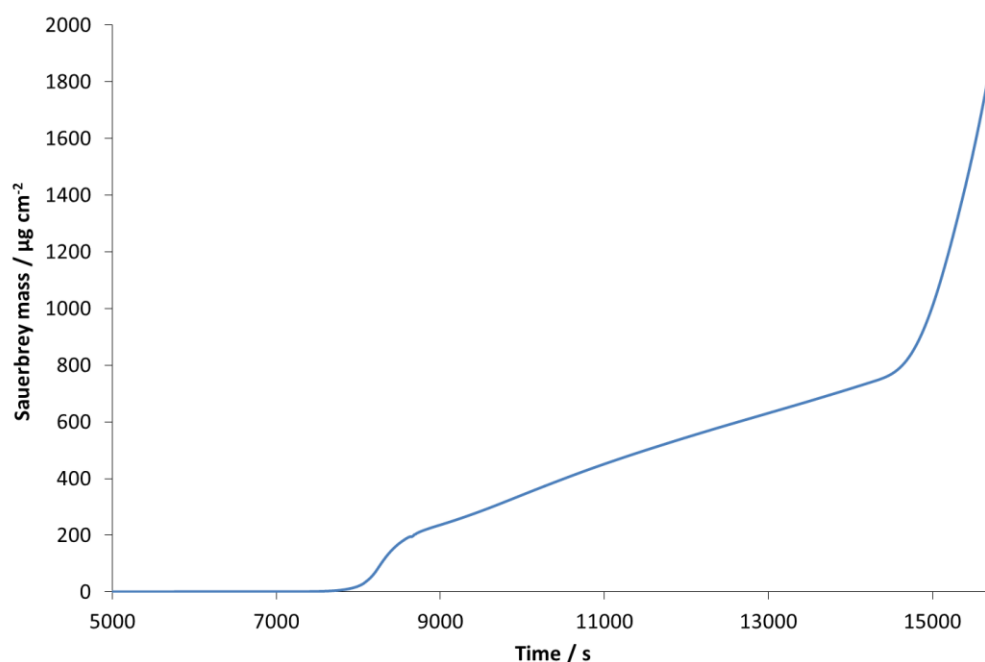
Figure 49. Graph showing the deposition rate of MA as a change in Sauerbrey mass over time, measured by the QCM. The graph shows three different deposition rates that were altered by manually changing the current through the tungsten filament. The steeper the gradient, the faster the deposition.

Deposition was carried out until either all the sample in the crucible had sublimed or the deposition was stopped due to time restrictions as the apparatus could not be operated overnight. The deposition time in most experiments was 3 – 4 hours.

Procedure following deposition. After the deposition experiment was stopped, the evaporation source was turned off and left to cool. The vacuum chamber was then vented before the deposition plate was removed. The sublimed product was scraped off the surface (Figure 50) and either loaded immediately into a PXRD capillary or stored in a sample vial for analysis.
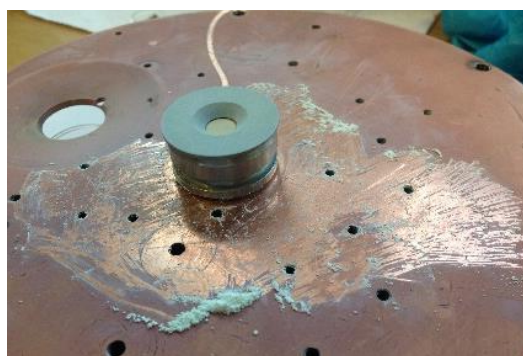
Figure 50. Scraping the sublimed product off the deposition plate around the QCM in the centre.

118

5.3.2   Results

Both MA and TA were studied with the apparatus described in section 5.3.1, with both the original evaporation source (temperature unknown) and then with the evaporation source where the temperature could be controlled. Results of the deposition experiments show that MA and TA behave differently from one another when deposited onto different surfaces at different deposition rates.

5.3.2.1   Tolfenamic Acid – New Polymorph (form VII)

The majority of the work with TA was carried out using the original evaporation source where the temperature of the crucible holding the commercial TA to be sublimed was unknown. The results show that a new form of TA was obtained. Furthermore, the deposition rate (as monitored by the QCM, but not quantified) affected the phase purity of TA deposited onto both copper and glass surfaces. Perhaps not unsurprisingly, the slower the deposition, the more phase pure the deposited product.

5.3.2.1.1   Powder X-ray Diffraction

Figure 51 shows the PXRD patterns of both commercial TA and the product from vapour deposition under vacuum onto the copper surface. The PXRD pattern of the deposited TA is different to the starting material (commercial TA, form I). Figure 52 shows the simulated PXRD patterns of the known forms of TA from single crystal data from the CSD (forms I – V) and this work (form VI). Comparisons of the PXRD patterns in Figure 51 and Figure 52 suggests that a new form of TA has been obtained. ^{1}H NMR spectroscopy confirmed that the TA had not decomposed and the sublimed product was pure TA (see section 5.3.2.1.2 on page 124 for additional information).

The PXRD pattern of deposited TA could not be initially indexed which suggested that phase impurities may be present in the deposited product. Therefore, the deposition experiment was repeated multiple times to try and obtain a phase pure product through slower deposition which was monitored by the QCM.

Figure 53 shows how multiple PXRD patterns were compared in order to differentiate between peaks that were due to the deposited TA and peaks that were due to a phase impurity in the sample. The relative intensity of some peaks change with variation of the deposition rate and other peaks disappear which indicates that they could be due to phase impurity. Diffraction peaks that were consistently present were assigned to the new form of TA. The arrows in Figure 53 indicate the regions in the PXRD spectra that showed the most variation between samples. The bottom PXRD pattern in Figure 53 is the most phase pure and the top spectrum is the least

phase pure. The highest phase purity of TA VII can be obtained from deposition onto a copper surface with a crucible temperature of 100 °C.
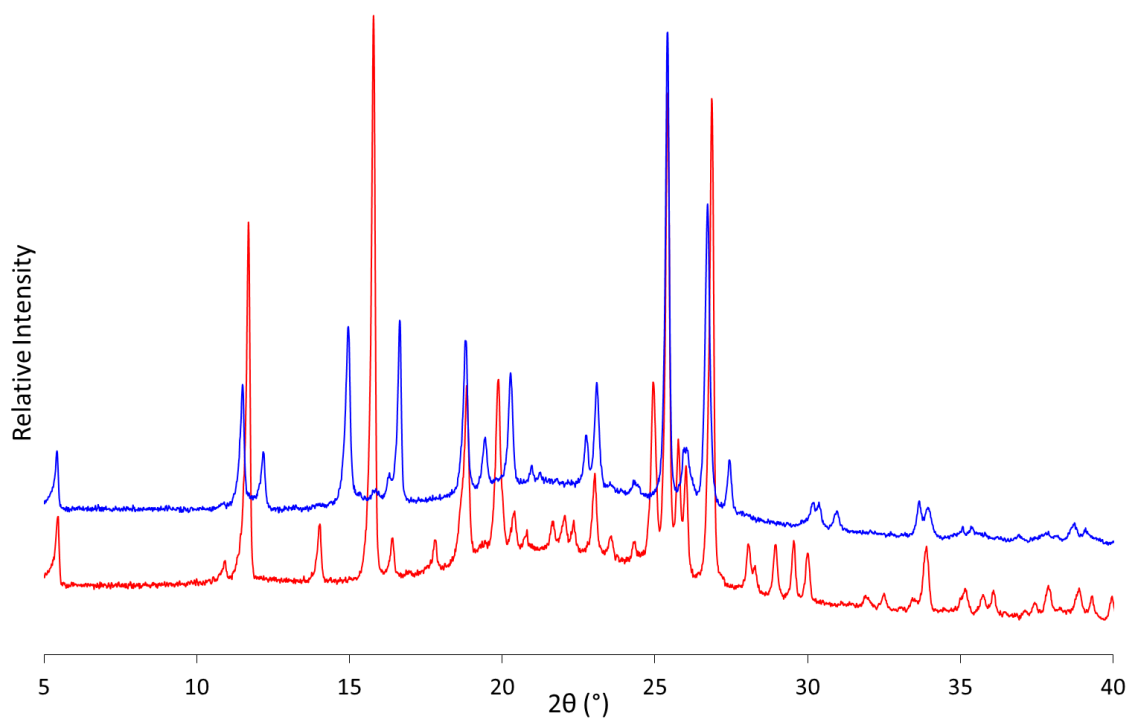
Figure 51. PXRD patterns in the range 5 – 40 2θ (°) of commercial TA, form I (red) and the product of vapour deposition of TA onto a copper surface held at room temperature (blue).
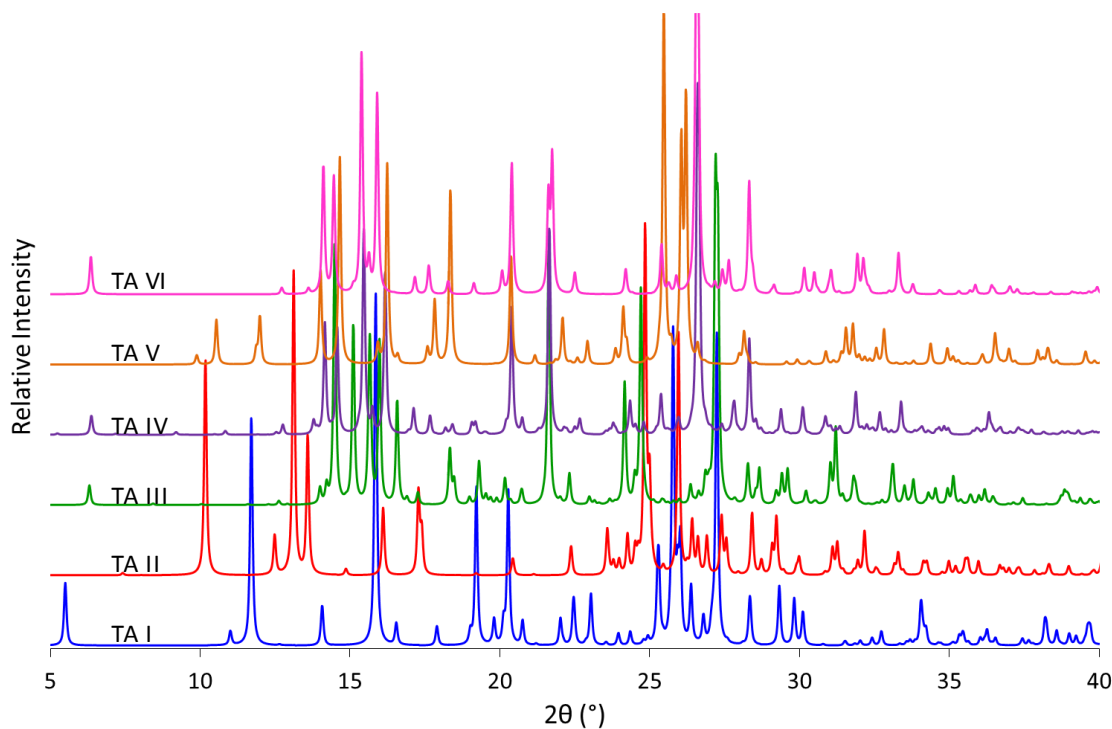
Figure 52. Simulated PXRD patterns of the five previously known polymorphs of TA from single crystal data stored in the CSD as well as TA VI from this work.
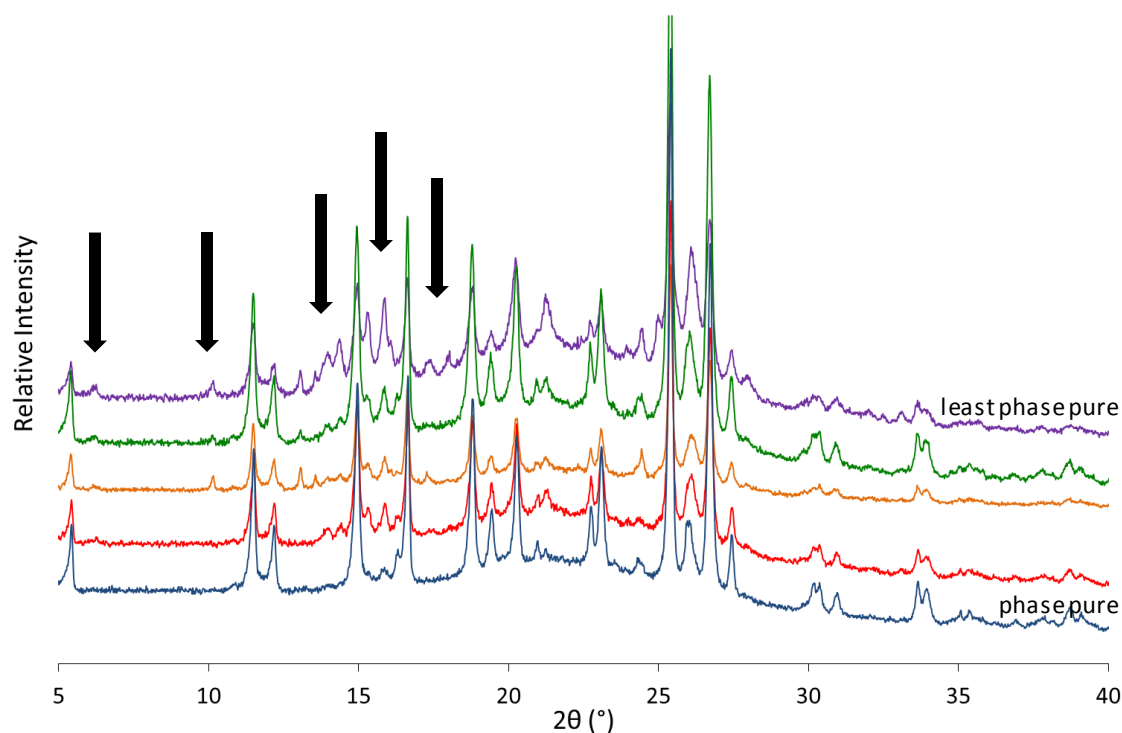
Figure 53. PXRD patterns of multiple depositions of TA onto the copper surface. Some areas of discrepancy (suggesting phase impurity) between the spectra are highlighted by the black arrows. The phase purity, identified by analysis of the PXRD patterns, decreases from the bottom spectrum to the top spectrum.

The PXRD pattern of the most phase pure sample was indexed, by Jeremy Cockcroft and Martin Vickers, and gave the crystal structure of the new polymorph of TA, now referred to as TA form VII.
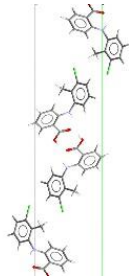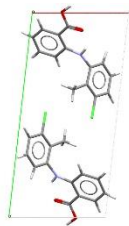
Crystallographic data for TA form VII is reported in Table 24. TA form VII belongs to the P-1 space group with one molecule in the symmetric unit. TA form VII consists of the $R_2^2(8)$ carboxylic acid dimers that are common amongst the fenamate crystal structures.

Crystal structure similarity calculations show that TA forms I and VII have a 13 molecule coordination sphere overlay with an $rmsd_{13}$ value of 0.145 Å. Figure 55 depicts the similarity in packings of the crystal structures of TA form I and TA form VII which consists of the same double layer of molecules of $R_2^2(8)$ carboxylic acid dimers, but differs in the stacking of the double layers. The conformations of TA in forms I and VII are similar, $rmsd_1 = 0.1243$ Å (Figure 54). The ξ_1 torsion angle of TA form VII is 85.91 ° compared to 74.95 ° in TA form I.

Figure 54. Molecular overlay of TA in forms I (coloured by element) and VII (orange), $rmsd_1 = 0.1243$ Å.

121

Table 24. Crystallographic data of TA form VII (this work) and TA form I.

Polymorph	I	VII[This work]
Unit Cell Diagram	(Viewed along a-axis)	(Viewed along c-axis)
Crystal System	monoclinic	triclinic
Space Group	P2$_1$/c	P-1
Temperature (K)	110	298
a (Å)	4.826(2)	8.00353
b (Å)	32.128(1)	16.48600
c (Å)	8.041(4)	4.84067
α (°)	90	95.720
β (°)	104.88(3)	105.246
γ (°)	90	94.754
Z	4	2
Z'	1	1
Cell Volume (Å^3)	1204.95	609.189
R-Factor	0.052	

TA form I   double layer   TA form VII
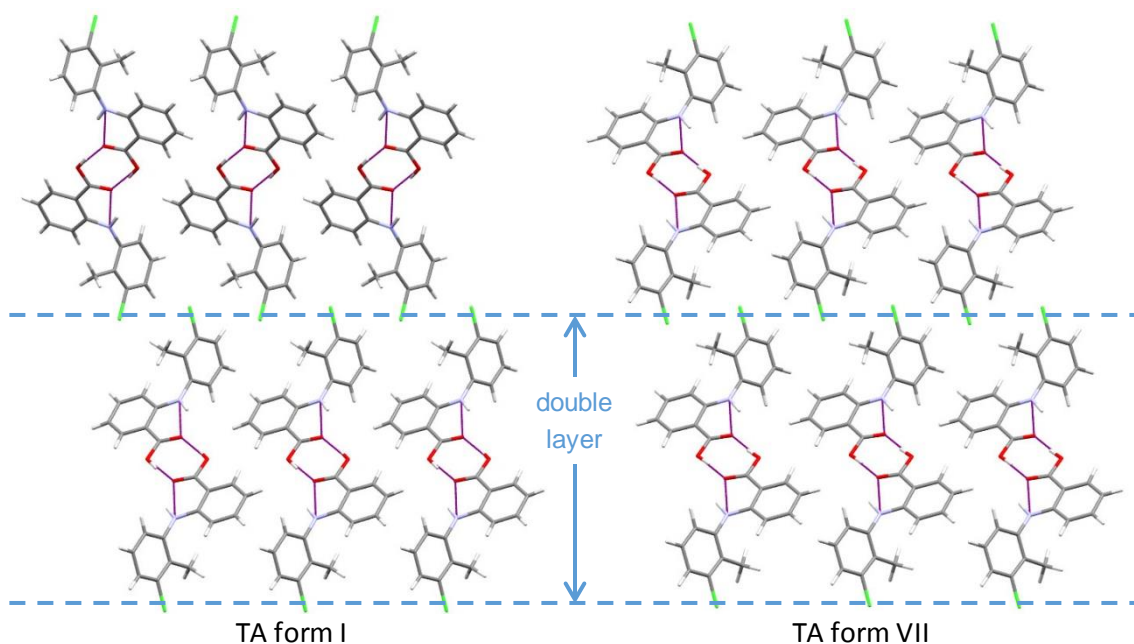
Figure 55. Diagram showing that TA form I and TA form VII differ in the packing of the same double layer of hydrogen bonded dimers.

122

Deposition of TA onto a glass surface was also investigated. PXRD patterns of experiments where TA was deposited simultaneously onto both copper and glass surfaces are shown in Figure 56. Although Figure 56 shows that the surface does not influence the polymorphic form of deposited TA under the current experimental conditions, the results suggest that deposition onto a glass surface negatively affects the phase purity of the product.
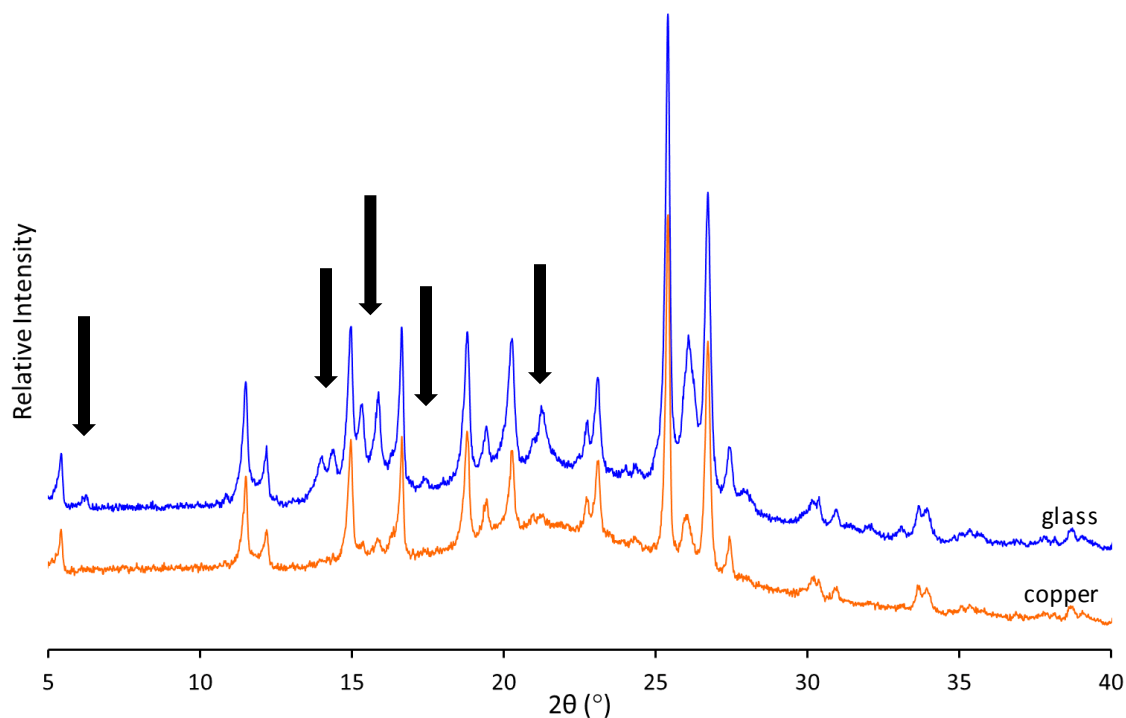
Figure 56. PXRD patterns of TA that has been deposited onto both glass and copper surfaces simultaneously. Some areas of discrepancy (suggesting phase impurity) between the spectra are highlighted by the black arrows.

To check that the TA had not decomposed upon heating in the crucible, the ^{1}H NMR spectra of commercial TA and of the TA form VII from the copper surface were collected. The ^{1}H NMR spectra are displayed in Figure 57 which show that the deposited product is the same as commercial TA, thus confirming decomposition upon heating had not occurred. In addition, the ^{1}H NMR spectrum of deposited TA does not indicate that there is evidence of any molecular impurities.
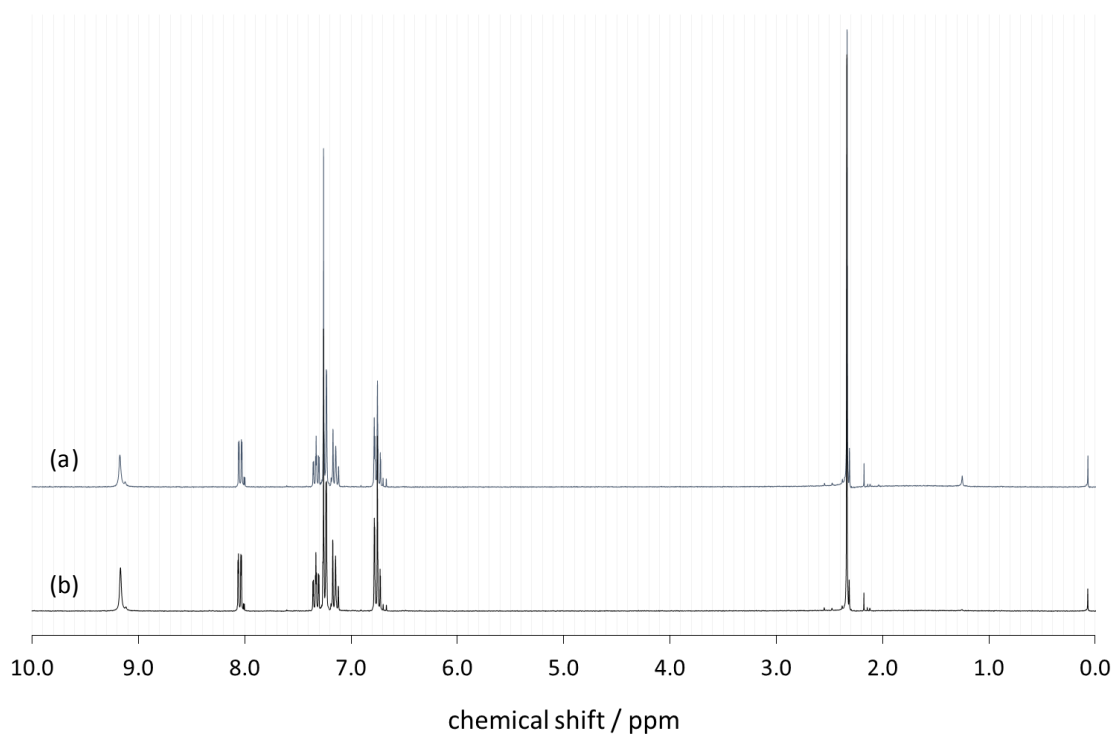
Figure 57. ^{1}H NMR spectra of (a) commercial TA and (b) TA deposited onto a copper surface.

Infrared spectra were collected from a number of samples of TA VII from deposition onto both copper and glass surfaces. The position of the N-H stretching peak of TA can be used to determine the polymorphic form.[106, 117] Figure 58 shows the position of the N-H stretching peak of TA that was deposited onto both copper and glass alongside the N-H stretching peak of TA form I (3339 cm^{-1}) and TA form II (3323 cm^{-1}) collected previously in this work. The N-H stretching peak for TA VII appears at 3336 cm^{-1} which is similar, but different, to that of TA form I at 3339 cm^{-1}. As the position of the N-H stretching peak changes depending on the conformation of the TA molecule in the different polymorphs,[106] the fact that the N-H stretching peak for TA form I and TA form VII occur at similar wavenumbers suggests that the conformation of TA in the two polymorphs would be similar, in agreement with the observations from the PXRD data. The molecular overlays of TA molecules in forms I and VII are shown in Figure 54 which confirms a high level of conformational similarity.

The infrared spectra of TA VII appear to have a shoulder peak towards lower wavenumbers. The suggestion that the presence of the shoulder peak could be due to TA form II can be ruled out from analysis of the PXRD data. The shoulder peak is present in all preparations of TA form VII (see Appendix 11 on page 211).
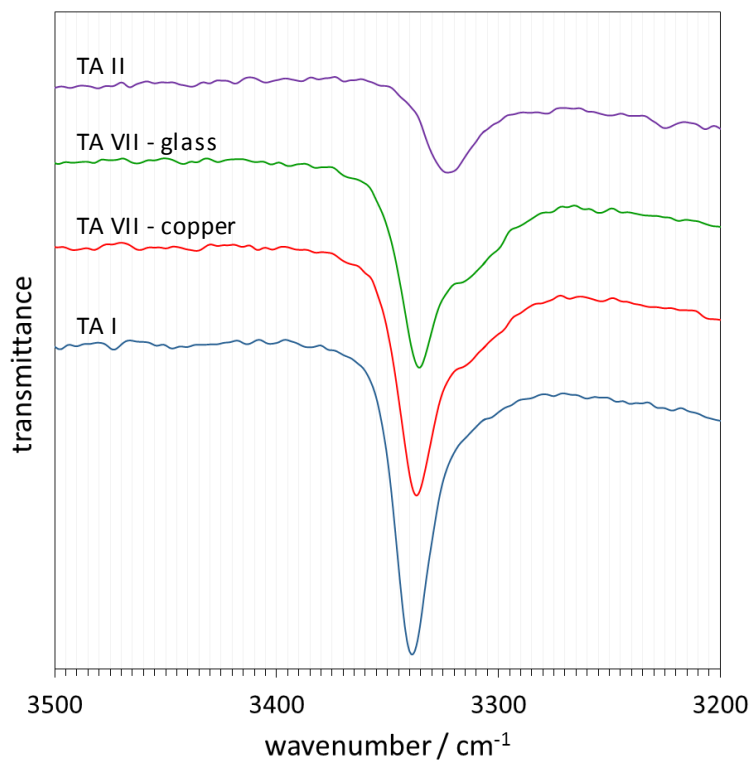
Figure 58. Infrared spectra of TA showing the position of the N-H stretching peak of TA form VII that has been deposited onto glass and copper surfaces alongside TA form I and TA form II.

A series of DSC experiments using heating rates of 10 °C min^{-1} and 100 °C min^{-1} in the range 0 – 250 °C were carried out on different preparations of TA form VII. DSC scans in the region 10 – 210 °C are shown in Figure 59 and Figure 60 for heating rates of 10 °C min^{-1} and 100 °C min^{-1} respectively. The sample of TA VII with the highest phase purity (evaporation source set to 100 °C and deposition onto copper) as identified from the PXRD data is indicated in the figures.

Figure 59 shows evidence of an exothermic phase transition around 125 – 133 °C. Similarly, Figure 60 shows evidence of an exothermic phase transition around 144 – 157 °C. Increasing the heating rate, from 10 °C min^{-1} to 100 °C min^{-1}, has the effect of raising the onset temperature at which the exothermic phase transition of TA VII occurs. The DSC data does not provide any further evidence to understand what is occurring during the exothermic phase transition. The phase transition is followed by a melting endotherm as shown in Figure 61.
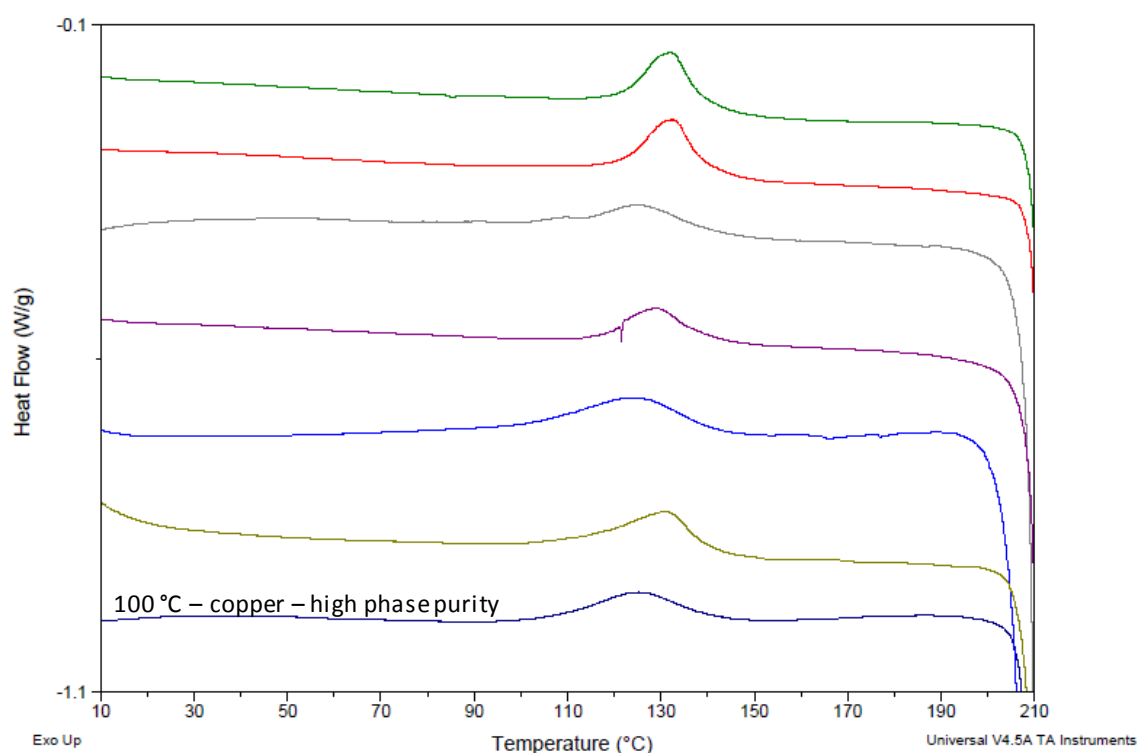
Figure 59. DSC scans of multiple preparations of TA VII at a heating rate of 10 °C min^{-1} in the range 10 – 210 °C.

Figure 61 shows the DSC scans of four different preparations of TA form VII deposited onto copper in the region 120 – 230 °C at a heating rate of 100 °C min^{-1}. Following the exothermic phase transition, the most phase pure sample, shown by the green line in Figure 61, has a single melting endotherm at 213.65 °C. Although the temperature of this melting endotherm is the same as that of TA form I,[32] DSC results alone cannot confirm that the deposited TA has

transformed to TA form I. However, further analysis of the samples, using simultaneous DSC-XRD (as discussed in section 5.3.2.1.6) confirms that TA VII transforms to TA form I upon heating and that the sample contains pure TA form I before melting at 213 °C.
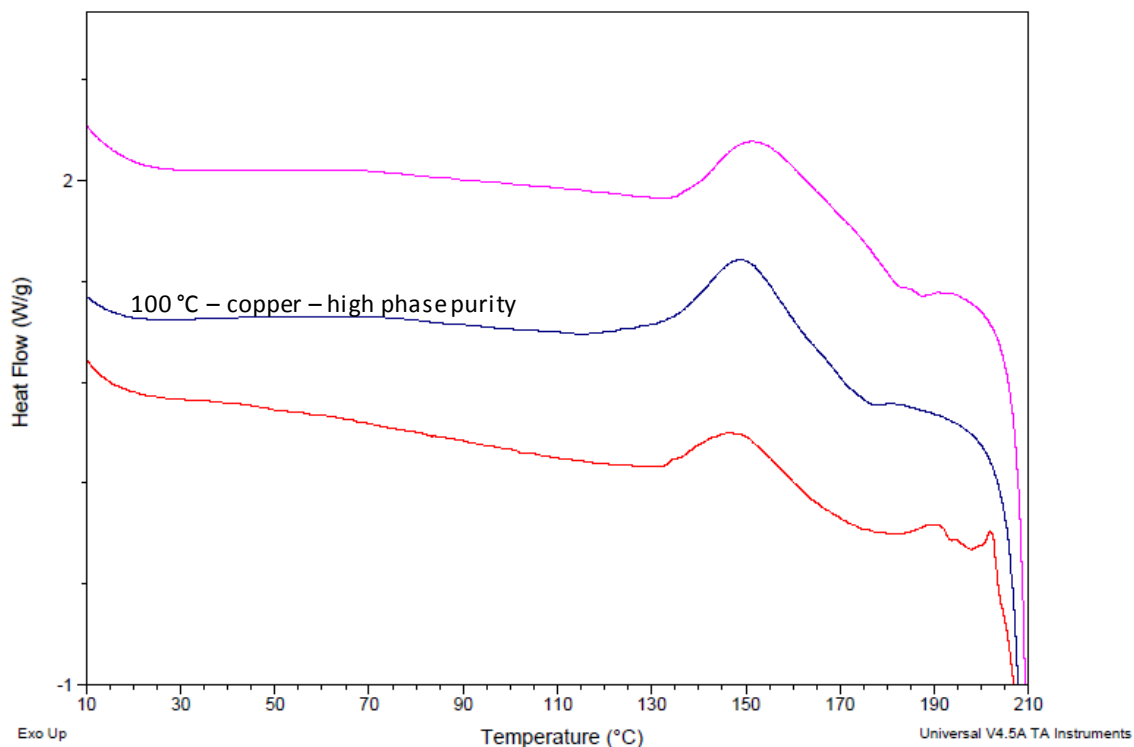
Figure 60. DSC scans of three preparations of TA VII at a heating rate of 100 °C min⁻¹ in the range 10 – 210 °C.
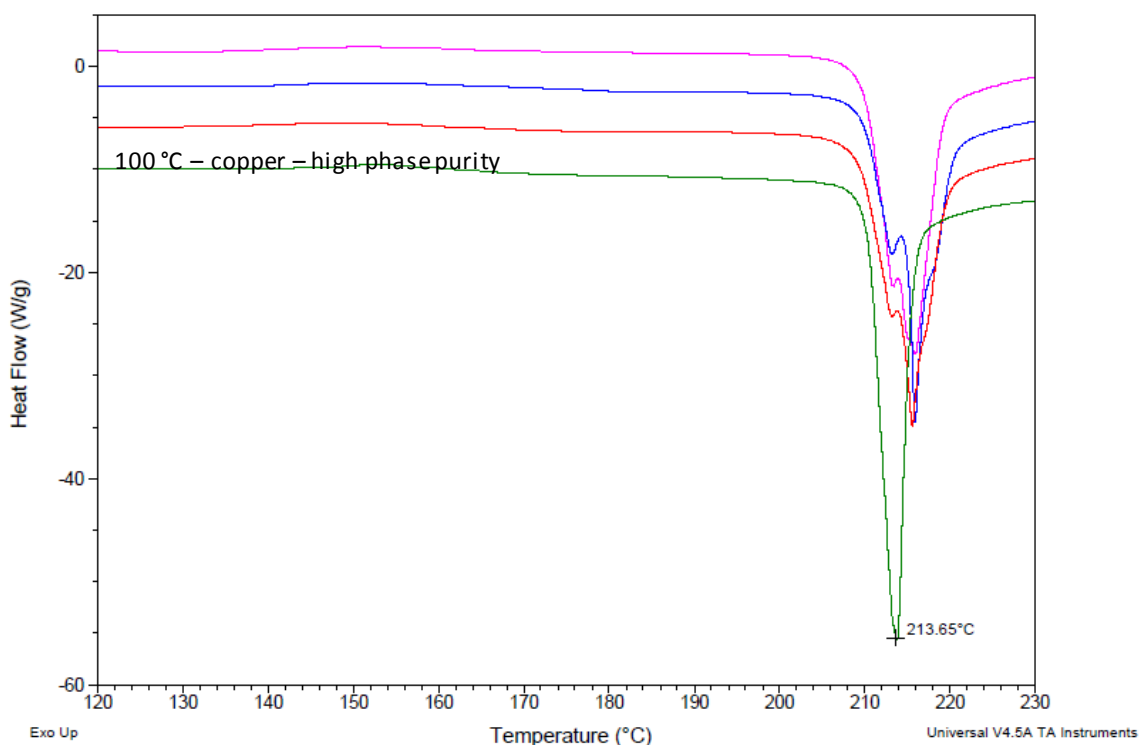
Figure 61. DSC scans at a heating rate of 100 °C min⁻¹ in the region 120 – 230 °C of four different preparations of TA VII on a copper surface including a phase pure sample prepared with a crucible temperature of 100 °C (green) and three other preparations where the temperature of the evaporation source was unknown.

The DSC thermograms of samples of TA form VII containing phase impurities, as identified from PXRD data, also indicate that the samples are not phase pure as there are two peaks in the melting endotherm (Figure 61). The double peak in the melting endotherm is not evident at a heating rate of 10 °C min^{-1} (Figure 62) suggesting that the whole sample of deposited TA has time to transform to the same form at a slower heating rate. The temperature of the melting endotherms when the samples is heated at 10 °C min^{-1} is again consistent with TA form I.

The DSC thermograms confirm that the most phase pure sample of TA VII is produced when the evaporation source temperature is 100 °C and the TA is deposited onto the copper surface which is shown by the single melting endotherm in Figure 61. The DSC data is consistent with the PXRD patterns already discussed in section 5.3.2.1.1 which indicated that the most phase pure sample of TA VII was produced with a crucible temperature of 100 °C when deposited onto copper.
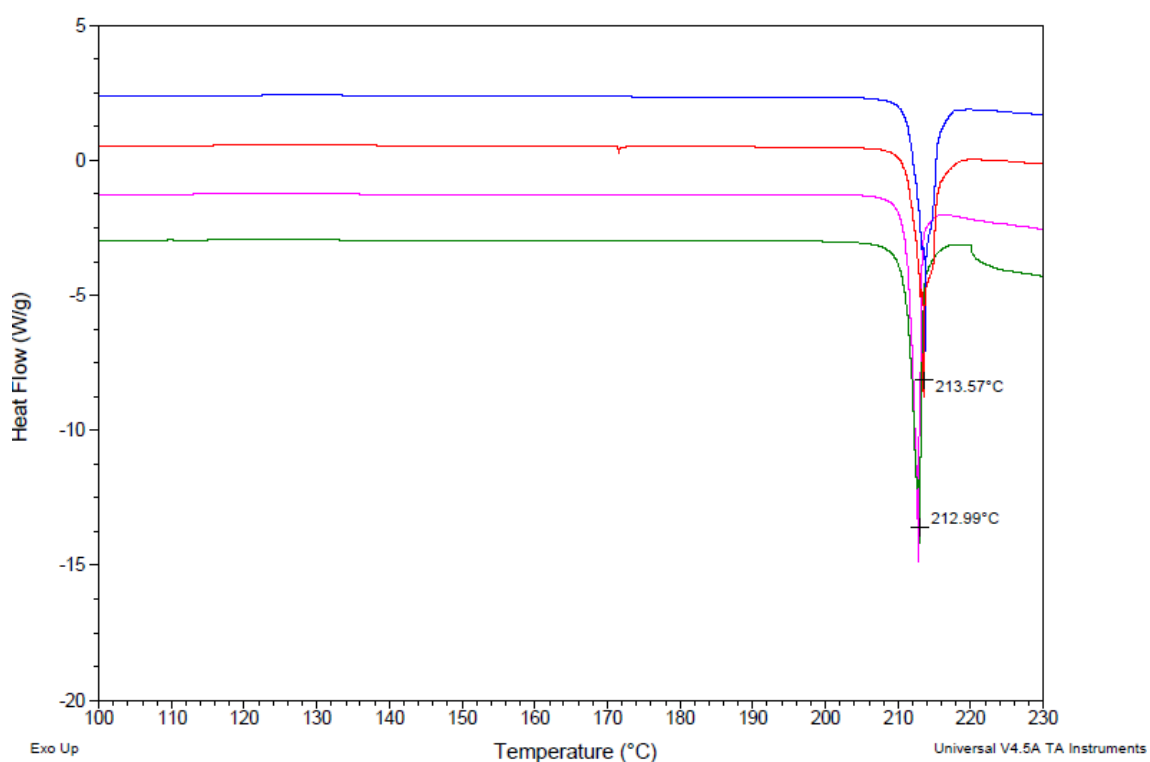
Figure 62. DSC scans at a heating rate of 10 °C min^{-1} in the region 120 – 230 °C of four different preparations of TA deposited onto a copper surface. The temperature of the evaporation source for all preparations is unknown.

5.3.2.1.5   Raman Spectroscopy

Raman spectra were collected for a number of preparations of TA VII and compared to the spectrum of TA form I. The Raman spectra are shown in Figure 63 which shows that there are small variations in the peak positions between TA VII and TA form I. The most noticeable differences between the Raman spectra of TA form I and TA form VII are the absence of a peak at 480 cm^{-1} and the appearance of an additional peak at 606 cm^{-1} in the spectrum of TA form VII.
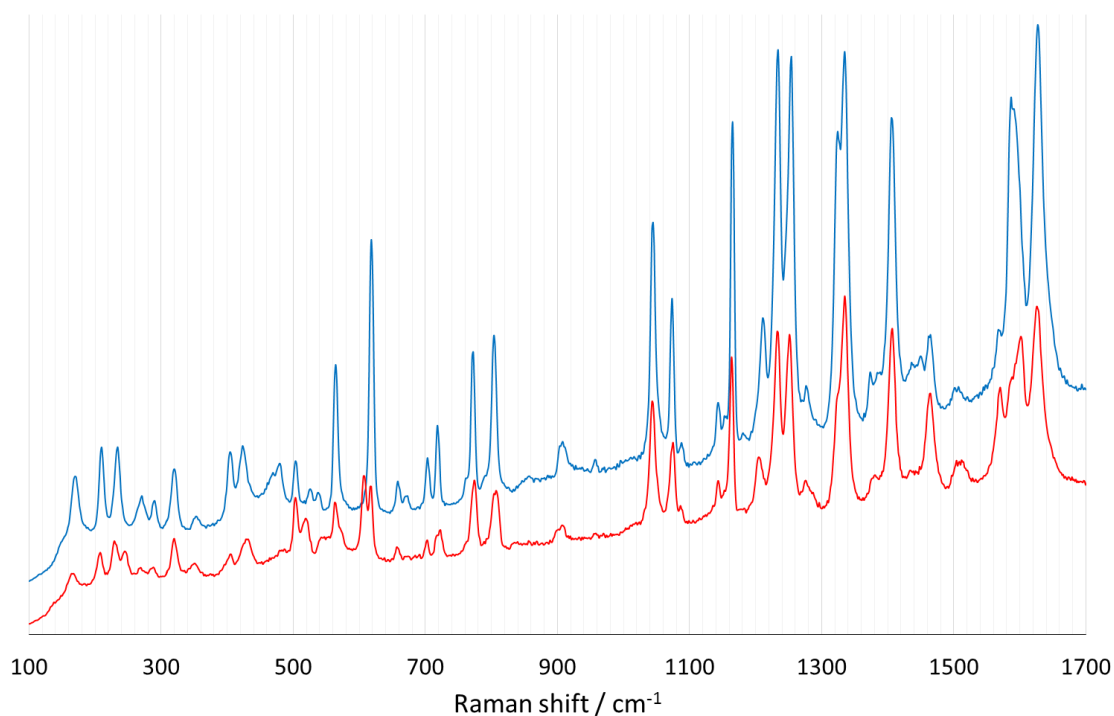
Figure 63. Raman spectra of TA form I (blue) alongside TA form VII (red).

5.3.2.1.6   Simultaneous DSC-Synchrotron X-ray Diffraction

Simultaneous DSC-synchrotron X-ray diffraction (DSC-XRD) experiments were carried out to provide information on the phase transition of TA form VII as identified by DSC in section 5.3.2.1.4. The DSC-XRD experiments were carried out by Asma Buanz, Alex Clout and Simon Gaisford and were performed on Beamline I12 of the Diamond Light Source, U.K.[176] Samples of TA form VII were heated at rates of 10 °C min^{-1} and 2 °C min^{-1} in a DSC and PXRD patterns were simultaneously collected.

The PXRD pattern of TA form I does not change upon heating although Figure 64 shows that, as expected, the reflections shift to a lower angle as the unit cell expands with increasing temperature. The relative intensity of the peaks increase slightly with temperature and the PXRD patterns show small variations as the sample approaches the temperature of the melting endotherm which occurs at around 213.5 °C.
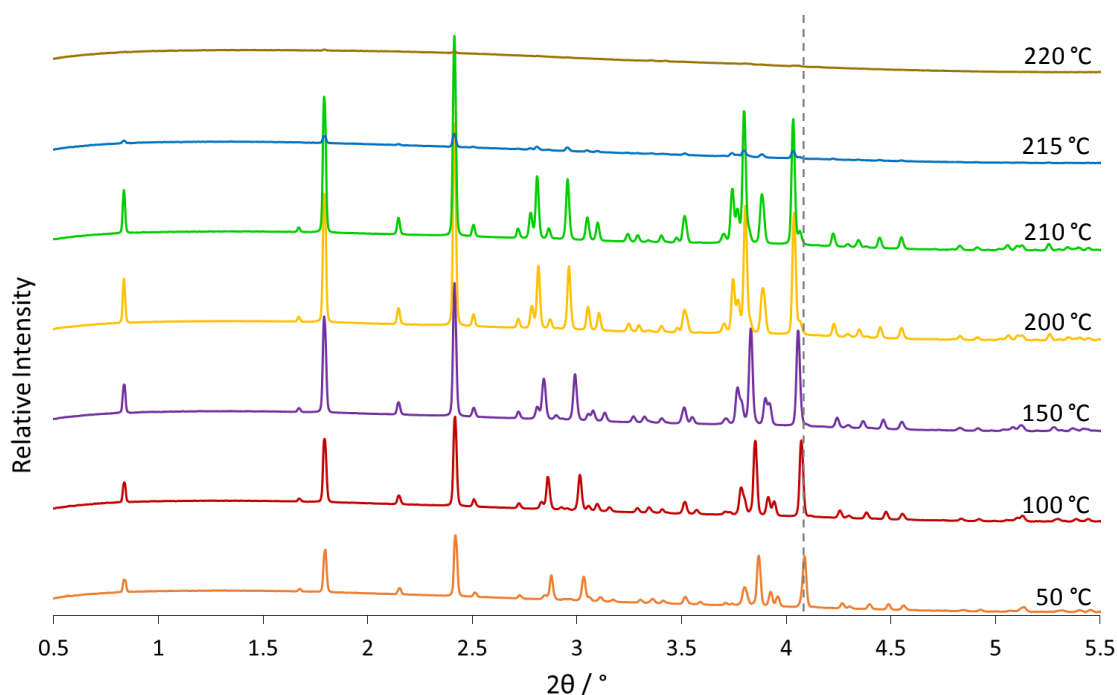
Figure 64. PXRD patterns of TA I collected *in situ* as the sample is heated at a rate of 10 °C min⁻¹.

In comparison to TA form I, the 2D graphs in Figure 65 show that the PXRD patterns of TA form VII change with increasing temperature (around scan number 80 for 10 °C min⁻¹ and around scan number 400 for 2 °C min⁻¹). The change in the PXRD pattern for TA form VII occurs at the same temperature at which the DSC thermograms (Figure 66) show an exothermic phase transition (132 °C for 10 °C min⁻¹ and 119 °C for 2 °C min⁻¹).

The changes observed in the diffraction pattern of TA VII upon heating at a rate of 10 °C min⁻¹ are depicted in Figure 67. The PXRD patterns were collected *in situ* as the sample was heated in the DSC. The corresponding DSC data, as shown by the blue line in Figure 66, indicates the presence of an exothermic phase transition at 132 °C which has previously been discussed in section 5.3.2.1.4. The diffraction data in Figure 67 indicates that the sample begins to transform at around 120 °C and has completed by 135 °C. The main changes in the PXRD patterns are the disappearance of diffraction peaks at 1.73, 1.88, 2.32, 2.56, 3.20, 4.00 and 4.16 ° 2θ and the appearance/increase in intensity of diffraction peaks at 1.79, 2.15, 2.41, 2.73, 2.99, 3.13, 3.76, 4.25, 4.30, 4.36 and 4.47 ° 2θ.

Figure 68 shows the diffraction patterns of TA form VII as the sample is heated at 2 °C min⁻¹. The corresponding DSC data, shown by the red line in Figure 66, indicates the phase transition occurs at around 119 °C which is confirmed by the PXRD data that indicate that the transition begins at around 105 °C and has completed by 130 °C.

130

TA VII (sample 1)

10 °C min^{-1} · · · · · · · · · · 2 °C min^{-1}

TA VII (sample 2)

10 °C min^{-1} · · · · · · · · · · 2 °C min^{-1}
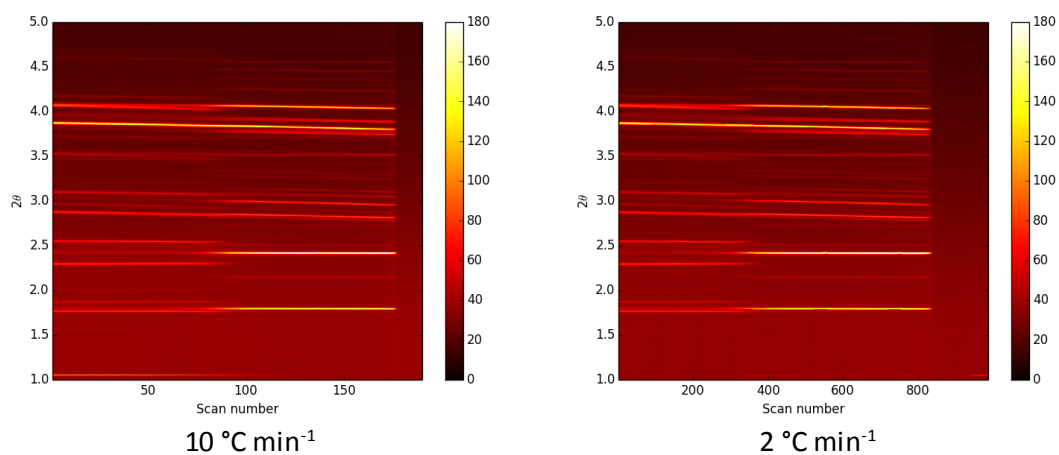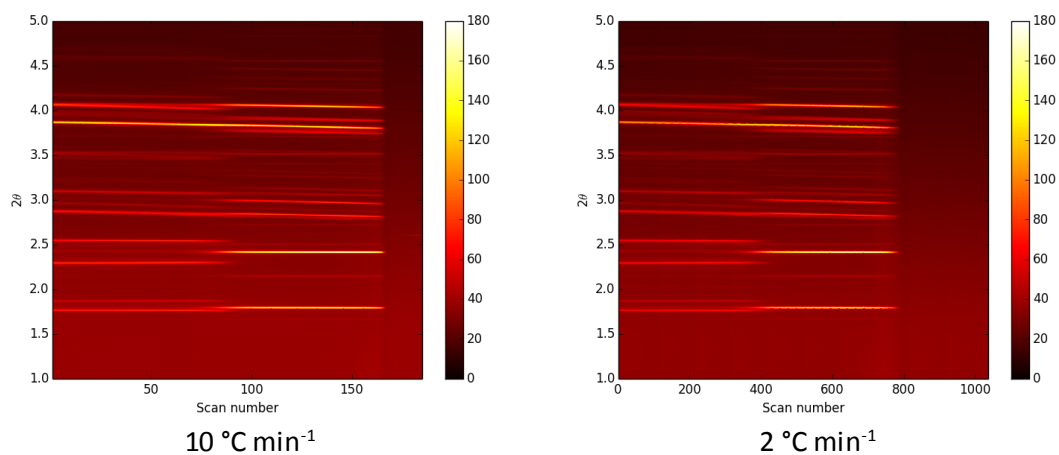
TA I (commercial material)

10 °C min^{-1}
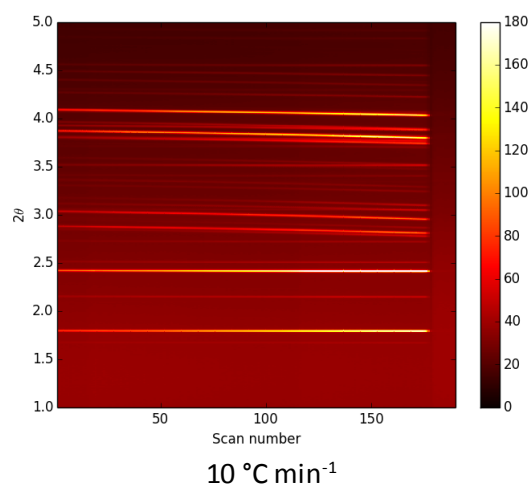
Figure 65. 2D graphs produced by Alex Clout showing the PXRD patterns of TA VII and TA I as the samples are heated. The increasing scan number relates to an increase in temperature. The colours of the lines reflect the intensity of the peaks.
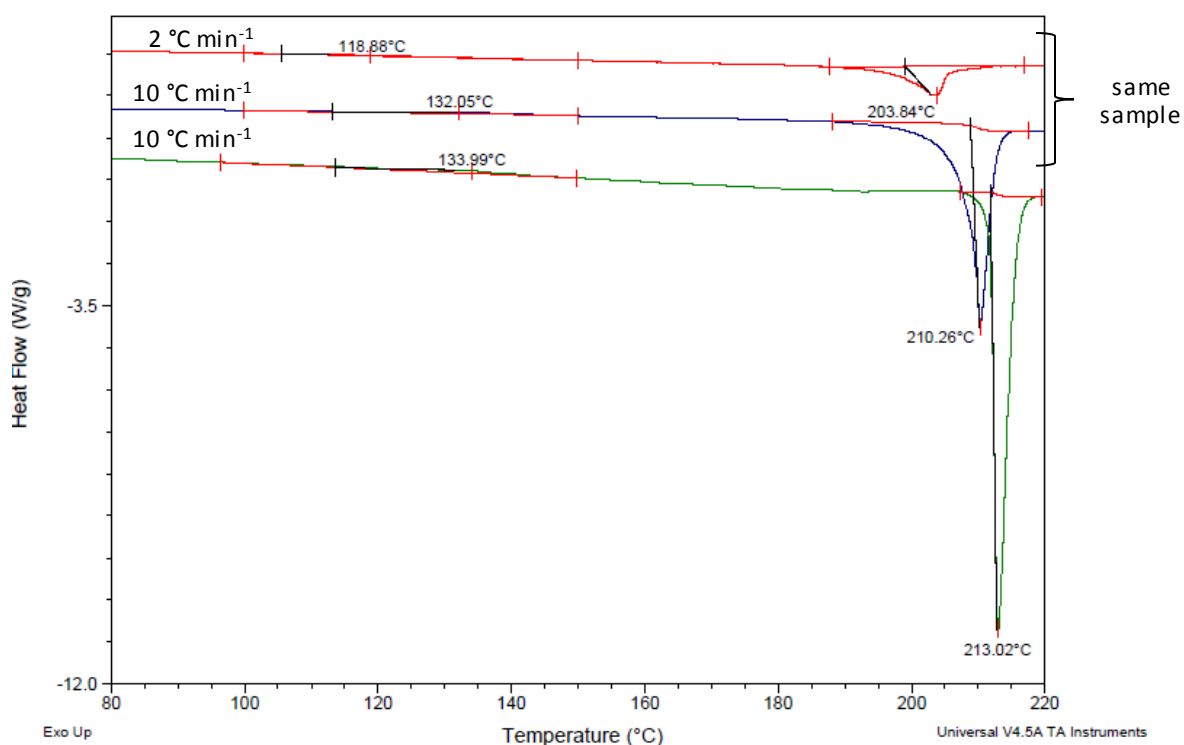
Figure 66. DSC scans of TA VII from the simultaneous DSC-XRD experiments performed at Diamond with heating rates of 10 °C min⁻¹ (blue and green) and 2 °C min⁻¹ (red). The temperatures of the exothermic phase transitions, that are dependant on heating rate, are highlighted.

Analysis of the PXRD patterns confirms that TA form VII transforms to TA form I upon heating above the exothermic phase transition temperature for the relevant heating rate. The subsequent melting endotherm is that of TA form I. Appendix 12 on page 212 depicts the PXRD data for a second sample of TA form VII which again shows that the phase transformation begins at around 120 °C and has completed by 135 °C. The corresponding DSC data is shown by the green line in Figure 66.

Increasing the heating rate has the effect of raising the temperature of the phase transition of TA form VII to TA form I from 119 °C at a heating rate of 2 °C min⁻¹ to 132 - 134 °C at a heating rate of 10 °C min⁻¹ (Figure 66). This change in transformation temperature was previously identified in section 5.3.2.1.4 in relation to heating rates of 10 °C min⁻¹ and 100 °C min⁻¹. The temperature of the melting endotherm of TA form I appears to vary depending on the sample and the heating rate. The melting endotherm of the same sample increases from 203.5 °C at a heating rate of 2 °C min⁻¹ to 210.3 °C at a heating rate of 10 °C min⁻¹.

The simultaneous DSC-XRD experiments were carried out around six months after the preparation of some samples of TA VII. The DSC-XRD experiments confirmed the samples were still TA form VII showing that it is stable under ambient storage conditions for up to six months.
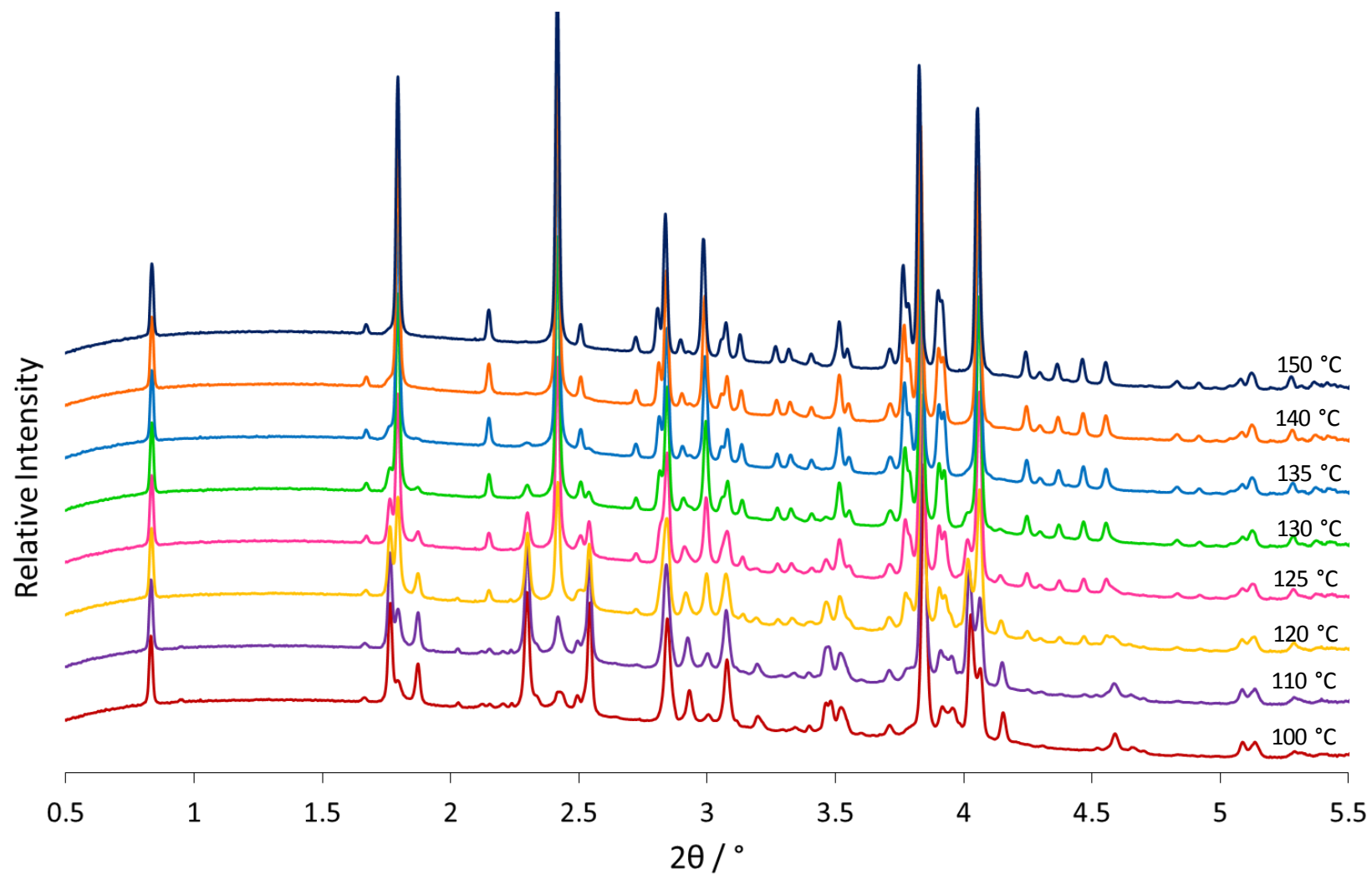
Figure 67. PXRD patterns of TA VII collected *in situ* as the sample is heated at a heating rate of 10 °C min⁻¹.
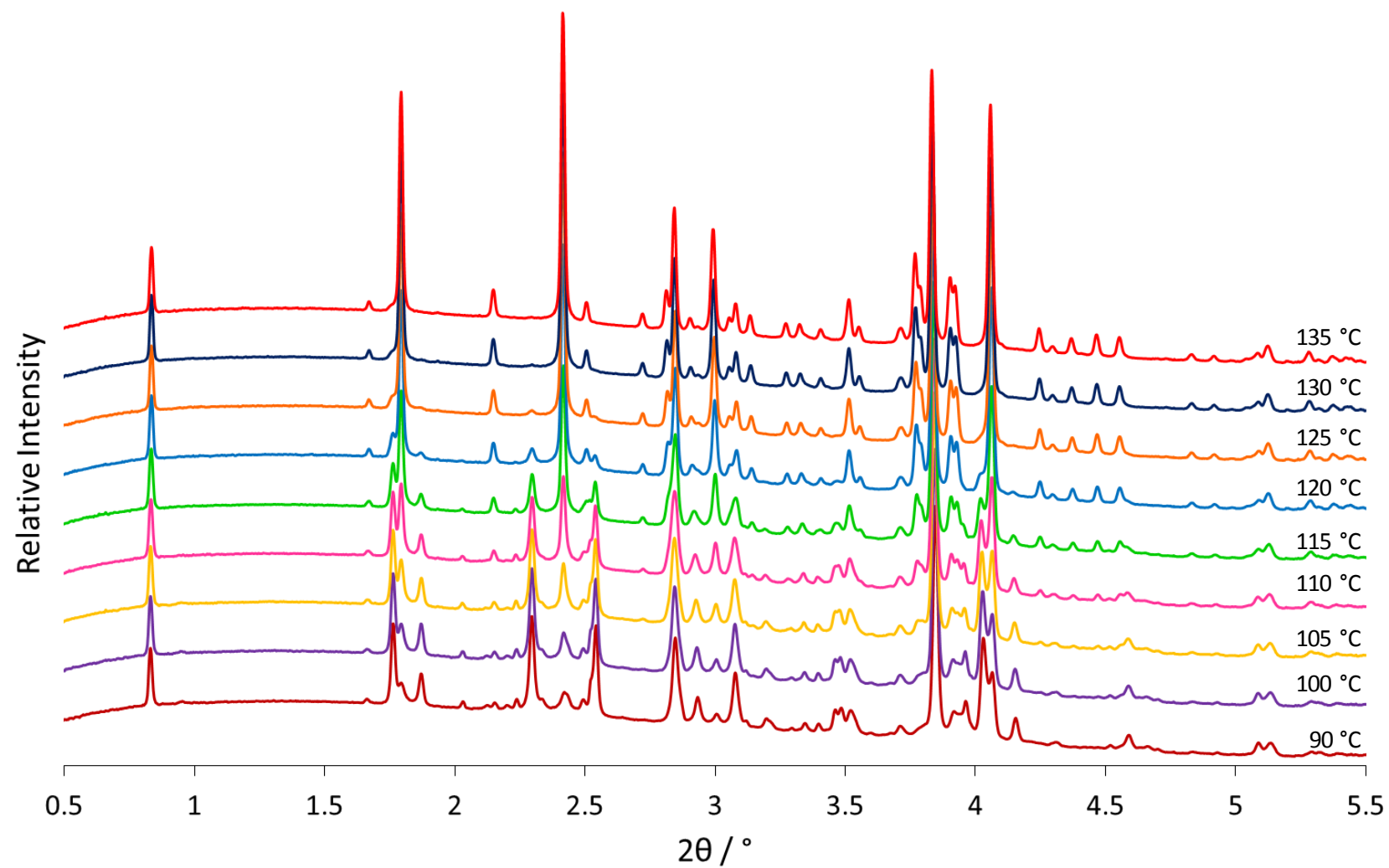
Figure 68. PXRD patterns of TA VII collected *in situ* as the sample is heated at a heating rate of 2 °C min⁻¹.

Using the Crystal Structure Similarity[67] module in Mercury,[181] the crystal structure of TA form VII was compared to the known crystal structures of other fenamate molecules and also to the CSP generated structures of MA from chapter 3. TA form VII is isostructural with CSP generated structure #5MA_510, $rmsd_{15}$ = 0.505 Å, as shown in Figure 70. TA form VII is also isostructural with *N*-(m-Tolyl)anthranilic acid (CSD refcode: PEFNAQ, Figure 69)[182], $rmsd_{15}$ = 0.420 Å, which is to be expected as PEFNAQ and #5MA_510 are also isostructural (Table 11 on page 71).
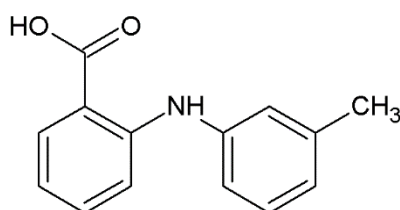
Figure 69. Structural diagram of *N*-(m-Tolyl)anthranilic acid, CSD structure PEFNAQ.

As TA form VII is isostructural to #5MA_510 and TA VII can be reliably reproduced, it is possible that it could be used as a template surface to target the nucleation of a new form of MA. Some deposition experiments, discussed later in section 5.3.2.2, have been attempted where TA VII is deposited on a glass slide and then subsequently MA is deposited on top of that layer.
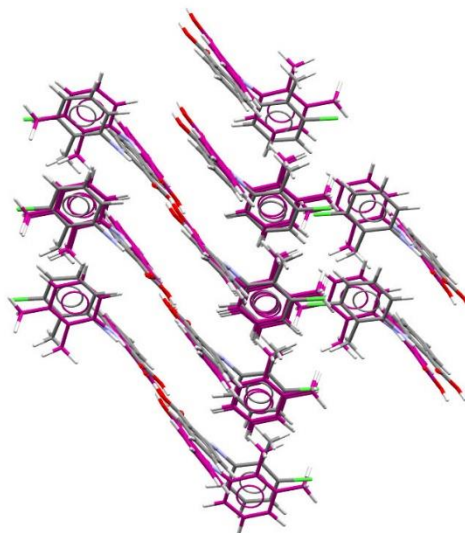
Figure 70. 15 molecule overlay of TA VII (coloured by element) with predicted structure #5MA_510 (purple) from the CSP study on MA, $rmsd_{15}$ = 0.505 Å.

5.3.2.1.8   Summary

In summary, TA form VII is readily reproduced using the bespoke sublimation/vapour deposition apparatus that was described in section 5.3.1.1. TA form VII grows on both copper and glass surfaces irrespective of the deposition rate. However, the phase purity of TA VII is a function of both the substrate and deposition rate. The use of glass and fast deposition rates reduce the phase purity of the sample.

The phase purity of TA VII can be qualitatively assessed by looking at the PXRD patterns and DSC scans. Some diffraction peaks appear to be due to a phase impurity and the absence (or a decrease in the relative intensity) of these peaks is consistent with a more phase pure sample. Additionally, a single melting endotherm in the DSC scan would suggest that the sample is phase pure. The presence of other impurities in the sample have been ruled out following analysis of ^{1}H NMR data.

The comparison of PXRD patterns of multiple preparations of TA form VII enabled the identification of peaks which were due to TA form VII and not a phase impurity. This led to the determination of the crystal structure from the PXRD pattern. The crystal structure of TA form VII is related to the crystal structure of TA form I as the molecules have a similar conformation and the same double layer of molecules consisting of $R_2^2(8)$ carboxylic acid dimers. However, TA forms I and VII differ in the stacking of the double layers of molecules.

Comparison of the crystal structure of TA form VII with crystal structures of known fenamate molecules as well as CSP generated structures of MA indicated that TA form VII is isostructural to both PEFNAQ (from the CSD) as well as #5MA_510 (from the MA CSP study).

DSC data on TA form VII indicated the presence of an exothermic phase transition followed by a melting endotherm which occurred at the same temperature as the melting endotherm of TA form I. The behaviour of TA form VII upon heating was investigated further using simultaneous DSC-XRD. The PXRD patterns of TA VII (performed on Beamline I12 of Diamond Light Source synchrotron) were collected *in situ* as the sample was heated in a DSC pan. Analysis of the DSC-XRD data showed that the PXRD pattern changed as the sample reached the transition temperature, from TA form VII to match the PXRD pattern of TA form I. The DSC-XRD experiments confirmed that TA form VII transforms to TA form I upon heating and the subsequent melting endotherm corresponds to the melting of TA form I.

Infrared data shows that the N-H stretching peak for TA form VII occurs at 3336 cm^{-1}. The N-H stretching peak of TA form I occurs at 3339 cm^{-1} (this work). The similarity in position of the N-H stretching peaks could be due to the fact that the conformation of TA has been shown to affect the position of the N-H stretching peak[106] and the conformations of TA form I and TA form VII are similar.

The majority of the experiments that deposited MA were carried out using the improved methodology where the temperature of sublimation was set and monitored. In this set of experiments, the effect of the deposition rate and the role of the surface were investigated.

To investigate the effect of deposition rate, the QCM was first used to monitor the rate of deposition as the temperature of the evaporation source was slowly increased. A crucible temperature of 100 °C was chosen for the majority of deposition experiments as it was the slowest deposition rate that yielded enough product for analysis. An increased crucible temperature of 120 °C was also studied and deposition of MA was carried out simultaneously onto both copper and glass surfaces. Although the crucible temperature is known to affect the rate of deposition, with a higher temperature increasing the rate of deposition, this study has not quantified the difference in deposition rates.

The role of the surface was further investigated when MA was simultaneously deposited onto three different surfaces: copper, glass and glass covered in microcrystalline TA form VII. Microcrystalline TA VII was chosen because, as discussed in section 5.3.2.1.7, TA form VII is isostructural with the predicted structure #5MA_510 of MA and therefore could be a potential template surface from which to nucleate #5MA_510 for the first time. #MA_510 is calculated to be competitive in energy with known polymorphs of MA, see chapter 3.

Simultaneous deposition onto multiple surfaces was achieved by first depositing TA (crucible temperature set to 100 °C) onto two glass microscope slides that were incorporated into the sublimation apparatus as shown in Figure 47. The evaporation source was set to 100 °C to allow slow deposition of TA as this has been shown to give the highest phase purity of TA form VII (see section 5.3.2.1). The microscope slides were then removed and the apparatus was cleaned before one microscope slide covered in TA form VII was replaced on the deposition plate alongside a clean microscope slide. The TA that was deposited onto the glass microscope slide was confirmed to be TA form VII (with a small amount of phase impurity) from PXRD data collected on the slide that was removed from the apparatus. MA was then sublimed with the evaporation source set to 100 °C. MA was deposited simultaneously onto the copper surface, the clean microscope slide and the microscope slide that was covered in microcrystalline TA. During the simultaneous deposition of MA onto copper, glass and TA form VII, the deposition rate is constant and has not affected the polymorphic form of the product, any differences are due to the role of the surface.

The effect the deposition rate had on the deposited products of MA onto both copper and glass surfaces were analysed using PXRD. Figure 71 shows the PXRD patterns of MA forms I and II alongside products of the deposition of MA onto copper (evaporation source set to 120 °C) and glass at two different deposition rates (evaporation source set to 100 °C and 120 °C). The polymorphic form of the deposited MA can be identified by comparison of PXRD patterns with the PXRD patterns of the known polymorphs.

The PXRD data shows that MA grows as form I on the copper surface, but as form II on the glass surface if the deposition rate is slow enough. This is in line with the results of the previous sublimation experiments in section 5.2 where SCXRD data showed that MA nucleated as form II on the glass walls of the sublimation tube, but as form I on the wire.

Figure 71 shows that MA grows as form II on the glass surface at a slow deposition rate (evaporation source set to 100 °C), however, when the deposition rate is increased (evaporation source set to 120 °C), concomitant polymorphism is observed as MA grows as both form I and form II. This observation is confirmed by the presence of diffraction peaks that correspond to both form I and II in the PXRD pattern of fast deposition of MA onto glass. In comparison, the MA that was deposited onto glass at a slower rate of deposition (evaporation source set to 100 °C) appears to be a sample of phase pure form II due to the absence of peaks that correspond to MA form I.
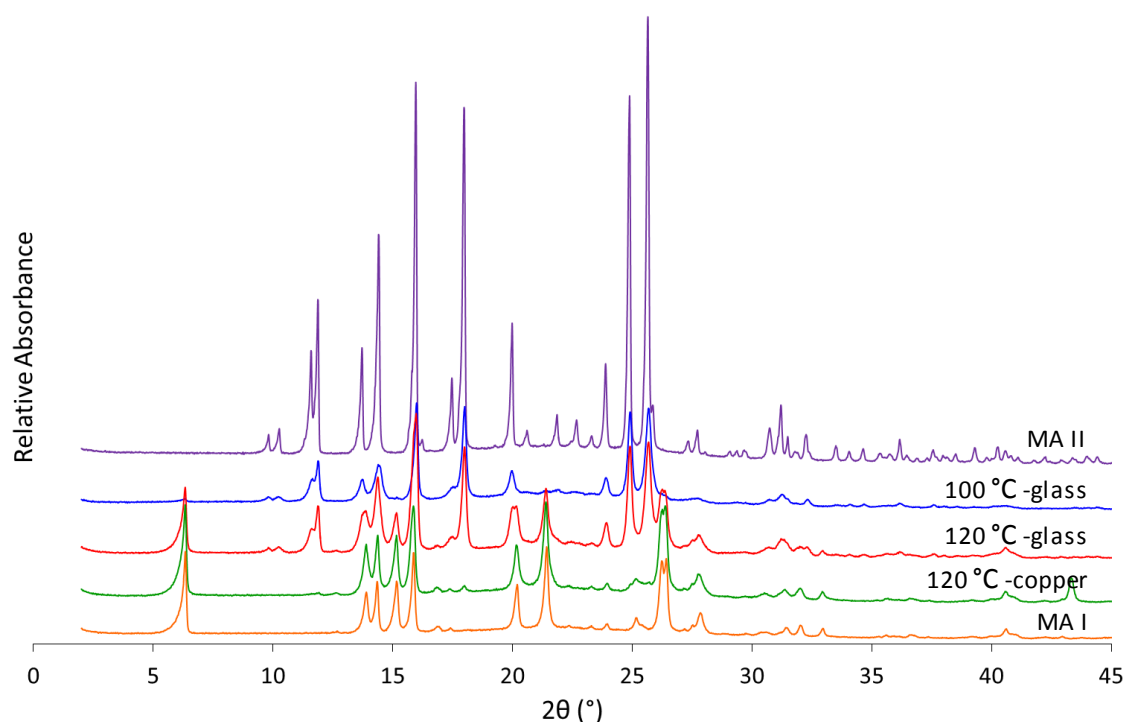
Figure 71. PXRD patterns of MA from depostion experiments alongside the PXRD patterns of MA form I and MA form II. The labels detail the temperature of the evaporation source and the surface of deposition.

Figure 71 only shows the PXRD pattern of MA deposited onto the copper surface with the evaporation source set to 120 °C. MA grows as form I on the copper surface irrespective of the deposition rate. Additional PXRD patterns are shown in Appendix 13, page 213, which show that the deposition rate does not affect the phase purity or polymorph selectivity when MA is deposited onto a copper surface.

The PXRD patterns of MA that has been simultaneously deposited onto different surfaces are shown in Figure 72 alongside PXRD data for MA form I and MA form II. The results of this set of experiments again confirm that when MA is deposited slowly onto glass, it grows as MA form II. In comparison, when MA is deposited at the same rate onto a copper surface, it grows as form I.

Additionally, when MA is deposited onto TA VII, the PXRD pattern shows weak diffraction peaks that correspond to MA form I. There is no evidence of growth of the predicted isostructural form of MA to TA VII, #5MA_510, from the CSP study in chapter 3. The poor quality of the PXRD data for MA deposited onto TA VII means the results are ambiguous with regards to the presence of TA form VII. However, the presence of TA VII in the same sample has been confirmed by infrared spectroscopy (see section 5.3.2.2.2 for more details).
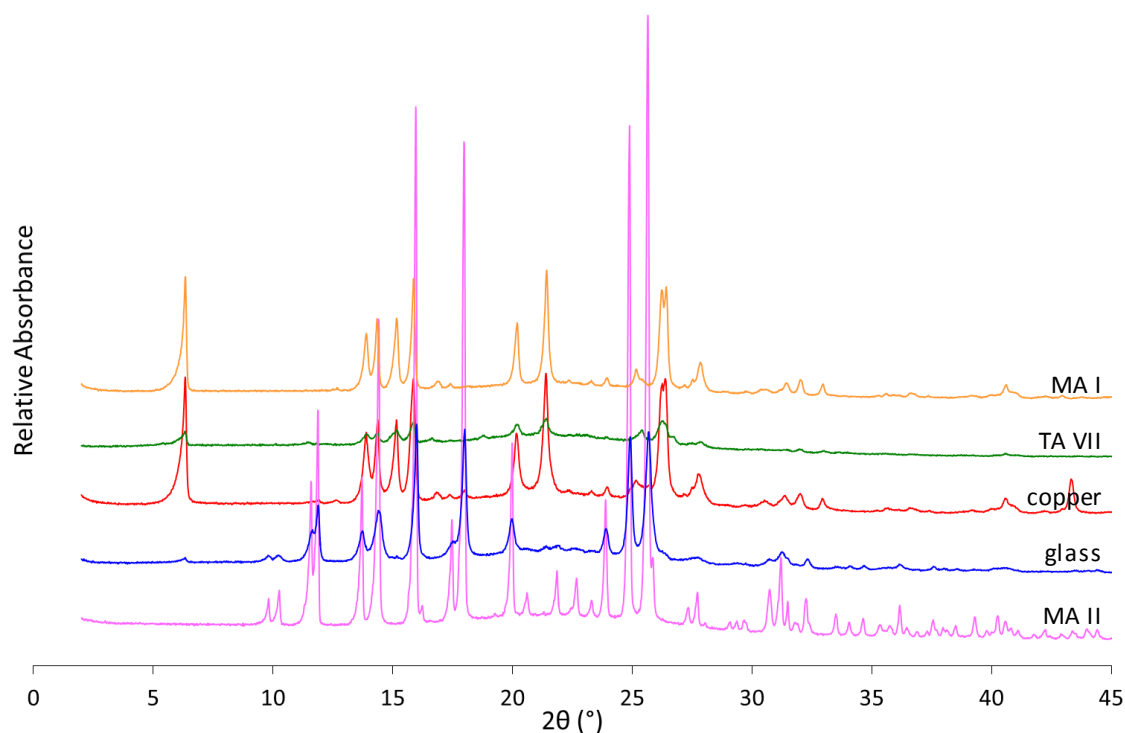
Figure 72. PXRD patterns of MA that has been simultaneously deposited (evaporation source set to 100 °C) onto three different surfaces alongside the PXRD patterns of MA forms I and II.

5.3.2.2.2   Infrared Spectroscopy

As has been mentioned in previous chapters, the position of the N-H stretching band in the infrared spectra can be used to help determine the polymorphic form of both MA and TA.[104, 106, 117, 160] This work has reported that MA forms I and II have peaks at 3308 cm^{-1} and 3342 cm^{-1} respectively and TA forms I and VII have peaks at 3339 cm^{-1} and 3336 cm^{-1} respectively.

The infrared spectra of MA on different surfaces are shown in Figure 73. The infrared data supports the observations and conclusions drawn from the PXRD data in section 5.3.2.2.1. When MA is deposited onto the copper surface, the infrared data suggests it grows as form I irrespective of the deposition rate, as shown by the N-H stretching peaks at 3309 cm^{-1}.
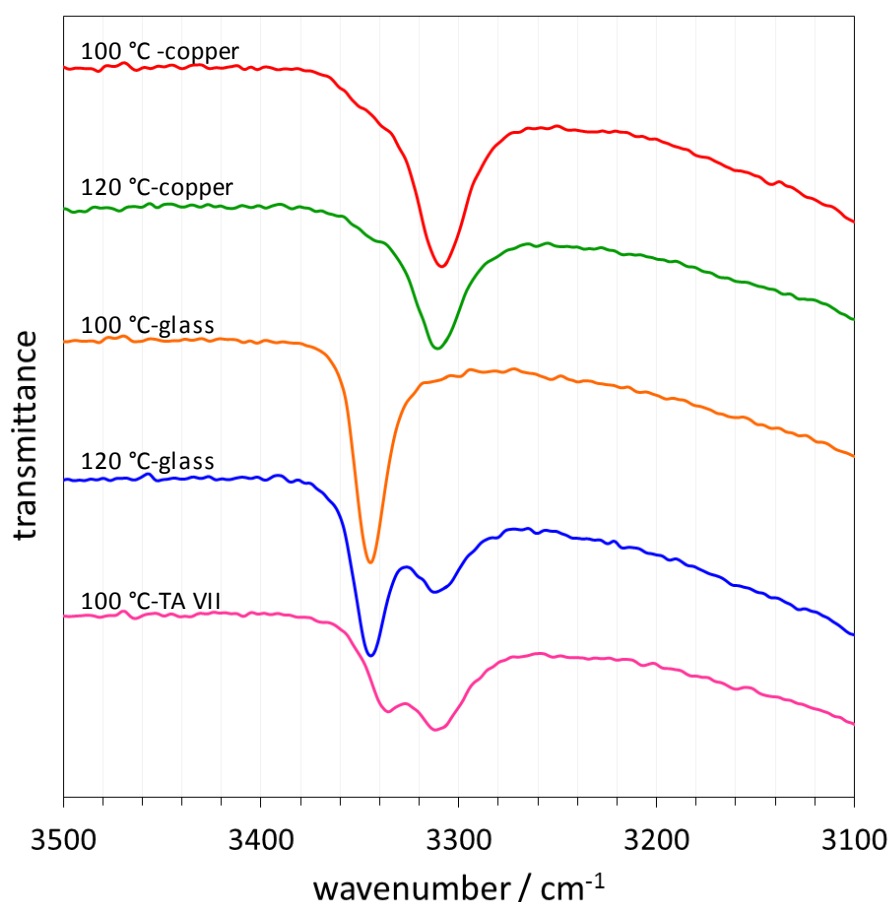
Figure 73. Infrared spectra of the N-H stretching band of MA that has been deposited onto a number of different surfaces. The spectra are labelled with the temperature of the crucible and the surface the MA was deposited onto.

In comparison, when MA is deposited onto a glass surface at the slower deposition rate (crucible temperature is 100 °C), the infrared data suggests that it nucleates as MA form II as the N-H stretching peak is at 3345 cm^{-1}. There is no evidence of MA nucleating as form I on glass at the slower deposition rate from the infrared data. However, when MA is deposited onto the glass surface at a faster rate (with a crucible temperature of 120 °C), the infrared spectrum shows evidence that both forms I and II are present with N-H stretching bands at 3345 cm^{-1} and

3310 cm^{-1}. Additional infrared spectra for three other separate samples of MA onto glass at the faster rate of deposition are given in Appendix 14 on page 214.

When MA is deposited onto TA form VII, the positions of the N-H stretching peaks in the infrared spectra suggest that both MA form I and TA form VII are present with bands at 3312 cm^{-1} and 3336 cm^{-1} respectively. The relative intensities of the N-H stretching bands attributed to MA form I and TA form VII in the infrared spectrum in Figure 73 indicate that significant amount of both MA I and TA VII are present.

5.3.2.2.3 *Thermal Analysis*

Figure 74 shows the DSC scans carried out on the MA that was deposited simultaneously onto copper, glass and microcrystalline TA form VII in the temperature range 0 – 250 °C at a heating rate of 10 °C min^{-1}. The DSC scan of MA onto copper shows an endothermic phase transition at around 156 °C followed by a melting endotherm at 230.9 °C. In comparison, the DSC trace for MA that has been deposited onto the glass shows a single melting endotherm at 231.4 °C. Comparison of the DSC scans in Figure 74 with literature[102] and previous DSC results in this work, confirms that MA grows as form I on the copper surface and as form II on the glass surface. MA form I has been reported to transform to MA form II by heating to around 150 °C – 160 °C.[35, 101, 102, 104, 105] The DSC results reported here are in agreement with the PXRD, infrared and Raman data.
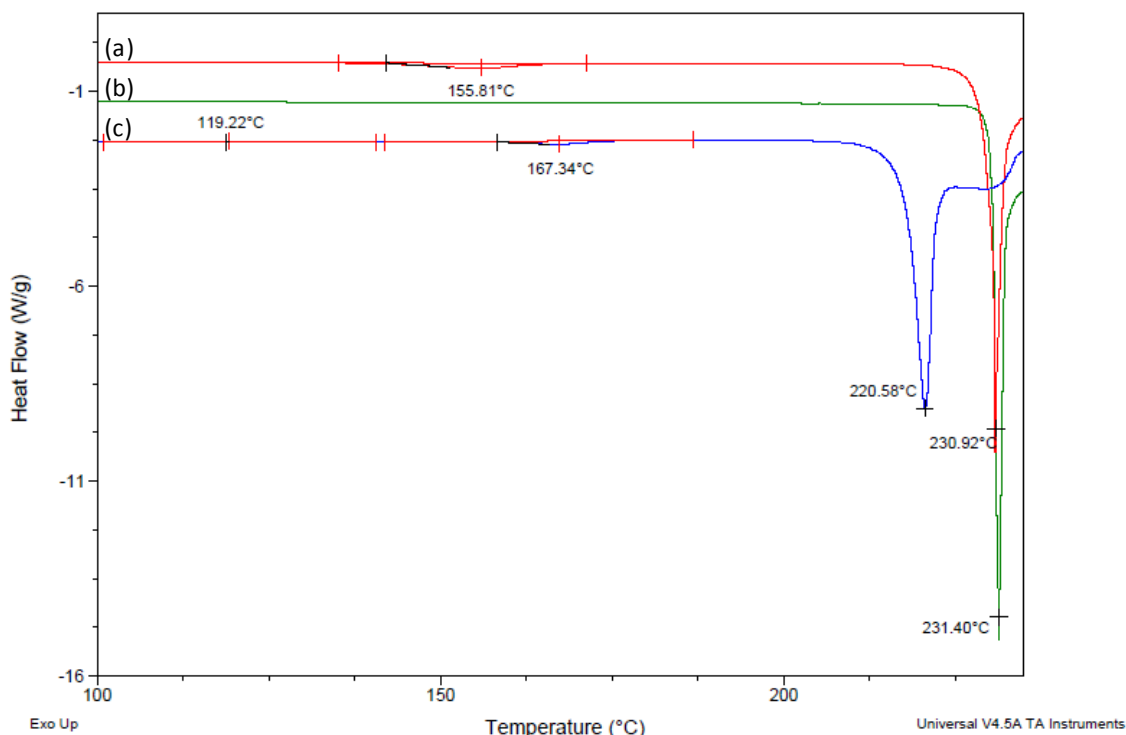
Figure 74. DSC scans of MA deposited simultaneously onto different surfaces. (a) MA onto copper, (b) MA onto glass and (c) MA onto TA form VII. The scans were carried out at a heating rate of 10 °C min^{-1}.

Evidence of both MA form I and TA form VII would be expected in the DSC scan of MA deposited onto microcrystalline TA form VII, following analysis of the infrared data on the same sample. For MA form I, an endothermic phase transition would be expected as MA form I transforms to MA form II at around 150 °C − 160 °C[35, 101, 102, 104, 105] followed by a melting endotherm for MA form II. Additionally, as discussed in section 5.3.2.1, an exothermic phase transition would be expected as TA form VII transforms to TA form I at around 125 − 133 °C (heating rate of 10 °C min^{-1}), followed by a melting endotherm around 213.7 °C.

The DSC scan for MA deposited onto TA form VII in Figure 74 shows a small exothermic transition at 119 °C followed by an endothermic phase transition at 167 °C followed by a melting endotherm at 220.6 °C. The endothermic phase transition is different to that observed for pure MA deposited onto copper, but in line with literature[36, 103, 104, 106, 162] and with DSC scans on MA form I reported earlier in this thesis (Figure 11, page 45) which show that MA form I transforms to MA form II at 168.5 °C. The melting endotherm at 220.6 °C does not relate to any known form of MA or TA, but is consistent with DSC data collected for the MA:TA solid solution series where the temperature of the melting endotherm is linearly dependent on the ratio of MA:TA. The MA:TA solid solution series have melting endotherms at temperatures between pure MA and pure TA (see chapter 4, section 4.2.2.3). Thus it is suggested that as the sample of MA on TA form VII is heated, a solid solution is formed at some point in the DSC.

5.3.2.2.4   Raman Spectroscopy

Raman spectra were collected for MA that had been deposited onto different surfaces as well as MA form I. Comparisons of the spectra bands can be used to determine the polymorphic form of MA.[183] Raman data suggests that when MA is deposited onto a glass surface it grows as form II. In comparison, when MA is deposited onto a copper surface or onto a surface covered in TA, MA grows as form I. The Raman data is in agreement with the PXRD, infrared and DSC data.

Figure 75 shows the Raman spectrum, in the region 550 cm^{-1} − 950 cm^{-1}, of MA deposited onto different surfaces. When MA is deposited slowly onto the glass surface (evaporation source set to 100 °C) the Raman spectrum has peaks at 573, 632, 693, 771 and 805 cm^{-1} in agreement with literature values for MA form II.[101, 106, 183] In comparison, the spectra bands for all other preparations of MA are observed at 578, 623, 703, 774, 809 cm^{-1}, again in agreement with literature on MA form I.[101, 106, 183]
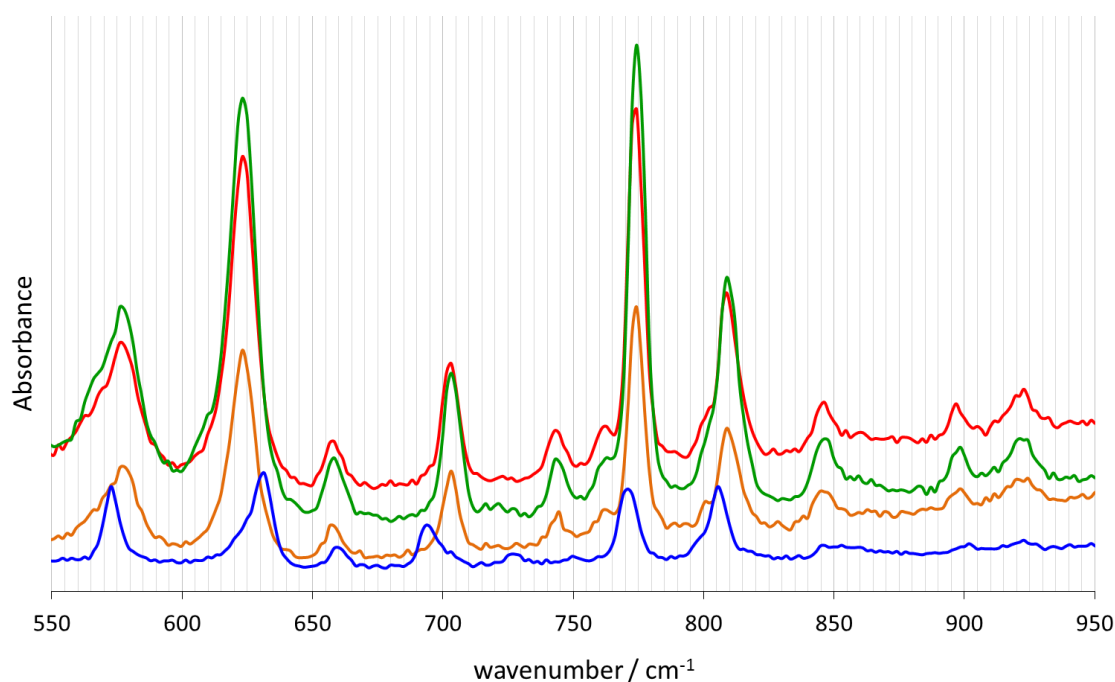
Figure 75. Raman spectra of MA form I (red), MA deposited onto TA form VII (green), MA deposited onto copper (orange) and MA deposited onto a glass microscope slide (blue).

5.3.2.2.5 Summary

The deposition experiments involving MA in this section have shown that the surface has a role in the polymorphic selectivity of the deposited MA. Results from PXRD analysis, infrared spectroscopy, DSC data and Raman spectroscopy confirm that when MA is deposited onto a copper surface (held at room temperature, under vacuum) it grows as MA form I. In comparison, the results show that when MA is deposited onto a glass surface (at room temperature, under vacuum) it grows as phase pure MA form II if the deposition rate is slow enough. When MA is deposited onto TA form VII (at room temperature, under vacuum) it nucleates as MA form I, not as the predicted isostructural polymorph (#5MA_510), that was generated during the CSP study on MA in chapter 3.

In addition to the role of the surface on the polymorphic selectivity of MA, the deposition rate has also been shown, by analysis of PXRD data, to affect the polymorphic phase purity of MA deposited onto a glass surface, but not a copper surface. Depending on the deposition rate, MA that was deposited onto the glass surface either nucleated as phase pure form II (evaporation source set to 100 °C) or a mixture of forms I and II (evaporation source set to 120 °C).

Although the deposition rate has been shown to affect the phase purity, the exact deposition rate has not been quantified or analysed in this work. The different deposition rates were assessed only by setting the evaporation source to two different temperatures, 100 °C and 120 °C. The higher the temperature of the evaporation source, the greater the vapour pressure and the faster the deposition.

5.3.3   Discussion

This section has investigated the behaviour of both MA and TA as they are deposited under vacuum using the bespoke sublimation apparatus described in section 5.3.1.1. Deposition is too fast to observe the nucleation of single crystals, thus much of the analysis in this section was carried out using PXRD. Further analysis and results were obtained using ^{1}H NMR spectroscopy, infrared spectroscopy, thermal gravimetric analysis, differential scanning calorimetry, Raman spectroscopy as well as simultaneous DSC-XRD.

The results have shown that MA and TA exhibit different behaviour from one another. The deposition of TA onto both copper and glass surfaces produces a new polymorph, TA form VII. In comparison, when MA is deposited onto copper or TA form VII it nucleates as MA form I and when it is deposited onto a glass surface it nucleates as MA form II. In both TA and MA, the phase purity of the deposited product is affected by the deposition rate with TA form VII showing evidence of increased phase impurity when the deposition rate increases. Similarly, the phase purity of MA form II from deposition onto a glass surface has been shown to decrease as the temperature of the evaporation source is increased and thus the deposition rate increases. The phase purity of MA form I on the copper surface is not affected by the deposition rate which suggests that the phase purity of the prepared sample is only affected if a metastable form nucleates.

The results have shown that the polymorphic form of TA is not influenced by the surface upon which the TA is deposited, although it should be noted that only copper and glass were investigated. In comparison, the choice of surface (be it copper, glass or TA form VII) affects the polymorphic selectivity of deposited MA.

5.4 Conclusion

This chapter has investigated the nucleation behaviour of both MA and TA from the vapour phase using two very different series of experiments. The series of experiments used a static vacuum of around 3.0 x 10^{-2} mbar and the deposition surfaces were held at an elevated temperature. In comparison, the second series of experiments involved the use of a dynamic vacuum of around 5.0 x 10^{-6} mbar and the deposition surfaces were held at room temperature.

Results from both sets of experiments suggest that the nucleation behaviour of MA is dependent upon the identity of the surface. When MA grows on a metallic surface (copper) from the vapour phase, it grows as MA form I irrespective of whether the surface is held at an elevated temperature (above the transition temperature when MA form I transforms to MA form II) or at room temperature. These results were confirmed by SCXRD from the first series of experiments and by PXRD from the second. Similarly, when MA is deposited on a glass surface, at both ambient and elevated temperatures, MA grows as MA form II. However, fast deposition rates can lead to concomitant growth of MA form I as well as MA form II. Lastly, deposition of MA onto TA surface templates, a single crystal of TA form I in the first series of experiments and microcrystalline TA form VII in the second series of experiments, produces MA form I. Although the above observations can be drawn from the data, the specific role of the surface remains unknown.

In comparison, the nucleation and growth behaviour of TA from the vapour phase does not appear to be affected by the surface. Two different polymorphs of TA were obtained from the two series of experiments, TA form I from the first and TA form VII from the second, irrespective of the surface. Observations suggest that the polymorphic form of TA is influenced by the sublimation procedure. The results do not eliminate the role the temperature of the surface may have in determining the polymorphic form of TA. Due to the experimental setup, the deposition surfaces in the original series of experiments were held at elevated temperatures which were likely to be above the transition temperature for conversion of TA form VII to TA form I.

The results reported in this chapter yet again highlight the different nucleation behaviour exhibited by TA and MA. Under the same conditions, the two molecules behave very differently. When deposited from the vapour phase onto the same surface, the two compounds nucleate as non-isostructural crystal structures. This suggests that the geometrical and/or chemical functionality of the surface influences the nucleation of TA and MA in different ways.

6 Validation of Crystal Structure Prediction methods through participation in The Sixth Blind Test of Organic Crystal Structure Prediction Methods organised by the CCDC

6.1   Introduction

Previous computational work in this thesis on the crystal structure prediction of MA was aided by prior knowledge of the three known polymorphs. These experimental structures helped validate the methodology and the results of the CSP study were used as a complement to experimental work. This is rather different from using CSP to decide whether a molecule will crystallise as a useful material, i.e. prediction of crystal structure prior to synthesis. This chapter further tests the crystal structure prediction methodology, followed previously in this thesis (chapter 3), through participation in the *Sixth Blind Test of Organic Crystal Structure Prediction Methods* organised by the CCDC. The Blind Tests assess how current methods of crystal structure prediction fare when given only the atomic connectivity of a compound/system as a starting point.

6.2   Previous Blind Tests

Following on from the success of the initial, invitation only, crystal structure prediction workshop held in 1999[184], the CCDC has organised five further blind test challenges (held in 2001[185], 2004[186], 2007[187], 2010[188] and this current test) that have been open to the international crystal structure prediction community. Each blind test has a number of target crystal structures that have been chosen to fit certain criteria and designed to test the ability of CSP methods to successfully predict increasingly challenging organic crystal systems. The CCDC blind tests have provided research groups across the globe with a unique opportunity to rigorously test different CSP methods for a range of organic molecules from small rigid molecules to larger, more flexible systems including salts and cocrystals. The molecular systems that have been submitted by the CCDC as candidate molecules in each test reflect the current perceived areas of interest and claimed capabilities in modelling organic crystal structures. It is for this reason that the most recent blind tests targets have increased in complexity and reflect the growth in the crystal structure prediction community.

Compared to current day challenges and capabilities, the targets in the first blind tests could now be considered on the simple side of crystal structure prediction indicating just how far the field has come in the past 17 years since the introduction of the CCDC blind tests. The

systems in the first three bind tests had no more than 40 atoms yet successes were limited and it wasn't until 2007 that there was a significant level of success with small molecules.[187]

As crystal structure prediction methods have progressed, the blind tests have involved more and more challenging test systems. The first three blind tests included molecules that belonged to one of the first three categories as described in Table 25. For the first time, the fourth blind test included a two component system (category 4, Table 25) that represents the growth in interest multiple component systems which present a more challenging search, as it is necessary to also include the relative positions and orientation of the molecules in the asymmetric unit. The inclusion of the cocrystal in the fourth test reflects the considerable interest in using salts and cocrystals of pharmaceuticals to improve the physical properties of the solid forms.[189, 190] Interest in the CSP studies of cocrystals has increased following the finding of an elusive predicted cocrystal of caffeine benzoic acid by heteronuclear seeding.[191] A pharmaceutically relevant molecule, i.e. one of sufficient size and flexibility that it was approaching the size of small molecule drugs in development, was considered for the first time in the fifth blind test (category 5, Table 25). A polymorphic system (category 6, Table 25) was also considered.

Table 25. Categories in the previous CCDC Blind tests.

CATEGORY	DESCRIPTION
1	a small, rigid molecule with only C,H,N,O atoms and less than 25 atoms
2	a small, rigid molecule with some less common elements
3	a molecule with some small amount of conformational freedom
4	multiple independent rigid molecules, e.g. solvates, cocrystals, salts or Z' = 2 structures; any space group; up to 30 atoms
5	a molecule with 4–8 internal degrees of freedom in any space group and with 50–60 atoms and either one or two independent molecules in the asymmetric unit
6	a molecule for which there is more than one known polymorph, that is also relevant to one of the first four categories

Though the successes in the first blind tests were limited, the fourth blind test in 2007 saw successful predictions from 13 of the 14 participating groups[187] for the small rigid system and finally, the fifth blind test saw two successful predictions of a highly flexible model pharmaceutical.[72] The CCDC determine a prediction in the blind tests as successful if a good representation of the experimental crystal structure was submitted as one of three structures that were allowed for each molecule for each participating group.

6.3 Sixth Blind Test of Crystal Structure Prediction

In September 2014, the CCDC announced the start of the sixth blind test that would yet again provide a standard platform upon which different collaborations and research groups could test their CSP methodologies. In preparation, the CCDC had retained the crystal structures of five different systems that were then released to the CSP community as molecular diagrams. The molecules were chosen to fit categories (Table 26) as determined by the CCDC and were similar, but not the same, as those that featured in the previous blind tests.

Participants were allowed to submit a list of 100 structures compared to just three in the previous five blind tests. Additionally, participants were allowed to submit a second list using different ranking criteria. This change in the submissions represents the more recent focus of CSP studies highlighting the importance of the solid form landscapes of a molecule or compound and not just the prediction of '*the*' crystal structure. Furthermore, to reflect the use of different methods in calculating final lattice energies, structures that were generated by one group were allowed to be re-ranked by another research group to provide insights into the uses of developing more specific ranking methods of lattice energies.

6.3.1 Target System XXV

The calculations reported in this chapter are on candidate system XXV which is shown in the diagram alongside the category description in Table 26. System XXV is a two component system containing 3,5-dinitrobenzoic acid (molecule 1) and 2,8-dimethyl-6H,12H-5,11-methanodibenzo[b,f][1,5]diazocine (molecule 2) which is also known as Tröger's Base. 3,5-dinitrobenzoic acid (3,5-DNBA) is known to be a corrosion inhibitor and is also used in photography[192] and Tröger's Base has a number of applications as building blocks in fields including new materials, enzyme inhibitors, molecular recognitions, catalysis and supramolecular chemistry[193].

Table 26. Criteria for each system in the sixth blind test

XXII	Rigid molecules, with functional groups restricted to CHNO, halogens, S, P and B; one molecule in the asymmetric unit; up to about 30 atoms	
XXIII	Partially flexible molecule with two to four internal degrees of freedom; one molecule in the asymmetric unit; up to about 40 atoms	
XXIV	Partially flexible molecule with one or two internal degrees of freedom as a salt; two charged components in the asymmetric unit, in any space group; up to about 40 atoms	
XXV	Multiple partially flexible (one or two degrees of freedom) independent molecules as a co-crystal or solvate in any space group; up to about 40 atoms	
XXVI	Molecules with 4-8 internal degrees of freedom; no more than two molecules in the asymmetric unit, in any space group; 50-60 atoms	

There are 19 entries on the CSD (refcode CUKCAM) of two known polymorphs of 3,5-DNBA which crystallises in space groups $P2_1/c$ and $C2/c$ from benzene and ethanol respectively.[194] Both polymorphs exist as carboxylic acid dimers that form via two hydrogen bonds in an $R_2^2(8)$ arrangement. Crystal structures of the $P2_1/c$ polymorph, determined with X-ray diffraction, have shown a degree of proton disorder within the carboxylic acid dimer of the

structure at room temperature but not at 100 K.[195] The different positions of the protons in the carboxylic acid dimer have been further investigated using neutron diffraction on crystals of the C2/c polymorph and high resolution X-ray diffraction on the P2$_1$/c polymorph.[196] Thirteen redeterminations of the two polymorphs of 3,5-DNBA, as well as diffraction data on the homodimers of 3,5-DNBA in binary complexes with 4-dimethylaminobenzoic acid, support the previous results that show at low temperatures there is no evidence of proton disorder, but as temperatures increase, proton disorder is evident (Figure 76).
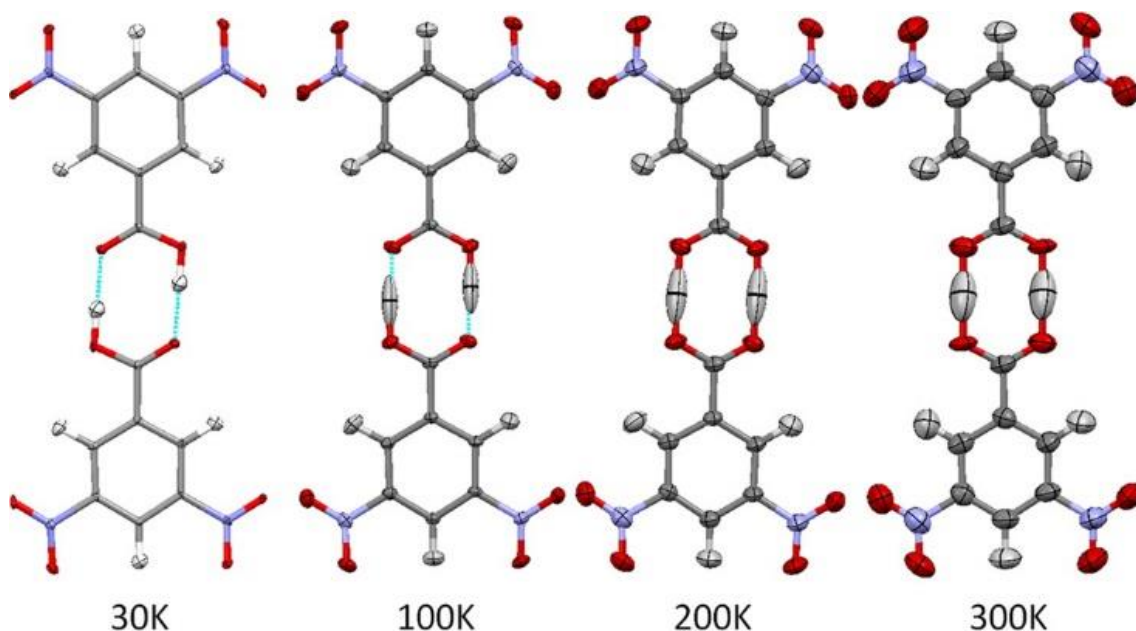
Figure 76. Evolution of the anisotropic displacement parameter of the hydrogen atom in the 3,5-DNBA homodimer in a binary complex with 4-dimethylaminobenzoic acid, determined from neutron diffraction data. A single, well localized position is observed at 30 K moving to an average central position with a significantly greater mean square displacement along the direction of the hydrogen bond as the temperature is increased.[196]

The known experimental structures of 3,5-DNBA show that the molecule adopts two different conformations in the two different polymorphs (Figure 77). The different conformations are due to rotation of the carboxylic acid and nitro groups away from planar.
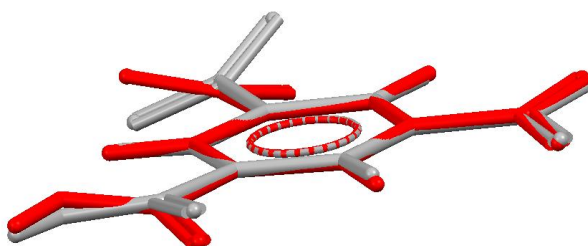
Figure 77. Molecular overlay of 3,5-DNBA in CUKCAM04 (grey) and CUKCAM22 (red) showing the rotation of the carboxylic acid and nitro groups that gives rise to different conformations in the crystal structures.

In comparison to 3,5-DNBA, Tröger's Base has just one racemic crystal structure determination on the CSD (refcode DILLEP[197]) and two determinations of enantiopure (R,R)-Tröger's Base (refcode AXAGEL[198] and redetermination, AXAGEL01[199]). There is only a 13 molecule overlay, $rmsd_{13} = 0.112$ Å, of AXAGEL with AXAGEL01 of which the latter is a better determination, carried out at 100 K, with a lower R-factor than AXAGEL which was determined at room temperature. Furthermore, the hydrogen atoms in AXAGEL01 were observed in difference electron density maps and were refined isotropically whereas they were fixed in the AXAGEL structure based on stereochemical considerations. Although there is no single crystal data for the (S,S)-Tröger's Base enantiomer on the CSD, this enantiomer cocrystallises with (S,S)-2,8-dichloro-6H,12H-5,11-methanodibenzo[b,f][1,5]diazocine in the same unit cell as the (R,R) enantiomer (refcode YOGDAB).[200] The (S,S)-Tröger's Base component of the cocrystal YOGDAB is crystallographically the same as the structure of the (R,R) enantiomer with a 30 molecule overlay, $rmsd_{30} = 0.081$ Å (Figure 78).
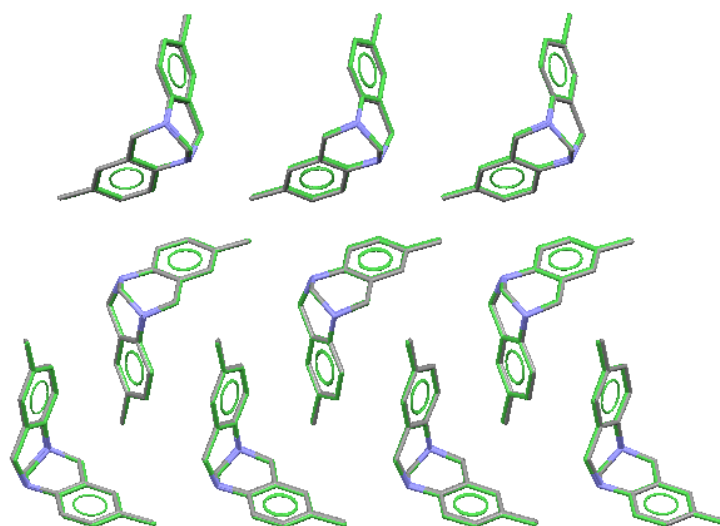
Figure 78. 30 molecule overlay of the (S,S)-Tröger's Base component of the cocrystal YOGDAB (coloured by element) with the crystal structure of (R,R)-Tröger's Base AXAGEL01 (green).

The chirality of Tröger's Base arises from the blocked conformation of the two N-atoms of the methanodiazocine bridge which gives the molecule a C_2 axis of symmetry.[198] A CSP search on Tröger's base alone would only have to consider the chiral space groups had it been known prior to calculations that Tröger's base was enantiopure. In the case of cocrystal XXV, the CCDC specified that target system XXV was crystallised from a racemic mixture of both enantiomers. However, only one enantiomer of Tröger's Base is required as the input in the search, reducing the potential computational cost of the calculations. The other enantiomer is automatically generated by inversion or mirror plane symmetry in racemic space groups.

The major conformational difference between the known experimental conformations (Figure 79) of Tröger's Base is due to the methyl group rotation which rotates to maximise the intermolecular interactions within the crystal lattices.
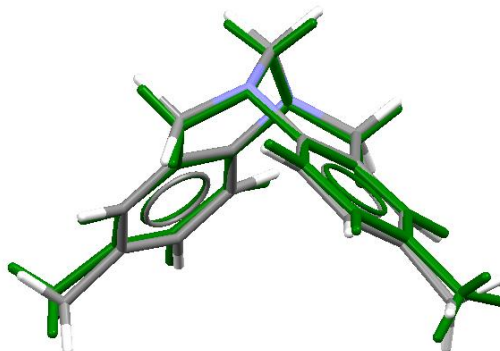
Figure 79. Molecular overlay of one molecule of Tröger's Base from DILLEP (coloured by element) with AXAGEL01 (green).

6.4 Computational Methodology

The computational methodology in this chapter is largely similar to that followed when carrying out the CSP study on MA (see chapter 3). The main difference in this chapter is that the target system is a cocrystal with two molecules in the asymmetric unit. Therefore, the search needs to take into consideration the relative orientations of the different components and as such, small amendments to the methodology have been made in line with previous CSP studies on cocrystals.[126, 127]

6.4.1 Verification of Chosen Level of Theory

As with chapter 3 in this thesis, the appropriate level of theory was tested prior to the CSP study. In this case, an indication of how appropriate the intermolecular forces were modelled for the XXV system, was given by analysis of the reproduction of experimental crystal structures of both the individual components of the cocrystal as well as related structures taken from the CSD.

Different levels of theory were initially tested to see how well the crystal structures of DILLEP, AXAGEL, AXAGEL01, CUKCAM04 and CUKCAM22 were reproduced. CUKCAM04 and CUKCAM22 were chosen from the 19 structures on the CSD of 3,5-DNBA as they were both low temperature determinations with small R-factors of the $P2_1/c$ and $C2/c$ polymorphs respectively. Reproduction of the crystal structure YOGDAB was not carried out due to the crystallographic similarity with AXAGEL01. Once an appropriate level of theory was chosen for the individual

components, the reproduction of crystal structures of related single component and cocrystal systems were tested using that same level of theory.

6.4.2 Conformational Analysis

The next step in the approach to the blind test was to determine which molecular conformations of the molecule should be considered in the search and to identify the potential degrees of freedom and flexibility of both components. In the case of the cocrystal XXV, the starting molecular conformations were extracted from the CIF files of known experimental crystal data of the two polymorphs of 3,5-DNBA (CUKCAM04 and CUKCAM22) and both the racemic (R,S)-Tröger's Base (DILLEP) and enantiopure (R,R)-Tröger's Base (AXAGEL01).

Ab initio, calculations were carried out on the isolated molecule of 3,5-DNBA using GAUSSIAN09 at the PBE0/6-31+G(d) level of theory to provide a relaxed conformational scan of the torsion angles that relate to the rotation of the carboxylic acid and nitro groups.

Additionally, CrystalOptimizer[135] was used to assess the conformational flexibility of both molecules by carrying out fully atomistic minimisations on the known experimental crystal structures of the individual components. This provided information about which degrees of freedom changed the most and should therefore be considered as flexible in latter stages of the production of the crystal energy landscape.

6.4.3 Crystal Structure Prediction

The crystal energy landscape for the cocrystal XXV was obtained in a series of steps. At each step the number of structures considered was reduced in line with the increasing computational cost of more accurately calculating the lattice energy of putative structures.

Initially, the conformations of both 3,5-DNBA and Tröger's Base were optimised to the gas phase minimum using GAUSSIAN09[138] at the PBE0/6-31+G(d) level of theory. The optimised rigid conformations of each component were then used as the input conformations in the CrystalPredictor[133] search that was used to generate potential cocrystal structures with two molecules in the asymmetric unit. The CrystalPredictor search generated structures in the following 59 space groups; *P1, P-1, P21, P21/c, P21212, P212121, Pna21, Pca21, Pbca, Pbcn, C2/c, Cc, C2, Pc, Cm, P21/m, C2/m, P2/c, C2221, Pmn21, Cmc21, Aba2, Fdd2, Iba2, Pnna, Pccn, Pbcm, Pnnm, Pmmn, Pnma, Fddd, Ibam, P41, P43, I-4, P4/n, P42/n, I4/m, I41/a, P41212, P43212, P-421c, I-42d, P31, P32, R3, P-3, R-3, P3121, P3221, R3c, R-3c, P61, P63, P63/m, P213, Pa-3, Cmcm and Cmca.* The lattice energies of the generated structures were calculated using the FIT, exp-6 atom-atom repulsion-dispersion, potential with empirically fitted parameters[145] and

atomic charges. A total of 2,000,000 structures were produced in two lots of 1,000,000 and structures that were the same were clustered using the criteria built into the CrystalPredictor program.

The energy rankings of the most stable 40,000 structures were evaluated with more accuracy by replacing the atomic charges with the distributed multipoles of the rigid gas phase conformations of both molecules and minimising the lattice energy using DMACRYS.[139, 140] The crystal structures were then clustered to remove duplicates. This was done by consideration of potential small energy and density differences between the same structures, calculated powder pattern similarity and finally $rmsd_n$ values[67] where n = 30. Routine clustering for Z' = 1 structures normally looks at an overlay of 15 molecules, but in the case of the cocrystal XXV this was increased to 30 to account for the fact that there are two molecules in the asymmetric unit.

Full CrystalOptimizer runs were carried out on the most stable unique crystal structures allowing the most flexible degrees of freedom, as determined in the fully atomistic CrystalOptimizer runs on the individual components, to vary as expected under packing forces. The converged CrystalOptimizer calculations are minima on the crystal energy landscape and are checked to be so by consideration of the Hessian matrix. In a small number of cases, the structures needed to be changed to Z' = 4 structures (two molecules of each component in the asymmetric unit) and re-minimised.

The CrystalOptimizer minima were then clustered again to remove structures that had minimised to the same structure and were therefore duplicates. The resulting lowest 100 structures formed List 1 that was submitted to the CCDC. After this step, the lowest 1000 structures were sent to Tkatchenko and Brandenberg for re-ranking using periodic dispersion-corrected electronic structure methods that were mentioned in chapter 3.

Uncertainties in the relative energy estimates of thermodynamically plausible structures following CrystalOptimizer were roughly estimated by looking at the sensitivity of the relative lattice energy to small changes in the energy model. The changes made to the energy model included estimating the effect of the crystal environment by applying the polarizable continuum model (PCM)[147] as well as estimating the Helmholtz free energy at 298 K from the rigid-body k=0 phonon modes and elastic constants for the unit cell[149]. The Williams potential, W99,[150] was also tested.

The PCM was applied to the unique crystal structures following CrystalOptimizer. The bulk crystalline environment was modelled using GAUSSIAN09 to calculate the wave function of the molecular structures in a dielectric of ε = 3.0 (shown to be typical of organic crystals).[146] DMACRYS was used to calculate the lattice energy and estimate the Helmholtz free energy at 298 K. The 100 lowest unique structures following the free energy calculations formed the second list of structures submitted to the CCDC, List 2.

6.5 Results and Discussion

6.5.1 Verification of Chosen Level of Theory

Table 27 shows the results of the reproductions of the unit cells of the individual components of the cocrystal XXV as calculated at different levels of theory (HF, B3LYP, PBE and PBE0) with the 6-31+G(d) basis set and the FIT potential. The unit cells of DILLEP, CUKCAM04 and CUKCAM22 were well reproduced at all levels of theory with low $rmsd_{15}$ values. Of the four levels of theory tested, the PBE0/6-31+G(d) level of theory gave the lowest $rmsd_{15}$ values and the best reproductions of the experimental unit cells.

AXAGEL, the first determination of the (R,R)-Tröger's Base, was poorly reproduced at all levels of theory. However, the subsequent redetermination AXAGEL01, released later on during this blind test study in version 5.36 of the CSD, was reproduced well at the PBE0/6-31+G(d) level of theory. The release of AXAGEL01 showed that the poor modelling of AXAGEL was because of the poor quality crystal structure, and removed some doubts about the suitability of the chosen model for the intermolecular forces.

The W99 potential was also tested at different levels of theory and whilst results for DILLEP and AXAGEL01 were satisfactory, the W99 potential fused the carboxylic acid dimers together in both CUKCAM04 and CUKCAM22. It was decided that the W99 potential was not suitable. This problem has been observed previously,[144] including for a carboxylic acid - pyridine hydrogen bond,[201] and appears to be due to insufficient repulsion from the polar hydrogen when the electrostatic forces are modelled by distributed multipoles.

The PBE0/6-31+G(d) level of theory with the FIT potential was then further validated by reproducing the crystal structures of 18 single and multicomponent systems that were related to the components of cocrystal XXV. All the related structures were well reproduced at the PBE0/6-31+G(d) level of theory with the FIT potential as shown in the table in Appendix 15 on page 215. In each case the $rmsd_{15}$ values are low which suggests that the chosen level of theory is an adequate choice for the cocrystal XXV.

Hence, the CSP study was carried out using distributed multipoles calculated at the PBE0/6-31+G(d) level of theory and using FIT potential. The confidence that this model was appropriate rather than just the best within our capabilities increased following the good reproductions of the related crystal structures and with the publication of the better crystal structure of Tröger's base, AXAGEL01.

Table 27. Reproduction of the experimental crystal structures of the individual components of the cocrystal XXV using the experimental conformation and the distributed multipoles of the specified level of theory with the 6-31+G(d) basis set and the FIT parameters for the exp-6 potential.

	Lattice Parameters						Lattice Energy	Density	$n(rmsd_n)$
	a (Å)	b (Å)	c (Å)	α (°)	β (°)	γ (°)	(kJ mol^{-1})	(g cm^{-3})	(Å)
CUKCAM04									
expt	**9.761(2)**	**8.9192(4)**	**9.444(2)**	**90**	**97.55(1)**	**90**			
HF	10.32	8.88	9.15	90	97.33	90	-150.55	1.69	15(0.269)
B3LYP	10.38	8.92	9.17	90	97.39	90	-136.40	1.67	15(0.285)
PBE	10.36	8.95	9.19	90	97.31	90	-130.20	1.67	15(0.276)
PBE0	10.34	8.94	9.19	90	97.30	90	-134.04	1.67	15(0.267)
CUKCAM22									
expt	**20.080(5)**	**8.700(5)**	**9.600(5)**	**90**	**109.750(10)**	**90**			
HF	21.11	8.66	9.37	90	108.33	90	-152.68	1.73	15(0.251)
B3LYP	21.14	8.72	9.39	90	108.32	90	-138.82	1.71	15(0.249)
PBE	21.11	8.76	9.41	90	108.56	90	-132.56	1.71	15(0.236)
PBE0	21.09	8.74	9.41	90	108.56	90	-136.38	1.71	15(0.233)
DILLEP									
expt	**12.774(2)**	**30.290(5)**	**10.386(2)**	**90**	**90**	**90**			
HF	12.74	29.72	10.88	90	90	90	-120.13	1.21	15(0.224)
B3LYP	12.76	29.72	10.88	90	90	90	-117.87	1.21	15(0.227)
PBE	12.76	29.73	10.88	90	90	90	-118.47	1.21	15(0.224)
PBE0	12.75	29.74	10.88	90	90	90	-119.80	1.21	15(0.221)
AXAGEL									
expt	**6.110(6)**	**7.934(7)**	**28.33(6)**	**90**	**90**	**90**			
HF	6.19	7.99	27.44	90	90	90	-121.50	1.23	13(0.119)
B3LYP	6.18	8.00	27.48	90	90	90	-119.17	1.22	13(0.117)
PBE	6.18	8.00	27.48	90	90	90	-119.22	1.22	13(0.117)
PBE0	6.19	7.99	27.47	90	90	90	-120.54	1.23	13(0.117)
AXAGEL01									
expt	**6.04092(12)**	**7.95113(18)**	**27.2870(6)**	**90**	**90**	**90**			
PBE0	6.13	8.11	27.46	90	90	90	-119.99	1.22	15(0.137)

6.5.2 Determining the conformational flexibility to be used in the CSP study

The torsion angles of the COOH and NO_2 groups in CUKCAM04 and CUKCAM22 are reported in Table 28. As the largest reported torsion angle is only 23.38 ° away from planar, it suggests that rotation of either group away from planar is minimal in the known polymorphs. This information is supported by the torsion angle scans (Figure 80) which show that the relative conformational energy increases significantly, to a maximum at 90 °, as either substituent group rotates more than 40 ° away from planar.

Table 28. Torsion angles for the COOH and NO_2 groups in the experimental crystal structures of CUKCAM04 and CUKCAM22.

	Torsion Angle (°)	
	CUKCAM04	CUKCAM22
COOH	7.76	9.21
NO_2	2.35	3.29
NO_2	23.38	19.09

As the substituent groups on 3,5-DNBA are unlikely to rotate significantly away from planar, it was decided that it would be sufficient for 3,5-DNBA to be held rigid in the search, with the input molecule fixed in the near planar, gas phase optimised, conformation. The small conformational flexibility of 3,5-DNBA could then be accounted for in the subsequent CrystalOptimizer calculations.
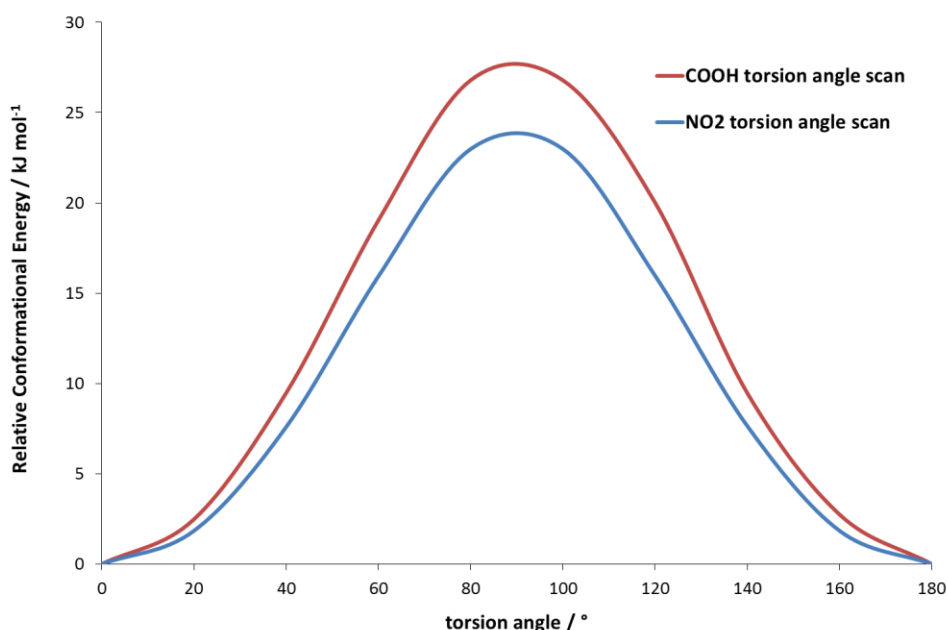
Figure 80. The relative conformational energy as a function of the torsion angles of the COOH and NO_2 groups in 3,5-DNBA (with the rest of the molecule kept planar) calculated at the PBE0/6-31+G(d) level of theory.

Tröger's Base can also be kept rigid in the search as the molecule shows very limited conformational flexibility illustrated by the fact that the conformations of the molecules in the known crystal structures of DILLEP and AXAGEL01 are very close to the gas phase optimum conformation (Figure 81). For this reason, a fully rigid search was carried out for cocrystal XXV which minimised the computational cost of the CrystalPredictor search as it reduced the number of conformational regions that needed to be searched to just one. The search variables covered in this CrystalPredictor search are the orientation and position of the two component molecules relative to each other and the unit cell parameters.
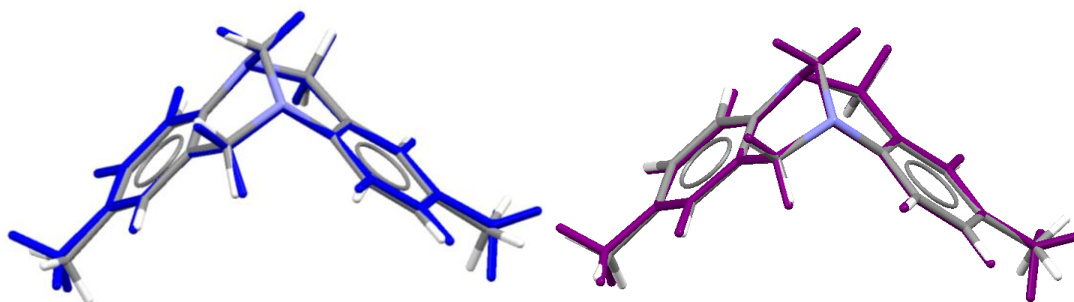
Figure 81. (a) Molecular overlay of Tröger's Base in DILLEP (coloured by element) with the gas phase optimum conformation (blue), $rmsd_1$ = 0.0820 Å. (b) Molecular overlay of Tröger's Base in AXAGEL01 (coloured by element) with the gas phase optimum conformation (purple), $rmsd_1$ = 0.0436 Å.

The next stage of conformational analysis involved determining the degrees of freedom that would require optimisation in the CrystalOptimizer calculations that follow the CrystalPredictor search. In order to do this, fully atomistic CrystalOptimizer calculations on the individual components CUKCAM04, CUKCAM22 and AXAGEL01 were carried out where every degree of freedom (bond lengths, angles and dihedrals) in the molecule was optimised. Fully atomistic CrystalOptimizer calculations were not possible on DILLEP as it is a Z' = 3 structure and therefore has too many degrees of freedom for the program to compute at the atomistic level. AXAGEL and AXAGEL01 minimised to the same structure.

The results of the fully atomistic CrystalOptimizer runs indicated the angles and dihedrals that were likely to be the most flexible and require optimisation in subsequent CrystalOptimizer calculations on the generated structures. Angles that changed by more than 0.5 ° and dihedrals that changed by more than 1.0 ° in the polymorphs of 3,5-DNBA (Appendix 16, page 220) were considered flexible. Angles and dihedrals that affected the conformation of the phenyl ring in 3,5-DNBA were not considered flexible as the conformational change resulting from these optimisations brought the conformation of the phenyl ring closer to the gas phase optimum which was used as the input in the CrystalPredictor search. A total of 9 degrees of freedom (Figure 82) were chosen as flexible degrees of freedom for the CrystalOptimizer calculations. Fully atomistic CrystalOptimizer calculations on AXAGEL and AXAGEL01 identified 8 degrees of freedom that required optimisation (Figure 82).

Table 29. Reproduction of the experimental crystal structures of some of the individual components of the cocrystal XXV following CrystalOptimizer calculations. The table provides the results of both fully atomistic CrystalOptimizer runs where all degress of freedom were optimised as well as runs where only selected degrees of freedom were optimised. Fully atomistic calculations were not carried out on DILLEP as it is a Z' = 3 structure and therefore has too many degrees of freedom for the CrystalOptimiser program.

	Lattice Parameters						Lattice Energy	Density	n(rmsd$_n$) with experimental structure	n(rmsd$_n$) with atomisitic CrystOpt model
	a (Å)	b (Å)	c (Å)	α (°)	β (°)	γ (°)	(kJ mol^{-1})	(g cm^{-3})	(Å)	
CUKCAM04										
Experimental	**9.761(2)**	**8.9192(4)**	**9.444(2)**	**90**	**97.55(1)**	**90**				
Fully atomistic CrystalOptimizer	10.37	8.98	9.07	90	97.88	90	-137.01	1.68	15(0.317)	
CrystalOptimizer (9 DOFs)	10.33	8.99	9.108	90	97.92	90	-121.61	1.68	15(0.322)	15(0.068)
CUKCAM22										
Experimental	**20.080(5)**	**8.700(5)**	**9.600(5)**	**90**	**109.750(10)**	**90**				
Fully atomistic CrystalOptimizer	21.26	8.83	9.26	90	107.64	90	-140.08	1.70	15(0.316)	
CrystalOptimizer (9 DOFs)	21.32	8.82	9.27	90	107.92	90	-125.06	1.70	15(0.322)	15(0.025)
DILLEP										
Experimental	**12.774(2)**	**30.290(5)**	**10.386(2)**	**90**	**90**	**90**				
CrystalOptimizer (8 DOFs)	12.83	30.05	10.80	90	90	90	-115.79	1.20	15(0.199)	
AXAGEL										
Experimental	**6.110(6)**	**7.934(7)**	**28.33(6)**	**90**	**90**	**90**				
Fully atomistic CrystalOptimizer	6.14	8.02	27.83	90	90	90	-118.03	1.21	13(0.136)	
CrystalOptimizer (8 DOFs)	6.19	8.02	27.71	90	90	90	-117.23	1.21	13(0.140)	
AXAGEL01										
Experimental	**6.04092(12)**	**7.95113(18)**	**27.2870(6)**	**90**	**90**	**90**				
Fully atomistic CrystalOptimizer	6.14	8.02	27.83	90	90	90	-117.98	1.21	15(0.177)	
CrystalOptimizer (8 DOFs)	6.17	8.05	27.69	90	90	90	-117.34	1.21	15(0.179)	15(0.054)
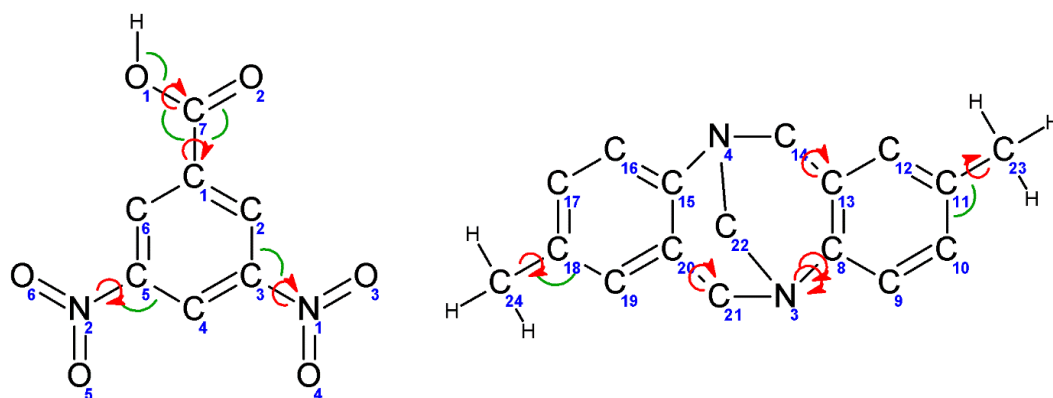
Figure 82. Diagram showing both the numbering of the atoms in cocrystal XXV and the degrees of freedom that were optimised by CrystalOptimizer. Dihedrals (red): H4-O1-C7-C1, O1-C7-C1-C2, O3-N1-C3-C2, O5-N2-C5-C4, C22-N3-C8-C13, C21-N3-C8-C13, C15-C20-C21-N3, N4-C14-C13-C8, H17-C23-C11-C10 and H20-C24-C18-C17. Bond angles (green): H4-O1-C7, O1-C7-C1, O2-C7-C1, N1-C3-C2, N2-C5-C4, C24-C18-C17 and C23-C11-C10.

CrystalOptimizer calculations were then carried out on the individual components CUCKAM04, CUKCAM22, DILLEP, AXAGEL and AXAGEL01 optimising only the selected degrees of freedom as shown in Figure 82. Table 29 reports the results of the fully atomistic CrystalOptimizer runs as well as the calculations where only the selected degrees of freedom were optimised. The results show a good agreement between the fully atomistic CrystalOptimizer runs and the runs optimising only the selected degrees of freedom which gives us confidence that the chosen degrees of freedom (totalling 17) for cocrystal XXV will give us an adequate model.

6.5.3 Rigid Body Crystal Energy Landscape

Analysis of how frequently CrystalPredictor generated the crystal structures, showed that most structures had only been found a few times when 1,000,000 structures were initially generated. To try and make sure the search space was covered adequately, an additional tranche of another 1,000,000 structures were generated which included some important new structures together with the structure that was eventually matched to the experimental structure. However, even after 2,000,000 structures, it was not clear that the search was complete as many low energy structures were still only found once or twice in the search. Due to time constraints on the blind test, no further searches were carried out and further calculations were carried out on the lowest energy structures from the 2,000,000 generated.

Refinement of the rigid CrystalPredictor structures by adding multipoles produced the crystal energy landscape shown in Figure 83. All structures contained the same $D_1^1(2)$ hydrogen bonding motif with a hydrogen bond forming between the acidic proton on 3,5-DNBA and a nitrogen atom on Tröger's Base. There were three structures grouped at the global minimum of which two were very similar P-1 structures and the other was a P2$_1$/c structure.
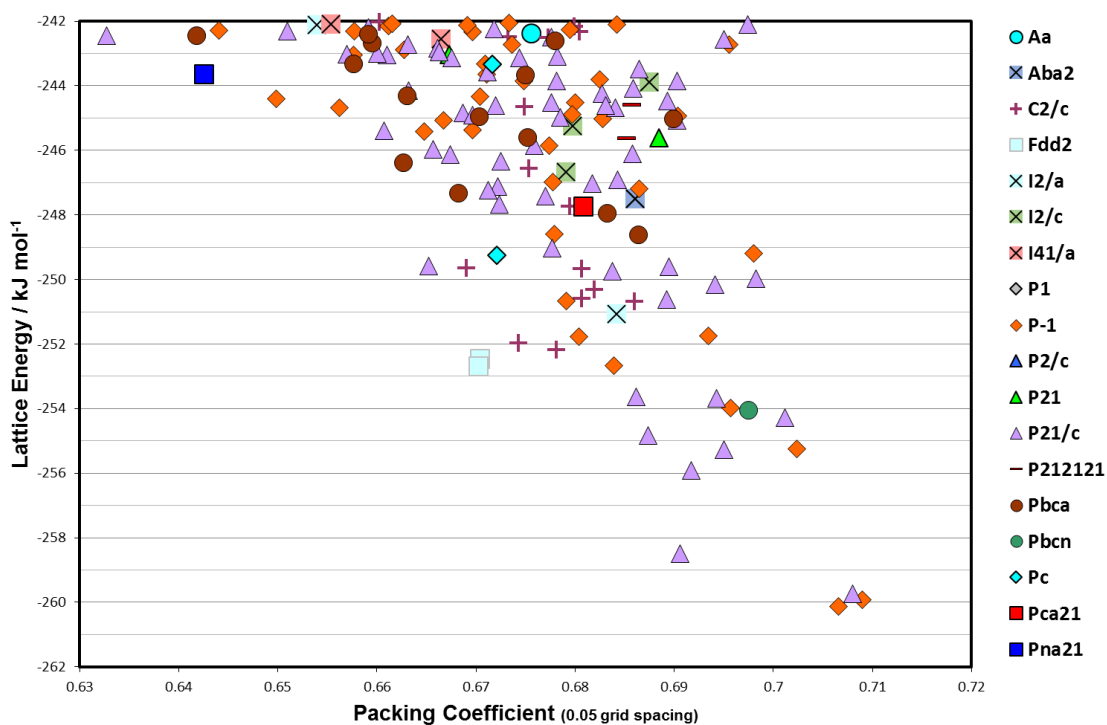
Figure 83. The lowest 20 kJ mol⁻¹ of the rigid body crystal energy landscape of cocrystal XXV where each symbol represents a crystal structure of the specified space group which is a minimum in the lattice energy calculated using DMACRYS.

6.5.4 Crystal Energy Landscape Following Refinement of the Flexible Degrees of Freedom
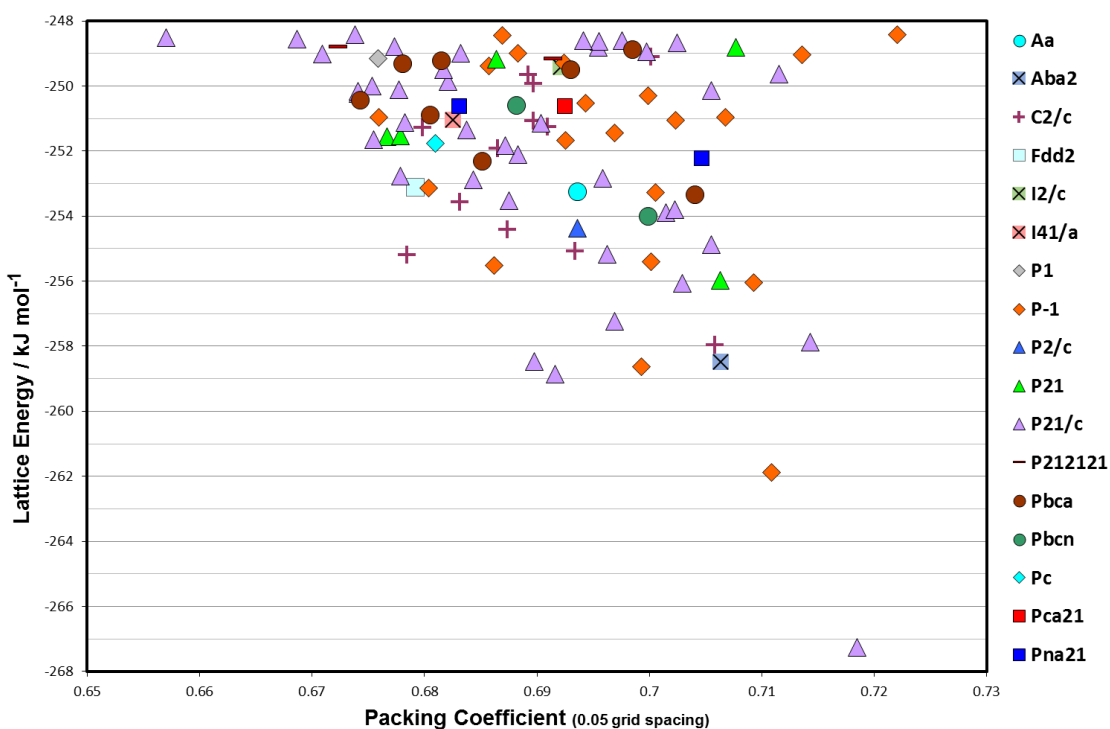
Figure 84. The lowest 100 structures, covering around 20 kJ mol⁻¹ of the crystal energy landscape of cocrystal XXV where each symbol represents a crystal structure of the specified space group which is a minimum in the lattice energy following CrystalOptimizer. The 17 degrees of freedom shown in Figure 83 were optimised using CrystalOptimizer. The P2₁/c global minimum structure is 5.4 kJ mol⁻¹ more stable than the next most thermodynamically stable structure.

161

The optimisation of the angles and dihedrals by CrystalOptimizer changed the relative rankings of the hypothetical crystal structures. The lowest P2$_1$/c structure on Figure 83 increases in density and significantly lowers its energy by 7.5 kJ mol^{-1}, in comparison the two low energy P-1 structures merged to the same structure and only lowered in lattice energy by about 2 kJ mol^{-1}. Hence, there is now a clear, thermodynamically favoured structure of P2$_1$/c symmetry that is more stable than the others by 5.4 kJ mol^{-1} (Figure 84). This energy gap is comparable to that observed on the crystal energy landscape of isocaffeine (6.05 kJ mol^{-1}) where calculations helped to highlight the difference between the crystallisation tendencies of caffeine and isocaffeine and helped to explain the singular solid form of isocaffeine compared to the disordered and multiple forms of caffeine.[83] The top 100 structures from calculations at this point were submitted as List 1.

6.5.5   Choice of Structures for Submission
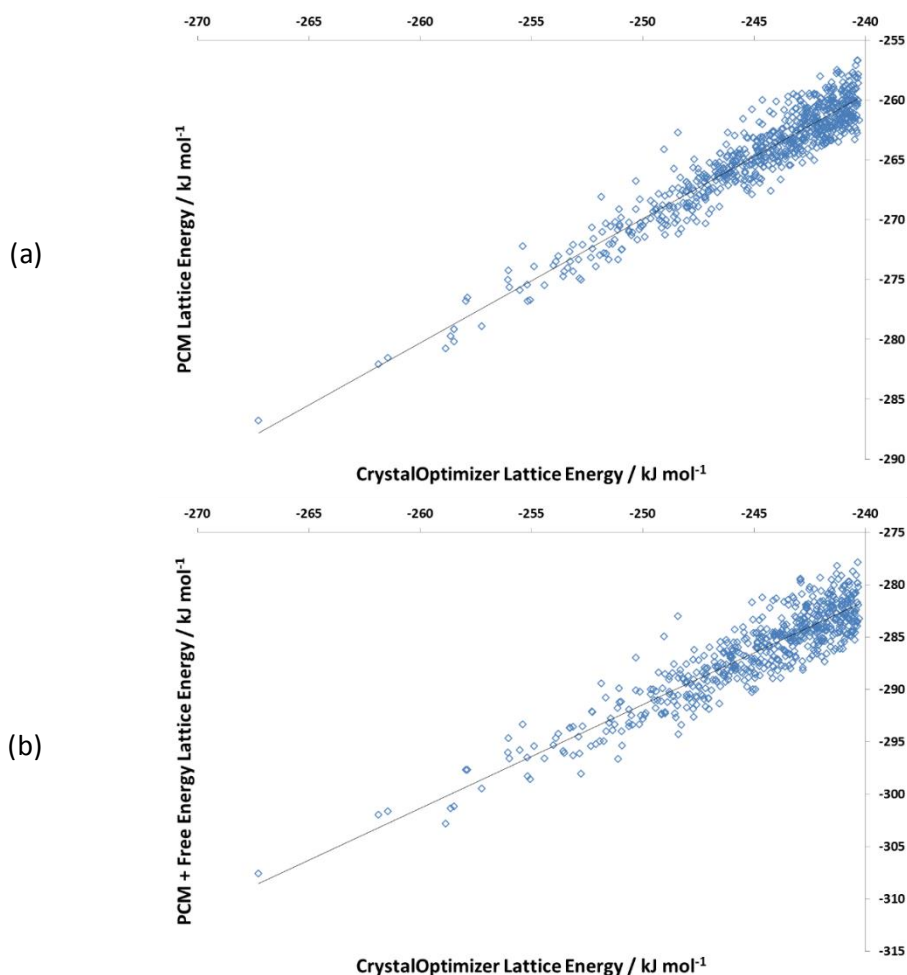
Figure 85. Comparing the relative lattice energies of hypothetical crystal structures of blind test target XXV using different methods of calculation. (a) The energies resulting from CrystalOptimizer calculations plotted against the results from DMACRYS+PCM calculations show a good agreement between the two methods with an average residual of 1.13 kJ mol^{-1}. (b) The energies resulting from CrystalOptimizer calculations plotted against the results from DMACRYS+PCM+Free Energy calculations again show a good agreement between the two methods with an average residual of 1.46 kJ mol^{-1}.

To establish whether or not the large energetic preference for the P2$_1$/c structure was an artefact of the choice of method, the sensitivity of the calculated lattice energies to two additional, different methods were tested. Figure 85 shows regression analysis comparing the lattice energies resulting from the CrystalOptimizer calculations with lattice energies calculated using (a) the PCM and (b) the PCM and the Helmholtz free energy estimation at 298 K. The strong correlation between the lattice energies calculated using different methods in the graphs in Figure 85 shows that there is no significant re-ranking in the structures when the method of lattice energy calculation is changed. This is supported further by the low average residual lattice energies of 1.13 kJ mol^{-1} and 1.46 kJ mol^{-1}, that result when comparing the CrystalOptimizer lattice energies with the PCM and Helmholtz free energies respectively. The ranking of the low energy generated structures of cocrystal XXV is not very sensitive to the choice of method for lattice energy evaluation and the P2$_1$/c structure is the global minimum structure in all three energy models following the CrystalOptimizer calculations.
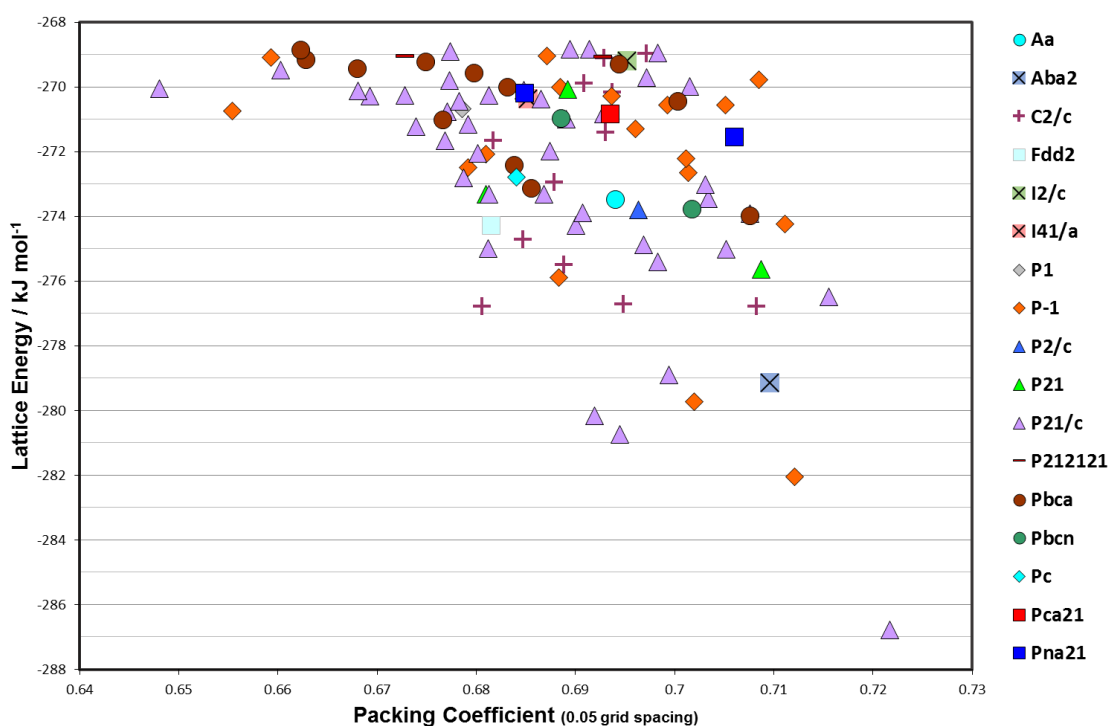
Figure 86. The crystal energy landscape of cocrystal XXV showing the lowest 100 structures where each symbol represents a crystal strcuture of the specified space group which is a minimum in the lattice energy calculated using the polarizable continuum (ε = 3.0) and estimating the free energy. The P2$_1$/c global minimum structure is 4.7 kJ mol^{-1} more stable than the next most thermodynamically stable structure.

In comparison to List 1 which was the 100 lowest unique structures following CrystalOptimizer calculations, for List 2, the PCM and the Helmholtz free energies were additionally calculated. The packings of the CSP generated structures were also manually examined to remove structures that were so closely related to a lower energy structure that it seemed unlikely that they would crystallise as separate polymorphs. The free energy could not

be calculated for roughly 10% of the structures, which were therefore omitted from List2. As only a handful of duplicate structures were manually removed from List 2 and the generated structures were not sensitive to the choice of method of evaluation of lattice energy, there is a large overlap between the two lists of submitted structures. Hence, Figure 86 (the crystal energy landscape of List 2) and Figure 84 (the crystal energy landscape of List 1) look fairly similar.

Both List 1 and List 2 suggest that the energetically favourable P2$_1$/c structure (first entry in Table 30) should be the experimental structure. The submission was expected to be successful as long as the search space was adequate and the experimental structure was found in our original search that generated 2,000,000 structures.
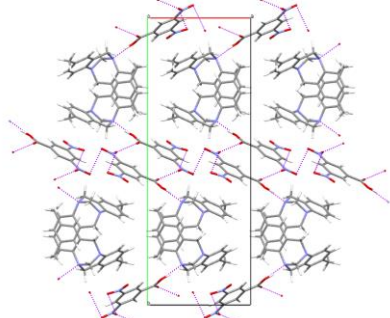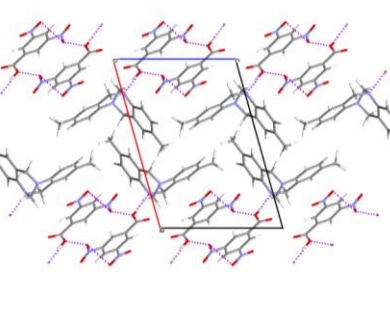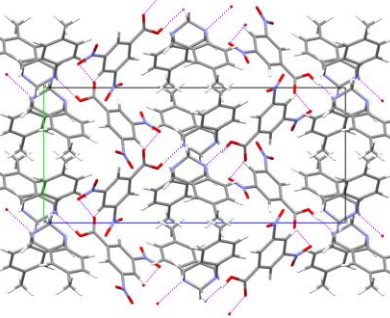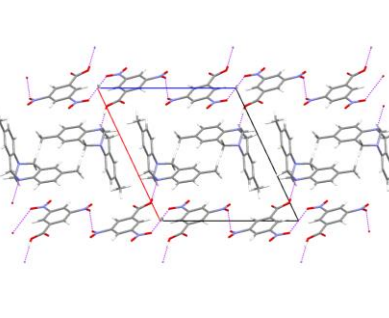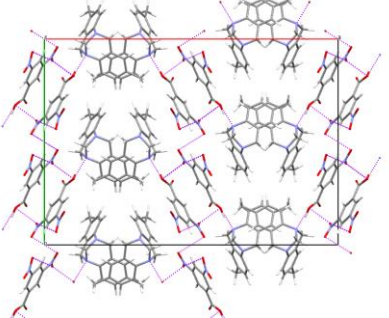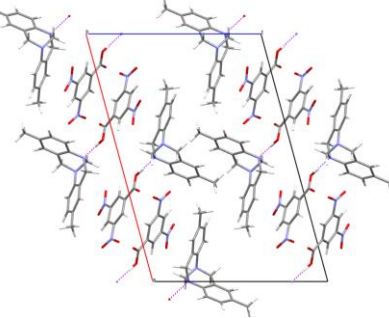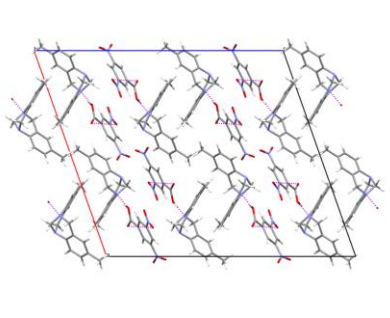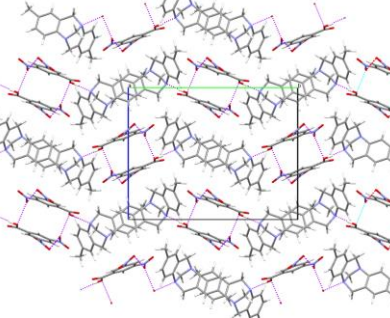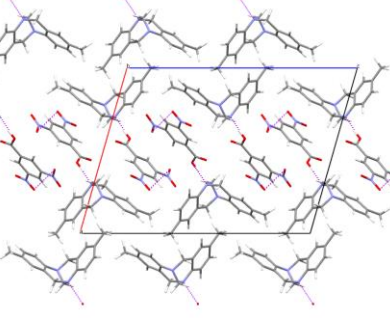
Inspection of the low energy hypothetical structures of the cocrystal XXV from List 1 (partly displayed in Table 30) shows that all of the structures contained the expected COOH···N hydrogen bond (the same $D_1^1(2)$ hydrogen bonding motif) and almost all of the cocrystals had layers of Tröger's Base molecules linked by layers of the 3,5-DNBA coformer. Within the layers of Tröger's Base, the molecules adopt the same packing motifs as observed in the individual component crystal structures and other derivatives of Tröger's Base found on the CSD (Figure 87).[200]
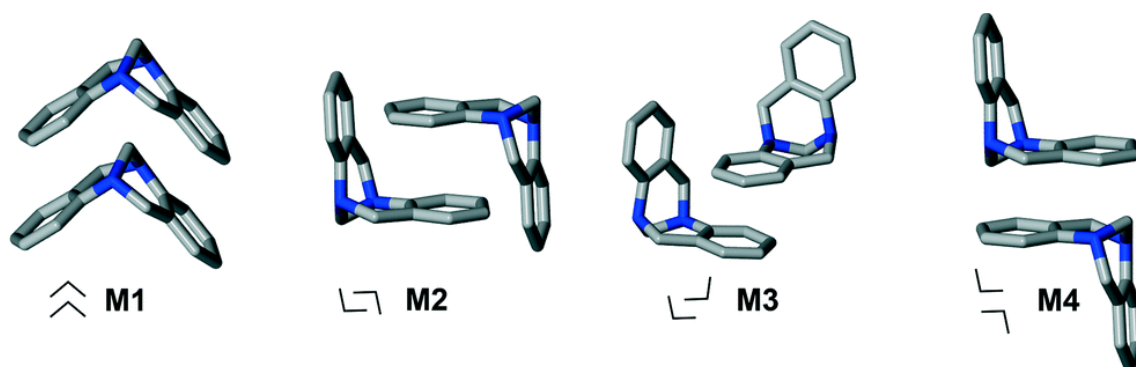
Figure 87. Packing motifs of Tröger's Base molecules and derivatives identified from inspection of the CSD (Version 5.35, November 2013) by Cross et al. 2014.[200] Motifs M2, M3 and M4 are often found within the hypothetical cocrystal structures of XXV.

There was a large variety of π···π stacking geometries within the layers of the individual components and also between the different components in the generated crystal structures. There was also a large range of different orientations of the molecules relative to the approximately linear O-H···N hydrogen bond which is the reason only a few structures were eliminated when considering structures (on List 2) that were too similar to be able to remain distinct during crystallization. The cocrystal was estimated to be significantly more stable than the components (by almost 25 kJ mol^{-1}), and the slow evaporation conditions suggest thermodynamic control of the crystallization.

Table 30. The nine lowest energy hypothetical structures of cocrystal XXV on List 1 following CrystalOptimizer calculations showing the ranking of the structures and their space groups. All structures have the same $D_1^1(2)$ hydrogen bonding motif.

1 P2₁/c		**4** P-1		**7** I2/a	
2 P-1		**5** Aba2		**8** P2₁/c	
3 P2₁/c		**6** P2₁/a		**9** P2₁/c	

6.5.6 Revelation of the experimental structure

Cell parameters	a (Å)	b (Å)	c (Å)	β (°)
(a)	10.7	27.9	7.8	69.2

Cell parameters	a (Å)	b (Å)	c (Å)	β (°)
(b)	10.408(3)	27.547(7)	8.112(2)	109.58(2)
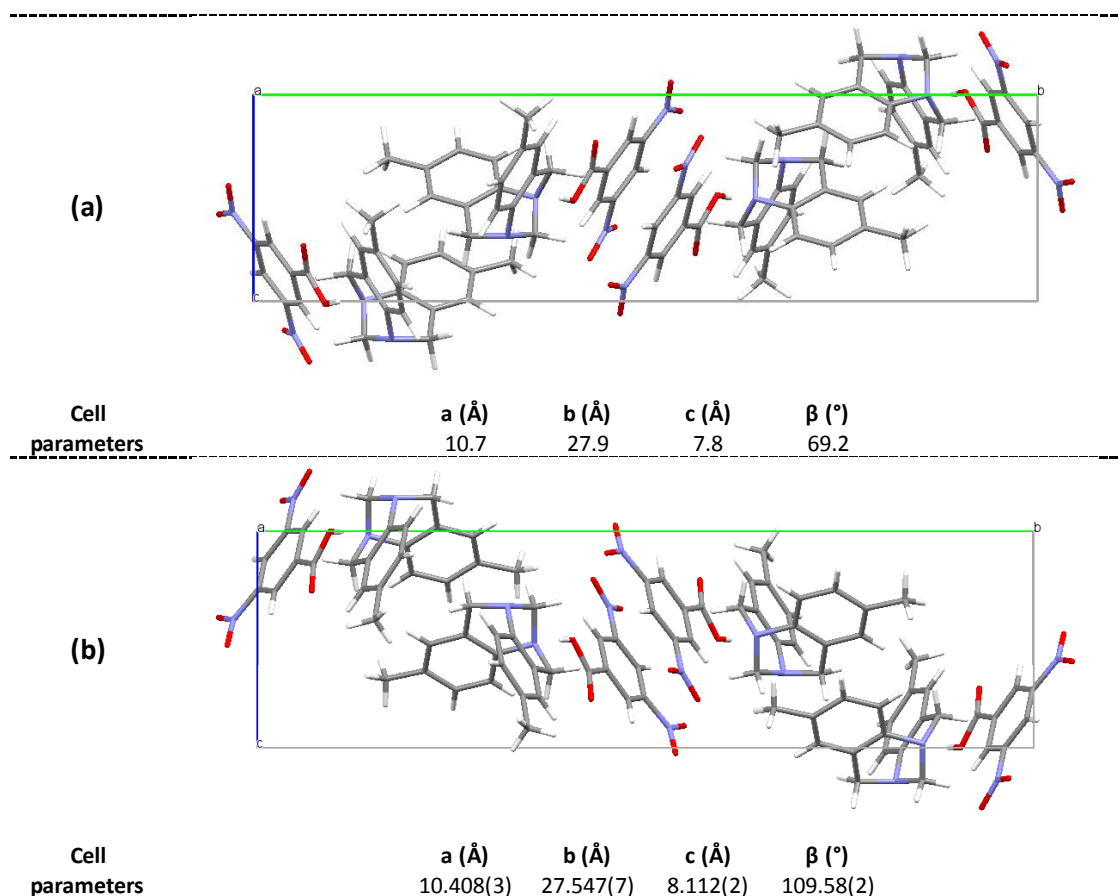
Figure 88. Diagrams and unit cell data for (a) the global minimum structure from List 1 of our predictions and (b) the experimental structure provided to partipicants by the CCDC at the end of the blind test. Both structures have P2$_1$/c symmetry.

The prediction for cocrystal XXV was successful as the global minimum predicted structure matched the experimental structure with not only a good 20 molecule overlay (rmsd$_{20}$ = 0.310 Å), as per the criteria from the CCDC for a successful prediction, but also a good 30 molecule overlay, rmsd$_{30}$ = 0.361 Å (Figure 89). These results are the rmsd$_n$ values from the comparison of the experimental structure with the global minimum P2$_1$/c structure from List 2, following PCM and Helmholtz free energy estimation calculations. The global minimum structure from List 1 also has a good overlay with the experimental structure (rmsd$_{20}$ = 0.317 Å and rmsd$_{30}$ = 0.367 Å), but as the rmsd$_n$ values are slightly greater. It can be concluded that performing the PCM and Helmholtz free energy estimation calculations in the case of this cocrystal XXV, alters the structure minimally so that it is closer to the observed experimental structure.
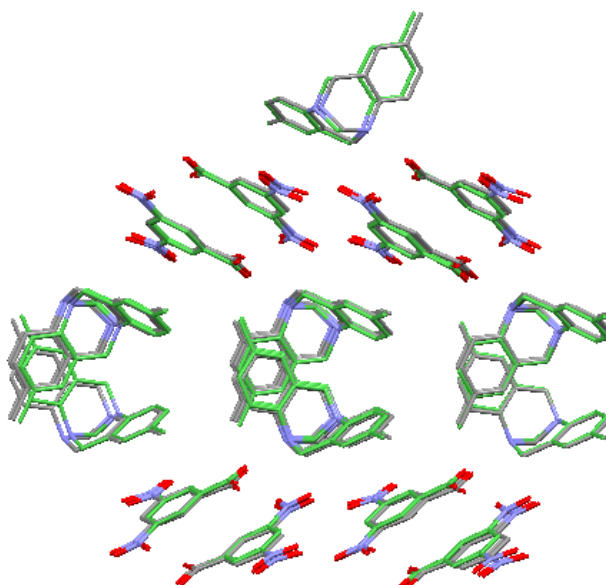
Figure 89. 30 molecule overlay of the experimental structure revealed by the CCDC (by element) with the hypothetical global minimum $P2_1/c$ structure from both List 1 and List 2, $rmsdn_{30} = 0.361$ Å.

During the year of the blind test, additional experimental work was performed on some of the systems. A low temperature (100 K) redetermination of the structure of XXV revealed that there was a significant amount of proton transfer from the carboxylic acid group to the amine. A competitive refinement determined proton occupancies of 0.58 on the carboxylic acid oxygen and 0.42 on the nitrogen.[202] Our method could not predict anything other than a cocrystal and the prediction of a salt was not attempted.

In principle, period electronic structure calculations could show proton transfer, and indeed some participants generated some salt structures, but not the observed salt components. Previous CSP studies of pyridine carboxylic acid cocrystals and the corresponding pyridinuium carboxylate salts have shown that the crystal energy landscapes are very different, with proton disorder only being observed when both the salt and cocrystal have the same structure low in energy on the crystal energy landscape.[59] Proton transfer will only occur in lattice energy minimisation if there is no barrier to transfer. It is therefore not surprising that this disorder was not predicted, and indeed if the disorder in cocrystal XXV had been known prior to the start of the blind test, it may not have been selected as a target.

6.5.6.1   Discussion of Results of Other Participants

14 other CSP methods were applied to XXV, plus three attempts to re-rank structures generated from this work or another group. Only five full CSP studies found the observed structure within their top 100, emphasising the difficulty in two component searches.

The Imperial group which used the same CrystalPredictor and CrystalOptimizer codes also found the experimental structure as the global minimum. Their approach differed by

including flexibility in the search and by using a different functional M06/6-31G(d,p) for the distributed multipoles and intramolecular energy penalties. Van Eijck used the UPACK[203, 204] search method, but used a method of lattice energy minimisation that was very similar to this work (based on distributed multipoles and the FIT potential), thus also had the experimental structure as the global minimum. A new search method, USPEX,[205] and the commercial program GRACE[75] also found the experimental form. However, these submissions used periodic electronic structure methods to re-rank the structures, placing the experimental structure 2nd and 6th respectively.

The re-ranking of structures from this work by the Tkatchenko group resulted in the known form being the global minimum, stable by about 4 kJ mol^{-1}, but Brandenburg's method placed it 2nd, being about 1 kJ mol^{-1} higher in energy than their global minimum structure. Thus, the energy gap between the experimental form and other alternative structures is quite sensitive to the method of evaluating the lattice energy, with a surprising range of rankings amongst the expensive periodic electronic structure calculations.

The rival structures to the global minimum structure that were generated vary considerably in density, over the range of packing coefficients (0.66 − 0.74) seen for organic crystals. Since periodic electronic structure methods differ in their dispersion corrections and the dispersion contribution is a major component of the lattice energy, this may be a major factor in their difference in rankings comparing Tkatchenko's many body dispersion correction, which is theoretically the most realistic, and single point energy evaluations. Since the empirically fitted FIT potential also ranked the experimental structure as the most stable, it appears that its dispersion coefficients are rather appropriate for cocrystal XXV.

6.5.6.2 Other Blind Test Results.

The success in predicting the structure of XXV cannot be taken in isolation. The rest of the UCL group, using essentially the same methodology, found the crystal structures of XXII as 2nd, and XXVI as 1st in their second lists, failed to find the salt XXIV, and found the Z'=1 polymorphs of XXIII though some were rather high in energy. Overall, the Crystal Predictor search appears to be a very competitive method, probably the strongest alternative to the commercial code GRACE. The lattice energies evaluated from ab initio calculations on one molecule and the empirically fitted potentials appear to be reasonably good, though need calibrating against alternative methods for each application.

The 6th blind test showed that there is considerable advance in CSP. The full description is being published[202] and has already attracted considerable publicity.[206]

7 Conclusions and Future Work

As chloro and methyl groups have similar van der Waals volumes, they are thought to be interchangeable within crystal lattices following the Kitaigorodsky principle of close packing.[62] This thesis aimed to explore the consequences of chloro-methyl replacement on crystal structures and solid form landscape of MA and TA using a joint computational and experimental approach.

The joint computational and experimental approach not only explored any similarities and differences in the polymorphs and nucleation behaviour of MA and TA, but also aimed to develop the idea of targeting the growth of unobserved, thermodynamically plausible, polymorphs using isostructural heteroseed surfaces. The use of template surfaces in targeting unobserved solid forms is a useful technique because the ability to first nucleate a polymorph is a function of both thermodynamics and kinetics. The presence of a template crystal surface can change the kinetics of nucleation and can catalyse overcoming the barrier to change the polymorphic form of a compound. For example, template crystal surfaces have successfully been used to target the growth of CBZ V and CYH III by vapour deposition onto isostructural DHC II.[84,] [88] Additionally, the phenomenon of disappearing polymorphs has largely been attributed to the presence of template seeds.[8]

7.1 Results Summary

To complement an earlier CSP study on TA,[89] computational work first focused on carrying out a CSP study on MA. The CSP study generated a number of low energy crystal structures of MA that were competitive in energy with known polymorphs. Comparisons of both experimental and low energy, generated crystal structures of MA with observed crystal structures of the similar compound, TA, identified a number of isostructural relationships including MA I – TA IV and MA II – TA V as well as TA III – #6MA_288 and TA I – #19MA_5643, where #6MA_288 and #19MA_5643 are computationally generated structures. The results of the CSP study on MA initially indicated that there were two low energy, hypothetical crystal structures that were isostructural with known forms of TA. However, following the vapour deposition experiments and the nucleation and growth of a new polymorph of TA (form VII) an additional isostructural relationship was identified between #5MA_510 and TA form VII (section 5.3.2.1.7 in chapter 5).

The relative stabilities of the putative structures of MA have been shown to be sensitive to the choice of computational model which is an added complication when considering if #6MA_288, #19MA_5643 and #5MA_510 could be found experimentally. #6MA_288 was not targeted experimentally as isostructural TA form III can only be obtained

using PIHn[32] and attempts to use TA form I to template #19MA_5643 and TA form VII to template #5MA_510 were unsuccessful (chapter 5, sections 5.2.2.3.1 and 5.3.2.2).

The isostructural relationship between MA form I and TA form IV appeared to satisfy the conditions for a solid solution, as stated by Kitaigorodsky.[63] Cocrystallisation of MA and TA from ethanol produced solid solution crystals that are isomorphous to MA form I with a bulk composition representative of the intended molar ratio of MA:TA. The MA-TA solid solution series (chapter 4) showed that TA was soluble in MA form I up to around 80 %. The identification of the MA-TA solid solution series led to heteroseeding experiments where MA form I seeds facilitated the first nucleation of TA form VI from a supersaturated solution of TA in ethanol. TA form VI is isomorphous with MA form I and has crystallographic similarities with TA form IV with $rmsd_{14}$ values around 0.3 Å. TA form VI was not found on the crystal energy landscape for TA produced by Uzoh[89] which emphasised the need for a greater number of computationally generated structures to be minimised than were evaluated by Uzoh.[170]

The isostructural relationships that exist between both hypothetical and experimentally observed crystal structures of MA and TA provided rationale for investigating the sublimation behaviour and vapour deposition of MA and TA. The sublimation experiments were guided by the initial successes of the methods used to first nucleate CBZ V[84] and were carried out at the same time as further experiments targeted the growth of CBZ V and CYH III on isostructural DHC II[88] as part of a project investigating templating by sublimation. Sublimation of TA onto a MA form I template crystal (section 5.2.2.3.2) grew single crystals of TA form I and not isomorphous TA form VI that was obtained from the solution seeding experiments (chapter 4, section 4.3).

The experiments highlighted how difficult analysis of deposition onto single crystals can be. As the template and target crystals are isomorphous, epitaxial growth might be expected to give rise to a uniform layer of the target crystal structure covering the template seed which would be hard to characterise.[88] It would also be difficult to distinguish new forms obtained from the deposition of different microcrystalline layers, one on top of another, of TA and MA. Additionally, as was evident with TA forms IV and VI, subtle differences between polymorphs of a compound can be hard to characterise.

The sublimation experiments that used the bespoke apparatus described in section 5.3.1.1 produced a new form of TA (form VII) when TA was deposited onto both copper and glass surfaces that were held at room temperature (section 5.3.2.1). TA form VII is related to TA form I and both crystal structures have the same double layer of molecules consisting of carboxylic acid dimers, but the structures differ in the stacking of the double layers. The simultaneous DSC-XRD experiments carried out at the Diamond Light Source proved to be a powerful tool in analysing the thermal behaviour of TA form VII, confirming that it transforms to TA I upon

heating in the DSC. TA form VII was not found on the crystal energy landscape for TA produced by Uzoh.[89]

TA form VII is isostructural with #5MA_510 from the CSP study on MA, however, deposition of MA onto the same copper surface under the same conditions produced MA form I and not the isostructural form. Furthermore, deposition of MA onto a template surface of microcrystalline TA form VII failed to nucleate the isostructural form of MA, #5MA_510.

The vapour deposition experiments showed that under the same conditions, MA and TA behave very differently. Results show that the polymorphic form of MA is dependent on the identity of the surface with form I growing on copper, TA form I single crystals and microcrystalline TA form VII, but form II growing on glass surfaces. In comparison, the identity of the deposition surface does not affect the polymorphic form of TA. It is possible that the temperature of the surface affects the polymorphic form of TA with TA form I obtained when the deposition surface temperature is high and TA form VII obtained when the deposition surfaces are held at room temperature.

Due to the nature of the experimental work in this thesis, analysis of the polymorphic form that results from any of the experiments, is limited to the polymorphic form observed at the end. Therefore, the growth of any short lived, kinetic polymorphs would not be observed if they have transformed to a more stable form even if it is not the most stable form. As of yet there is no *in situ* method of characterising the polymorphic form of a compound from either solution based or vapour deposition experiments.

The computational and experimental results in this thesis highlight the complexity of the MA and TA polymorphic systems. The results suggest that even though MA and TA are molecularly isostructural and chloro and methyl groups have similar van der Waals volumes, these facts alone are not enough to ensure that isostructural crystals will be observed experimentally even though a number of isostructural relationships between MA and TA do exist and isostructural structures are generated by CSP methods. The extent of polymorphism of MA and TA is molecule specific and the differences between chloro and methyl group interactions significantly contributes to the differences that are observed in the polymorphs of MA and TA.

7.2   Revisiting the Crystal Energy Landscape of Tolfenamic Acid

Even though TA form VI and TA form VII are Z' = 1 structures, they were not on the crystal energy landscape produced for TA by Uzoh.[89] The experimental identification of two new polymorphs of TA in this thesis highlighted the need to minimise thousands of putative structures rather than hundreds to ensure that all structures, that minimise to be competitive in energy with known polymorphs or the global minimum, have been refined at the optimum level of theory (discussed in section 4.4). With this in mind, the crystal energy landscape of TA

was recalculated by Louise Price so that the crystal energy landscapes of MA and TA could be compared and contrasted to evaluate how chloro-methyl replacement within crystal structures affects the relative stability of the crystal structures.

The recalculated crystal energy landscape of TA is shown alongside the crystal energy landscape of MA in Figure 90. The crystal structures on both landscapes (calculated within the polarisable continuum) have been evaluated at the same level of theory, PBE0/6-31+G(d), and a similar number of structures were optimised using CrystalOptimizer, 1859 for MA and 1872 for TA. The lattice energies for fewer structures of TA than MA were calculated within the polarisable continuum, 659 for TA compared to 1260 for MA, yet the low energy region of the crystal energy landscape for TA is more populated than the crystal energy landscape of MA. The more populated landscape of TA shows that there appears to be a number of more favourable packings of molecules of TA compared to MA which is mirrored experimentally as there are now seven forms of TA compared to three for MA.

In additional to the previously known forms of TA (I – V) both of the new polymorphs obtained experimentally in this thesis (VI and VII) were found on the crystal energy landscape of TA that was produced by Louise Price. Furthermore, Figure 90b shows that both forms appear to be competitive in energy with known forms of TA.

Figure 90 highlights the isostructural relationships that exist between experimentally observed polymorphs of MA and TA with either (a) other experimentally observed polymorphs or (b) CSP generated crystal structures. There are also many additional isostructural relationships that exist between hypothetical crystal structures of MA and hypothetical crystal structures of TA. Upon replacement of a methyl group with a chloro group, the relative stabilities and rank order of the crystal structures are significantly altered.

The cluster of structures around the global minimum on the crystal energy landscape for MA that relate to MA form I are not isostructural with the global minimum structure for TA. However, MA form I is isostructural with known forms of TA (IV and VI) that are relatively low in energy on the crystal energy landscape in Figure 90. In comparison, TA form I is isostructural with a hypothetical crystal structure of MA (#19MA_5643) which is relatively high in energy, around 5 kJ mol^{-1} less stable that TA form I. If the respective lattice energies of MA and TA from this computational model are to be believed, it could help explain the existence of the MA-TA solid solution that is isomorphous to MA form I and not TA form I even though both MA form I and TA form I crystallise from ethanol.
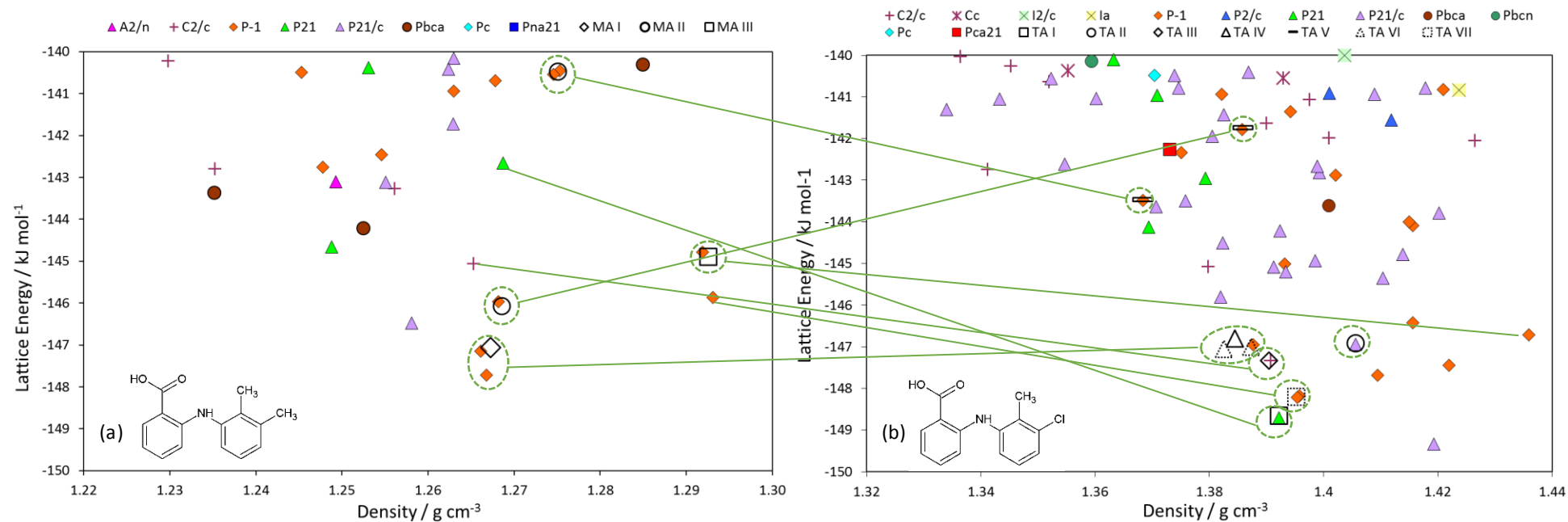
Figure 90. Comparison of the crystal energy landscapes of (a) MA and (b) TA. Each symbol represents a crystal structure of the specified space group which is a minimum in the lattice energy (calculated within the polarizable continuum). In total, 1260 lattice energy minimisations were carried out for MA in comparison to 659 for TA. The dashed green circles group isostructural crystal structures where one structure is observed experimentally. The green lines link isostructural MA and TA structures where at least one structure is observed experimentally. Two ordered structures are included for the disordered crystal structures MA II, TA V and TA VI.
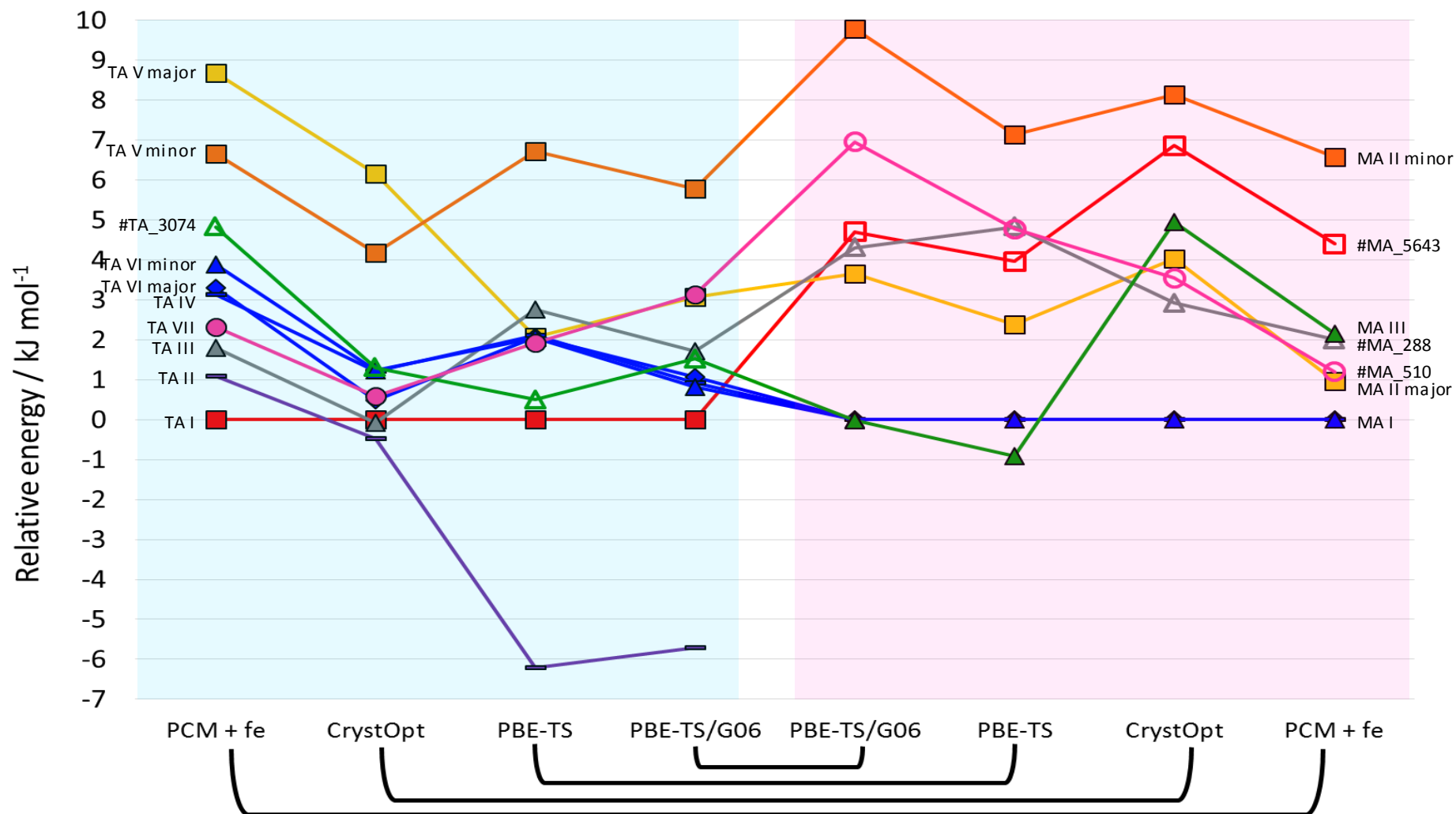
Figure 91. Comparison of the relative energies of different structures of TA (left hand side, blue box) and MA (right hand side, pink box) calculated using four different computational models. All energies are relative to the most stable experimental structure which are TA I and MA I. Filled markers represent experimental structures and unfilled markers represent hypothetical structures that are isostructural to known polymorphs of the other compound. Data for the figure was collated by Louise Price.

It is important to evaluate the lattice energies using different computational models so that the sensitivity of the structures to the method of calculation can be evaluated. Figure 91 shows the energies of structures of MA and TA relative to the energy of MA form I and TA form I respectively. The lattice energies were evaluated using four different computational models: by using CrystalOptimizer (CrystOpt); by applying the polarisable continuum and estimating the Helmholtz free energy (PCM + fe); by carrying out periodic DFT+D calculations with the Tkatchenko-Scheffler dispersion correction (PBE-TS); by recalculating the lattice energy of the PBE-TS structures with the Grimme, G06, dispersion correction (PBE-TS/G06). The PBE-TS and PBE-TS/G06 calculations were carried out by Rui Guo on the UK National High Performance Computing Facility, ARCHER (as in chapter 3).

The relative energies and ranking of the crystal structures in Figure 91 are shown to be dependent on the choice of computational model which has implications when isostructural templates are identified to target the nucleation of predicted forms. For example, the three unobserved, predicted forms of MA, appear to increase in energy when calculated using periodic electronic structure calculations, so that they may be too high in energy to be found experimentally.

The stability of TA form II is of particular interest because it significantly increases when calculated using periodic electronic structure calculations. As the hydrogen bonding is the same amongst all the generated structures, the dispersion contribution is a major component of the lattice energy. Dispersion corrections tend to favour more dense structures and TA form II is the most dense observed polymorph of TA. The effect of the dispersion correction on the lattice energies of putative structures has already been discussed in chapter 6 in the context of the blind test. Dispersion corrections are empirical and many research groups are continually developing and improving dispersion corrections such as Tkatchenko-Scheffler,[154, 207] Grimme[208] and Neumann-Perrin[209] to name but a few. Hence, the stability of TA form II may be an artifact of using early models for the dispersion correction. Otherwise, the calculations are broadly in agreement with each other and experiment, confirming that the ordered polymorphs are very close in energy.

7.3 Conclusions in Light of the Recalculated Crystal Energy Landscape of Tolfenamic Acid

It is important to note that CSP studies only consider the thermodynamics of a system and do not take into account the kinetics of nucleation. Therefore, although all structures on the crystal energy landscapes in Figure 90 might be considered thermodynamically feasible for conformational polymorphs,[2] not all structures will be observed experimentally due to kinetics. Price suggests that predicted polymorphs might not be observed experimentally because the

right crystallisation experiment is yet to be carried out.[210] The serendipitous discovery of TA form VII from vapour phase deposition under vacuum could be seen as an example of this.

The successful prediction of the XXV cocrystal in the blind test increases the confidence in the CSP methodology that was used for the calculation of crystal energy landscapes of MA and TA. Furthermore, Uzoh's crystal energy landscape for TA was reproduced when the CSP study was revisited and recalculated by Louise Price which confirmed that the only issue with the initial CSP study was the limited number of crystal structure minimisations.

In this thesis, the CSP calculations on MA and TA have helped to evaluate the experimental results with regards to the identification of TA VI and TA VII and the MA-TA solid solution. The calculated lattice energies of structures of MA and TA show that chloro-methyl replacement within crystal structures affects the relative stability of isostructural crystal structures, whatever the method of calculation or computational model. However, the relative stabilities of the MA and TA structures are sensitive to the choice of computational model which highlights the difficulties faced by the CSP community in accurately modelling the lattice energies of compounds that are considered 'small molecules'. Even greater challenges are faced for larger, more pharmaceutically relevant, molecules.

7.4   Future Work

Although generated crystal structures of MA were found to be isostructural with observed forms of TA, template surfaces failed to nucleate new polymorphs of MA in the experiments carried out in this thesis. This could be due to lack of control in the experiments, because the correct experiment has yet to be carried out or because of limitations on the CSP theory which can't account for factors such as molecular rearrangement during nucleation, thermal effects and disorder components.[210]

The bespoke sublimation apparatus (section 5.3) provides control over the temperature of the evaporation source, the distance between the deposition plate and the starting material and the temperature of the deposition plate. Thus, further development of this sublimation technique could prove useful as many experimental variables can be changed and different surfaces can be investigated. An initial deposition experiment would look at the effect of changing the temperature of the deposition surface on the polymorphic form of TA as the original set of sublimation experiments nucleated TA form I, but the more sophisticated sublimation experiments nucleated TA form VII.

Another interesting series of sublimation experiments would be to deposit a layer of TA on top of microcrystalline MA form I to target isostructural TA form VI (or IV) in the absence of a solvent. Additionally, single crystals of observed polymorphs of MA and TA could be introduced into the sublimation experiments as template seeds. TA form III would be a template

seed of interest as the computational work suggests it was one of the most promising template crystals. If deposition onto single crystals or microcrystalline layers was carried out then much thought would be required in order to develop methods that enable detection and characterisation of the polymorphic form of the deposited material.

Overall, this comparison of MA and TA shows that chloro-methyl replacement produces some isostructural polymorphs, but also results in sufficient energy differences to affect the relative stability of the known and competitive computer generated structures. Further polymorphs of either system may well be found, with the work in this thesis illustrating the challenges in controlling their crystallisation.

Bibliography

(1)   Lohani, S.; Grant, D. J. W., Thermodynamics of Polymorphism. In *Polymorphism in the Pharmaceutical Industry*, Hilfiker, R., Ed. Wiley: 2007; Vol. First Edition, pp 21-41.

(2)   Cruz-Cabeza, A. J.; Reutzel-Edens, S. M.; Bernstein, J., Facts and fictions about polymorphism. *Chemical Society Reviews* **2015,** 44, 8619-8635.

(3)   Vippagunta, S. R.; Brittain, H. G.; Grant, D. J. W., Crystalline solids. *Advanced Drug Delivery Reviews* **2001,** 48, (1), 3-26.

(4)   Buanz, A. B. M.; Telford, R.; Scowen, I. J.; Gaisford, S., Rapid preparation of pharmaceutical co-crystals with thermal ink-jet printing. *CrystEngComm* **2013,** 15, (6), 1031-1035.

(5)   Bauer, J.; Spanton, S.; Henry, R.; Quick, J.; Dziki, W.; Porter, W.; Morris, J., Ritonavir: An extraordinary example of conformational polymorphism. *Pharmaceutical Research* **2001,** 18, (6), 859-866.

(6)   Chemburkar, S. R.; Bauer, J.; Deming, K.; Spiwek, H.; Patel, K.; Morris, J.; Henry, R.; Spanton, S.; Dziki, W.; Porter, W.; Quick, J.; Bauer, P.; Donaubauer, J.; Narayanan, B. A.; Soldani, M.; Riley, D.; McFarland, K., Dealing with the impact of ritonavir polymorphs on the late stages of bulk drug process development. *Organic Process Research & Development* **2000,** 4, (5), 413-417.

(7)   Dunitz, J. D.; Bernstein, J., Disappearing Polymorphs. *Accounts of Chemical Research* **1995,** 28, (4), 193-200.

(8)   Bucar, D. K.; Lancaster, R. W.; Bernstein, J., Disappearing Polymorphs Revisited. *Angewandte Chemie-International Edition* **2015,** 54, (24), 6972-6993.

(9)   Lancaster, R. W.; Karamertzanis, P. G.; Hulme, A. T.; Tocher, D. A.; Lewis, T. C.; Price, S. L., The Polymorphism of Progesterone: Stabilization of a 'Disappearing' Polymorph by Co-Crystallization. *Journal of Pharmaceutical Sciences* **2007,** 96, (12), 3419-3431.

(10)   Raw, A. S.; Furness, M. S.; Gill, D. S.; Adams, R. C.; Holcombe Jr, F. O.; Yu, L. X., Regulatory considerations of pharmaceutical solid polymorphism in Abbreviated New Drug Applications (ANDAs). *Advanced Drug Delivery Reviews* **2004,** 56, 397-414.

(11)   Aaltonen, J.; Alleso, M.; Mirza, S.; Koradia, V.; Gordon, K. C.; Rantanen, J., Solid form screening - A review. *European Journal of Pharmaceutics and Biopharmaceutics* **2009,** 71, (1), 23-37.

(12)   Morissette, S. L.; Almarsson, O.; Peterson, M. L.; Remenar, J. F.; Read, M. J.; Lemmo, A. V.; Ellis, S.; Cima, M. J.; Gardner, C. R., High-throughput crystallization: polymorphs, salts, co-crystals and solvates of phan-naceutical solids. *Advanced Drug Delivery Reviews* **2004,** 56, (3), 275-300.

(13)   Llinas, A.; Goodman, J. M., Polymorph Control: past, present and future. *Drug Discovery Today* **2008,** 13, (5/6), 198-210.

(14) Braun, D. E.; Karamertzanis, P. G.; Arlin, J. B.; Florence, A. J.; Kahlenberg, V.; Tocher, D. A.; Griesser, U. J.; Price, S. L., Solid-State Forms of beta-Resorcylic Acid: How Exhaustive Should a Polymorph Screen Be? *Crystal Growth & Design* **2011,** 11, (1), 210-220.

(15) Hilfiker, R.; De Paul, S. M.; Szelagiewicz, M., Approaches to Polymorph Screening. In *Polymorphism in the Pharmaceutical Industry*, Hilfiker, R., Ed. Wiley-VCH Verlag GmbH & Co. KGA: Weinham, 2008; pp 287-308.

(16) Nyvlt, J., The Ostwald Rule of Stages. *Crystal Research and Technology* **1995,** 30, (4), 443-449.

(17) Burley, J. C.; Duer, M. J.; Stein, R. S.; Vrcelj, R. M., Enforcing ostwald's rule of stages: Isolation of paracetamol forms III and II. *European Journal of Pharmaceutical Sciences* **2007,** 31, (5), 271-276.

(18) Bergfors, T., Seeds to crystals. *Journal of Structural Biology* **2003,** 142, (1), 66-76.

(19) Gu, C. H.; Chatterjee, K.; Young, V., Jr.; Grant, D. J. W., Stabilization of a metastable polymorph of sulfmerazine by structurally related additives. *Journal of Crystal Growth* **2002,** 235, (1-4), 471-481.

(20) Polito, M.; D'Oria, E.; Maini, L.; Karamertzanis, P. G.; Grepioni, F.; Braga, D.; Price, S. L., The crystal structures of chloro and methyl ortho-benzoic acids and their co-crystal: rationalizing similarities and differences. *CrystEngComm* **2008,** 10, 1848-1854.

(21) Braga, D.; Grepioni, F.; Maini, L.; Polito, M.; Rubini, K.; Chierotti, M. R.; Gobetto, R., Hetero-Seeding and Solid Mixture to Obtain New Crystalline Forms. *Chemistry-A European Journal* **2009,** 15, (6), 1508-1515.

(22) Lee, E. H.; Byrn, S. R.; Carvajal, M. T., Additive-induced metastable single crystal of mefenamic acid. *Pharmaceutical Research* **2006,** 23, (10), 2375-2380.

(23) Price, C. P.; Grzesiak, A. L.; Matzger, A. J., Crystalline polymorph selection and discovery with polymer heteronuclei. *Journal of the American Chemical Society* **2005,** 127, (15), 5512-5517.

(24) Desiraju, G. R.; Sarma, J. A. R. P., The chloro-methyl exchange rule and its violations in the packing of organic molecular solids. *Proceedings of the Indian Academy of Sciences-Chemical Sciences* **1986,** 96, (6), 599-605.

(25) Edwards, M. R.; Jones, W.; Motherwell, W. D. S., Cocrystal formation of 4-methyl and 4-chlorobenzamide with carboxylic acids: Chloro/methyl interchange and crystal structure. *CrystEngComm* **2006,** 8, (7), 545-551.

(26) Lopez-Mejias, V.; Knight, J. L.; Brooks, C. L.; Matzger, A. J., On the Mechanism of Crystalline Polymorph Selection by Polymer Heteronuclei. *Langmuir* **2011,** 27, (12), 7575-7579.

(27) Diao, Y.; Helgeson, M. E.; Siam, Z. A.; Doyle, P. S.; Myerson, A. S.; Hatton, T.; Trout, B. L., Nucleation under Soft Confinement: Role of Polymer-Solute Interactions. *Crystal Growth & Design* **2012,** 12, (1), 508-517.

(28) Pfund, L. Y.; Price, C. P.; Frick, J. J.; Matzger, A. J., Controlling Pharmaceutical Crystallization with Designed Polymeric Heteronuclei. *Journal of the American Chemical Society* **2015,** 137, (2), 871-875.

(29) Grzesiak, A. L.; Lang, M. D.; Kim, K.; Matzger, A. J., Comparison of the four anhydrous polymorphs of carbamazepine and the crystal structure of form I. *Journal of Pharmaceutical Sciences* **2003,** 92, (11), 2260-2271.

(30) Lang, M. D.; Grzesiak, A. L.; Matzger, A. J., The use of polymer heteronuclei for crystalline polymorph selection. *Journal of the American Chemical Society* **2002,** 124, (50), 14834-14835.

(31) Lopez-Mejias, V.; Kampf, J. W.; Matzger, A. J., Nonamorphism in Flufenamic Acid and a New Record for a Polymorphic Compound with Solved Structures. *Journal of the American Chemical Society* **2012,** 134, (24), 9872-9875.

(32) Lopez-Mejias, V.; Kampf, J. W.; Matzger, A. J., Polymer-Induced Heteronucleation of Tolfenamic Acid: Structural Investigation of a Pentamorph. *Journal of the American Chemical Society* **2009,** 131, (13), 4554-4555.

(33) Love, J. C.; Estroff, L. A.; Kriebel, J. K.; Nuzzo, R. G.; Whitesides, G. M., Self-Assembled Monolayers of Thiolates on Metals as a Form of Nanotechnology. *Chemical Reviews* **2005,** 105, (4), 1103-1170.

(34) Newman, A., Specialized Solid Form Screening Techniques. *Organic Process Research & Development* **2013,** 17, (3), 457-471.

(35) Lee, I. S.; Lee, A. Y.; Myerson, A. S., Concomitant polymorphism in confined environment. *Pharmaceutical Research* **2008,** 25, (4), 960-968.

(36) Yang, X.; Sarma, B.; Myerson, A. S., Polymorph Control of Micro/Nano-Sized Mefenamic Acid Crystals on Patterned Self-Assembled Monolayer Islands. *Crystal Growth & Design* **2012,** 12, (11), 5521-5528.

(37) Lee, E. H.; Boerrigter, S. X.; Byrn, S. R., Epitaxy of a Structurally Related Compound on the (100) Faces of Flufenamic Acid Form I and III Single Crystals. *Crystal Growth & Design* **2010,** 10, (2), 518-527.

(38) Mitchell, C. A.; Yu, L.; Ward, M. D., Selective nucleation and discovery of organic polymorphs through epitaxy with single crystal substrates. *Journal of the American Chemical Society* **2001,** 123, (44), 10830-10839.

(39) Gardner, C. R.; Almarsson, O.; Chen, H. M.; Morissette, S.; Peterson, M.; Zhang, Z.; Wang, S.; Lemmo, A.; Gonzalez-Zugasti, J.; Monagle, J.; Marchionna, J.; Ellis, S.; McNulty, C.; Johnson, A.; Levinson, D.; Cima, M., Application of high throughput technologies to drug substance and drug product development. *Computers & Chemical Engineering* **2004,** 28, (6-7), 943-953.

(40) Pfund, L. Y.; Matzger, A. J., Towards Exhaustive and Automated High-Throughput Screening for Crystalline Polymorphs. *ACS Combinatorial Science* **2014,** 16, (7), 309-313.

(41) Alvarez, A. J.; Singh, A.; Myerson, A. S., Polymorph Screening: Comparing a Semi-Automated Approach with a High Throughput Method. *Crystal Growth & Design* **2009,** 9, (9), 4181-4188.

(42) Gillon, A. L.; Feeder, N.; Davey, R. J.; Storey, R., Hydration in molecular crystals - A Cambridge Structural Database analysis. *Crystal Growth & Design* **2003,** 3, (5), 663-673.

(43) Khankari, R. K.; Grant, D. J. W., Pharmaceutical Hydrates. *Thermochimica Acta* **1995,** 248, 61-79.

(44) Jones, W.; Motherwell, S.; Trask, A. V., Pharmaceutical cocrystals: An emerging approach to physical property enhancement. *Mrs Bulletin* **2006,** 31, (11), 875-879.

(45) Elder, D. P.; Holm, R.; de Diego, H. L., Use of pharmaceutical salts and cocrystals to address the issue of poor solubility. *International Journal of Pharmaceutics* **2013,** 453, (1), 88-100.

(46) Desiraju, G. R., Crystal Engineering: From Molecule to Crystal. *Journal of the American Chemical Society* **2013,** 135, (27), 9952-9967.

(47) Sarma, B.; Saikia, B., Hydrogen bond synthon competition in the stabilization of theophylline cocrystals. *Crystengcomm* **2014,** 16, (22), 4753-4765.

(48) Delori, A.; Galek, P. T.; Pidcock, E.; Jones, W., Quantifying Homo- and Heteromolecular Hydrogen Bonds as a Guide for Adduct Formation. *Chemistry - A European Journal* **2012,** 18, (22), 6835-6846.

(49) Delori, A.; Galek, P. T.; Pidcock, E.; Patni, M.; Jones, W., Knowledge-based hydrogen bond prediction and the synthesis of salts and cocrystals of the anti-malarial drug pyrimethamine with various drug and GRAS molecules. *CrystEngComm* **2013,** 15, (15), 2916-2928.

(50) Morissette, S. L.; Almarsson, O.; Peterson, M. L.; Remenar, J. F.; Read, M. J.; Lemmo, A. V.; Ellis, S.; Cima, M. J.; Gardner, C. R., High-throughput crystallization: Polymorphs, salts, co-crystals and solvates of pharmaceutical solids. *Advanced Drug Delivery Reviews* **2004,** 56, (3), 275-300.

(51) Remenar, J. F.; MacPhee, J. M.; Larson, B. K.; Tyagi, V. A.; Ho, J. H.; McIlroy, D. A.; Hickey, M. B.; Shaw, P. B.; Almarsson, Ö., Salt Selection and Simultaneous Polymorphism Assessment via High-Throughput Crystallization: The Case of Sertraline. *Organic Process Research & Development* **2003,** 7, (6), 990-996.

(52) Kojima, T.; Tsutsumi, S.; Yamamoto, K.; Ikeda, Y.; Moriwaki, T., High-throughput cocrystal slurry screening by use of in situ Raman microscopy and multi-well plate. *International Journal of Pharmaceutics* **2010,** 399, (1-2), 52-59.

(53) Schultheiss, N.; Newman, A., Pharmaceutical Cocrystals and Their Physicochemical Properties. *Crystal Growth & Design* **2009,** 9, (6), 2950-2967.

(54) Gao, Y.; Zu, H.; Zhang, J., Enhanced dissolution and stability of adefovir dipivoxil by cocrystal formation. *Journal of Pharmacy and Pharmacology* **2011,** 63, (4), 483-490.

(55) Trask, A. V.; Motherwell, W. D. S.; Jones, W., Pharmaceutical cocrystallization: Engineering a remedy for caffeine hydration. *Crystal Growth & Design* **2005,** 5, (3), 1013-1021.

(56) Trask, A. V.; Motherwell, W. D. S.; Jones, W., Physical stability enhancement of theophylline via cocrystallization. *International Journal of Pharmaceutics* **2006,** 320, (1-2), 114-123.

(57) Cruz-Cabeza, A. J., Acid-base crystalline complexes and the pK(a) rule. *CrystEngComm* **2012,** 14, (20), 6362-6365.

(58) Mohamed, S.; Tocher, D. A.; Vickers, M.; Karamertzanis, P. G.; Price, S. L., Salt or cocrystal? A new series of crystal structures formed from simple pyridines and carboxylic acids. *Crystal Growth & Design* **2009,** 9, (6), 2881-2889.

(59) Mohamed, S.; Tocher, D. A.; Price, S. L., Computational prediction of salt and cocrystal structures-Does a proton position matter? *International Journal of Pharmaceutics* **2011,** 418, (2), 187-198.

(60) Eddleston, M. D.; Sivachelvam, S.; Jones, W., Screening for polymorphs of cocrystals: a case study. *CrystEngComm* **2013,** 15, (1), 175-181.

(61) Cherukuvada, S.; Nangia, A., Eutectics as improved pharmaceutical materials: design, properties and characterization. *Chemical Communications* **2014,** 50, (8), 906-923.

(62) Kitaigorodski, A. I., *Molecular Crystals and Molecules*. ed.; Academic Press: New York, 1973.

(63) Kitaigorodsky, A. I., *Mixed Crystals*. 1st ed.; Springer-Verlag: 1984; p 389.

(64) Kalman, A.; Parkanyi, L.; Argay, G., Classification Of The Isostructurality Of Organic-Molecules In The Crystalline State. *Acta Crystallographica Section B-Structural Science* **1993,** 49, 1039-1049.

(65) Fabian, L.; Kalman, A., Volumetric measure of isostructurality. *Acta Crystallographica Section B* **1999,** 55, (6), 1099-1108.

(66) Gelbrich, T.; Hursthouse, M. B., A versatile procedure for the identification, description and quantification of structural similarity in molecular crystals. *CrystEngComm* **2005,** 7, 324-336.

(67) Chisholm, J. A.; Motherwell, S., COMPACK: a program for identifying crystal structure similarity using distances. *Journal of Applied Crystallography* **2005,** 38, 228-231.

(68) Oliveira, M. A.; Peterson, M. L.; Klein, D., Continuously Substituted Solid Solutions of Organic Co-Crystals. *Crystal Growth & Design* **2008,** 8, (12), 4487-4493.

(69) Lusi, M.; Vitorica-Yrezabal, I. J.; Zaworotko, M. J., Expanding the Scope of Molecular Mixed Crystals Enabled by Three Component Solid Solutions. *Crystal Growth & Design* **2015,** 15, (8), 4098-4103.

(70) Price, S. L., Predicting crystal structures of organic compounds. *Chemical Society Reviews* **2014,** 43, (7), 2098-2111.

(71) Bardwell, D. A.; Adjiman, C. S.; Arnautova, Y. A.; Bartashevich, E.; Boerrigter, S. X. M.; Braun, D. E.; Cruz-Cabeza, A. J.; Day, G. M.; Della Valle, R. G.; Desiraju, G. R.; van Eijck, B. P.; Facelli, J. C.; Ferraro, M. B.; Grillo, D.; Habgood, M.; Hofmann, D. W. M.; Hofmann, F.; Jose, K. V. J.; Karamertzanis, P. G.; Kazantsev, A. V.; Kendrick, J.; Kuleshova, L. N.; Leusen, F. J. J.; Maleev, A. V.; Misquitta, A. J.; Mohamed, S.; Needs, R. J.; Neumann, M. A.; Nikylov, D.; Orendt, A. M.; Pal, R.; Pantelides, C. C.; Pickard, C. J.; Price, L. S.; Price, S. L.; Scheraga, H. A.; van de Streek, J.; Thakur, T. S.; Tiwari, S.; Venuti, E.; Zhitkov, I. K., Towards crystal structure prediction of complex organic compounds - a report on the fifth blind test. *Acta Crystallographica Section B-Structural Science* **2011,** 67, 535-551.

(72) Kazantsev, A. V.; Karamertzanis, P. G.; Adjiman, C. S.; Pantelides, C. C.; Price, S. L.; Galek, P. T. A.; Day, G. M.; Cruz-Cabeza, A. J., Successful prediction of a model pharmaceutical in the fifth blind test of crystal structure prediction. *International Journal of Pharmaceutics* **2011,** 418, (2), 168-178.

(73) Florence, A. J.; Johnston, A.; Price, S. L.; Nowell, H.; Kennedy, A. R.; Shankland, N., An automated parallel crystallisation search for predicted crystal structures and packing motifs of carbamazepine. *Journal of Pharmaceutical Sciences* **2006,** 95, (9), 1918-1930.

(74) Price, S. L., The computational prediction of pharmaceutical crystal structures and polymorphism. *Advanced Drug Delivery Reviews* **2004,** 56, (3), 301-319.

(75) Neumann, M. A. *GRACE (the Generation, Ranking and Characterisation Engine)*, 1.0; Avant-garde Materials Simulation Deutschland GmbH: 2007.

(76) Price, S. L.; Braun, D. E.; Reutzel-Edens, S. M., Can computed crystal energy landscapes help understand pharmaceutical solids? *Chemical Communications* **2016**.

(77) Price, L. S.; McMahon, J. A.; Lingireddy, S. R.; Lau, S. F.; Diseroad, B. A.; Price, S. L.; Reutzel-Edens, S. M., A molecular picture of the problems in ensuring structural purity of tazofelone. *Journal of Molecular Structure* **2014,** 1078, 26-42.

(78) Ismail, S. Z.; Anderton, C. L.; Copley, R. C.; Price, L. S.; Price, S. L., Evaluating a Crystal Energy Landscape in the Context of Industrial Polymorph Screening. *Crystal Growth & Design* **2013,** 13, (6), 2396-2406.

(79) Blagden, N.; Cross, W. I.; Davey, R. J.; Broderick, M.; Pritchard, R. G.; Roberts, R. J.; Rowe, R. C., Can crystal structure prediction be used as part of an integrated strategy for ensuring maximum diversity of isolated crystal forms? The case of 2-amino-4-nitrophenol. *Physical Chemistry Chemical Physics* **2001,** 3, (17), 3819-3825.

(80)   Cross, W. I.; Blagden, N.; Davey, R. J.; Pritchard, R. G.; Neumann, M. A.; Roberts, R. J.; Rowe, R. C., A whole output strategy for polymorph screening: Combining crystal structure prediction, graph set analysis, and targeted crystallization experiments in the case of diflunisal. *Crystal Growth & Design* **2003,** 3, (2), 151-158.

(81)   Price, S. L., Computed crystal energy landscapes for understanding and predicting organic crystal structures and polymorphism. *Accounts of Chemical Research* **2009,** 42, (1), 117-126.

(82)   Price, S. L., From crystal structure prediction to polymorph prediction: interpreting the crystal energy landscape. *Physical Chemistry Chemical Physics* **2008,** 10, (15), 1996-2009.

(83)   Habgood, M., Form II Caffeine: A Case Study for Confirming and Predicting Disorder in Organic Crystals. *Crystal Growth & Design* **2011,** 11, (8), 3600-3608.

(84)   Arlin, J. B.; Price, L. S.; Price, S. L.; Florence, A. J., A strategy for producing predicted polymorphs: catemeric carbamazepine form V. *Chemical Communications* **2011,** 47, (25), 7074-7076.

(85)   Cabeza, A. J. C.; Day, G. M.; Motherwell, W. D. S.; Jones, W., Amide pyramidalization in carbamazepine: A flexibility problem in crystal structure prediction? *Crystal Growth & Design* **2006,** 6, (8), 1858-1866.

(86)   Welch, G. W. A.; Karamertzanis, P. G.; Misquitta, A. J.; Stone, A. J.; Price, S. L., Is the induction energy important for modeling organic crystals? *Journal of Chemical Theory and Computation* **2008,** 4, (3), 522-532.

(87)   Florence, A. J.; Leech, C. K.; Shankland, N.; Shankland, K.; Johnston, A., Control and prediction of packing motifs: a rare occurrence of carbamazepine in a catemeric configuration. *CrystEngComm* **2006,** 8, (10), 746-747.

(88)   Srirambhatla, V. K.; Guo, R.; Price, S. L.; Florence, A. J., Isomorphous template induced crystallisation: a robust method for the targeted crystallisation of computationally predicted metastable polymorphs. *Chemical Communications* **2016,** 52, 7384-7386.

(89)   Uzoh, O. G.; Cruz-Cabeza, A. J.; Price, S. L., Is the Fenamate Group a Polymorphophore? Contrasting the Crystal Energy Landscapes of Fenamic and Tolfenamic Acids. *Crystal Growth & Design* **2012,** 12, (8), 4230-4239.

(90)   Mason, R. M.; Kendall, P. H., Fenamates in Medicine. *Rheumatology* **1966,** VIII, (suppl 1), 5-6.

(91)   Delgado, J.; Simonin, G.; Servier, C.; Garcia, R.; Yoma, J., Tolfenamic Acid And Mefenamic-Acid In The Treatment Of Primary Dysmenorrhea. *Pharmacology & Toxicology* **1994,** 75, 89-91.

(92)   Myles, A. B.; Bacon, P. A.; Williams, K. A., Mefenamic Acid In Rheumatoid Arthritis. *Annals of the Rheumatic Diseases* **1967,** 26, (6), 494-&.

(93)   Cahill, W. J.; Hill, R. D.; Jessop, J.; Kendall, P. H., Trial Of Mefenamic Acid. *Annals of physical medicine* **1965,** 8, 26-9.

(94)   Hakkarainen, H.; Vapaatalo, H.; Gothoni, G.; Parantainen, J., Tolfenamic Acid Is As Effective As Ergotamine During Migraine Attacks. *Lancet* **1979,** 2, (8138), 326-328.

(95)   Zeidan, T. A.; Trotta, J. T.; Tilak, P. A.; Oliveira, M. A.; Chiarella, R. A.; Foxman, B. M.; Almarsson, O.; Hickey, M. B., An unprecedented case of dodecamorphism: the twelfth polymorph of aripiprazole formed by seeding with its active metabolite. *Crystengcomm* **2016,** 18, (9), 1486-1488.

(96)   Macrae, C. F.; Edgington, P. R.; McCabe, P.; Pidcock, E.; Shields, G. P.; Taylor, R.; Towler, M.; van de Streek, J., Mercury: visualization and analysis of crystal structures. *Journal of Applied Crystallography* **2006,** 39, 453-457.

(97)   Macrae, C. F.; Bruno, I. J.; Chisholm, J. A.; Edgington, P. R.; McCabe, P.; Pidcock, E.; Rodriguez-Monge, L.; Taylor, R.; van de Streek, J.; Wood, P. A., Mercury CSD 2.0 - new features for the visualization and investigation of crystal structures. *Journal of Applied Crystallography* **2008,** 41, 466-470.

(98)   McConnell, J. F., FZ Company. N-(2, 3-xylyl) anthranilic acid, C15H15NO2 mefenamic acid. *Cryst.Struct.Commun* **1976,** 5, 861-864.

(99)   SeethaLekshmi, S.; Guru Row, T. N., Conformational Polymorphism in a Non-steroidal Anti-inflammatory Drug, Mefenamic Acid. *Crystal Growth & Design* **2012,** 12, (8), 4283-4289.

(100)   Wittering, K. E.; Agnew, L. R.; Klapwijk, A. R.; Robertson, K.; Cousen, A. J. P.; Cruickshank, D. L.; Wilson, C. C., Crystallisation and physicochemical property characterisation of conformationally-locked co-crystals of fenamic acid derivatives. *Crystengcomm* **2015,** 17, (19), 3610-3618.

(101)   Cesur, S.; Gokbel, S., Crystallization of mefenamic acid and polymorphs. *Crystal Research and Technology* **2008,** 43, (7), 720-728.

(102)   Kato, F.; Otsuka, M.; Matsuda, Y., Kinetic study of the transformation of mefenamic acid polymorphs in various solvents and under high humidity conditions. *International Journal of Pharmaceutics* **2006,** 321, (1), 18-26.

(103)   Panchagnula, R.; Sundaramurthy, P.; Pillai, O.; Agrawal, S.; Raj, Y. A., Solid-state characterization of mefenamic acid. *Journal of Pharmaceutical Sciences* **2004,** 93, (4), 1019-1029.

(104)   Gilpin, R. K.; Zhou, W., Infrared studies of the thermal conversion of mefenamic acid between polymorphic states. *Vibrational spectroscopy* **2005,** 37, (1), 53-59.

(105)   Roy, S.; Chamberlin, B.; Matzger, A. J., Polymorph Discrimination Using Low Wavenumber Raman Spectroscopy. *Organic Process Research & Development* **2013,** 17, (7), 976-980.

(106) Jabeen, S.; Dines, T. J.; Leharne, S. A.; Chowdhry, B. Z., Raman and IR spectroscopic studies of fenamates–Conformational differences in polymorphs of flufenamic acid, mefenamic acid and tolfenamic acid. *Spectrochimica Acta Part A: Molecular and Biomolecular Spectroscopy* **2012**.

(107) Dolomanov, O. V.; Bourhis, L. J.; Gildea, R. J.; Howard, J. A. K.; Puschmann, H., OLEX2: a complete structure solution, refinement and analysis program. *Journal of Applied Crystallography* **2009,** 42, 339-341.

(108) Sheldrick, G. M., A short history of SHELX. *Acta Crystallographica Section A - Foundations of Crystallography* **2008,** 64, (1), 112-122.

(109) Sheldrick, G. M., Crystal structure refinement with SHELXL. *Acta Crystallographica Section C-Structural Chemistry* **2015,** 71, 3-8.

(110) *ACD/Spectrus Processor 2015.2.5*, 14.00; Advanced Chemistry Development, Inc.: 2015.

(111) *Thermal Advantage Universal Analysis 2000*, 5.5.3; TA Instruments: 2013.

(112) Surov, A. O.; Szterner, P.; Zielenkiewicz, W.; Perlovich, G. L., Thermodynamic and structural study of tolfenamic acid polymorphs. *Journal of Pharmaceutical and Biomedical Analysis* **2009,** 50, (5), 831-840.

(113) Andersen, K. V.; Larsen, S.; Alhede, B.; Gelting, N.; Buchardt, O., Characterization of two polymorphic forms of tolfenamic acid, N-(2-methyl-3-chlorophenyl)anthranilic acid: their crystal structures and relative stabilities. *Journal of the Chemical Society, Perkin Transactions 2* **1989**, (10), 1443-1447.

(114) Mattei, A.; Li, T., Polymorph Formation and Nucleation Mechanism of Tolfenamic Acid in Solution: An Investigation of Pre-nucleation Solute Association. *Pharmaceutical Research* **2012,** 29, (2), 460-470.

(115) Mattei, A.; Li, T., Nucleation of Conformational Polymorphs: A Computational Study of Tolfenamic Acid by Explicit Solvation. *Crystal Growth & Design* **2014,** 14, (6), 2709-2713.

(116) Lopez-Mejias, V.; Matzger, A., Structure-Polymorphism Study of Fenamates: Toward Developing an Understanding of the Polymorphophore. *Crystal Growth & Design* **2015,** 15, (8), 3955-3962.

(117) Gilpin, R. K.; Zhou, W., Infrared studies of the polymorphic states of the fenamates. *Journal of Pharmaceutical and Biomedical Analysis* **2005,** 37, (3), 509-515.

(118) Jetti, R. K. R.; Thallapally, P. K.; Xue, F.; Mak, T. C. W.; Nangia, A., Hexagonal Nanoporous Host Structures Based on 2,4,6-Tris-4-(halo-phenoxy)-1,3,5-triazines (Halo=Chloro, Bromo). *Tetrahedron* **2000,** 56, (36), 6707-6719.

(119) Edwards, M. R.; Jones, W.; Motherwell, W. D. S.; Shields, G. P., Crystal engineering and chloro-methyl interchange - a CSD analysis. *Molecular Crystals and Liquid Crystals* **2001,** 356, 337-353.

(120) Dabros, M.; Emery, P. R.; Thalladi, V. R., A supramolecular approach to organic alloys: Cocrystals and three- and four-component solid solutions of 1,4-diazabicyclo[2.2.2]octane and 4-X-phenols (X = Cl, CH3, Br). *Angewandte Chemie-International Edition* **2007,** 46, (22), 4132-4135.

(121) Nath, N. K.; Nangia, A., Isomorphous Crystals by Chlorof_"Methyl Exchange in Polymorphic Fuchsones. *Crystal Growth & Design* **2012,** 12, (11), 5411-5425.

(122) van de Streek, J.; Motherwell, S., GRX: a program to search the CSD for functional group exchanges. *Journal of Applied Crystallography* **2005,** 38, (4), 694-696.

(123) Nath, N. K.; Nangia, A., Isomorphous Crystals by Chloro-Methyl Exchange in Polymorphic Fuchsones. *Crystal Growth & Design* **2012,** 12, (11), 5411-5425.

(124) Bhardwaj, R. M.; Price, L. S.; Price, S. L.; Reutzel-Edens, S. M.; Miller, G. J.; Oswald, I. D. H.; Johnston, B.; Florence, A. J., Exploring the Experimental and Computed Crystal Energy Landscape of Olanzapine. *Crystal Growth & Design* **2013,** 13, (4), 1602-1617.

(125) Issa, N.; Karamertzanis, P. G.; Welch, G. W. A.; Price, S. L., Can the Formation of Pharmaceutical Cocrystals Be Computationally Predicted? I. Comparison of Lattice Energies. *Crystal Growth & Design* **2009,** 9, (1), 442-453.

(126) Issa, N.; Barnett, S. A.; Mohamed, S.; Braun, D. E.; Copley, R. C. B.; Tocher, D. A.; Price, S. L., Screening for cocrystals of succinic acid and 4-aminobenzoic acid. *CrystEngComm* **2012,** 14, (7), 2454-2464.

(127) Karamertzanis, P. G.; Kazantsev, A. V.; Issa, N.; Welch, G. W. A.; Adjiman, C. S.; Pantelides, C. C.; Price, S. L., Can the Formation of Pharmaceutical Co-Crystals Be Computationally Predicted? II. Crystal Structure Prediction. *Journal of Chemical Theory and Computation* **2009,** 5, (5), 1432-1448.

(128) Braun, D. E.; Gelbrich, T.; Kahlenberg, V.; Griesser, U. J., Insights into Hydrate Formation and Stability of Morphinanes from a Combination of Experimental and Computational Approaches. *Molecular Pharmaceutics* **2014,** 11, (9), 3145-3163.

(129) Braun, D. E.; Bhardwaj, R. M.; Florence, A. J.; Tocher, D. A.; Price, S. L., Complex Polymorphic System of Gallic Acid-Five Monohydrates, Three Anhydrates, and over 20 Solvates. *Crystal Growth & Design* **2013,** 13, (1), 19-23.

(130) Vasileiadis, M.; Kazantsev, A. V.; Karamertzanis, P. G.; Adjiman, C. S.; Pantelides, C. C., The polymorphs of ROY: application of a systematic crystal structure prediction technique. *Acta Crystallographica Section B-Structural Science* **2012,** 68, 677-685.

(131) Yao, J. W.; Cole, J. C.; Pidcock, E.; Allen, F. H.; Howard, J. A. K.; Motherwell, W. D. S., CSDSymmetry: the definitive database of point-group and space- group symmetry relationships in small-molecule crystal structures. *Acta Crystallographica Section B - Structural Science* **2002,** 58, 640-646.

(132) Karamertzanis, P. G.; Pantelides, C. C., Ab initio crystal structure prediction - I. Rigid molecules. *Journal of Computational Chemistry* **2005,** 26, (3), 304-324.

(133) Karamertzanis, P. G.; Pantelides, C. C., Ab initio crystal structure prediction. II. Flexible molecules. *Molecular Physics* **2007,** 105, (2-3), 273-291.

(134) Holden, J. R.; Du, Z. Y.; Ammon, H. L., Prediction of Possible Crystal-Structures For C-, H-, N-, O- and F-Containing Organic Compounds. *Journal of Computational Chemistry* **1993,** 14, (4), 422-437.

(135) Kazantsev, A. V.; Karamertzanis, P. G.; Adjiman, C. S.; Pantelides, C. C., CrystalOptimizer. An efficient Algorithm for Lattice Energy Minimisation of Organic Crystal using Isolated-Molecule Quantum Mechanical Calculations. In *Molecular System Engineering*, Adjiman, C. S.; Galindo, A., Eds. WILEY-VCH Verlag GmbH & Co.: Weinheim, 2010; Vol. 6, pp 1-42.

(136) Kazantsev, A. V.; Karamertzanis, P. G.; Adjiman, C. S.; Pantelides, C. C., Efficient Handling of Molecular Flexibility in Lattice Energy Minimization of Organic Crystals. *Journal of Chemical Theory and Computation* **2011,** 7, (6), 1998-2016.

(137) Frisch, M. J.; Trucks, G. W.; Schlegel, H. B.; Scuseria, G. E.; Robb, M. A.; Cheeseman, J. R.; Montgomery, Jr.; Vreven, T.; Kudin, K. N.; Burant, J. C.; Millam, J. M.; Iyengar, S. S.; Tomasi, J.; Barone, V.; Mennucci, B.; Cossi, M.; Scalmani, G.; Rega, N.; Petersson, G. A.; Nakatsuji, H.; Hada, M.; Ehara, M.; Toyota, K.; Fukuda, R.; Hasegawa, J.; Ishida, M.; Nakajima, T.; Honda, Y.; Kitao, O.; Nakai, H.; Klene, M.; Li, X.; Knox, J. E.; Hratchian, H. P.; Cross, J. B.; Bakken, V.; Adamo, C.; Jaramillo, J.; Gomperts, R.; Stratmann, R. E.; Yazyev, O.; Austin, A. J.; Cammi, R.; Pomelli, C.; Ochterski, J.; Ayala, P. Y.; Morokuma, K.; Voth, G. A.; Salvador, P.; Dannenberg, J. J.; Zakrzewski, V. G.; Dapprich, S.; Daniels, A. D.; Strain, M. C.; Farkas, O.; Malick, D. K.; Rabuck, A. D.; Raghavachari, K.; Foresman, J. B.; Ortiz, J. V.; Cui, Q.; Baboul, A. G.; Clifford, S.; Cioslowski, J.; Stefanov, B. B.; Liu, G.; Liashenko, A.; Piskorz, P.; Komaromi, I.; Martin, R. L.; Fox, D. J.; Keith, T.; Al Laham, M. A.; Peng, C. Y.; Nanayakkara, A.; Challacombe, M.; Gill, P. M. W.; Johnson, B.; Chen, W.; Wong, M. W.; Gonzalez, C.; Pople, J. A. *Gaussian 03*, Gaussian Inc.: Wallingford CT, 2004.

(138) Frisch, M. J.; Trucks, G. W.; Schlegel, H. B.; Scuseria, G. E.; Robb, M. A.; Cheeseman, J. R.; Scalmani, G.; Barone, V.; Mennucci, B.; Petersson, G. A.; Nakatsuji, H.; Caricato, M.; Li, X.; Hratchian, H. P.; Izmaylov, A. F.; Bloino, J.; Zheng, G.; Sonnenberg, J. L.; Hada, M.; Ehara, M.; Toyota, K.; Fukuda, R.; Hasegawa, J.; Ishida, M.; Nakajima, T.; Honda, Y.; Kitao, O.; Nakai, H.; Vreven, T.; Montgomery Jr., J. A.; Peralta, J. E.; Ogliaro, F.; Bearpark, M. J.; Heyd, J.; Brothers, E. N.; Kudin, K. N.; Staroverov, V. N.; Kobayashi, R.; Normand, J.; Raghavachari, K.; Rendell, A. P.; Burant, J. C.; Iyengar, S. S.; Tomasi, J.; Cossi, M.; Rega, N.; Millam, N. J.; Klene, M.; Knox, J. E.; Cross, J. B.; Bakken, V.; Adamo, C.; Jaramillo, J.; Gomperts, R.; Stratmann, R. E.; Yazyev, O.; Austin, A. J.; Cammi, R.; Pomelli, C.; Ochterski, J. W.; Martin, R. L.; Morokuma, K.; Zakrzewski, V. G.; Voth, G. A.; Salvador, P.; Dannenberg, J. J.; Dapprich, S.; Daniels, A. D.; Farkas, Ö.; Foresman, J. B.; Ortiz, J. V.; Cioslowski, J.; Fox, D. J. *Gaussian 09*, Gaussian, Inc.: Wallingford, CT, USA, 2009.

(139) Price, S. L.; Leslie, M.; Welch, G. W. A.; Habgood, M.; Price, L. S.; Karamertzanis, P. G.; Day, G. M., Modelling Organic Crystal Structures using Distributed Multipole and Polarizability-

Based Model Intermolecular Potentials. *Physical Chemistry Chemical Physics* **2010,** 12, (30), 8478-8490.

(140) Welch, G. W. A.; Karamertzanis, P. G.; Price, S. L.; Leslie, M. *DMACRYS*, 1.05, is a substantial revision of DMAREL; 2010.

(141) Stone, A. J., Distributed Multipole Analysis, or How to Describe a Molecular Charge Distribution. *Chemical Physics Letters* **1981,** 83, (2), 233-239.

(142) Stone, A. J.; Alderton, M., Distributed Multipole Analysis - Methods and Applications. *Molecular Physics* **1985,** 56, (5), 1047-1064.

(143) Stone, A. J. *GDMA: A Program for Performing Distributed Multipole Analysis of Wave Functions Calculated Using the Gaussian Program System*, 2.2; University of Cambridge: Cambridge, United Kingdom, 2010.

(144) Beyer, T.; Price, S. L., Dimer or catemer? Low-energy crystal packings for small carboxylic acids. *Journal of Physical Chemistry B* **2000,** 104, (12), 2647-2655.

(145) Coombes, D. S.; Price, S. L.; Willock, D. J.; Leslie, M., Role of Electrostatic Interactions in Determining the Crystal Structures of Polar Organic Molecules. A Distributed Multipole Study. *Journal of Physical Chemistry* **1996,** 100, (18), 7352-7360.

(146) Cooper, T. G.; Hejczyk, K. E.; Jones, W.; Day, G. M., Molecular Polarization Effects on the Relative Energies of the Real and Putative Crystal Structures of Valine. *Journal of Chemical Theory and Computation* **2008,** 4, (10), 1795-1805.

(147) Cossi, M.; Scalmani, G.; Rega, N.; Barone, V., New developments in the polarizable continuum model for quantum mechanical and classical calculations on molecules in solution. *Journal of Chemical Physics* **2002,** 117, (1), 43-45.

(148) Hylton, R. K.; Tizzard, G. J.; Threlfall, T. L.; Ellis, A. L.; Coles, S. J.; Seaton, C. C.; Schulze, E.; Lorenz, H.; Seidel-Morgenstern, A.; Stein, M.; Price, S. L., Are the Crystal Structures of Enantiopure and Racemic Mandelic Acids Determined by Kinetics or Thermodynamics? *Journal of the American Chemical Society* **2015,** 137, (34), 11095-11104.

(149) Day, G. M.; Price, S. L.; Leslie, M., Elastic constant calculations for molecular organic crystals. *Crystal Growth & Design* **2001,** 1, (1), 13-27.

(150) Williams, D. E., Improved intermolecular force field for molecules containing H, C, N, and O atoms, with application to nucleoside and peptide crystals. *Journal of Computational Chemistry* **2001,** 22, (11), 1154-1166.

(151) Schmidt, M. W.; Baldridge, K. K.; Boatz, J. A.; Elbert, S. T.; Gordon, M. S.; Jensen, J. H.; Koseki, S.; Matsunaga, N.; Nguyen, K. A.; Su, S.; Windus, T. L.; Dupuis, M.; Montgomery, J. A., General Atomic and Molecular Electronic Structure Systems. *Journal of Computational Chemistry* **1993,** 14, 1347-1363.

(152) Karamertzanis, P. G.; Price, S. L., Energy Minimization of Crystal Structures Containing Flexible Molecules. *Journal of Chemical Theory and Computation* **2006,** 2, (4), 1184-1199.

(153) Clark, S. J.; Segall, M. D.; Pickard, C. J.; Hasnip, P. J.; Probert, M. J.; Refson, K.; Payne, M. C., First principles methods using CASTEP. *Zeitschrift fur Kristallographie* **2005,** 220, (5-6), 567-570.

(154) Tkatchenko, A.; Scheffler, M., Accurate Molecular Van Der Waals Interactions from Ground-State Electron Density and Free-Atom Reference Data. *Physical Review Letters* **2009,** 102, (7), 073005.

(155) Mattei, A.; Li, T. L., Interplay between molecular conformation and intermolecular interactions in conformational polymorphism: A molecular perspective from electronic calculations of tolfenamic acid. *International Journal of Pharmaceutics* **2011,** 418, (2), 179-186.

(156) Gavezzotti, A., The Calculation of Molecular Volumes and the Use of Volume Analysis in the Investigation of Structured Media and of Solid-State Organic- Reactivity. *Journal of the American Chemical Society* **1983,** 105, (16), 5220-5225.

(157) *ACD/NMR Processor Academic Edition*, 12.01; Advanced Chemistry Development, Inc.: 2010.

(158) *WiRE*, 2.0; Renishaw.

(159) Umeda, T.; Ohnishi, N.; Yokoyama, T.; Kuroda, T.; Kita, Y.; Kuroda, K.; Tatsumi, E.; Matsuda, Y., A Kinetic Study on the Isothermal Transition of Polymorphic Forms of Tolbutamide and Mefenamic Acid in the Solid State at High Temperatures. *CHEMICAL & PHARMACEUTICAL BULLETIN* **1985,** 33, (5), 2073-2078.

(160) Romero, S.; Escalera, B.; Bustamante, P., Solubility behavior of polymorphs I and II of mefenamic acid in solvent mixtures. *International Journal of Pharmaceutics* **1999,** 178, (2), 193-202.

(161) Thybo, P.; Kristensen, J.; Hovgaard, L., Characterization and physical stability of tolfenamic Acid-PVP K30 solid dispersions. *Pharmaceutical Development and Technology* **2007,** 12, (1), 43-53.

(162) Lee, E. H.; Byrn, S. R.; Pinal, R., The solution properties of mefenamic acid and a closely related analogue are indistinguishable in polar solvents but significantly different in nonpolar environments. *Journal of Pharmaceutical Sciences* **2012,** 101, (12), 4529-4539.

(163) Abdul Mudalip, S. K.; Abu Bakar, M. R.; Jamal, P.; Adam, F., Solubility and Dissolution Thermodynamic Data of Mefenamic Acid Crystals in Different Classes of Organic Solvents. *Journal of Chemical & Engineering Data* **2013,** 58, (12), 3447-3452.

(164) Gaglioti, K.; Chierotti, M. R.; Grifasi, F.; Gobetto, R.; Griesser, U. J.; Hasa, D.; Voinovich, D., Improvement of the water solubility of tolfenamic acid by new multiple-component crystals produced by mechanochemical methods. *Crystengcomm* **2014,** 16, (35), 8252-8262.

(165) Schur, E.; Nauha, E.; Lusi, M.; Bernstein, J., Kitaigorodsky Revisited: Polymorphism and Mixed Crystals of Acridine/Phenazine. *Chemistry-a European Journal* **2015,** 21, (4), 1735-1742.

(166) Madhavi, N. N. L.; Katz, A. K.; Carrell, H. L.; Nangia, A.; Desiraju, G. R., Evidence for the characterisation of the C-H-pi interaction as a weak hydrogen bond: toluene and chlorobenzene solvates of 2,3,7,8-tetraphenyl-1,9,10-anthyridine (pg 1953, 1997). *Chemical Communications* **1997**, (22), 2249-2249.

(167) Omondi, B.; Lemmerer, A.; Fernandes, M. A.; Levendis, D. C.; Layh, M., Formation of isostructural solid solutions in 2,6-disubstituted N-phenylformamides and N-phenylthioamides. *Acta Crystallogr B Struct Sci Cryst Eng Mater* **2014,** 70, (Pt 1), 106-14.

(168) Gaisford, S.; Buanz, A. B. M., Pharmaceutical physical form characterisation with fast (> 200 degrees C min(-1)) DSC heating rates. *Journal of Thermal Analysis and Calorimetry* **2011,** 106, (1), 221-226.

(169) Habgood, M.; Grau-Crespo, R.; Price, S. L., Substitutional and orientational disorder in organic crystals: a symmetry-adapted ensemble model. *Physical Chemistry Chemical Physics* **2011,** 13, (20), 9590-9600.

(170) Uzoh, O. G. Modelling molecular flexibility for crystal structure prediction. University College London, 2015.

(171) Chandra, T., Safe chemical manipulations using a Schlenk line. *Abstracts of Papers of the American Chemical Society* **2013,** 246, 1.

(172) Schlenk, W., The constitution of Grignard magnesium compounds. *Berichte Der Deutschen Chemischen Gesellschaft* **1929,** 62, 920-924.

(173) Chadwick, K.; Chen, J.; Myerson, A. S.; Trout, B. L., Toward the Rational Design of Crystalline Surfaces for Heteroepitaxy: Role of Molecular Functionality. *Crystal Growth & Design* **2012,** 12, (3), 1159-1166.

(174) Shephard, J. J.; Evans, J. S. O.; Salzmann, C. G., Structural Relaxation of Low-Density Amorphous Ice upon Thermal Annealing. *Journal of Physical Chemistry Letters* **2013,** 4, (21), 3672-3676.

(175) Shephard, J. J. Structure-Property Relationships In Two-Component Liquids: Hydrophobic Effects and Azeotropy. Durham University, 2014.

(176) http://www.diamond.ac.uk/Home/Beamlines/I12.html.

(177) P, H. A. *FIT2D V9.129 Reference Manual V3.1*; 1998.

(178) Hammersley, A. P.; Svensson, S. O.; Hanfland, M.; Fitch, A. N.; Hausermann, D., Two-dimensional detector software: From real detector to idealised image or two-theta scan. *High Pressure Research* **1996,** 14, (4-6), 235-248.

(179) Buanz, A.; Prior, T. J.; Burley, J. C.; Raimi-Abraham, B. T.; Telford, R.; Hart, M.; Seaton, C. C.; Davies, P. J.; Scowen, I. J.; Gaisford, S.; Williams, G. R., Thermal Behavior of Benzoic Acid/Isonicotinamide Binary Cocrystals. *Crystal Growth & Design* **2015,** 15, (7), 3249-3256.

(180) Clout, A.; Buanz, A. B. M.; Prior, T. J.; Reinhard, C.; Wu, Y.; O'Hare, D.; Williams, G. R.; Gaisford, S., Simultaneous Synchrotron X-Ray Diffraction – Differential Scanning Calorimetry: A Powerful Technique For Physical Form Characterisation In Pharmaceutical Materials. **In preparation**.

(181) Copyright, C. *Mercury CSD 2.2 (Build RC5)*, 2009.

(182) Mei, X.; August, A. T.; Wolf, C., Regioselective Copper-Catalyzed Amination of Chlorobenzoic Acids: Synthesis and Solid-State Structures of N-Aryl Anthranilic Acid Derivatives. *The Journal of Organic Chemistry* **2006,** 71, (1), 142-149.

(183) Cunha, V. R. R.; Izumi, C. M. S.; Petersen, P. A. D.; Magalhães, A.; Temperini, M. L. A.; Petrilli, H. M.; Constantino, V. R. L., Mefenamic Acid Anti-Inflammatory Drug: Probing Its Polymorphs by Vibrational (IR and Raman) and Solid-State NMR Spectroscopies. *The Journal of Physical Chemistry B* **2014,** 118, (16), 4333-4344.

(184) Lommerse, J. P. M.; Motherwell, W. D. S.; Ammon, H. L.; Dunitz, J. D.; Gavezzotti, A.; Hofmann, D. W. M.; Leusen, F. J. J.; Mooij, W. T. M.; Price, S. L.; Schweizer, B.; Schmidt, M. U.; van Eijck, B. P.; Verwer, P.; Williams, D. E., A test of crystal structure prediction of small organic molecules. *Acta Crystallographica Section B - Structural Science* **2000,** 56, 697-714.

(185) Motherwell, W. D. S.; Ammon, H. L.; Dunitz, J. D.; Dzyabchenko, A.; Erk, P.; Gavezzotti, A.; Hofmann, D. W. M.; Leusen, F. J. J.; Lommerse, J. P. M.; Mooij, W. T. M.; Price, S. L.; Scheraga, H.; Schweizer, B.; Schmidt, M. U.; van Eijck, B. P.; Verwer, P.; Williams, D. E., Crystal structure prediction of small organic molecules: a second blind test. *Acta Crystallographica Section B - Structural Science* **2002,** 58, 647-661.

(186) Day, G. M.; Motherwell, W. D. S.; Ammon, H. L.; Boerrigter, S. X. M.; Della Valle, R. G.; Venuti, E.; Dzyabchenko, A.; Dunitz, J. D.; Schweizer, B.; van Eijck, B. P.; Erk, P.; Facelli, J. C.; Bazterra, V. E.; Ferraro, M. B.; Hofmann, D. W. M.; Leusen, F. J. J.; Liang, C.; Pantelides, C. C.; Karamertzanis, P. G.; Price, S. L.; Lewis, T. C.; Nowell, H.; Torrisi, A.; Scheraga, H. A.; Arnautova, Y. A.; Schmidt, M. U.; Verwer, P., A third blind test of crystal structure prediction. *Acta Crystallographica Section B - Structural Science* **2005,** 61, (5), 511-527.

(187) Day, G. M.; Cooper, T. G.; Cruz-Cabeza, A. J.; Hejczyk, K. E.; Ammon, H. L.; Boerrigter, S. X. M.; Tan, J.; Della Valle, R. G.; Venuti, E.; Jose, J.; Gadre, S. R.; Desiraju, G. R.; Thakur, T. S.; van Eijck, B. P.; Facelli, J. C.; Bazterra, V. E.; Ferraro, M. B.; Hofmann, D. W. M.; Neumann, M.; Leusen, F. J. J.; Kendrick, J.; Price, S. L.; Misquitta, A. J.; Karamertzanis, P. G.; Welch, G. W. A.; Scheraga, H. A.; Arnautova, Y. A.; Schmidt, M. U.; van de Streek, J.; Wolf, A.; Schweizer, B., Significant progress in predicting the crystal structures of small organic molecules - a report on the fourth blind test. *Acta Crystallographica Section B - Structural Science* **2009,** 65, (2), 107-125.

(188) Bardwell, D. A.; Adjiman, C. S.; Arnautova, Y. A.; Bartashevich, E.; Boerrigter, S. X.; Braun, D. E.; Cruz-Cabeza, A. J.; Day, G. M.; la Valle, R. G.; Desiraju, G. R.; van Eijck, B. P.; Facelli, J. C.; Ferraro, M. B.; Grillo, D.; Habgood, M.; Hofmann, D. W.; Hofmann, F.; Jose, K. V.; Karamertzanis, P. G.; Kazantsev, A. V.; Kendrick, J.; Kuleshova, L. N.; Leusen, F. J.; Maleev, A. V.; Misquitta, A. J.; Mohamed, S.; Needs, R. J.; Neumann, M. A.; Nikylov, D.; Orendt, A. M.; Pal, R.; Pantelides, C. C.; Pickard, C. J.; Price, L. S.; Price, S. L.; Scheraga, H. A.; van de Streek, J.; Thakur, T. S.; Tiwari, S.; Venuti, E.; Zhitkov, I. K., Towards crystal structure prediction of complex organic compounds - a report on the fifth blind test. *Acta Crystallographica Section B - Structural Science* **2011,** 67, (6), 535-551.

(189) Blagden, N.; Colesb, S.; Berry, D., Pharmaceutical co-crystals - are we there yet? *Crystengcomm* **2014,** 16, (26), 5753-5761.

(190) Elder, D.; Patterson, J.; Holm, R., The solid-state continuum: a perspective on the interrelationships between different solid-state forms in drug substance and drug product. *Journal of Pharmacy and Pharmacology* **2015,** 67, (6), 757-772.

(191) Bucar, D. K.; Day, G. M.; Halasz, I.; Zhang, G. G. Z.; Sander, J. R. G.; Reid, D. G.; MacGillivray, L. R.; Duer, M. J.; Jones, W., The curious case of (caffeine).(benzoic acid): how heteronuclear seeding allowed the formation of an elusive cocrystal. *Chemical Science* **2013,** 4, (12), 4417-4425.

(192) J., E.; C.R., G., *The Dictionary of Drugs: Chemical Data, Structures and Bibliography*. First ed.; Springer-Science + Business Media, B.V.: Pennsylvania, 1990; p 1.

(193) Runarsson, O. V.; Artacho, J.; Warnmark, K., The 125th Anniversary of the Troger's Base Molecule: Synthesis and Applications of Troger's Base Analogues. *European Journal of Organic Chemistry* **2012**, (36), 7015-7041.

(194) Prince, P.; Fronczek, F. R.; Gandour, R. D., 2 POLYMORPHS OF 3,5-DINITROBENZOIC ACID. *Acta Crystallographica Section C-Crystal Structure Communications* **1991,** 47, 895-898.

(195) Kanters, J. A.; Kroon, J.; Hooft, R.; Schouten, A.; Vanschijndel, J. A. M.; Brandsen, J., Temperature-dependent order-disorder phenomena in crystal-structures containing dimers of carboxylic-acids - the crystal and molecular-structure of 3,5-dinitrobenzoic acid at room and liquid-nitrogen temperature and statistics of the geometries of hydrogen-bonded carboxyl groups. *Croatica Chemica Acta* **1991,** 64, (3), 353-370.

(196) Jones, A. O. F.; Blagden, N.; McIntyre, G. J.; Parkin, A.; Seaton, C. C.; Thomas, L. H.; Wilson, C. C., Tuning Proton Disorder in 3,5-Dinitrobenzoic Acid Dimers: the Effect of Local Environment. *Crystal Growth & Design* **2013,** 13, (2), 497-509.

(197) Larson, S. B.; Wilcox, C. S., Structure of 5,11-methano-2,8-dimethyl-5,6,11,12-tetrahydrodibenzo b,f 1,5 diazocine (troger base) at 163-k. *Acta Crystallographica Section C-Crystal Structure Communications* **1986,** 42, 224-227.

(198) Worlitschek, J.; Bosco, M.; Huber, M.; Gramlich, V.; Mazzotti, M., Solid-liquid equilibrium of Troger's base enantiomers in ethanol: Experiments and modelling. *Helvetica Chimica Acta* **2004,** 87, (2), 279-291.

(199) Maria Tejedor, R.; Uriel, S.; Graus, S.; Sierra, T.; Luis Serrano, J.; Claramunt, R. M.; Lopez, C.; Perz-Torralba, M.; Alkorta, I.; Elguero, J., A Facile Method to Determine the Absolute Structure of Achiral Molecules: Supramolecular-Tilt Structures. *Chemistry-a European Journal* **2013,** 19, (19), 6044-6051.

(200) Cross, J. T.; Rossi, N. A.; Serafin, M.; Wheeler, K. A., Troger's base quasiracemates and crystal packing tendencies. *Crystengcomm* **2014,** 16, (31), 7251-7258.

(201) Karamertzanis, P. G.; Kazantsev, A. V.; Issa, N.; Welch, G. W. A.; Adjiman, C. S.; Pantelides, C. C.; Price, S. L., Can the Formation of Pharmaceutical Cocrystals Be Computationally Predicted? 2. Crystal Structure Prediction. *Journal of Chemical Theory and Computation* **2009,** 5, (5), 1432-1448.

(202) Reilly, A. M.; Cooper, R. I.; Adjiman, C. S.; Bhattacharya, S.; Boese, A. D.; Brandenburg, J. G.; Bygrave, P. J.; Bylsma, R.; Campbell, J. E.; Car, R.; Case, D. H.; Chadha, R.; Cole, J. C.; Cosburn, K.; Cuppen, H. M.; Curtis, F.; Day, G. M.; DiStasio Jr, R. A.; Dzyabchenko, A.; van Eijck, B. P.; Elking, D. M.; van den Ende, J. A.; Facelli, J. C.; Ferraro, M. B.; Fusti-Molnar, L; Gatsiou, C.-A.; Gee, T. S.; de Gelder, R.; Ghiringhelli, L. M.; Goto, H.; Grimme, S.; Guo, R.; Hofmann, D. W. M.; Hoja, J.; Hylton, R. K.; Iuzzolino, L.; Jankiewicz, W.; de Jong, D. T.; Kendrick, J.; de Klerk, N. J. J.; Ko, H.-Y.; Kuleshova, L. N.; Li, X.; Lohani, S.; Leusen, F. J. J.; Lund, A. M.; Lv, J.; Ma, Y.; Marom, N.; Masunov, A. E.; McCabe, P.; McMahon, D. P.; Meekes, H.; Metz, M. P.; Misquitta, A. J.; Mohamed, S.; Monserrat, B.; Needs, R. J.; Neumann, M. A.; Nyman, J.; Obata, S.; Oberhofer, H.; Oganov, A. R.; Orendt, A. M.; Pagola, G. I.; Pantelides, C. C.; Pickard, C. J.; Podeszwa, R.; Price, L. S.; Price, S. L.; Pulido, A.; Read, M. G.; Reuter, K.; Schneider, E.; Schober, C.; Shields, G. P.; Singh, P.; Sugden, I. J.; Szalewicz, K.; Taylor, C. R.; Tkatchenko, A.; Tuckerman, M. E.; Vacarro, F.; Vasileiadis, M.; Vazquez-Mayagoitia, A.; Vogt, L.; Wang, Y.; Watson, R. E.; de Wijs, G. A.; Yang, J. Z.; Zhu, Q.; Groom, C. R., Report on the sixth blind test of organic crystal-structure prediction methods. *Acta Crystallographica Section B - Structural Science* **2016,** submitted.

(203) van Eijck, B. P.; Kroon, J., UPACK program package for crystal structure prediction: Force fields and crystal structure generation for small carbohydrate molecules. *Journal of Computational Chemistry* **1999,** 20, (8), 799-812.

(204) van Eijck, B. P.; Kroon, J., Structure predictions allowing more than one molecule in the asymmetric unit. *Acta Crystallographica Section B - Structural Science* **2000,** 56, 535-542.

(205) Glass, C. W.; Oganov, A. R.; Hansen, N., USPEX - Evolutionary crystal structure prediction. *Computer Physics Communications* **2006,** 175, (11-12), 713-720.

(206) Gibney, E., Chemistry software predicts crystal structures. *Nature* **2015,** 527, (7576), 20-21.

(207) Tkatchenko, A.; DiStasio, R. A. J.; Car, R.; Scheffler, M., Accurate and efficient method for many-body van der Waals interactions. *Physical Review Letters* **2012,** 108, (23), 236402-236402.

(208) Grimme, S., Semiempirical GGA-type density functional constructed with a long-range dispersion correction. *Journal of Computational Chemistry* **2006,** 27, (15), 1787-1799.

(209) Neumann, M. A.; Perrin, M. A., Energy ranking of molecular crystals using density functional theory calculations and an empirical van der Waals correction. *Journal of Physical Chemistry B* **2005,** 109, (32), 15531-15541.

(210) Price, S. L., Why don't we find more polymorphs? *Acta Crystallographica Section B - Structural Crystallography and Crystal Chemistry* **2013,** 69, 313-328.

Appendix 1

Comparison of the relative conformational energy of MA, as a function of the ξ_1 torsion angle, calculated at the PBE0/6-31+G(d) level of theory using GAUSSIAN (blue) and at the B3LYP/6-31G(d,p) level of theory using GAMESS (red). The GAMESS calculations at the B3LYP/6-31G(d,p) level of theory were used as the input for CrystalPredictor, and the PBE0/6-31+G(d) level of theory was used in the CrystalOptimiser refinements.
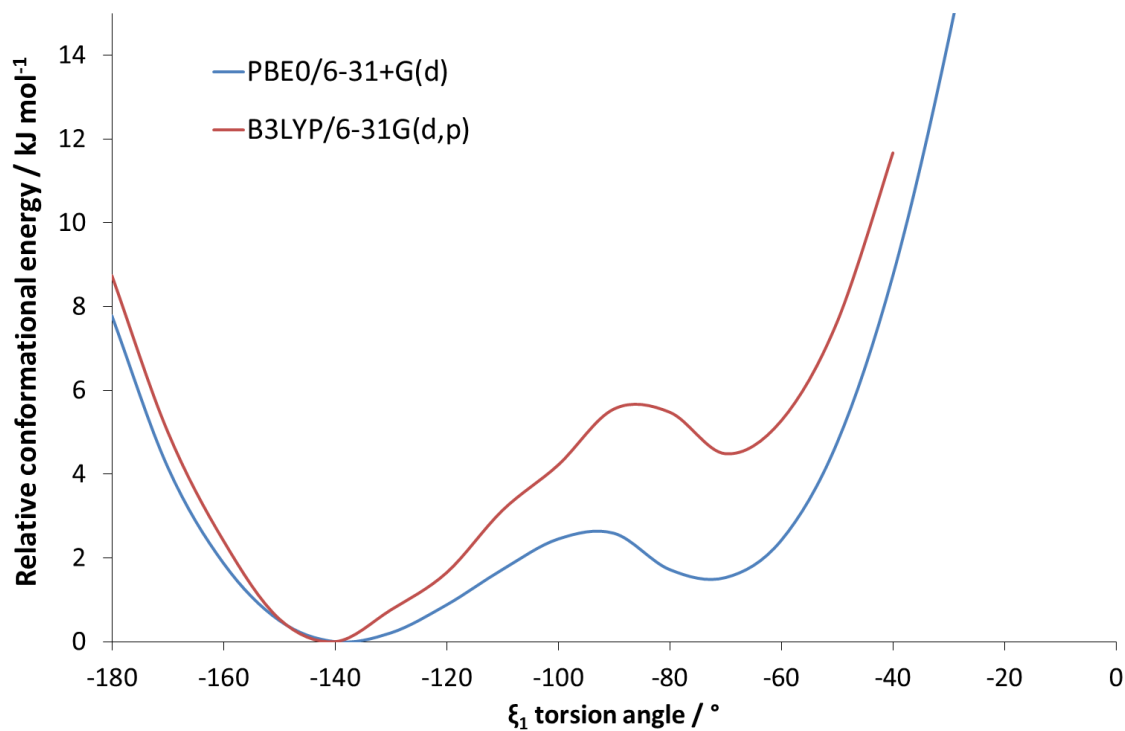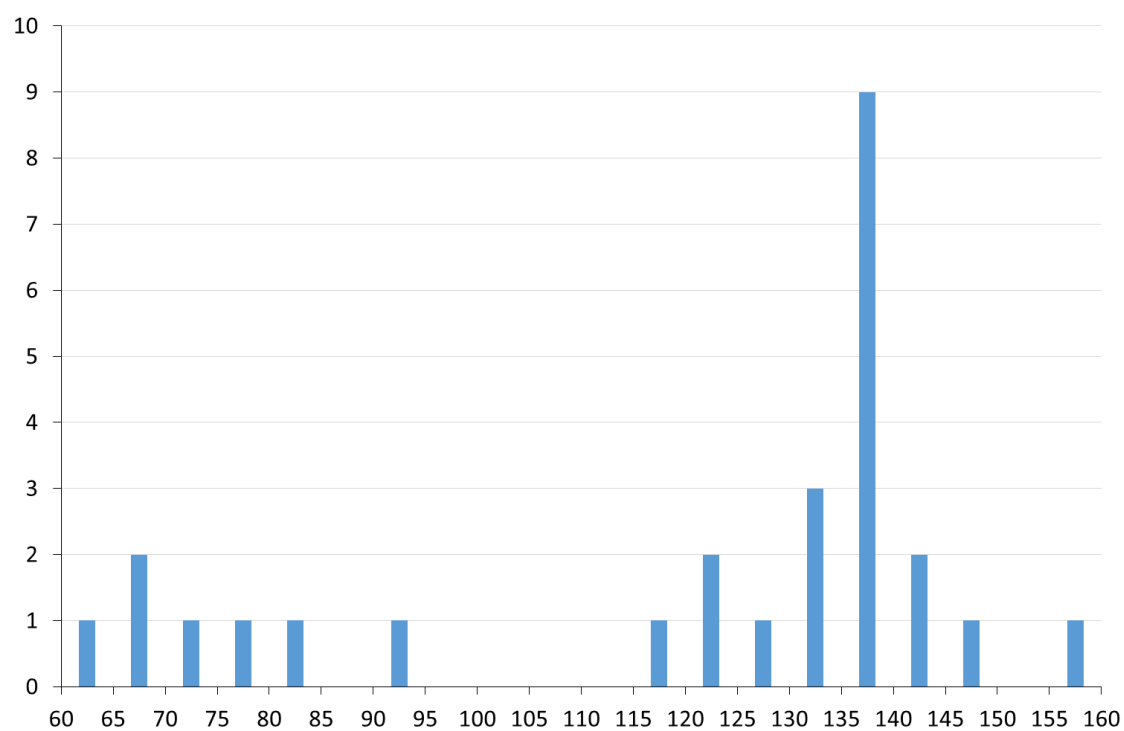
Appendix 2

MA lattice minima of the 23 structures with the lowest lattice energies following the PCM calculations. Structures with two entries in the ξ_1 torsion column are Z′ = 2 structures produced by a reduction in symmetry when the Z′=1 structure was found to correspond to a transition state.

| Structure	Space Group	ξ_1 torsion (°)	a (Å)	b (Å)	c (Å)	α (°)	β (°)	γ (°)	Density (g cm^{-3})	Lattice Energy (kJ mol^{-1})
#1MA_128	P-1	117.15	6.9638	7.4392	13.9823	103.237	99.545	64.113	1.2668	-147.717
#2MA_978	P-1	134.19	7.2107	20.5931	7.0497	118.403	113.72	43.67	1.2661	-147.148
#3MA_237	P2$_1$/c	140.06	13.2989	7.0209	15.8495	90	59.41	90	1.2581	-146.482
#4MA_889	P-1	83.38	9.8269	7.95	8.7544	97.883	70.662	84.472	1.2682	-145.970
#5MA_510	P-1	60.66	5.1175	8.3861	14.8621	80.231	93.907	81.999	1.2931	-145.867
#6MA_288	C2/c	140.98	7.8511	11.8101	27.3939	90	85.791	90	1.2653	-145.064
#7MA_1666	P-1	70.02	8.2988	11.1219	7.812	81.065	117.808	103.032	1.2919	-144.785
#8MA_2853	P2$_1$	138.13, 138.03	7.0665	28.205	7.0058	90	66.794	90	1.2488	-144.663
#9MA_1592	P2$_1$	138.68, 138.92	7.0013	28.1836	7.0742	90	66.824	90	1.2489	-144.626
#10MA_5611	P2$_1$	138.24, 138.24	7.7504	28.1702	7.0087	90	56.976	90	1.2491	-144.595
#11MA_1069	Pbca	138.42	23.1487	15.6265	7.0746	90	90	90	1.2525	-144.223
#12MA_1090	Pbca	139.00	23.1594	15.5654	7.0976	90	90	90	1.2528	-144.081
#13MA_664	Pbca	133.58	22.9546	16.1393	7.0044	90	90	90	1.2352	-143.377
#14MA_318	C2/c	124.50	24.5861	6.8828	16.3127	90	67.575	90	1.2561	-143.269
#15MA_538	P2$_1$/c	120.83	11.8977	6.8978	16.293	90	72.737	90	1.2551	-143.122
#16MA_1055	A2/n	137.84	19.2644	7.0779	19.5909	90	73.845	90	1.2493	-143.111
#17MA_540	C2/c	126.61	11.5628	7.5673	30.0694	90	80.49	90	1.2352	-142.791
#18MA_1918	P-1	76.43	11.4466	5.5602	11.6628	99.929	61.94	89.819	1.2478	-142.760
#19MA_5643	P2$_1$	65.48, 65.51	5.0085	31.1164	8.7911	90	67.221	90	1.2687	-142.656
#20MA_333	P-1	131.17	8.8122	10.208	7.7088	86.728	71.557	101.68	1.2546	-142.453
#21MA_3317	P2$_1$/c	148.83	7.868	7.2532	23.1917	90	73.505	90	1.2629	-141.723
#22MA_223	P-1	157.07	7.5172	7.4275	12.6161	87.759	64.676	85.162	1.263	-140.938
#23MA_497	P-1	93.65	8.138	8.5174	9.9067	70.081	96.146	82.731	1.2678	-140.695

Appendix 3

Distribution of ξ_1 tosion angles in the 23 most stable structures on the crystal energy landscape of MA.

Appendix 4

The calculated crystal energy landscapes of MA after (a) DMAfelx-Quick, (d) CrystalOptimizer and (c) PCM calculations. Note in (b) there are two energetically similar P-1 structures that are the most stable computationally generated structures which are separated following the PCM calculations in (c).
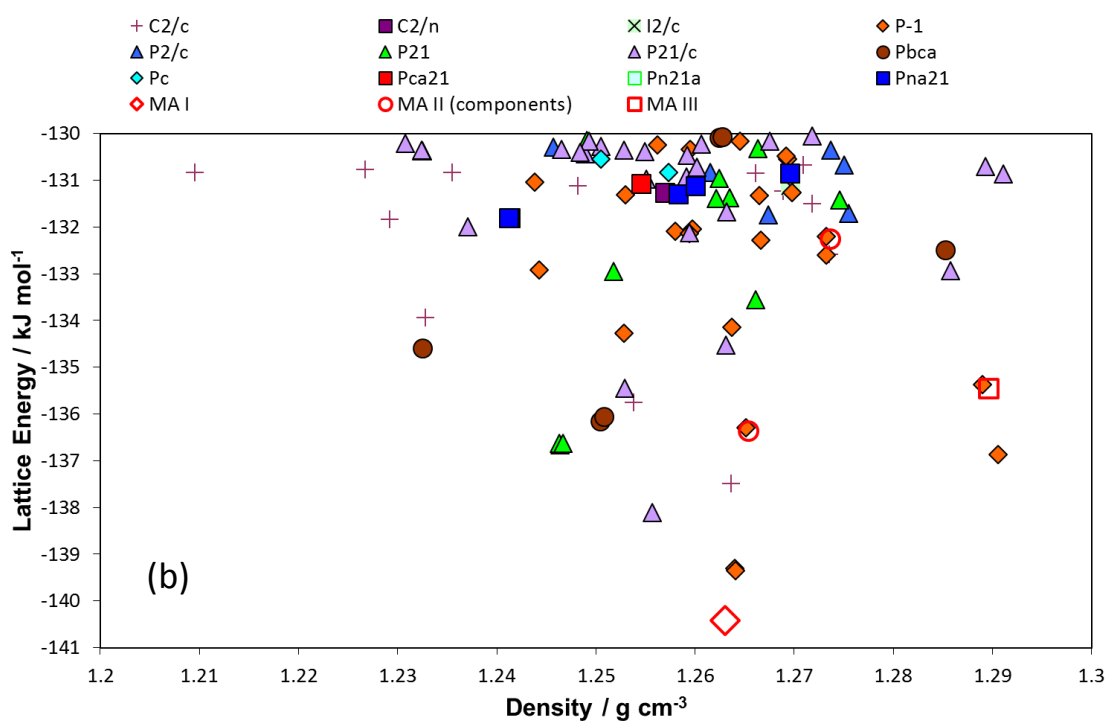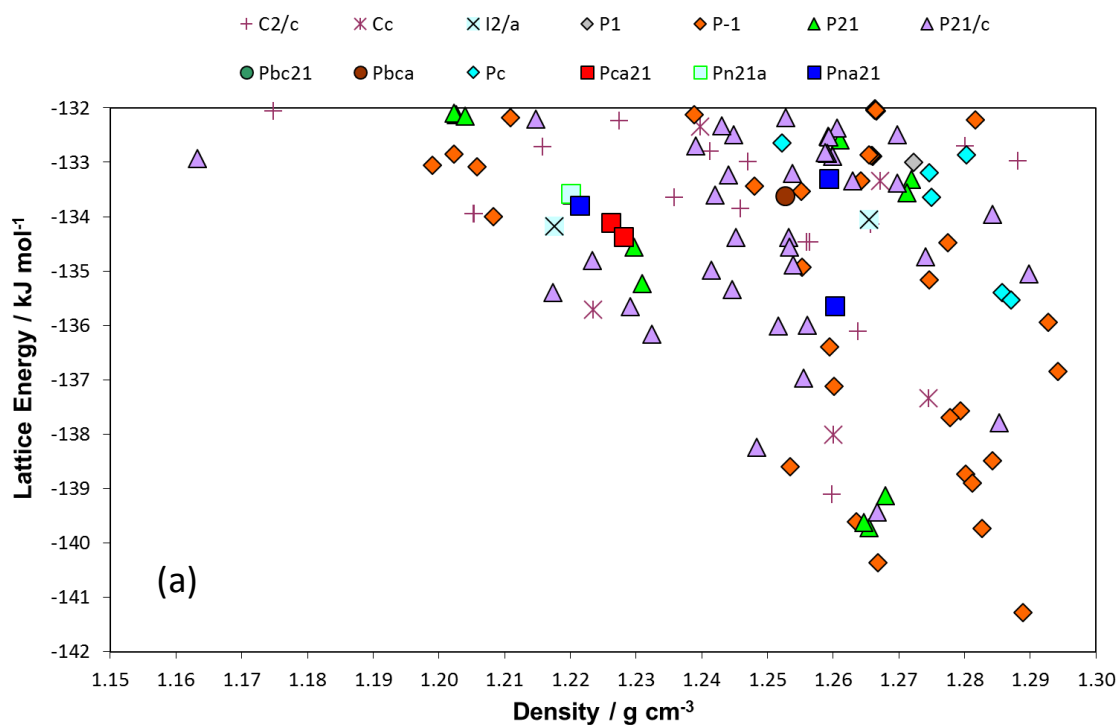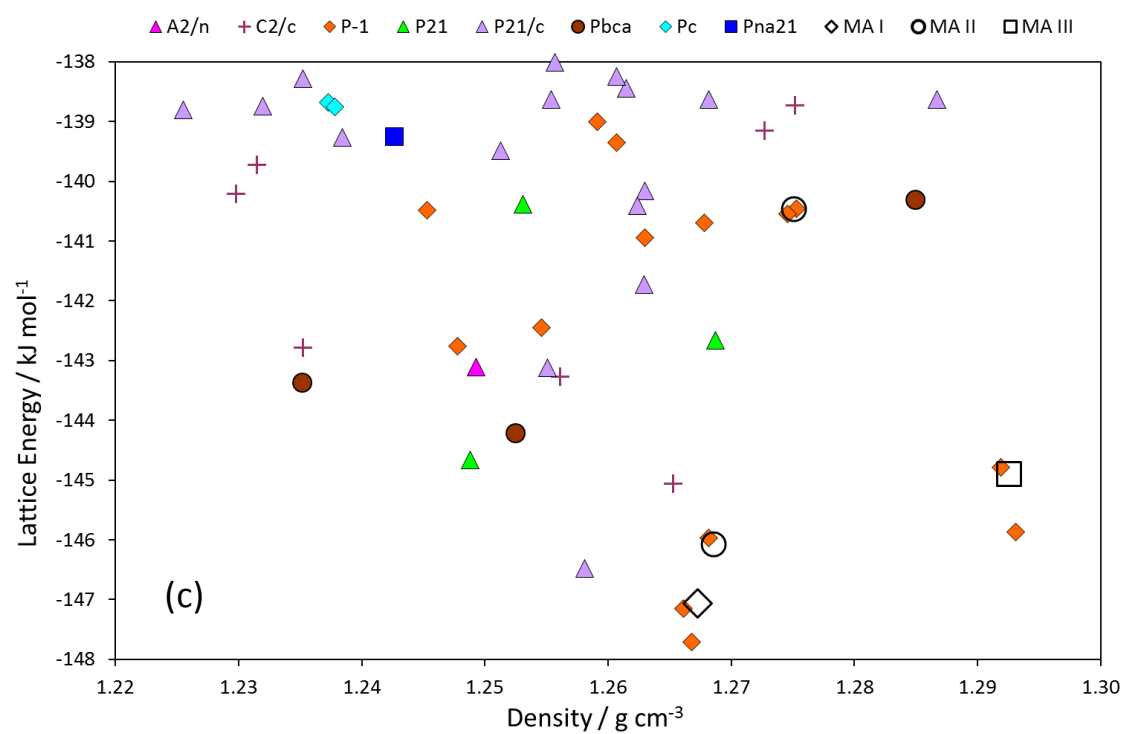
Appendix 5

Comparisons of the generated crystal structures of MA with the crystal structures of known fenamates. The table only shows comparisons that matched 7 molecules or above.

MA structure	Comparison structure from CSD	Number of similar molecules within coordination sphere (n)	$rmsd_n$ (Å)	PXRD similarity
#48MA_480	SURMOI	15	0.19065	0.981188
#6MA_288	KAXXAI02	15	0.343126	0.962881
#1MA_128	KAXXAI03	15	0.395037	0.952818
#19MA_5643	KAXXAI01	15	0.420326	0.943436
#4MA_889	KAXXAI04-major	15	0.421761	0.950993
#23MA_497	KAXXAI04-minor	15	0.585146	0.951515
#5MA_510	PEFNAQ	15	0.634555	0.928514
#2MA_978	KAXXAI03	14	0.465334	0.938267
#17MA_540	KAXXAI02	13	0.198347	0.924293
#8MA_2853	KAXXAI02	13	0.279487	0.950537
#9MA_1592	KAXXAI02	13	0.28105	0.950866
#10MA_5611	KAXXAI02	13	0.282975	0.951031
#2MA_978	KAXXAI02	13	0.382087	0.938069
#19MA_5643	PEFNAQ	13	0.461693	0.95004
#1MA_128	KAXXAI02	13	0.541632	0.939676
#39MA_1682	KAXXAI02	13	0.590419	0.964251
#5MA_510	KAXXAI01	13	0.728654	0.846431
#32MA_747	KAXXAI02	13	0.759515	0.935314
#17MA_540	PEFMET	12	0.21235	0.926023
#8MA_2853	PEFMET	12	0.31153	0.958896
#9MA_1592	PEFMET	12	0.31207	0.959583
#10MA_5611	PEFMET	12	0.314911	0.959433
#17MA_540	KAXXAI03	12	0.370597	0.928148
#6MA_288	PEFMET	12	0.383979	0.951777
#2MA_978	PEFMET	12	0.397873	0.944525
#8MA_2853	KAXXAI03	12	0.414948	0.925942
#10MA_5611	KAXXAI03	12	0.416233	0.92622
#9MA_1592	KAXXAI03	12	0.420174	0.925834
#6MA_288	KAXXAI03	12	0.428786	0.931182
#39MA_1682	PEFMET	12	0.443817	0.927677
#1MA_128	SURMEY	12	0.473674	0.920983
#1MA_128	PEFMET	12	0.513751	0.923492
#32MA_747	KAXXAI03	12	0.575143	0.89928
#17MA_540	SURMEY	12	0.604147	0.91974
#2MA_978	SURMEY	12	0.610812	0.903335
#32MA_747	SURMEY	12	0.663033	0.936945
#8MA_2853	SURMEY	12	0.679809	0.94479
#6MA_288	SURMEY	12	0.68142	0.94463
#10MA_5611	SURMEY	12	0.681536	0.945093

|				
#32MA_747	PEFMET	12	0.682244	0.947314
#39MA_1682	KAXXAI03	12	0.683284	0.940686
#9MA_1592	SURMEY	12	0.687273	0.944758
#24MA_282	KAXXAI04-minor	12	1.10724	0.918475
#4MA_889	KAXXAI04-minor	10	0.709745	0.955898
#48MA_480	KAXXAI	10	0.720254	0.959321
#23MA_497	KAXXAI04-major	10	0.926142	0.934797
#57MA_50	BIXGIY02	10	1.41026	0.88956
#57MA_50	SURMOI	9	0.238512	0.938812
#55MA_44	SURMOI	9	0.361787	0.949408
#55MA_44	KAXXAI	9	0.447587	0.920401
#41MA_3896	SURMOI	9	0.45763	0.932419
#57MA_50	KAXXAI	9	0.567763	0.897208
#41MA_3896	PEFNAQ	9	0.868828	0.810622
#41MA_3896	KAXXAI01	9	1.0591	0.723262
#57MA_50	PEFNAQ	9	1.07345	0.780808
#46MA_109	KAXXAI	8	0.236007	0.921364
#46MA_109	SURMOI	8	0.350944	0.942459
#48MA_480	BIXGIY02	8	0.465538	0.922441
#33MA_5471	KAXXAI01	8	0.520056	0.658909
#34MA_3912	SURMOI	8	0.546015	0.914474
#33MA_5471	PEFNAQ	8	0.553461	0.73157
#36MA_3365	SURMOI	8	0.580582	0.90793
#36MA_3365	PEFNAQ	8	0.794415	0.811371
#41MA_3896	KAXXAI	8	0.801068	0.886662
#34MA_3912	PEFNAQ	8	0.806843	0.809947
#55MA_44	BIXGIY02	8	0.826653	0.86816
#34MA_3912	KAXXAI	8	0.888886	0.872906
#36MA_3365	KAXXAI	8	0.921631	0.867465
#36MA_3365	KAXXAI01	8	0.938324	0.720654
#34MA_3912	KAXXAI01	8	0.960238	0.720369
#48MA_480	PEFNAQ	8	1.04391	0.774013
#25MA_1982	PEFNAQ	8	2.18761	0.695255
#40MA_1556	FPAMCA	7	0.374772	0.945777
#3MA_237	KAXXAI03	7	0.374941	0.856619
#45MA_550	KAXXAI04-minor	7	0.708799	0.880248
#39MA_1682	SURMEY	7	0.712997	0.955145
#41MA_3896	BIXGIY02	7	0.959515	0.882072
#56MA_440	KAXXAI03	7	1.12181	0.776292
#7MA_1666	KAXXAI04-minor	7	1.20951	0.888203
#26MA_14	KAXXAI04-major	7	1.24578	0.92187
#55MA_44	FPAMCA13	7	1.28649	0.869014
#31MA_1249	KAXXAI03	7	1.32405	0.832632
#7MA_1666	PEFNAQ	7	1.76383	0.809215
#22MA_223	FPAMCA12	7	2.48996	0.78989
#28MA_638	FPAMCA12	7	2.64786	0.848497

Appendix 6

The unit cell similarities of #6MA_288 with TA form III and #19MA_5643 with TA form I.

	TA form III	#6MA_288
Space Group	P2$_1$/c	C2/c
a	7.6356(15)	7.9
b	11.305(2)	11.8
c	28.065(6)	27.4
α	90	90
β	93.03(3)	85.8
γ	90	90
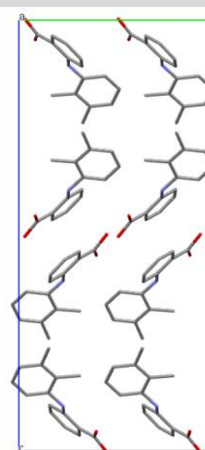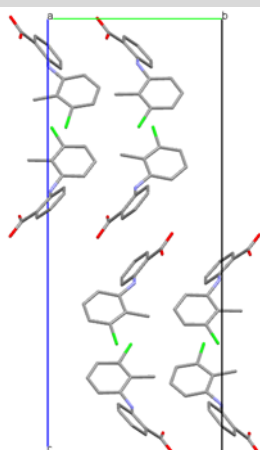
	TA form I	#19MA_5643
Space Group	P2$_1$/c	P2$_1$
a	4.826(2)	5.0
b	32.128(11)	31.1
c	8.041(4)	8.8
α	90	90
β	104.88(3)	67.2
γ	90	90
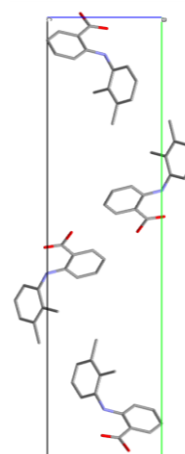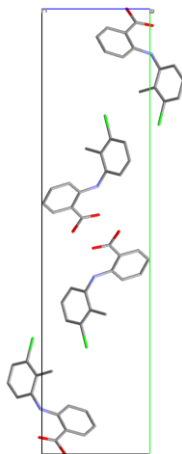
Appendix 7

^{1}H NMR spectra of the MA-TA solid solution series. The spectra show the integration values of the methyl peaks used to determine the relative ratio of TA:MA in the crystals.

Target mole fraction of TA – 0.5

Acquisition Time (sec)	3.9999	Comment	RW-MATA01 PROTON.ucl CDCl3 {C:\Bruker\TOPSPIN} dat 7	Date		04 Nov 2014 14:15:28
Date Stamp	04 Nov 2014 14:15:28			File Name		D:\Users\Rona\Documents\PhD\NMR\MATA01\pdata\1\1r
Frequency (MHz)	299.87	Nucleus	1H	Number of Transients	16	Origin	spect
Original Points Count	24691	Owner	av300	Points Count	32768	Pulse Sequence	zg30
Receiver Gain	2048.00	SW(cyclical) (Hz)	6172.84	Solvent	CHLOROFORM-d		
Spectrum Offset (Hz)	1848.1602	Spectrum Type	STANDARD	Sweep Width (Hz)	6172.65	Temperature (degree C) 24.080	

No.	(ppm)	Value	Absolute Value	Non-Negative Value
1	1589 .. 2.18	0.07215013	3.96810200e+7	0.07215013
2	3109 .. 2.34	0.12739122	7.00624400e+7	0.12739122

Target mole fraction of TA – 0.6

Acquisition Time (sec)	3.9999	Comment	RW-MATA02 PROTON.ucl CDCl3 {C:\Bruker\TOPSPIN} dat 8	Date	04 Nov 2014 14:19:44
Date Stamp	04 Nov 2014 14:19:44		File Name	D:\Users\Rona\Documents\PhD\NMR\MATA02\pdata\1\1r	
Frequency (MHz)	299.87	Nucleus	1H	Number of Transients	16	Origin	spect
Original Points Count	24691	Owner	av300	Points Count	32768	Pulse Sequence	zg30
Receiver Gain	1625.50	SW(cyclical) (Hz)	6172.84	Solvent	CHLOROFORM-d	
Spectrum Offset (Hz)	1848.1602	Spectrum Type	STANDARD	Sweep Width (Hz)	6172.65	Temperature (degree C)	24.080

No.	(ppm)	Value	Absolute Value	Non-Negative Value
1	1521 .. 2.23	0.09000359	1.01728176e+8	0.09000359
2	2946 .. 2.40	0.22211123	2.51045200e+8	0.22211123

Target mole fraction of TA − 0.7

Acquisition Time (sec)	3.9999	Comment	RW-MATA03 PROTON.ucl CDCl3 {C:\Bruker\TOPSPIN} dat 9	Date	04 Nov 2014 14:26:08
Date Stamp	04 Nov 2014 14:26:08			File Name	D:\Users\Rona\Documents\PhD\NMR\MATA03\pdata\1\1r
Frequency (MHz)	299.87	Nucleus	1H	Number of Transients	16	Origin	spect
Original Points Count	24691	Owner	av300	Points Count	32768	Pulse Sequence	zg30
Receiver Gain	2048.00	SW(cyclical) (Hz)	6172.84	Solvent	CHLOROFORM-d
Spectrum Offset (Hz)	1848.1602	Spectrum Type	STANDARD	Sweep Width (Hz)	6172.65	Temperature (degree C)	24.080

No.	(ppm)	Value	Absolute Value	Non-Negative Value
1	1761 .. 2.19	0.05963841	4.67667320e+7	0.05963841
2	3176 .. 2.35	0.19058315	1.49449840e+8	0.19058315

Target mole fraction of TA – 0.8

Acquisition Time (sec)	3.9999	Comment		RW-MATA04 PROTON.ucl CDCl3 {C:\Bruker\TOPSPIN} dat 13			
Date	04 Nov 2014 14:32:32			Date Stamp	04 Nov 2014 14:32:32		
File Name	D:\Users\Rona\Documents\PhD\NMR\MATA04\pdata\1\1r			Frequency (MHz)	299.87	Nucleus	1H
Number of Transients	16	Origin	spect	Original Points Count	24691	Owner	av300
Points Count	32768	Pulse Sequence	zg30	Receiver Gain	1625.50	SW(cyclical) (Hz)	6172.84
Solvent	CHLOROFORM-d			Spectrum Offset (Hz)	1848.1602	Spectrum Type	STANDARD
Sweep Width (Hz)	6172.65	Temperature (degree C)	24.080				

No.	(ppm)	Value	Absolute Value	Non-Negative Value
1	1663 .. 2.19	0.05187771	4.13026480e+7	0.05187771
2	3075 .. 2.36	0.21940650	1.74681376e+8	0.21940650

Appendix 8

Raman spectrum of three different crystals of TA form VI alongside the peak list in the range 3200 cm^{-1} to 100 cm^{-1}.

TA form VI	
3075	809
2921	796
1626	774
1602	723
1581	702
1570	658
1513	621
1463	606
1407	571
1383	558
1335	546
1285	519
1276	503
1250	488
1234	432
1204	396
1162	349
1143	320
1085	283
1072	245
1043	229
908	208
898	162
835	141
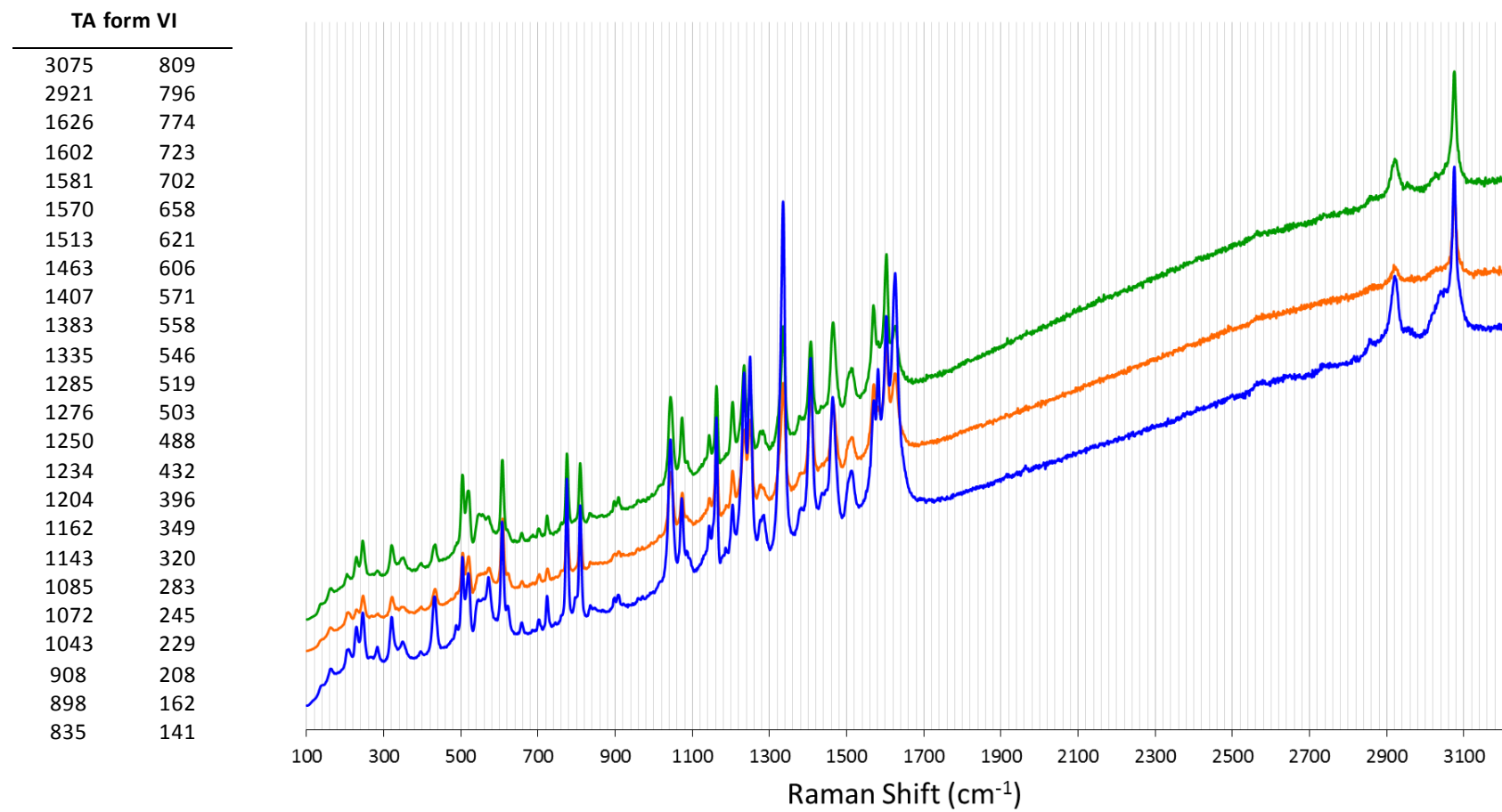
Appendix 9

Screen grab of the QTZ program used to monitor the deposition of sublimed MA/TA onto the QCM. The program shows that the resonant frequency of the crystal decreases as the mass on the crystal increases.
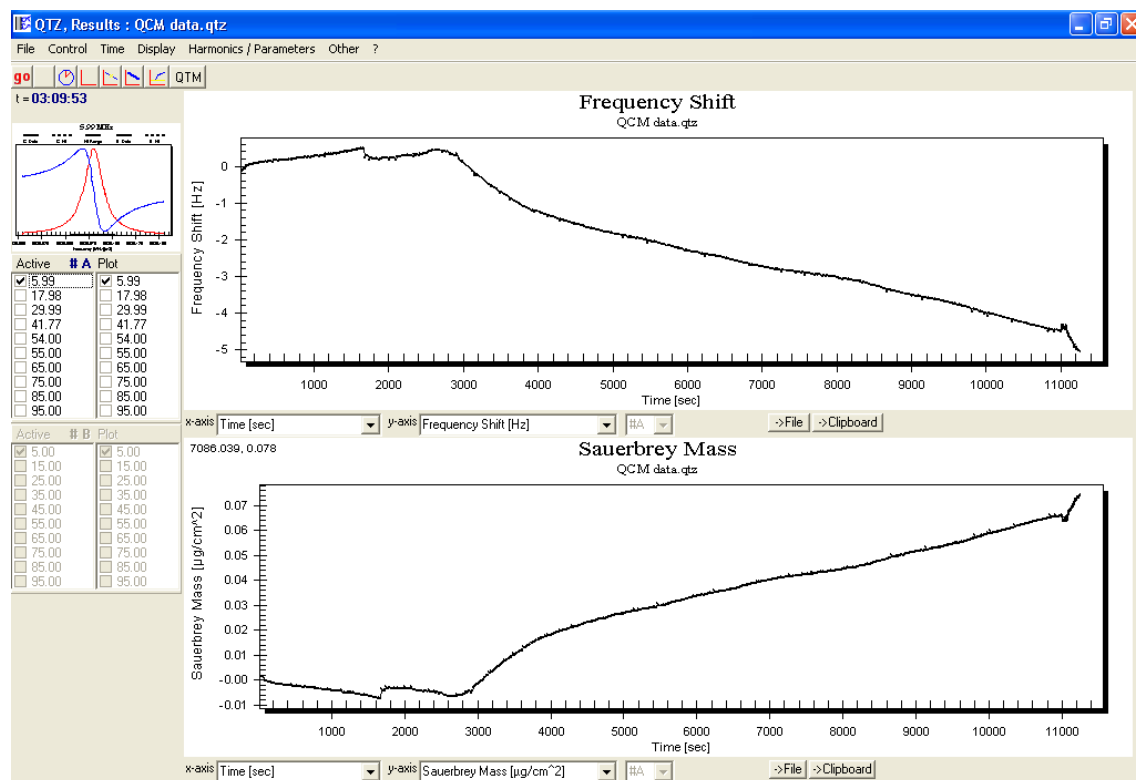
Appendix 10

PXRD patterns of TA that has been deposited onto both glass and copper surfaces with the evaporation source set to different temperatures. The PXRD patterns are labelled with the temperature of the evaporation source and the surface the TA was deposited onto. For each evaporation source temperature, 100 °C and 150 °C, the TA was deposited onto both the glass and copper surfaces simultanesouly.
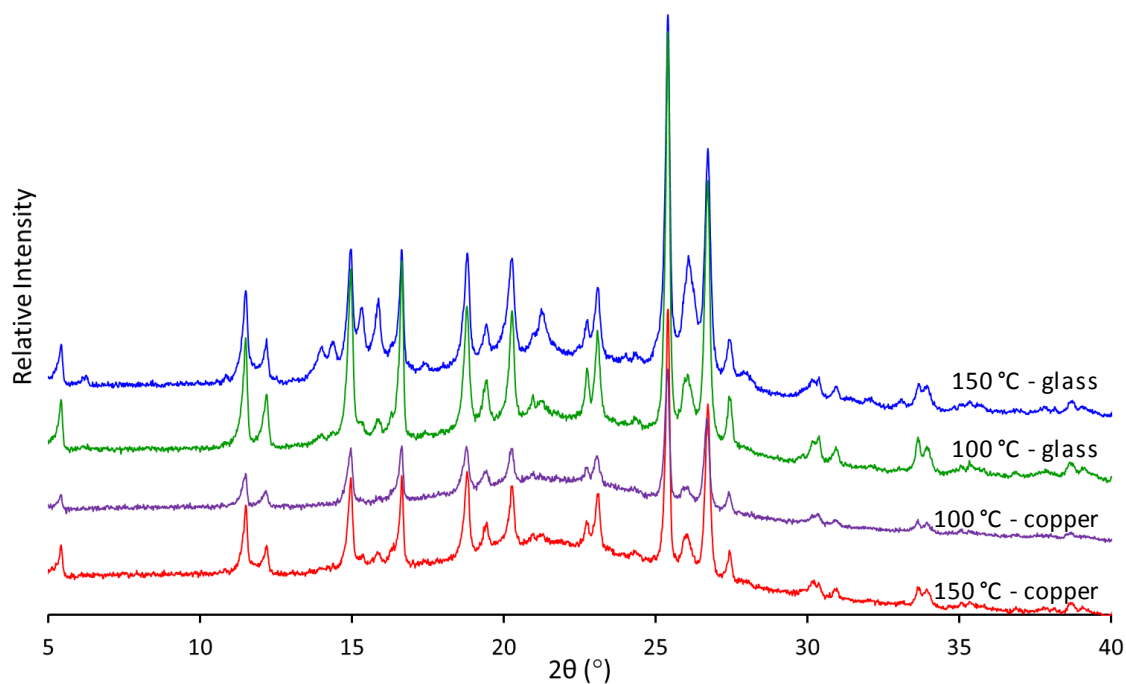
Appendix 11

Infrared spectra of multiple preparations of TA that has been deposited onto both glass (top three spectra) and copper surfaces (bottom five spectra). All the spectra have a N-H stretching peak at 3336 cm^{-1} with a slight shoulder to lower wavenumbers which could be due to the phase purity of the sample.
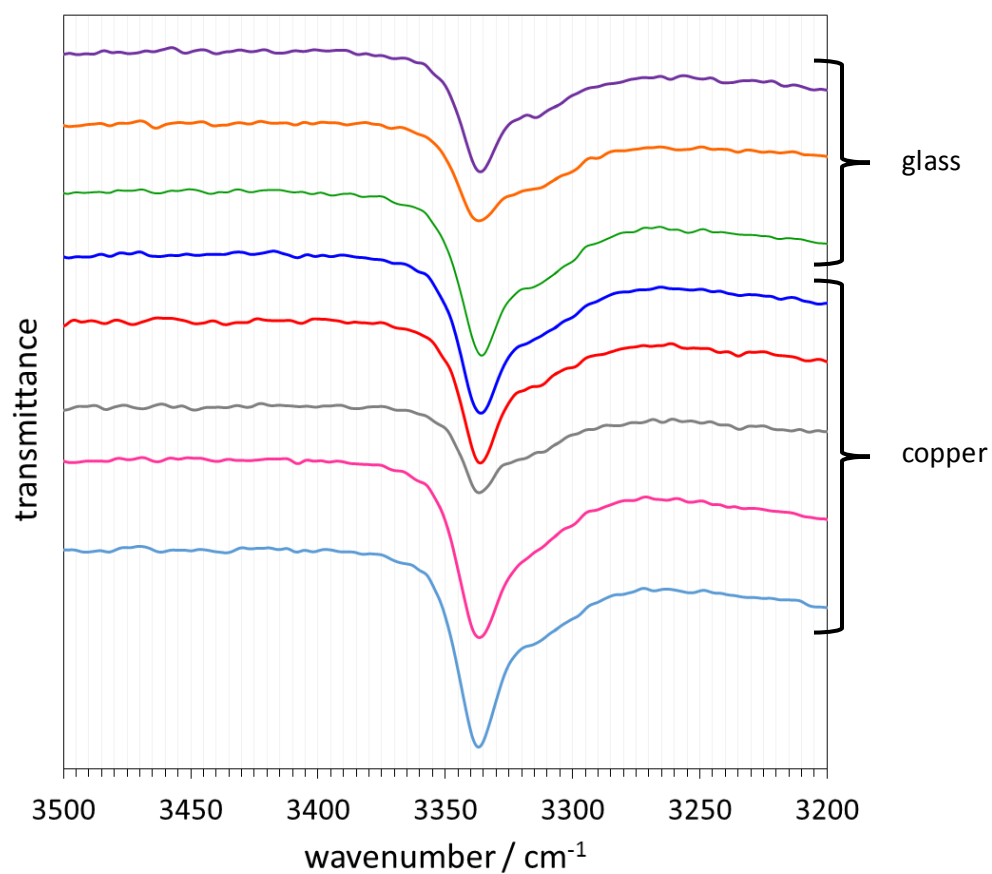
Appendix 12

PXRD patterns of an additional sample of TA VII collected *in situ* as the sample is heated at a heating rate of 10 °C min⁻¹.
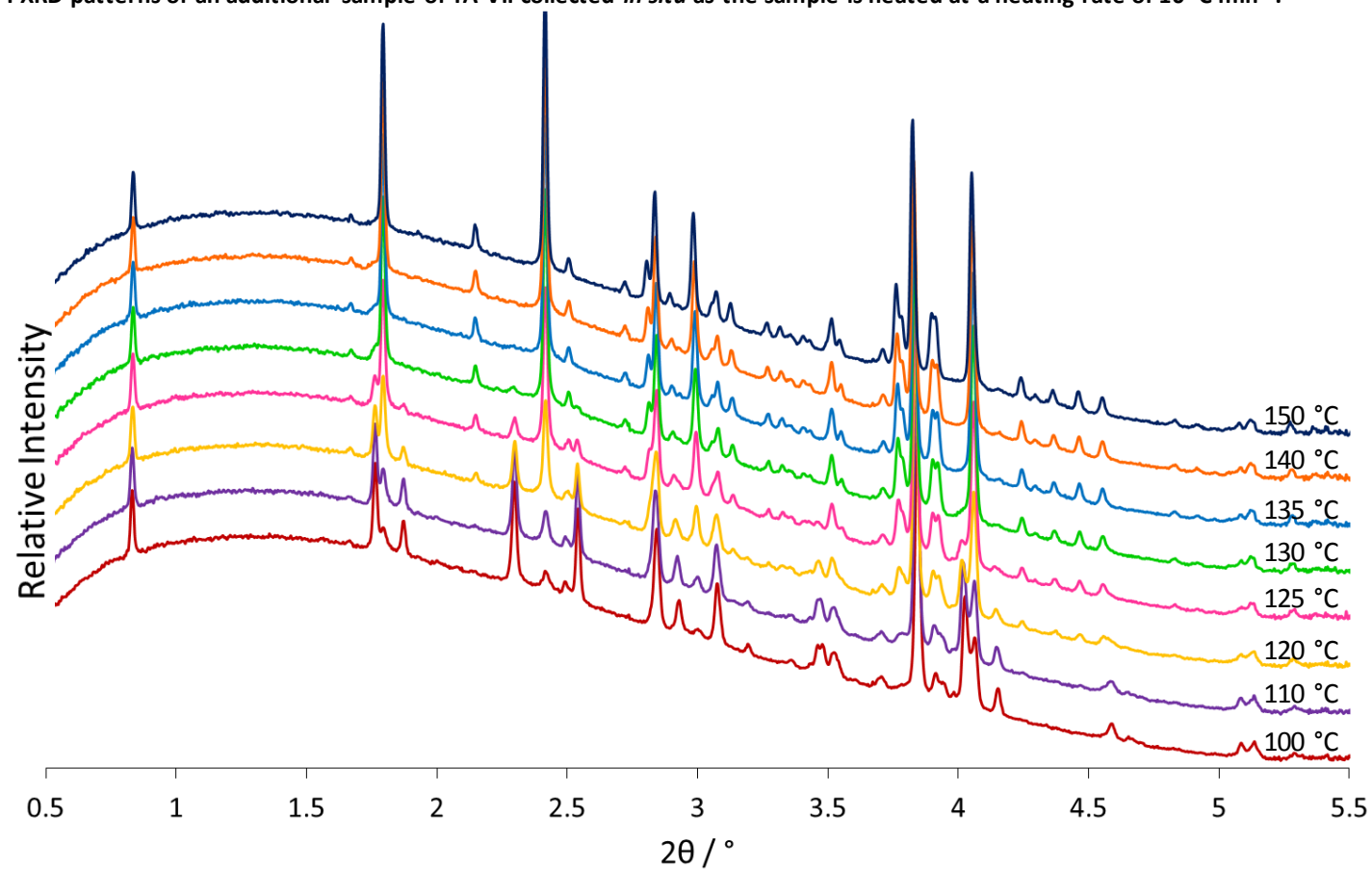
Appendix 13

PXRD patterns of three separate experiments where MA was onto deposited onto the copper depostion plate at 120 °C (blue), at 100 °C (orange) and at an unknown temperature (green). The top two diffraction patterns are experiments where the temperature of the evaporation source could be set, the bottom diffraction pattern is from the apparatus where the temperature is unkown.
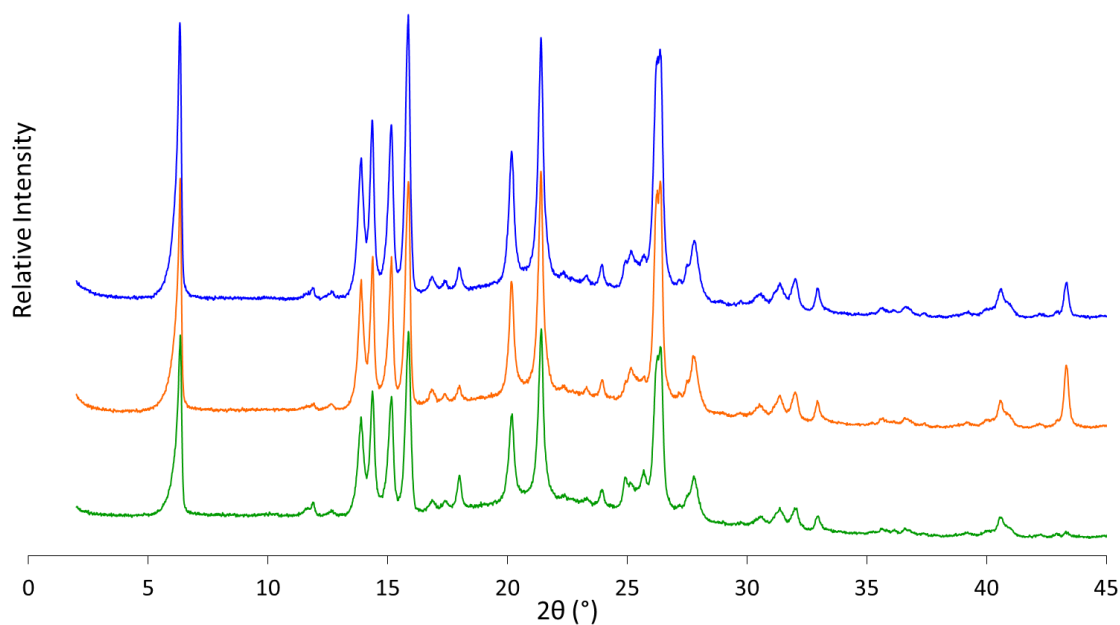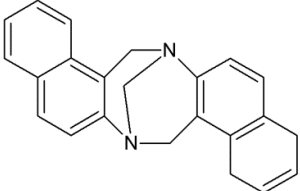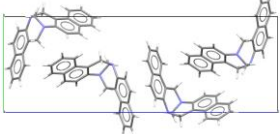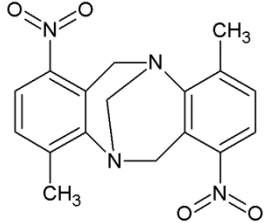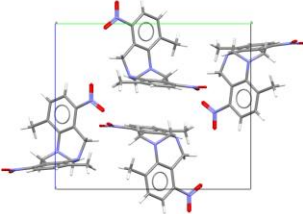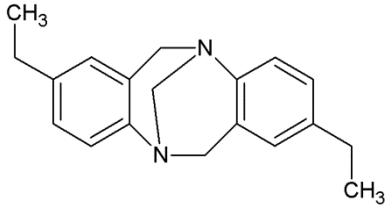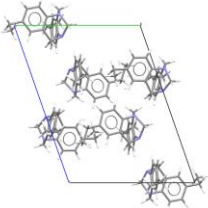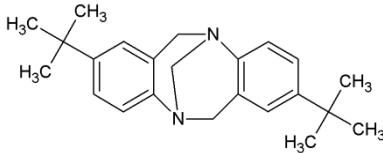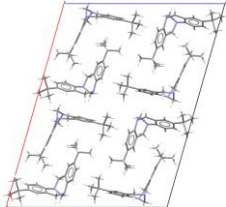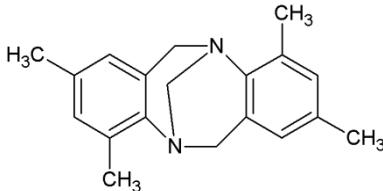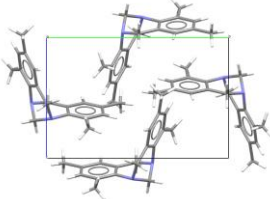
Appendix 14
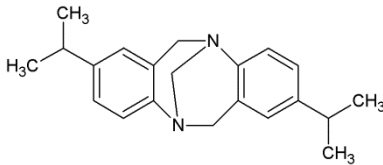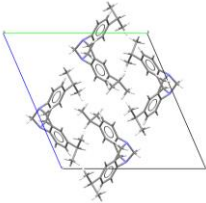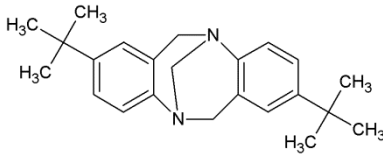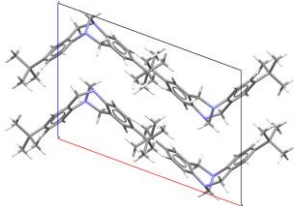
Infrared spectra of the N-H streching band in three different samples of MA that has been deposited onto the glass microscope slide with a crucible temperature set to 120 °C. The figure suggests that the proportion of MA I:MA II varies depending on the sample.
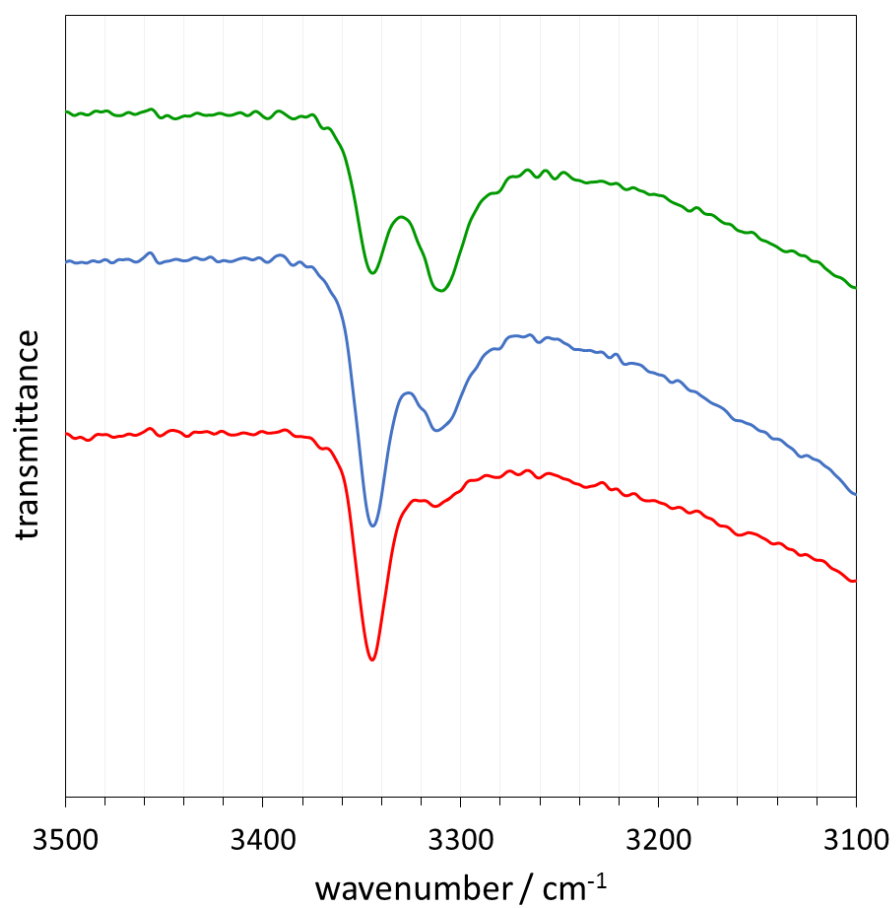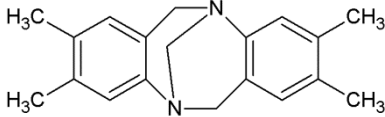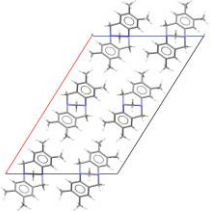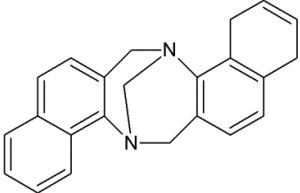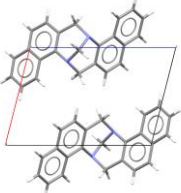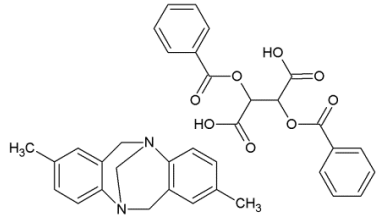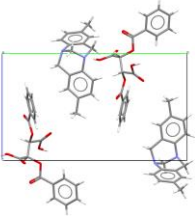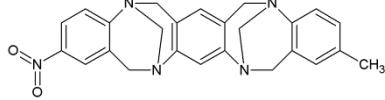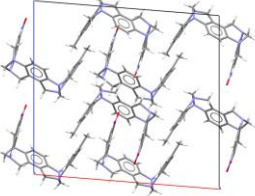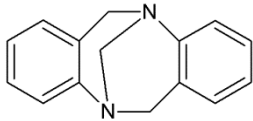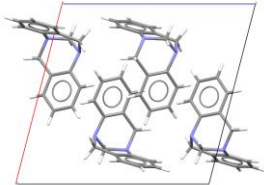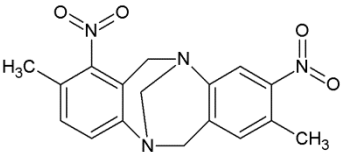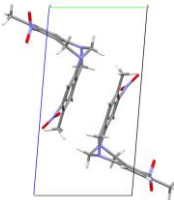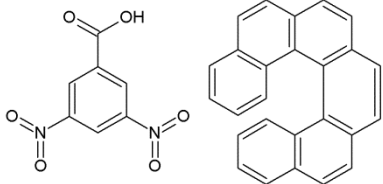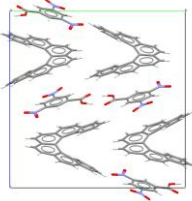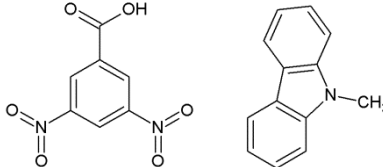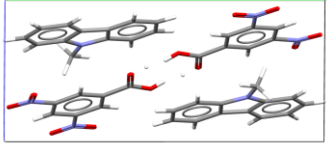
Appendix 15
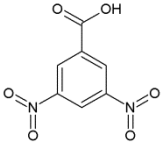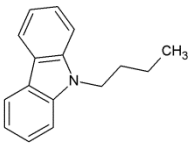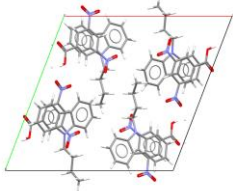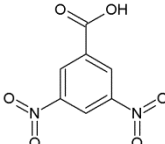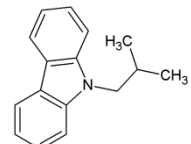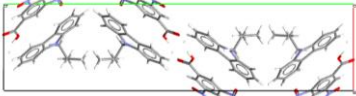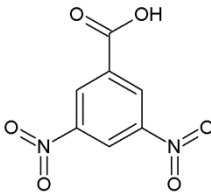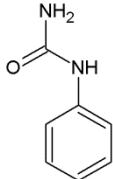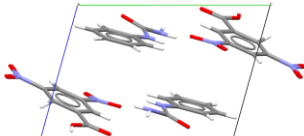
Reproduction of the experimental crystal structures of crystal structures that are closely related to the cocrystal XXV using the experimental conformations and the distributed multipoles at the PBE0/6-31+G(d) level of theory and the FIT pasratters for the exp-6 potential. The results show that this method gives a good reproduction of all the crsytal structures that were tested as all reproductions give a good overlay of 15 molecules with the experimental structures.

CDC Refcode	Molecular structure	Unit Cell		a / Å	b / Å	c / Å	α / °	β / °	γ / °	$n(\text{rmsd}_n)$ / Å
DEFQAG			exp	6.454	9.45	27.15	90	90	90	15(0.106638)
			comp	6.4705	9.4771	27.5199	90	90	90	
DORJEA			exp	8.3118	14.586	12.386	90	95.854	90	15(0.139514)
			comp	8.4232	14.6078	12.5547	90	96.2126	90	
DUWBON			exp	10.9907	13.8123	17.224	71.469	88.621	70.319	15(0.153361)
			comp	11.0531	14.0963	17.3523	71.5858	88.2927	70.2999	

				exp/comp	a	b	c	α	β	γ	

DUWBUT			**exp**	7.6347	15.454	15.936	66.214	82.257	85.37	15(0.187412)
			comp	7.7262	15.5889	15.9618	66.4686	84.0388	87.1388	
DUWCII			**exp**	15.529	12.186	10.764	90	110.147	90	15(0.153968)
			comp	15.397	12.3226	10.9792	90	109.7788	90	
DUWCOO			**exp**	28.37	6.6841	21.6271	90	105.94	90	15(0.139802)
			comp	28.7087	6.7985	21.621	90	105.246	90	
FUPKUW			**exp**	14.9491	12.5597	8.3034	90	92.276	90	15(0.126623)
			comp	14.7396	12.6856	8.3225	90	92.9298	90	

FUPLEH			exp	21.661	5.486	14.906	90	122.04	90	15(0.169719)
			comp	21.5122	5.637	14.806	90	122.1036	90	
LUDROS			exp	7.9017	10.4132	11.0932	103.385	98.365	110.022	15(0.320331)
			comp	7.8716	10.7351	11.2236	104.4191	98.1104	107.8512	
RELCUH			exp	8.1272	18.1103	10.4433	90	90.568	90	15(0.113515)
			comp	8.1516	18.1001	10.4465	90	90.0221	90	
XICRIK			exp	20.273	10.6934	18.936	90	94.567	90	15(0.180958)
			comp	20.1053	10.9586	19.0589	90	95.287	90	

XIFTAI			**exp**	12.266	7.362	12.759	90	104.457	90	15(0.150596)
			comp	12.498	7.4329	13.0345	90	104.3953	90	
YEYNAS			**exp**	7.526	8.057	13.932	92.944	92.93	115.649	15(0.109832)
			comp	7.6432	8.1542	13.9122	93.0203	92.6623	116.2737	
ABUNOA			**exp**	7.7752	18.2049	18.6065	90	101.444	90	15(0.282457)
			comp	7.7834	17.7316	18.4737	90	101.7816	90	
KIZQIT			**exp**	8.414	15.763	6.991	91.82	99.91	81.59	15(0.235907)
			comp	8.2518	15.8157	7.1082	92.1886	97.1876	79.7187	

KIZQUF			**exp**	16.723	16.784	8.4129	102.36	92.34	109.91	15(0.244149)
			comp	16.3594	17.0274	8.4012	100.9691	91.7013	110.965	
KIZREQ			**exp**	8.212	31.924	8.438	90	106.54	90	15(0.199687)
			comp	8.251	31.4749	8.3647	90	104.635	90	
NEMSUT			**exp**	10.908	11.001	7.159	106.02	94.47	65.78	15(0.269362)
			comp	10.9503	11.0468	7.0355	108.361	95.9533	66.6832	

Appendix 16

The bond lengths, angles and dihedrals that changed as a result of the fully atomistic CrystalOptimizer calculations of CUKCAM04 and CUKCAM22. The rows highlighted in grey refer to the degrees of freedom that were chosen to be optimised in subsequent CrystalOptimizer calculations. The criteria for choosing a degree of freedom was angles and dihedrals with a change in value greater that 0.5° and 1.0° respectively. In general, changes within the phenyl ring were ignored as they were tending towards the gas phase optimised molecular conformation which is the input in the search.

CUKCAM04

Name (as input)	Start (Å,°)	-	New (Å,°)	Change (Å,°)
bnd2(C2_C1)	1.394545	-	1.395879	0.001334
bnd3(C3_C2)	1.382907	-	1.389116	0.00621
ang3(C3_C2_C1)	118.2872	-	118.4928	0.2056
bnd4(C4_C3)	1.383194	-	1.386677	0.003483
ang4(C4_C3_C2)	123.309	-	122.7253	-0.5838
dih4(C4_C3_C2_C1)	0.7956	-	-1.4376	-2.2331
bnd5(C5_C4)	1.382529	-	1.388995	0.006466
ang5(C5_C4_C3)	116.3074	-	116.9802	0.6728
dih5(C5_C4_C3_C2)	0.5753	-	1.7372	1.1619
bnd6(C6_C1)	1.390217	-	1.395027	0.00481
ang6(C6_C1_C2)	120.5172	-	120.4936	-0.0236
dih6(C6_C1_C2_C3)	-1.176	-	1.0605	2.2365
bnd7(C7_C1)	1.490009	-	1.489612	-0.0004
ang7(C7_C1_C2)	120.3718	-	121.3765	1.0047
dih7(C7_C1_C2_C3)	176.5042	-	178.3795	1.8753
bnd8(N1_C3)	1.473546	-	1.463751	-0.0098
ang8(N1_C3_C2)	117.9376	-	118.5249	0.5873
dih8(N1_C3_C2_C1)	-177.536	-	-179.881	-2.3457
bnd9(N2_C5)	1.474017	-	1.46409	-0.00993
ang9(N2_C5_C4)	118.192	-	118.2155	0.0235
dih9(N2_C5_C4_C3)	-179.388	-	-179.42	-0.0325
bnd10(O2_C7)	1.305315	-	1.335664	0.030349
ang10(O2_C7_C1)	114.3164	-	113.0159	-1.3005
dih10(O2_C7_C1_C2)	7.7572	-	6.0831	-1.6741
bnd11(O1_C7)	1.231707	-	1.219626	-0.01208
ang11(O1_C7_C1)	120.649	-	122.5087	1.8597
dih11(O1_C7_C1_C2)	-171.764	-	-173.664	-1.8999

bnd12(O3_N1)	1.225995	-	1.218319	-0.00768
ang12(O3_N1_C3)	117.6912	-	117.3039	-0.3872
dih12(O3_N1_C3_C2)	-23.3795	-	-22.0085	1.3711
bnd13(O4_N1)	1.224963	-	1.219023	-0.00594
ang13(O4_N1_C3)	117.5165	-	117.3836	-0.1329
dih13(O4_N1_C3_C2)	155.1213	-	157.3187	2.1974
bnd14(O5_N2)	1.221965	-	1.220478	-0.00149
ang14(O5_N2_C5)	117.3374	-	117.1275	-0.2099
dih14(O5_N2_C5_C4)	-0.0287	-	-2.0638	-2.0351
bnd15(O6_N2)	1.22375	-	1.219965	-0.00379
ang15(O6_N2_C5)	118.3935	-	118.0287	-0.3647
dih15(O6_N2_C5_C4)	-179.802	-	-182.259	-2.4567
bnd16(H1_C2)	0.921787	-	1.083998	0.162211
ang16(H1_C2_C3)	120.4631	-	120.3005	-0.1626
dih16(H1_C2_C3_C4)	178.4868	-	177.8576	-0.6292
bnd17(H2_C4)	0.950219	-	1.08385	0.133631
ang17(H2_C4_C3)	121.5509	-	121.7014	0.1505
dih17(H2_C4_C3_C2)	178.8642	-	181.5405	2.6764
bnd18(H3_C6)	0.952448	-	1.084924	0.132476
ang18(H3_C6_C1)	120.6794	-	120.1596	-0.5199
dih18(H3_C6_C1_C2)	177.8938	-	179.1398	1.246
bnd19(H4_O1)	0.960258	-	0.971458	0.0112
ang19(H4_O1_C7)	111.2888	-	110.4004	-0.8884
dih19(H4_O1_C7_C1)	-178.314	-	-179.353	-1.0385

CUKCAM22

Name (as input)	Start (Å,°)	-	New (Å,°)	Change (Å,°)
bnd2(C2_C1)	1.387831	-	1.395784	0.007953
bnd3(C3_C2)	1.38059	-	1.389143	0.008553
ang3(C3_C2_C1)	118.3237	-	118.506	0.1823
bnd4(C4_C3)	1.37792	-	1.386698	0.008778
ang4(C4_C3_C2)	123.0281	-	122.7046	-0.3235
dih4(C4_C3_C2_C1)	-2.2834	-	0.3398	2.6232
bnd5(C5_C4)	1.383298	-	1.389005	0.005707
ang5(C5_C4_C3)	116.4606	-	117.0415	0.5809
dih5(C5_C4_C3_C2)	1.5875	-	0.1587	-1.4288
bnd6(C6_C1)	1.385043	-	1.39507	0.010027
ang6(C6_C1_C2)	120.7762	-	120.4798	-0.2963
dih6(C6_C1_C2_C3)	0.6102	-	-1.4473	-2.0575
bnd7(C7_C1)	1.479656	-	1.488628	0.008972
ang7(C7_C1_C2)	120.5219	-	121.4447	0.9228
dih7(C7_C1_C2_C3)	-178.461	-	-180.479	-2.018
bnd8(N1_C3)	1.459842	-	1.46346	0.003618
ang8(N1_C3_C2)	118.078	-	118.6131	0.5352
dih8(N1_C3_C2_C1)	177.2856	-	180.6524	3.3668
bnd9(N2_C5)	1.45792	-	1.461989	0.00407
ang9(N2_C5_C4)	118.4848	-	118.4023	-0.0825
dih9(N2_C5_C4_C3)	179.8969	-	179.7117	-0.1853
bnd10(O2_C7)	1.299281	-	1.335558	0.036277
ang10(O2_C7_C1)	113.9344	-	113.1053	-0.8291
dih10(O2_C7_C1_C2)	-9.2136	-	-7.4467	1.7669
bnd11(O1_C7)	1.221099	-	1.219975	-0.00112
ang11(O1_C7_C1)	120.9827	-	122.2623	1.2796
dih11(O1_C7_C1_C2)	171.2998	-	173.1587	1.8589
bnd12(O3_N1)	1.213933	-	1.218409	0.004476
ang12(O3_N1_C3)	117.6916	-	117.2908	-0.4008
dih12(O3_N1_C3_C2)	18.1402	-	17.4328	-0.7074
bnd13(O4_N1)	1.217854	-	1.220335	0.002482
ang13(O4_N1_C3)	117.7782	-	117.6294	-0.1489
dih13(O4_N1_C3_C2)	-160.502	-	-162.434	-1.9317
bnd14(O5_N2)	1.217319	-	1.219748	0.002429

ang14(O5_N2_C5)	117.3995	-	117.1836	-0.2159
dih14(O5_N2_C5_C4)	4.5182	-	5.5932	1.075
bnd15(O6_N2)	1.218622	-	1.220494	0.001872
ang15(O6_N2_C5)	118.0171	-	117.9147	-0.1024
dih15(O6_N2_C5_C4)	-175.847	-	-174.734	1.1131
bnd16(H1_C2)	1.074548	-	1.083945	0.009397
ang16(H1_C2_C3)	121.0064	-	120.2954	-0.7111
dih16(H1_C2_C3_C4)	179.6346	-	180.2227	0.5881
bnd17(H2_C4)	1.080961	-	1.083876	0.002916
ang17(H2_C4_C3)	121.9237	-	121.6865	-0.2372
dih17(H2_C4_C3_C2)	-177.711	-	-179.421	-1.7098
bnd18(H3_C6)	1.079081	-	1.084871	0.00579
ang18(H3_C6_C1)	121.0138	-	120.2621	-0.7517
dih18(H3_C6_C1_C2)	-177.814	-	-178.959	-1.1446
bnd19(H4_O1)	1.00634	-	0.971707	-0.03463
ang19(H4_O1_C7)	110.3293	-	110.0085	-0.3208
dih19(H4_O1_C7_C1)	-179.995	-	-180.274	-0.2783

CIF Files

File name	Description
MA_I	MA form I redetermination
MA_II	MA form II redetermination
Prelim_MA-TA	Solid solution - preliminary cocrystallisation experiment
0.5-TA	Solid solution – target mole fraction of TA = 0.5
0.6-TA	Solid solution – target mole fraction of TA = 0.6
0.8-TA	Solid solution – target mole fraction of TA = 0.8
TA_VI(a)	TA form VI – crystal (a) from seeding with MA form I
TA_VI(b)	TA form VI – crystal (b) from seeding with MA form I
TA_VII	TA form VII – vapour deposition onto copper. Refinement by Jeremy Cockcroft